ABSTRACT

Title of Dissertation: INTERACTIONS BETWEEN MASSIVE STELLAR FEEDBACK AND INTERSTELLAR GAS IN THE EAGLE NEBULA

Ramsey Lee Karim
Doctor of Philosophy, 2024

Dissertation Directed by: Professor Lee G. Mundy
Dr. Marc W. Pound
Professor Alexander G. G. M. Tielens
Department of Astronomy

My thesis describes multi-scale stellar feedback processes observed in the Eagle Nebula star forming region in our Milky Way galaxy. Stellar feedback from massive stars encompasses bright ultraviolet radiation which ionizes atoms and dissociates molecules in gas surrounding the stars as well as supersonic winds which impact the gas and create hot shocked layers. I study the interaction of stellar radiative and mechanical feedback with pre-existing density inhomogeneities in the molecular cloud in order to learn about the effects of the interstellar environment on the relative efficiency of various forms of feedback.

This work informs our understanding of the life cycle of interstellar gas: gas forms stars and is then exposed to their winds and radiation, and we would like to know how that affects the formation of future generations of stars. The Eagle Nebula's relative proximity to us means we observe the H II region with high spatial resolution. Extra-galactic studies observe many H II

regions simultaneously and at a variety of cosmic ages, but lack the resolution to understand the structure of the individual regions. High resolution studies of Galactic sources such as the Eagle serve as templates for what extra-galactic astronomers are seeing in far-away galaxies. The work also contributes to sub-grid feedback prescriptions in large-scale simulations of galaxy formation and evolution. Stars and their feedback are too small to be simulated in these contexts, so theorists require accurate approximations for the effects of stellar feedback.

Massive stars form in massive molecular gas clouds and then deliver vast quantities of energy back into the clouds in the form of radiation and stellar winds. They form H II regions, 1-to-10-light-year scale areas of ionized hydrogen, which are often overpressured bubbles compared to the surrounding interstellar medium, and their supersonic winds sweep up a compressed shell of gas.

Around the edge of the H II region, there lies a layer of gas which receives no $>$13.6 eV extreme-ultraviolet H-ionizing radiation (EUV), but is rich in 6-13.6 eV far-ultraviolet radiation (FUV) which can photodissociate molecules such as CO and H_2 and ionize C. These photodissociation regions (PDRs) are heated via the photoelectric effect as FUV radiation interacts with organic molecules called polycyclic aromatic hydrocarbons (PAHs), and the regions are cooled by the collisionally excited far-infrared fine structure transitions of ionized carbon and atomic oxygen.

The FEEDBACK SOFIA C^+ Legacy Project (Schneider et al., 2020) studies the coupling efficiency of that energetic feedback to the gas by observing one such transition of singly ionized carbon at 158 μm referred to as C^+ or [C II]. In this astrophysical context, the line is emitted primarily within PDRs. With modern heterodyne receivers and an observatory above Earth's atmosphere, we can both detect and spectroscopically resolve the [C II] line and therefore trace the morphology and kinematics of the PDR regions surrounding massive stars. We contextualize these observations with velocity-resolved observations tracing the un-illuminated molecular gas beyond the PDRs and a variety of archival data spanning the electromagnetic spectrum from radio to X-ray.

I use these observations to study the Eagle Nebula, home to the iconic Pillars of Creation, and learn how pre-existing density structure evolves when exposed to stellar feedback and what that implies for the energetic coupling of the stellar feedback to the gas. My first study covers the Pillars of Creation in a detailed, multi-wavelength analysis published in the Astronomical Journal. We find that these pillars are long-lasting structures on the scale of the H II region age and that they must arise from pre-existing density structures. My second study zooms out to the greater Eagle Nebula H II region to learn how the massive stars affect the rest of the region. This analysis concludes that the primordial filamentary structure which must have led to the formation of the stellar cluster also governs the shape of the H II region and how much of the surrounding gas is affected by the feedback. Finally, I describe a software package, scoby, which I developed to aid these two studies. The software connects theoretical feedback estimates to observed star catalogs and delivers results tuned for observational studies like these. It has been used for several published analyses of other regions.

INTERACTIONS BETWEEN MASSIVE STELLAR FEEDBACK AND INTERSTELLAR GAS IN THE EAGLE NEBULA

by

Ramsey Lee Karim

Dissertation submitted to the Faculty of the Graduate School of the
University of Maryland, College Park in partial fulfillment
of the requirements for the degree of
Doctor of Philosophy
2024

Advisory Committee:
Professor Lee G. Mundy, Chair/Advisor
Professor Alexander G. G. M. Tielens, Co-Advisor
Dr. Marc W. Pound, Co-Advisor
Professor Andrew Harris
Professor Loren D. Anderson
Professor Amy Mullin

Preface

The work presented in Chapter 2 of this thesis has been published in *The Astronomical Journal*. The content is unchanged and the formatting, particularly of the Tables, has been adjusted as necessary. Chapter 3 is in preparation for submission to the same journal soon after submission of this thesis.

Acknowledgments

I am grateful to my dissertation committee for their valuable time and feedback, which I found invaluable as I crafted my thesis. I thank my advisers Professor Alexander Tielens, Dr. Marc Pound, and Professor Lee Mundy, for their roles in guiding me to be the scientist I am today. I thank Professor Amy Mullin, Professor Loren Anderson, and Professor Andrew Harris for agreeing to serve on my dissertation committee.

My colleagues here at UMD have been the highlight of my graduate experience. My wonderful classmates turned housemates, Harrison, Milena, Vicente, Sergio, Teal, Tomás, Ellis, and Umisha, thank you for the wild and interesting times we endured. We survived everything from power outages to floods and we will never forget our time amongst the rats. Julian, Erica, Jegug, Ben, Gabe, Carrie, and Joe, I appreciate the time I spent with you all playing pool or D&D, visiting the dining hall, or seeing you headline DC9. Liz, thank you for the many enlightening conversations about H II regions. Vicente, thank you dearly for your friendship and the many conversations we shared in our office and at Town Hall. Thank you, Town Hall, for hosting many cherished conversations with my dear friends.

To my senior colleagues in FEEDBACK, the LMA, and at UMD; Maitraiyee, Ümit, Lars, Kim, Becca, Laura, and Sara: thank you all for setting excellent examples as researchers and collaborators and being a pleasure to work with along the way.

I thank my mother and my father for their enthusiasm for science and the natural world and for putting me through college. None of this would be possible otherwise. Thank you Celia, Nathan, and the rest of my family for your support.

I thank all the friends who feel like family. Paul, Ben, I deeply appreciate you both and, no matter where in the world we find each other, you make me feel at home.

Erica, thank you from the bottom of my heart for your boundless love and support.

Table of Contents

List of Tables

List of Figures

List of Abbreviations

ACIS	Advanced CCD Imaging Spectrometer
APEX	Atacama Pathfinder Experiment
API	Application programming interface
BICE	Balloon-borne Infrared Carbon Explorer
BRC	Bright-rimmed cloud
CARMA	Combined Array for Millimeter-wave Astronomy
CCD	Charge-coupled device
COBE	Cosmic Background Explorer
EUV	Extreme ultraviolet
FIR	Far infrared
FIRAS	Far Infrared Absolute Spectrophotometer
FUV	Far ultraviolet
FWHM	Full width at half-maximum
GMC	Giant molecular cloud
GMF	Giant molecular filament
HCH II	Hyper-compact H II (region)
HFS	Hub-filament system
HST	Hubble Space Telescope
IR	Infrared
IRAC	Infrared Array Camera
IRAS	Infrared Astronomical Satellite
IRDC	Infrared-dark cloud
ISM	Interstellar medium
JWST	James Webb Space Telescope
LABOCA	Large APEX BOlometer CAmera

MIPS	Multiband Imaging Photometer
MYSO	Massive young stellar object
NGC	New General Catalogue
NIR	Near infrared
PACS	Photodetector Array Camera and Spectrometer
PAH	Polycyclic Aromatic Hydrocarbon
PDR	Photodissociation Region (equivalently but less commonly, Photon-dominated Region)
PMO	Purple Mountain Observatory
PMS	Pre-main sequence
RCW	Rodgers, Campbell, and Whiteoak (catalog)
RDI	Radiation-driven implosion
RT	Rayleigh-Taylor
SF	Star formation
SOFIA	Stratospheric Observatory for Infrared Astronomy
SPIRE	Spectral and Photometric Imaging REceiver
UCH II	Ultra-compact H II (region)
UV	Ultraviolet
VSG	Very small grain
WFI	Wide Field Imager
WISE	Wide-field Infrared Survey Explorer
YSO	Young stellar object

Chapter 1: Introduction

Stars form in cold ($T \sim 10$ K) clouds of interstellar gas when dense clumps and cores of gas fail to resist the gravitational pull towards collapse. If the collapsing core is sufficiently dense, runaway compression ignites fusion in the gas and a star, by definition, is born. Stars are bright and pump radiation back into their cold and previously un-illuminated surroundings. The most impactful radiative feedback is in the far and extreme ultraviolet (FUV, EUV) bands which are respectively defined as radiation between 6–13.6 eV, which photodissociates simple molecules and ionizes carbon, and $>$13.6 eV, which photoionizes hydrogen atoms which carry $\sim$75% of the mass in our Galaxy. Massive stars constantly blow off thin outer layers at high speed via radiation pressure in what we call stellar winds, and these can impart energy and momentum into surrounding gas as they shock against it. Massive, early-type stars of type B3 and earlier (approximately more than 8 times more massive than our Sun, or $\gtrsim$8 $M_\odot$) deliver the lion's share of both radiative and mechanical feedback (Motte et al., 2018).

Stellar feedback regulates the evolution of galaxies. Feedback stirs up and heats gas and governs the cloud and inter-cloud phases of the interstellar medium (ISM), driving the energetic life cycle of the interstellar medium diagrammed in Figure 1.1. Stars modify the structure of their natal clouds with jets and winds as protostars, with winds and radiation as main sequence and evolved stars, and finally with explosive supernova, impacting the star formation efficiency of molecular clouds (Elmegreen, 2011; Hopkins et al., 2014). Locally, winds and radiation can shred the natal cloud in just a few cloud free-fall times (Geen et al., 2016; Kim et al., 2018; Matzner, 2002), while feedback-driven compressive shocks can overcome cloud-supporting forces in marginally stable gas and promote collapse into stars (Elmegreen & Lada, 1977; Zavagno et al., 2010a,b). On a galactic scale, stellar photons escaping the immediate cloud vicinity may join the galactic interstellar radiation field which maintains the ionization of the widespread inter-cloud warm ionized medium (WIM; $\sim 10^4$ K). Hot $\sim 10^6$ K plasma from wind-gas interactions or supernovae may burst out of the galactic plane as a galactic wind.

The Spitzer/GLIMPSE Galactic plane survey revealed our Galaxy to be full of parsec-scale bubbles around O and B type clusters, like those seen in W51 in Figure 1.2, which are driven by thermal pressure from photoionized gas, radiation pressure by stellar photons, or mechanical energy from stellar winds (Churchwell et al., 2006, 2007). The ubiquity of these bubbles in our Galaxy and of telltale spectroscopic signs of star formation in distant galaxies attests to the importance of star formation in stirring up the ISM in galactic ecosystems. Properly accounting for star formation feedback is critical to the accuracy of galaxy evolution models. Authors of galaxy-scale and cosmological simulations do not simulate the physics of individual stars, and instead use sub-grid stellar feedback prescriptions which boil down to the essential understanding that stars are engines in the interstellar medium, converting inert fuel into heat and motion, churning and instigating phase changes in the interstellar gas. It is our responsibility as observers of the interstellar medium to provide them with the most up-to-date information about how feedback couples to the surrounding gas and influences further star formation so that analyses of their large-scale models are founded on accurate assumptions.

We detail in the following sections in Chapter 1 the favorable conditions leading to the formation of high-mass stars (Section 1.1) and the subsequent injection of considerable thermal and kinetic energy into these environments by the stars (Section 1.2). We discuss the observable nature of these gas phases (Section 1.3) and introduce the FEEDBACK survey from which this thesis uses data (Section 1.4). Lastly, we present an overview of the Eagle Nebula (Section 1.6), the subject of the studies in this thesis. In Chapters 2 and 3 we approach the Eagle Nebula with a handful of core questions: How is nearby dense gas affected by NGC 6611? Is the dense gas being cleared away? Can future generations of stars form, or does one massive cluster spell the end of star formation in those clouds? Is feedback-induced gas compression facilitating more star formation? In Chapter 2 we focus on the Pillars of Creation within the Eagle, discussing their origin, geometry, kinematics, and stability with respect to gravitational collapse and photoevaporation. In Chapter 3 we expand our scope to the greater Eagle Nebula star forming complex and H II region and explore the interactions of cluster-scale feedback with dense gas clouds and filaments. In Chapter 4 we describe the `scoby` software library used to support these and other observational feedback studies. We discuss the significance of our findings in Chapter 5 and outline future projects which complement and extend this research.

1.1 High-Mass Star Formation in Ridges and Hubs

The most massive stars stars, also called early-type or OB stars, are of type ∼B3 or earlier; they have luminosities $> 1000\ L_\odot$ and range from ∼8–150 $M_\odot$ (Martins et al., 2008; Motte et al., 2018). They form in massive parsec-scale complexes of gas (Hill et al., 2011; Motte et al., 2018; Nguyen Luong et al., 2011; Tigé et al., 2017) such as ridges and hubs like those pictured in Figure 1.3. Ridges are high density $>10^5$ cm^{-3} filaments (Bonne et al., 2023a; Nguyen-Lu'o'ng

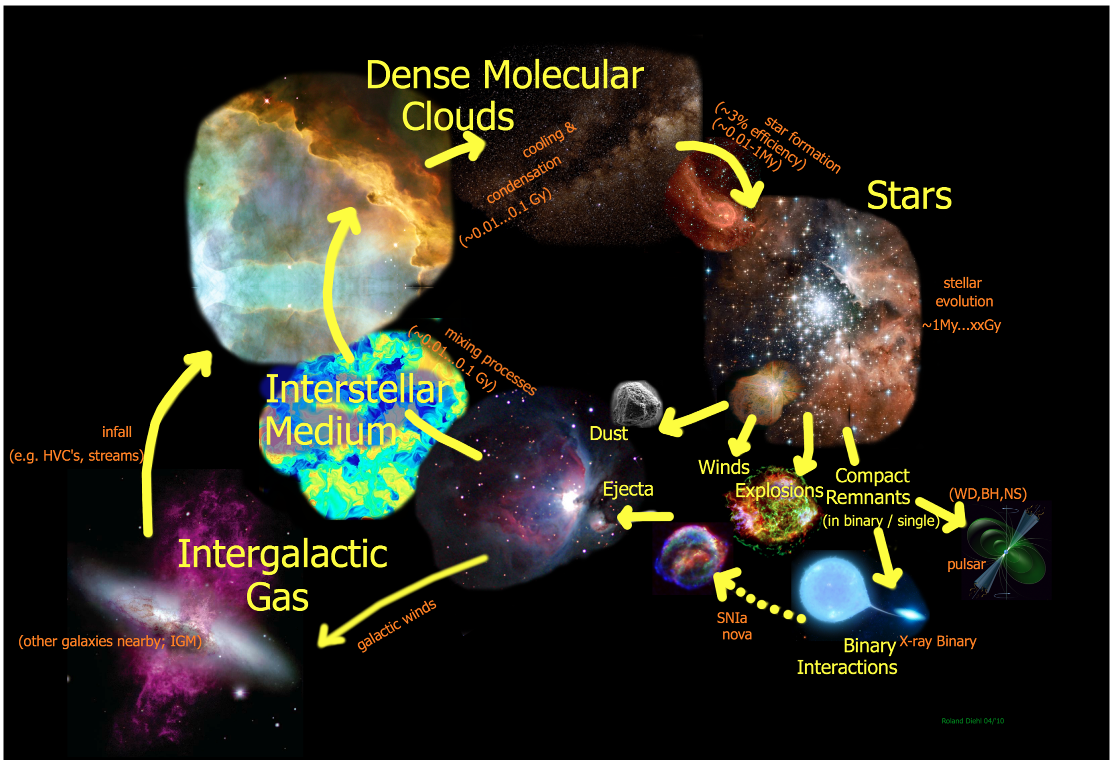

Figure 1.1 Diagram of the cycle of interstellar gas from the presentation by Diehl et al. (2011). Gas is consumed to form stars, and those stars evolve and return energy and enriched gas into the environment. Particularly energetic star formation/destruction events may lead to the ejection of gas from the Galaxy, and gas is also accreted onto the Galaxy from the intergalactic medium. Thus energy and progressively more metal-enriched gas is cycled throughout the Galaxy.

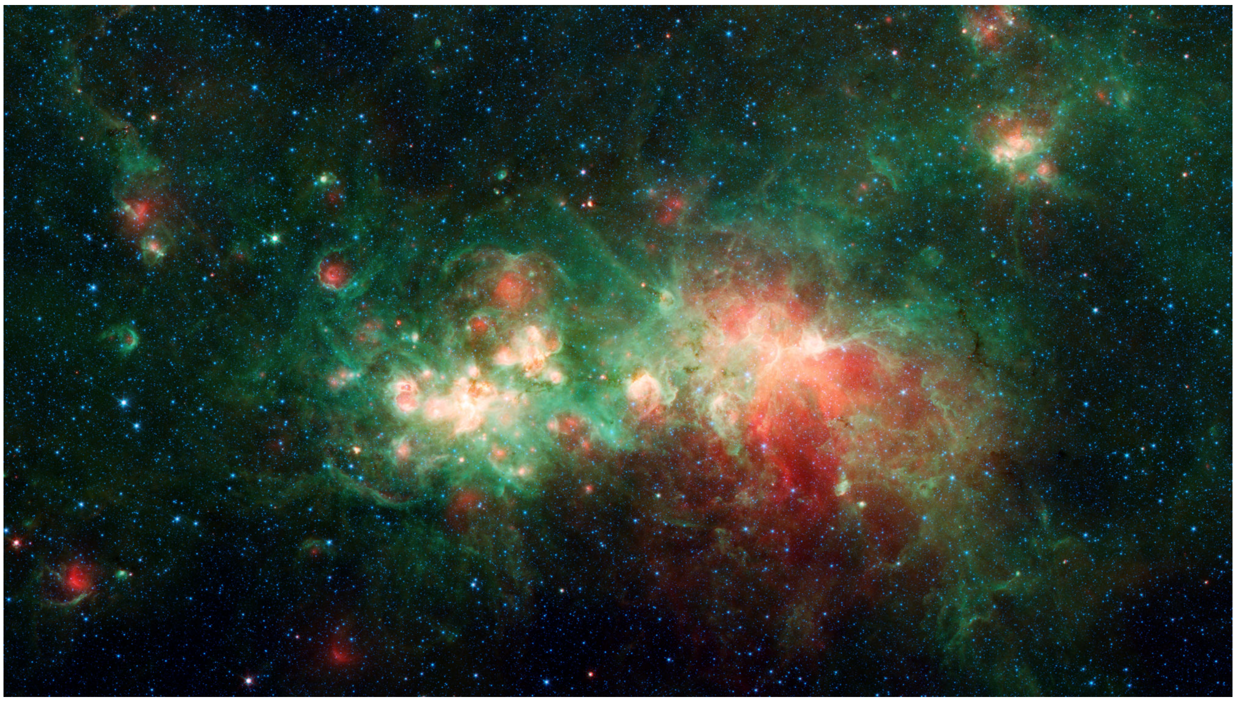

Figure 1.2 The Spitzer GLIMPSE and MIPSGAL survey view of the massive star-forming complex W51. Red and green show 8 and 24 μm and blue shows 3.6 and 4.5 μm. All the bright red and green emission traces stellar feedback. Green FUV-illuminated neutral gas rings are filled with red photoionized gas. These bubbles, embedded in nonuniform clouds and driven by stars or clusters of different masses, come in a variety of shapes and sizes. Image courtesy NASA/JPL-Caltech/GLIMPSE & MIPSGAL Teams.

et al., 2013) which form large clusters of high-mass stars, and hubs are dense clouds found where filaments intersect which can form small handfuls of high-mass stars (Didelon et al., 2015). The hub-filament system (HFS, sometimes also referred to as a hub-spoke system) model describes high-mass cluster formation in hierarchical networks of hubs within webs of filaments which feed them mass (Zhou et al., 2023). All of these models describe high-mass star formation systems based on large density contrasts and structures within cloud complexes.

This sets up an interstellar environs that is highly fragmented and organized surrounding the forming stars. When high-mass stars "turn on" and begin to emit their radiative and mechanical feedback, that feedback encounters a highly non-uniform gas environment like the one seen in Cygnus X in Figure 1.4. Those stars don't inhabit the environment randomly, but are born within the ridges and hubs, so their feedback will encounter and sculpt those structures from the inside out. This is one of the foundations of this thesis.

1.2 Feedback-Driven H II Regions and Stellar Wind Bubbles

When a high-mass star's radiation escapes its natal envelope, it rapidly photoionizes a region around it called an H II region. For $\sim 10^5$ years, the H II region is constrained in size to be $\lesssim$0.05 pc by the dense envelope of unused pre-stellar material (Churchwell, 2002) and the ionization front may even be "trapped" by ongoing accretion flows into the star (Hoare et al., 2007). This phase may last longer for lone massive stars rather than binaries/systems (He & Ricotti, 2023). These earliest H II region phases are called hyper-compact and ultra-compact H II regions (HCH II and UCH II). The H II region is eventually able to thermally expand up to $\sim$0.1–10 pc (Motte et al., 2018; Tigé et al., 2017). A cluster of stars will behave much the same way and

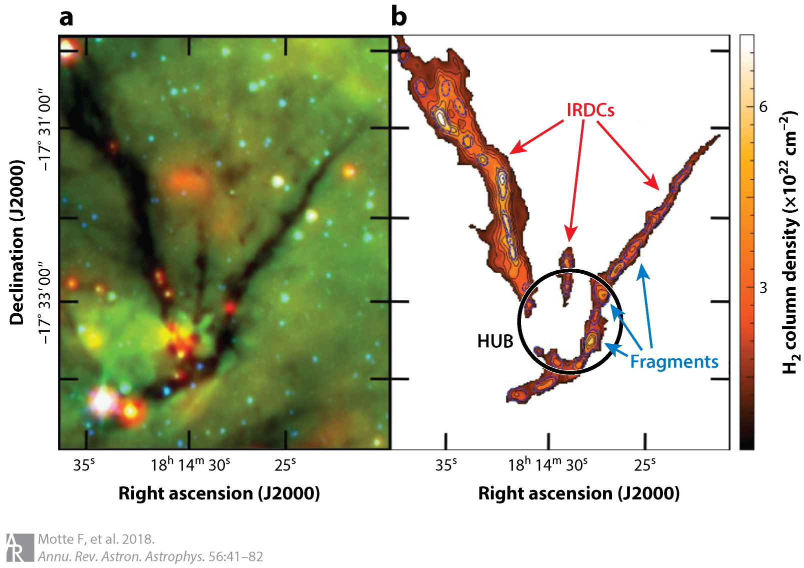

Hub and filaments

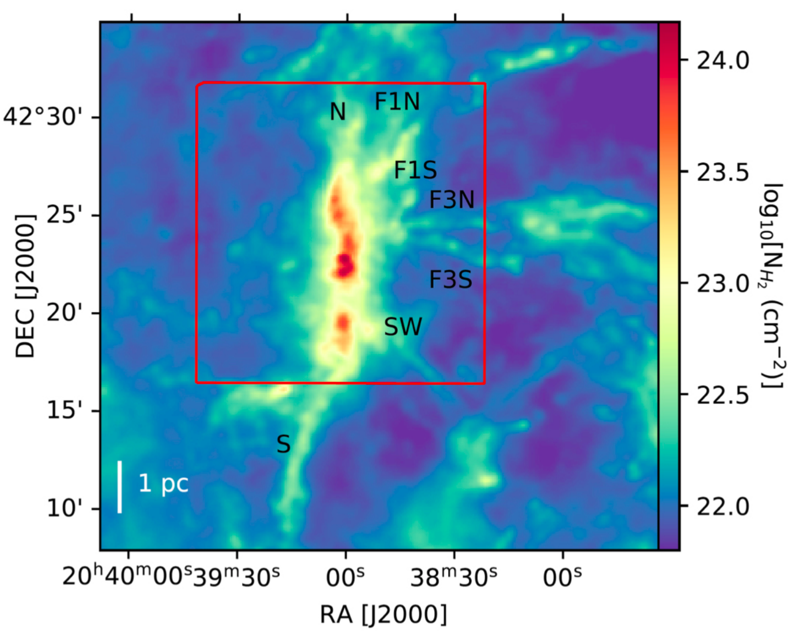

Ridge

Figure 1.3 Two examples of the 1–10 parsec-scale dense molecular cloud environments in which stars form. The top figure, from Peretto & Fuller (2010) and adapted by Motte et al. (2018), shows infrared-dark clouds (IRDCs) arranged in 10-pc long filaments and joined at a hub. The color composite on the left panel represents 3.6, 8, and 24 μm Spitzer maps with blue, green, and red, respectively. The right panel shows the H_2 column density map constructed from 8 μm emission. The bottom figure, which appears inside Figure 1 by Bonne et al. (2023a), shows the Herschel FIR H_2 column density map of the DR21 ridge within the Cygnus X star-forming complex.

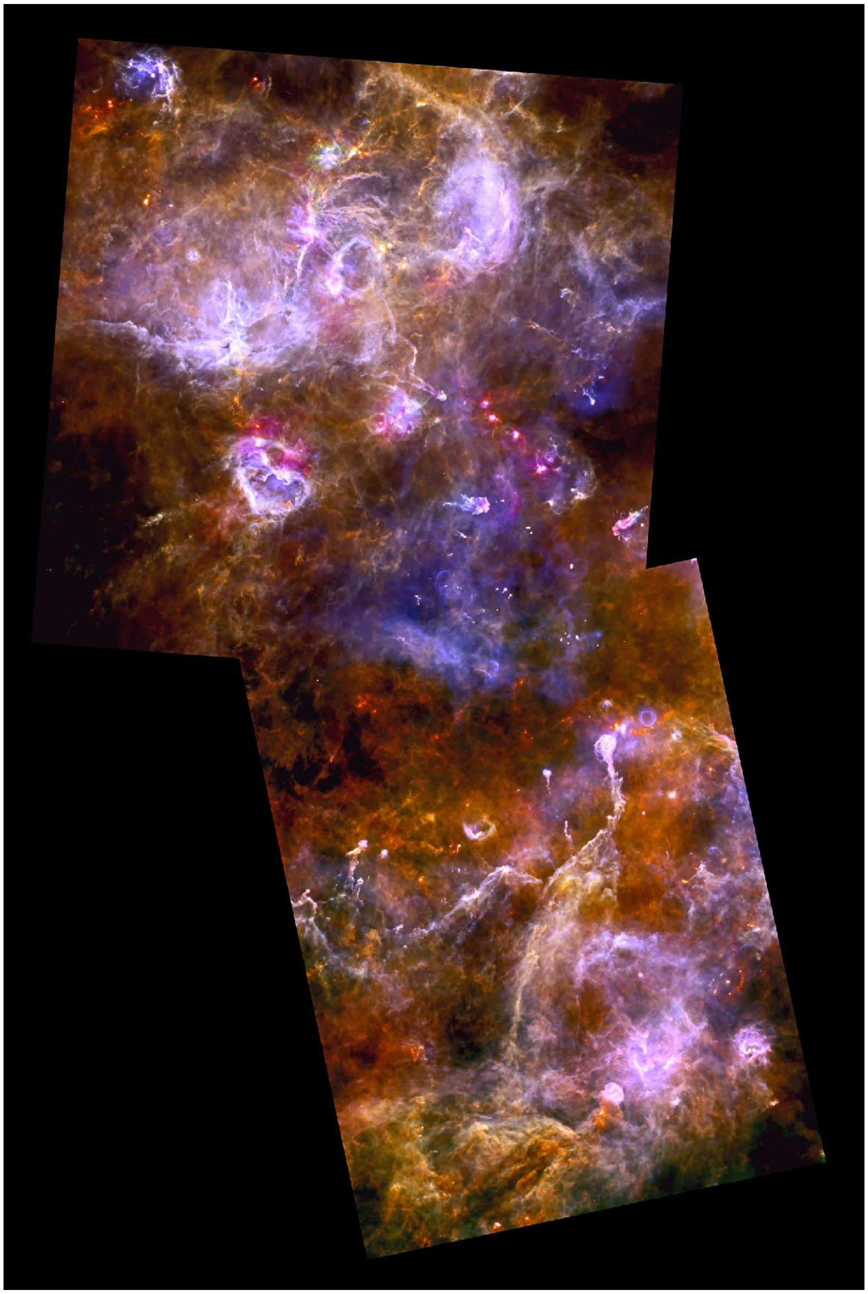

Figure 1.4 The Cygnus X star formation complex in the far infrared from Schneider et al. (2016). The Herschel 70, 160, and 500 μm images are shown in blue, green, and red, respectively. Dense gas structures, in red, are illuminated by radiation and impacted by winds from massive stars. Warm ($T \sim$ 30–75 K), FUV-illuminated gas appears in blue. The image is aligned in RA-Dec, so that north is at the top and east is to the left, and spans about 120 pc from north-to-south. The dense DR21 ridge, pictured in Figure 1.3, appears toward the north end.

will form a larger H ii region when the compact H ii regions merge as there will be more Lyman continuum photons available.

Simulations by He et al. (2019, 2020), supported by previous analytical results (Blitz & Shu, 1980; Matzner, 2002), show that a high-mass cluster can radiatively dissipate its natal cloud within a few 10s of Myr (compared to massive star lifetimes as low as 5 Myr, discussed below). Many of the Lyman continuum photons will escape into the surrounding ISM during and after that process, contributing to the ionization of the Galactic ISM. Photoionized H ii gas tends to reach a temperature of $\sim 10^4$ K and tends to be overpressured compared to its surroundings until it has sufficiently expanded to a lower density. This expansion acts on the surrounding gas, imparting kinetic energy and momentum into the interstellar medium (Spitzer, 1978).

Stars eject their outer layers as stellar winds, and the winds from massive stars represent a significant energy injection into the surrounding gas. These winds shock against the H ii region, already rapidly formed around the stars, and the shocked wind forms a layer of $\sim 10^6$ K collisionally-ionized plasma which is transparent to stellar radiation. The model by Weaver et al. (1977) describes the expansion of a wind-blown bubble due to the momentum injected by the stellar winds and the thermal energy of this hot plasma (Figure 1.5). A shock will be driven through the H ii region as this happens. If that shock moves out into the surrounding neutral molecular gas, the molecular gas will cool rapidly via radiation after passing through the shock and will remain neutral. The shock will sweep up a dense shell of neutral gas and potentially trap the H ii region behind the shell; this is the typical shell arrangement observed by the FEEDBACK survey (Section 1.4) around massive star forming regions. With the hot inner layers trapped within the outer shells, the bubble formation and expansion imparts thermal and mechanical energy into the surrounding interstellar medium and can mechanically disrupt the natal molecular clouds. The

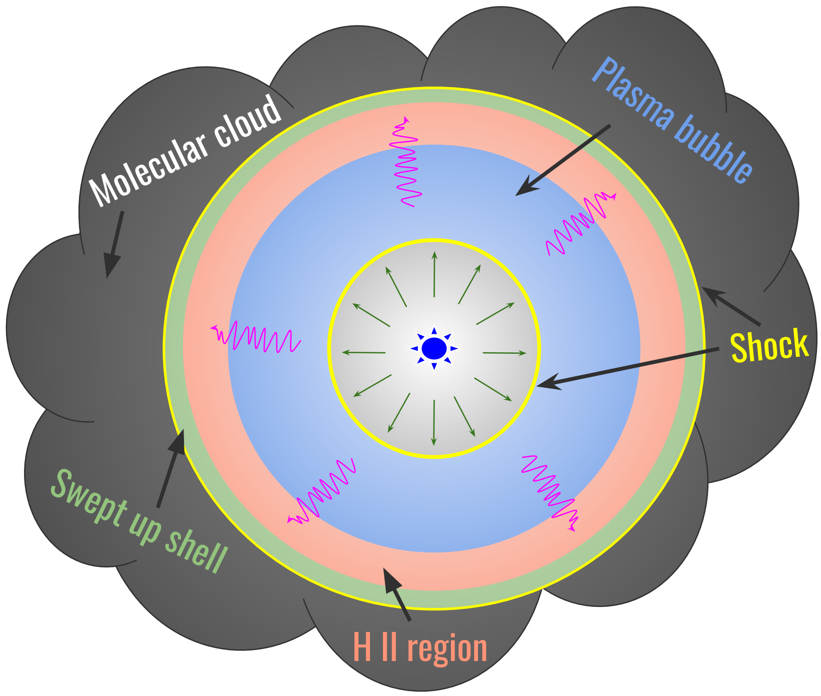

Figure 1.5 Cartoon depicting the Weaver et al. (1977) solution of a wind-blown bubble expanding in a uniform-density medium, adapted from Figure 1 in their paper and including the shocked neutral shell (green). The star at the center represents any number of OB stars, from a single star to a cluster of dozens. The straight green lines radiating from the star represent stellar winds and the wavy purple lines represent UV photons.

bubble shell will eventually be breached, perhaps by Rayleigh-Taylor instabilities or stellar jets, venting hot gas into the surrounding low-density medium. The shell will continue to coast, with momentum imparted only by ionization and radiation pressure.

The feedback potential of supernovae, the cataclysmic explosion of massive stars, is enormous, but this thesis is focused on pre-supernova stellar feedback. Stellar lifetime is inversely proportional to stellar mass, the single most important factor that determines most stellar properties. Supernovae will start to go off when the most massive stars evolve, typically around $\sim$5 Myr for early O-type stars.We consider a high-mass cluster "old" when supernovae have already gone off or are liable to occur soon. Stellar feedback via winds and radiation is intriguing because it activates far earlier, at the beginning of the cluster's lifetime instead of towards the end, and sets the stage for how the supernova feedback will interact with the surrounding gas. Pre-supernova feedback governs the conditions of the gas that the first supernova will see. Massive stars are often ejected from their clusters via binary interactions (Carretero-Castrillo et al., 2023; Gies & Bolton, 1986), so they may have travelled far from their natal cloud by the time their supernova occurs. In those cases, main-sequence feedback dominates the effects on the cloud. Understanding main-sequence stellar feedback is therefore key to understanding the full interstellar energetic life cycle.

1.2.1 Types of Observed H ɪɪ Regions and Bubbles

Photoionized H ɪɪ regions and wind-blown bubbles come in a variety of shapes and sizes depending on their age and environment. As mentioned above, young (no more than a few 10^5 years old) H ɪɪ regions can remain very small ($\lesssim$0.05 pc), and the details may depend on binarity, accretion, and disk conditions. As an H ɪɪ region expands and the ionization front advances into the surrounding cloud, the larger shape and density profile of the cloud begins to govern its evolution. The classical H ɪɪ region expands spherically into a uniform environment or a spherically symmetric, gently declining radial density profile (Didelon et al., 2015; Spitzer, 1978). The blister-type or champagne flow H ɪɪ region forms near an edge of a cloud and breaks out along the thinnest path out of the cloud, venting its hot, pressurized interior into the thin inter-cloud medium (Henney et al., 2005; Kim & Koo, 2001; Tenorio-Tagle, 1979). The bipolar H ɪɪ region forms inside thin sheets of molecular gas, and the region breaks out of the sheet on either side so that there are two cavities (Deharveng et al., 2015; Samal et al., 2018; Whitworth et al., 2022). These H ɪɪ region structure classifications are founded on observations of diverse morphologies in our Galaxy as well as a rich debate as to whether the ubiquitous projected rings seen in infrared surveys (Churchwell et al., 2006, 2007) are bubbles or rings in 3 dimensions (Anderson et al., 2014, 2011; Bania et al., 2010; Beaumont & Williams, 2010; Deharveng et al., 2015; Samal et al., 2018).

1.2.2 H II Regions in Non-uniform Density Environments

The bipolar H II region case is of particular interest to me because it enthusiastically embraces the non-uniformity of the ISM, which is composed of clumps, filaments, and sheets (Molinari et al., 2010). The bipolar case specifically deals with H II region evolution from within sheets, but simulations have predicted H II region evolution inside/near filaments and ridges (Fukuda & Hanawa, 2000; Whitworth & Priestley, 2021; Zamora-Avilés et al., 2019). The consensus is that dense structures like filaments, ridges, and clumps take much longer to be dissipated by photoionization and cause the H II region to expand non-isotropically and preferentially along low-density lines of sight.

There is a growing body of evidence that the density structure of the star formation environment is important to how efficiently feedback couples to the nearby dense gas and affects future star formation. Simulations suggest that a dense filament or ridge can be shielded from ionization by recombinations (Whitworth & Priestley, 2021), and observational evidence suggests that structures like ridges do in fact resist dissipation, but also that feedback may reduce or halt further accretion onto the ridge (Watkins et al., 2019). Observational evidence of some suspected wind-blown bubbles indicates that a significant amount of the available stellar wind energy is missing in the surrounding gas (Bonne et al., 2022; Tiwari et al., 2021, and Chapter 3 of this thesis). This poor coupling efficiency is likely due to hot plasma venting out of the bubble through low-density lines of sight like air from a burst balloon, which underscores the importance of density structure to the energetic coupling of feedback to the gas.

To better understand the role of density structure alongside stellar cluster properties in feedback efficiency and further corroborate these theories, detailed studies of individual star-forming regions are necessary. Each study must treat its region with care, as nature is messy and looks can be deceiving. These studies must be holistic, using as much available data as the authors can find from across the EM spectrum. Much of this thesis work studies the Eagle Nebula with this necessary detail in order to determine its history and morphology so that the relationship between gas and stellar energy can be known. When some tens of these studies are completed, patterns will emerge and we will advance in our understanding of stellar feedback.

1.3 Photodissociation Regions

A region of the interstellar medium whose heating or chemistry is dominated by FUV radiation is known as a photodissociation region (PDR). PDRs are found in a variety of astrophysical settings (Wolfire et al., 2022), and this thesis is concerned with only one of those settings: dense ($\gtrsim 10^3\ \mathrm{cm}^{-3}$) PDRs surrounding the H II regions around massive stars and clusters. H II regions and the inner bubbles of hot plasma are both transparent to FUV radiation, so it passes through uninterrupted until it illuminates the neutral and molecular gas which remains untouched by the ionization front. Gas conditions vary with depth ($\propto A_V$, visual extinction) into the PDR from the H-ionization front, and properties of typical PDRs are almost entirely defined by FUV radiation

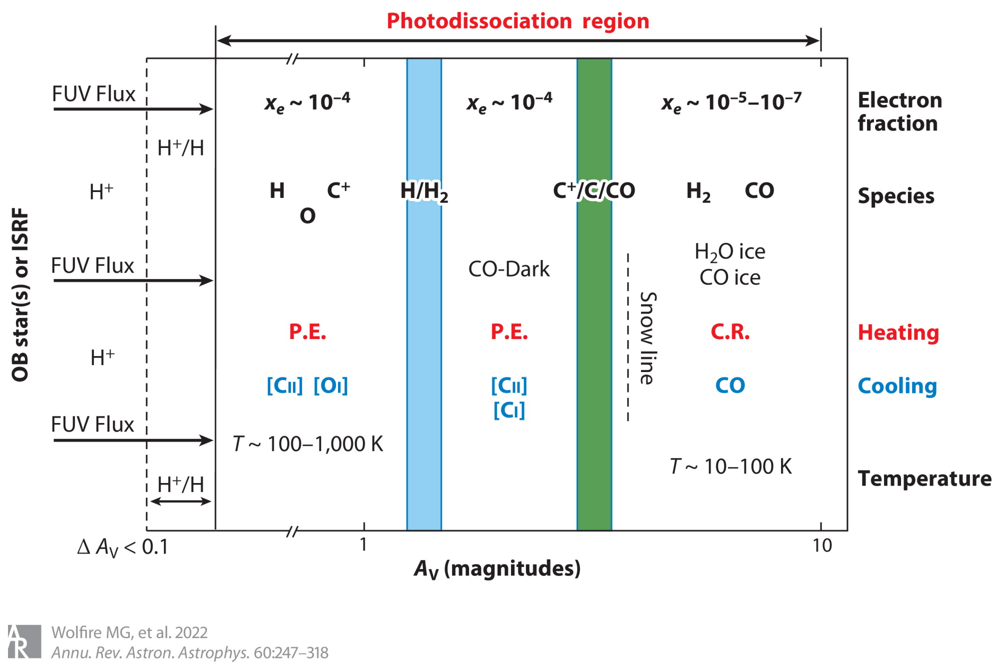

Figure 1.6 PDR chemical structure shown schematically as a function of visual extinction A_V from the review article by Wolfire et al. (2022). $A_V = 1$ is equal to a hydrogen column density $N_{\rm H} = 1.9 \times 10^{21}$ cm^{-2} (Bohlin et al., 1978). The physical width of any section depends on the density structure.

field[1] G_0 and density n. The H_2 molecule is radiatively dissociated by FUV photons (Sternberg et al., 2014) into H I creating a neutral atomic zone for a few A_V into the neutral cloud as seen in Figure 1.6. CO is photodissociated into C, which is photoionized into C^+, forming a C^+/C/CO transition layer a few A_V into the PDR where the number of free electrons significantly decreases. Temperature varies as a function of depth as FUV-driven heating is balanced by radiative cooling, which in turn depends on the available atoms/molecules at a given depth.

PDRs are distinguished from their surroundings by their chemistry and heating/cooling mechanisms and the dependence of these on incident FUV radiation. An important heating mech-

[1]The FUV radiation field strength is known as G and defined between 6–13.6 eV. Tielens & Hollenbach (1985) defined G_0 to be G expressed in Habing units where one Habing unit is 1.6×10^{-3} erg cm^{-2} s^{-1} (Habing, 1968), corresponding to about 10^8 photons cm^{-2} s^{-1} at 10 eV per photon. This thesis will only consider G as a one-dimensional flux incident on a PDR since we are concerned only with PDRs illuminated by stars, but see Footnote 7 in the review by Hollenbach & Tielens (1999) for notes on the effect of source geometry and PDR optical depth on G.

anism in PDRs is the photoelectric effect on small dust grains and large organic molecules called polycyclic aromatic hydrocarbons (PAHs) (Tielens, 2008). Photoelectric efficiency is controlled by the ionization rate over the recombination rate and scales with $G_0 T_e^{1/2}/n_e$. Other heating mechanisms include collisional de-excitation of radiatively excited H_2 rovibrational levels, dissociation of H_2 molecules, and cosmic ray ionization, which is more important deeper into the PDR where gas is mostly molecular (i.e. H and C are found in H_2 and CO) and the FUV radiation has been mostly absorbed (Wolfire et al., 2022). PDR temperatures are typically 100–1000 K where gas is atomic and 10–100 K where gas is molecular.

Cooling in PDRs happens largely through collisional excitation and radiative de-excitation of atomic fine-structure transitions, particularly the 158 μm transition[2] of [C II] ($^2P_{3/2} \rightarrow\ ^2P_{1/2}$; singly ionized carbon) and the 145 μm and 63 μm transitions of [O I] ($^3P_0 \rightarrow\ ^3P_1$ and $^3P_1 \rightarrow\ ^3P_2$; neutral oxygen) (Hollenbach & Tielens, 1999; Tielens & Hollenbach, 1985; Wolfire et al., 2022). The [C II] line is one of the brightest ISM cooling lines in the Milky Way (Bennett et al., 1994) and towards other galaxies (Herrera-Camus et al., 2015; Kennicutt et al., 2011; Malhotra et al., 1997), and all these lines contribute significantly to the total FIR flux. In the molecular gas, where carbon is found in CO and other molecules, CO rotational transitions dominate cooling. Neutral atomic C fine structure lines ([C I]) contribute to cooling in the C^+/C/CO transition layer, but their contribution is considerably ($\gtrsim$100$\times$) smaller than [C II] or CO cooling due to the relatively low energy of the transitions ($\Delta E/k_B \approx 24$ K for $^3P_1 \rightarrow\ ^3P_0$ at 609 μm and 39 K

[2]The term symbols used to describe the states involved in each transition describe the spin multiplicity $2S+1$, the total orbital quantum number L, and the total angular momentum quantum number J as $^{2S+1}L_J$ where L is written in spectroscopic notation. The upper state of the [C II] transition is $^2P_{3/2}$, which means that the total electron spin is $S = 1/2$ and the state is a doublet since there are two possible states, the total orbital quantum number is $L = 1$, or P in spectroscopic notation, and the total angular momentum of both the spin and orbit is $J = 3/2$. The [C II] transition is a fine-structure transition, which means that the electron spin-orbit coupled total angular momentum J is changing.

for $^3P_2 \rightarrow\ ^3P_1$ at 370 μm) and the low C abundance compared to C^+ and CO (Hollenbach & Tielens, 1997). Observations by Tauber et al. (1995) and Cuadrado et al. (2019) suggest that the C^+/C/CO transition may not exist as theorized as such a distinct layer (Figure 1.6) and that, in fact, there may not be a PDR layer inside which C is the dominant carbon phase, so that [C I] is never a primary coolant. Radiative line cooling is efficient at temperatures greater than the level separation energy, so the gas tends to cool down to that equivalent temperature. The [C II] excitation energy is 92 K, so the C^+-dominated gas tends toward $\sim$100 K. A variety of CO rotational transitions with excitation and transition energies ranging from 5–10 K to well over 100 K cool molecular gas to a few 10s of Kelvins.

Collisions of gas particles with dust grains can either heat or cool the gas depending on the relative temperature of the grains. Full radiative transfer simulations suggest that gas is hotter than grains at $A_V \lesssim 3$, and beyond that grains are hotter (Hocuk et al., 2017; Hollenbach et al., 1991; Röllig et al., 2013). The bulk of the FUV radiation in PDRs is reprocessed by dust into FIR continuum, which can pump the aforementioned fine-structure lines and heat the gas if those transitions are collisionally de-excited.

The key importance of PDRs to the study of massive star formation and feedback is that they are the interface between the H II region and the surrounding molecular gas. On one side of PDRs lie the photoionized gas and hot shocked plasma which carry thermal and kinetic energy from stellar feedback. On the other side of PDRs lies molecular gas not yet dispersed, dissociated, and ionized—not yet rendered unsuitable for a next generation of star formation—by this generation of stellar feedback. FUV radiation, which dominates the energy budget of stars, couples mainly to the PDR. The fate of star-forming molecular gas beyond the PDR depends on the energy transfers across its threshold. Through detailed study of the PDR, we can learn if future generations of stars are encouraged to form due to shock-induced density enhancements, discouraged from forming due to their natal molecular gas being rapidly transformed and dispersed, or not much affected either way due to inefficiencies or competing effects. The physics and chemistry of PDRs are relatively simple, so we can translate observed line intensities into physical conditions (Wolfire et al., 2022). Some crucial PDR tracers can be spectroscopically resolved to obtain kinematic information, which is a huge boon to the study of atomic and molecular gas dynamics and the transfer of kinetic energy into the different phases of ISM.

1.3.1 Observation of PDRs

PDRs emit a variety of uniquely bright radiation which can unambiguously be traced back to them. UV-illuminated PAHs emit mid-IR emission in bands near 3.3, 6–8, and 12 μm, to name a few, in what were called the "unidentified infrared emission bands" before they were more confidently associated with PAHs (Hollenbach & Tielens, 1999; Tielens, 2008). JWST NIRCam 3.3 μm, Spitzer IRAC 8 μm, and WISE 12 μm images are all dominated by PAH emission from PDRs.

FUV radiation is reprocessed into FIR continuum by dust, and that dust is typically $\sim$30–75 K in PDRs and will therefore emit strongly at FIR wavelengths $\lesssim$100 μm (Hollenbach & Tielens, 1997). WISE 22 μm and Spitzer MIPS 24 μm technically trace this but tend to be dominated by $\sim$100-200 K grain emission from within the photoionized gas (Churchwell et al., 2006). Warm dust in PDRs is more unambiguously traced in the FIR, for example by Herschel PACS 70 μm images where FUV-illuminated regions are significantly brighter than colder regions (compare the blue and red in Cygnus X in Figure 1.4 or in Orion on the left panel of Figure 1.7).

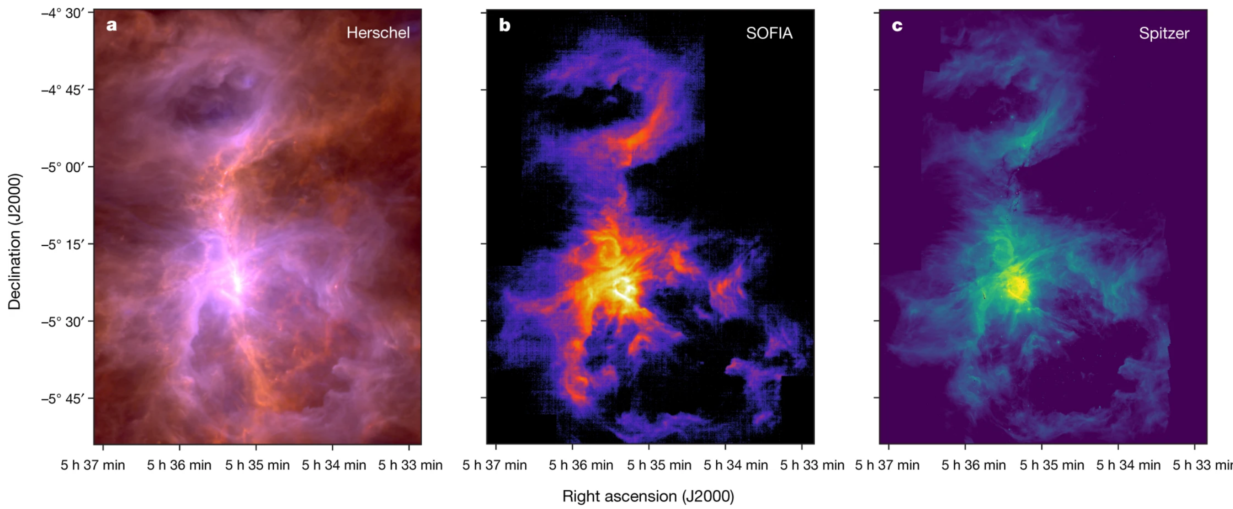

Figure 1.7 The Orion Nebula in the FIR (left), velocity-integrated [C II] (middle), and 8 μm (right), from Pabst et al. (2019). The FIR image on the left uses 70 μm and 350 μm as blue and red, respectively. 70 μm, [C II], and 8 μm all trace FUV illumination, while 350 μm traces high gas column densities. The [C II] observations in the central panel comprise over 2 million spectra which are used to turn the 2-dimensional image into a "cube" containing detailed velocity information.

PDR dust is still traced by Herschel PACS and SPIRE $\gtrsim$160 μm images, but emission from high column densities of cold and ambient dust contributes more at longer wavelengths and the PDRs don't stand out as much. Longer wavelength sub-millimeter bands, such as the 850 μm LABOCA receiver at the APEX observatory, trace dust from cold, dense gas well but do not trace PDRs.

Atomic fine-structure lines are a very effective way to observe PDRs. Not only does the emission unambiguously originate from PDRs, but these lines can be spectroscopically resolved with modern heterodyne receivers to provide kinematic information about the gas. These observations pair well with kinematically resolved observations of CO lines, which are frequently observable/observed by radio and submillimeter telescopes, and FIR/submillimeter [C I] lines (370 and 609 μm), which are less commonly observed. The spectral proximity of the [C II] and [O I] lines lends itself to simultaneous observations of the lines in parallel, with the same telescope/instrument.

Observations show that [C II] is a promising star formation tracer (Goldsmith et al., 2012). The line was mapped over almost the entire sky by the FIRAS instrument on COBE (Abdullah & Tielens, 2020; Bennett et al., 1994; Fixsen et al., 1999) and by balloon experiments such as BICE (Nakagawa et al., 1998), which foreshadowed its ubiquity in the interstellar medium. [C II] was spectroscopically resolved by HIFI on Herschel, revealing the typically $\sim 10~\mathrm{km~s^{-1}}$ full-width at half-maximum (FWHM) line spectra to be complex with multiple components and demonstrating the line's utility in determining the UV illumination and density around star-forming regions (Goicoechea et al., 2015; Pineda et al., 2010) and tracing CO-dark molecular gas (Velusamy et al., 2010). All these studies find that [C II] pairs well with mid-IR (i.e., 8 μm) and far-IR (i.e., 70 μm) observations (these two are shown alongside [C II] in Figure 1.7), which trace the FUV field as reprocessed by dust, and CO line maps which trace molecular gas where C is not ionized.

The primary challenge faced by would-be observers of PDRs is water vapor the Earth's atmosphere, which renders our atmosphere opaque to most of the tracers of atomic PDRs. Of the lines discussed above, only those of CO and [C I] can be observed from the ground. Herschel, Spitzer, WISE, and JWST are all space-based observatories, and these sorts of missions typically have a hard limit on their lifetimes set by coolant or propellant which is consumed during operation. JWST, which is online at the time of submission of this thesis, can observe near- and mid-IR emission from PAHs or some relevant atomic/molecular lines (e.g., H_2 from within the PDR or ionized gas tracers like [S III] or [Ne II]), but does not reach longer wavelengths where the far-IR fine-structure lines lie. The remarkable far-infrared observatory SOFIA overcame the atmospheric obstacle from the stratosphere, flying above most of the water in the atmosphere and successfully mapping star-forming regions in [C II] and [O I] (Schneider et al., 2020).

[C II] dominates the gas cooling in the atomic PDR, where all carbon is C^+; its intensity can be modeled to probe physical conditions; and it can be mapped with sub-$\mathrm{km\,s^{-1}}$ velocity resolution. With SOFIA, we can harness the full capacity of [C II] as the probe of choice for measuring the radiative and mechanical feedback from massive stars.

1.4 The FEEDBACK SOFIA Legacy Project

The FEEDBACK Legacy Program uses the upGREAT receiver on SOFIA to map 11 Galactic high-mass star-forming regions in these two atomic lines, [C II] and [O I] (Schneider et al., 2020). Complementary CO(J=3–2) line maps are made using the APEX telescope for all target regions. With this rich, spatially- and kinematically-resolved dataset, it is possible to study PDRs individually, in great detail, as well as collectively so that insightful comparisons can be made. The 11 targets span a variety of stellar feedback parameter space: driving stars ranging from single late-type O stars to massive 50-member clusters, FUV radiation field $G_0 = 10^2$–10^5, cloud geometries from ridges to rings to clumps, and H II region geometries from single and bipolar bubbles to irregular or evolved regions. Much of the work in this thesis is the detailed study of one of these high-mass star-forming FEEDBACK survey sources, the Eagle Nebula.

Recent studies use SOFIA upGREAT to map the [C II] line in star-forming regions including Orion (Kavak et al., 2022a,b; Pabst et al., 2019, 2020, 2021, 2022), RCW 120 (Kabanovic et al., 2022; Luisi et al., 2021), RCW 36 (Bonne et al., 2022), RCW 79 (Bonne et al., 2023b), NGC 7538 (Beuther et al., 2022; Kavak et al., 2023), RCW 49 (Tiwari et al., 2021, 2022), and Cygnus (Emig et al., 2022; Schneider et al., 2012, 2021). Key takeaways from these studies include:

1. O-type stars tend to inflate bubbles with their winds. B star winds aren't strong enough, so

their cavities' expansions are driven by thermal pressure from photoionized gas.

2. Bubbles tend to burst in the first few 10^5 yr, venting out hot plasma and photoionized gas and, along with them, a significant portion of the mechanical feedback energy. Plasma quickly wraps around and fills the low-density areas outside the bubble.

3. Many of the PDR rings seen on the sky around H II regions really are projected 3-dimensional bubbles, though bipolar H II regions are also observed.

The FEEDBACK survey and its studies have rapidly pushed forward the state of the art in the fields of stellar feedback and PDRs, and there is more exciting work to be done. We already knew that high-mass stars form in dense gas (Motte et al., 2018), and we began to suspect that photoionization is inefficient at dispersing the densest gas (Watkins et al., 2019; Whitworth & Priestley, 2021; Zamora-Avilés et al., 2019, though it may still quench star formation by stopping further accretion onto ridges). Now we know burst bubbles are a mode of feedback energy being diverted away from the nearby dense gas. The density structure of the star formation environment is clearly of paramount importance. Observational studies must continue to build statistics through these deep, high-resolution studies on individual sources. Analytical and computational theory must continue to refine stellar feedback models which consider density structure.

1.5 Pillar Structures Surrounding Massive Stars

A study of density inhomogeneities interacting with ionization fronts would be incomplete without a discussion of pillars. These elongated features are observed along the surface of some H II regions, reaching out from the surrounding molecular gas and protruding into the ionized region. Pillars themselves are composed of molecular gas, are surrounded by a dense PDR interface separating them from surrounding photoionized gas, and harbor some internal, organized flows of gas (Frieman, 1954; Hester et al., 1996; Pound, 1998; Spitzer, 1954). The prototypical pillar system lies in the Eagle Nebula: the Pillars of Creation, whose JWST portrait is shown in Figure 1.8 (Hester et al., 1996; McLeod et al., 2015; Pound, 1998; Sofue, 2020). These are studied in great detail in the next chapter of this thesis. Other examples are plentiful, with remarkable pc-scale pillars observed in the Rosette Nebula (Carlqvist et al., 2002), NGC 7822 (Gahm et al., 2006), Cygnus-X (Schneider et al., 2016), the Carina Nebula (Klaassen et al., 2020; McLeod et al., 2016), the Pelican Nebula (Bally & Reipurth, 2003), and the Horsehead Nebula (Pound et al., 2003) to name a few.

Pillars and other extended structures come in a variety of size scales. The examples above are typically ∼1–2 pc in length. Pillars of all sizes between 0.1–2 pc are observed towards RCW 49 (Churchwell et al., 2004; Tiwari et al., 2022; Zeidler et al., 2015), with the more plentiful smaller pillars closer into the cluster. Some of the evaporating gas globules on the scale of ∼0.01 pc observed towards the head of Pillar 1 in M16 have cometary tails connecting them back to the larger clump of gas. It is important to both recognize similarities between these different sizes of pillars, in that they may share some formation mechanisms in common, and also differences in distribution that may indicate key differences in their formations.

1.5.1 Pillar Formation Theories

Once thought to be large-scale Rayleigh-Taylor (RT) instabilities along the surfaces of H II regions (Frieman, 1954; Spitzer, 1954), kinematic information (Pound, 1998) indicates that

Figure 1.8 The Pillars of Creation in the Eagle Nebula as seen by JWST. In this composite image, NIRCam colors: Purple: F090W, Blue: F187N, Cyan: F200W, Yellow: F335M, Orange: F444W, Red: F470N. Image is nearly RA-Dec aligned, "up" in the image is $2\overset{\circ}{.}3$ east of north. Image courtesy NASA, ESA, CSA, STScI; processing by Joseph DePasquale (STScI), Anton M. Koekemoer (STScI), Alyssa Pagan (STScI). For additional information: `https://webbtelescope.org/contents/media/images/2022/052/01GF423GBQSK6ANC89NTFJW8VM`.

their bodies are instead more like cometary tails. RT instability can be suppressed by recombinations (Axford, 1964; Newman & Axford, 1967; Ricotti, 2014) but may be important for strong perturbations (Mizuta et al., 2006, 2007). Evolution of pillars into free-floating globules is theorized (Schneider et al., 2016) and it is generally accepted that pillars are seeded by dense clumps that slow down the ionization front as it passes over them and shadow the gas behind them. Radiation-driven implosion (RDI) is theorized to enhance the density in slightly overdense pre-existing clumps as ionization drives a shock through the clump (Bertoldi, 1989; Bertoldi & McKee, 1990). Depending on initial conditions, these clumps may develop a cometary appearance which can last $\sim$1 Myr (Kessel-Deynet & Burkert, 2003; Lefloch & Lazareff, 1994). Clumps which are approximately radially co-aligned can be collimated by a combination of RDI and shadowing, producing the signature columnar appearance of a pillar (Mackey & Lim, 2010).

The role of turbulence has been more recently studied, as it seeds the gas with a variety of density inhomogeneities, and simulations suggest it produces the swarms of small-scale pillars seen at the surface of some H II regions (Dale et al., 2012; Gritschneder et al., 2010; Tremblin et al., 2012a,b). Magnetic fields may play a role in shaping pillars (Carlqvist et al., 2002; Gahm et al., 2006) and polarization studies towards the Pillars of Creation confirm the presence of an aligned magnetic field and suggest that magnetic support dominates over turbulent and thermal support in the molecular gas (Pattle et al., 2018). Simulations by Williams et al. (2001) indicate that pillar shapes can be formed through multiple pathways, and the variety of viable theories and diversity of observed pillar morphologies suggest that there may indeed be more than one pillar origin. With a better understanding of pillar formation pathways, we may be able to use their existence and characteristics to learn about the pre-star-formation conditions in their molecular clouds.

1.6 M16, the Eagle Nebula

The Eagle Nebula (M16, S49, or RCW 165) is a well-studied H II region lying above the Galactic midplane at $(l,\ b) = 16.9540,\ +0.7934$ (RA, Dec: 18:18:48.0, −13:48:24 ICRS). The H II region is illuminated by a ∼2 Myr old cluster, NGC 6611 (Hillenbrand et al., 1993), which was born from the giant molecular cloud (GMC) W 37, from which the H II region bursts out (Zhan et al., 2016). Gaia DR2 parallax measurements analyzed by Kuhn et al. (2019) place NGC 6611 at a heliocentric distance of 1740 pc.

1.6.1 A Foreword on Names and their Histories

The Eagle is most commonly referred to by its Messier (1781) catalog name M16. It appears in a number of classic H II region catalogs, including Sharpless (1959) as S49, Gum (1955) as Gum 83, and Rodgers et al. (1960) as RCW 165 and is sometimes referred to in literature by these names up until the 2000s. All the above names refer interchangeably to the bright optical/radio H II region. We use "M16" a little more liberally in this thesis to refer to all the gas generally influenced by and associated with the massive cluster, so we refer to the PDR shell as the M16 shell and so on. The Westerhout (1958)[3] catalog number W 37 refers to the radio-emitting region towards the Eagle; we follow Zhan et al. (2016) in using this name to refer to the giant molecular cloud. The New General Catalog (Sulentic et al., 1973) number NGC 6611 is now most commonly used to refer to the massive stellar cluster illuminating the region. The distinction between the W 37 GMC and the H II region is important because, as Chapter 3 in this

[3]Dr. Gart Westerhout was the first director of the University of Maryland Astronomy Program and brought with him the traditional Dutch speeches which are delivered at the beginning and end of dissertation defenses.

thesis will go on to describe, not all the molecular gas in the cloud is illuminated by the cluster. The distinction between NGC 6611 and the H II region is, far more obviously, the difference between stars and gas.

Within M16 lies another H II region bubble called N19, discussed in detail in Chapter 3. The name N19 comes from the bubble catalog by Churchwell et al. (2006), and N19 was also identified by the Milky Way Project (Jayasinghe et al., 2019) as 2G0170780+0095101. In the Herschel study by Hill et al. (2012), they refer to N19 as the "Arch." We note that at the time of submission of this thesis, the name "N19" returns an incorrect result (NGC 19) when searched on SIMBAD, but the identifier "[CPA2006] N19" (specifying the Churchwell et al. 2006 catalog) returns the correct result. The central star is an O9 V (Hillenbrand et al., 1993) named W584 for its number in the Walker (1961) catalog of NGC 6611 stars, according to de Winter et al. (1997); it is not clear from presently available online catalogs that the Walker (1961) catalog exceeds 555 stars in NGC 6611, and I am unable to find the original source of this designation. More recent studies (i.e. Guarcello et al. 2010b) have continued to refer to this star as W584, so we adopt this name.

RCW 165 refers to the entire M16 H II region in the Rodgers et al. (1960) catalog, but was used by Xu et al. (2019) to refer to the parsec-scale IR-bright region surrounding IRAS 18156–1343 in the Bright Northern Ridge. We point out here that, while this smaller region may eventually require its own name for easier study, the use of RCW 165 as its name may cause confusion and so we recommend against it. One could argue, however, that changing the meaning of names has precedent in this very region: NGC 6611 is presented in the New General Catalogue as synonymous with M16 and must refer to the entire H II region, but now refers unambiguously to the star cluster. We leave this to the reader to decide for themselves, but we will refrain from using the name RCW 165 to identify the small H II region around the IRAS source. This IR-bright region has also been referred to as SFO 30 by Guarcello et al. (2012) for its entry in the bright rimmed cloud (BRC) catalog by Sugitani et al. (1991), but the description by Oliveira (2008) and the image in the catalog by Sugitani et al. (1991) both imply that the name "SFO 30" might refer to the optically dark triangular piece of cloud which hangs down into the H II region just a couple arcminutes (1 pc) from the cluster.

1.6.2 The W 37 GMC

The W 37 GMC is a cloud of $\geq 1.7 \times 10^5\ M_\odot$ (Zhan et al., 2016) which continues south from M16 and tapers into a giant molecular filament (GMF) as it crosses the Galactic plane (Figure 1.9). Li et al. (2016) define traditional filaments to be molecular gas structures ~2–20 pc in length and of $\sim 10^2$–$10^4\ M_\odot$, while GMFs can be many parsecs long and have masses $\sim 10^4$–$10^5\ M_\odot$. The FIR Herschel images presented by Hill et al. (2012) using HOBYS observations (Motte et al., 2010) as well as the large Hi-GAL maps which cover the Galactic plane within $|b| \leq 1^\circ$ reveal that the W 37/GMF complex extends at least $1\overset{\mathrm{d}}{.}3$ (~40 pc in projection at 1740 pc LOS). Many individual parsec-scale clouds and clumps which make up the W 37 GMF appear in dark nebula catalogs such as those by Rygl et al. (2010), Peretto et al. (2016), and Eden et al. (2019).

Moriguchi et al. (2002) use CO and H data to link this filament to M17 as well. They suggest that the filament is the projected edge of a ~100 pc radius supershell, which formed around 6 Myr ago from winds or supernovae in some distant massive cluster, and that the H II regions M16 and M17 were both triggered by the arrival of this supershell 2–3 Myr ago. The chronology of star formation in the M16 region is consistent with the estimated arrival time of the supershell, and direction of the supershell's advance is consistent with the internal stellar age gradient in M16 according to Guarcello et al. (2010b) (see Section 1.6.3 below).

W 37 is associated by virtue of its position and radial velocity with the giant molecular filament GMF 18.0–16.8, which extends off to the east (hereafter the Eastern GMF; Li et al. 2016), and with another GMF 16.5–15.8 to the west (hereafter the Western GMF; Zhan et al. 2016). These two filaments extend in Galactic $\pm l$, perpendicular to the $\pm b$-extended W 37 GMF. Ragan et al. (2014) refer to both the $\pm b$ GMF connected to W 37 as well as the Eastern GMF by the name GMF 18.0–16.8; this is explained in Section 4.1 in the paper by Zhan et al. (2016), who analyze W 37 and the Eastern GMF separately. The Eastern GMF is not aligned with the supershell edge described by Moriguchi et al. (2002). I make two suggestions regarding the naming of the GMF running towards the Galactic plane from W 37: 1) this GMF should not be grouped with the Eastern GMF under the name GMF 18.0–16.8, for the reason given above; and 2) this GMF should also be distinguished from W 37, since W 37 near M16 comprises filamentary gas as well as diffuse molecular gas surrounding it which may be accreting onto the filaments, while the GMF specifically refers to filamentary gas that extends tens of parsecs away from M16. Zhan et al. (2016) summarizes this picture in their Figures 1, 4, and 8 (which we reproduce here in Figure 1.9), in which the Eastern and Western GMFs are outlined in red and the W 37 GMF is called a "dense ridge," while the more diffuse W 37 GMC is labeled above it. See Section 4.1 in the paper by Zhan et al. (2016) for more detail.

Zhan et al. (2016) find both the Eastern and Western GMFs to be at least $10^4\ M_\odot$ based on ^{13}CO and C^{18}O J=1–0. Zhan et al. (2016) finds W 37 GMC to be $1.7 \times 10^5\ M_\odot$. Ragan et al. (2014) and Li et al. (2016) give a mass of $1.5 \times 10^5\ M_\odot$ for the combination of W 37, the

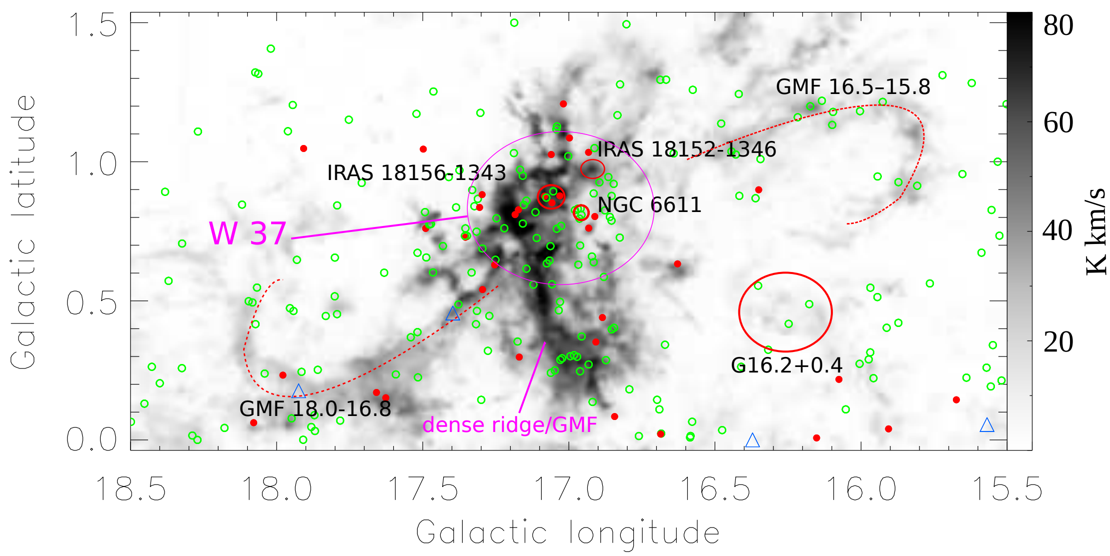

Figure 1.9 W 37 in ^{12}CO(J=1–0) by Zhan et al. (2016) (Fig. 8 in their paper). We added some labels. The points represent YSO candidates from their study. The Eastern and Western GMFs are labelled, while W 37 is the gas in the center between the two GMFs and the "dense ridge" is the gas which runs below W 37 at $l = 17°$ and $b < 0.5°$. The G16.2+0.4 cloud is unrelated. The cluster NGC 6611 and IR-bright sources IRAS 18152–1356 and IRAS 18156–1343 are marked in unfilled red circles.

$\pm b$ GMF, and the Eastern GMF (they refer to these collectively as GMF 18.0–16.8, as explained above). W 37 and the GMFs described here all lie between $\mathrm{V_{LSR}} = 20\text{–}25\ \mathrm{km\ s^{-1}}$ based on CO line observations.

Close inspection of W 37 near the location of M 16 reveals a series of parsec-scale filamentary structures primarily extended in the Galactic b direction, parallel to the larger scale elongation of W 37. These filaments, which are components of both the $\pm b$ GMF and the W 37 GMC, are traced by dust emission and therefore appear in the high spatial resolution Herschel PACS and SPIRE images presented by Hill et al. (2012) (see their Figures 1 and 4; we reproduce their Figure with some modifications in our Figure 1.10). Below M16, the GMF forks into two filaments which reconnect above M16. Hill et al. (2012) identify the "Eastern filament" (not to be confused with the Eastern GMF) running along the eastern side of M 16, from which a pillar

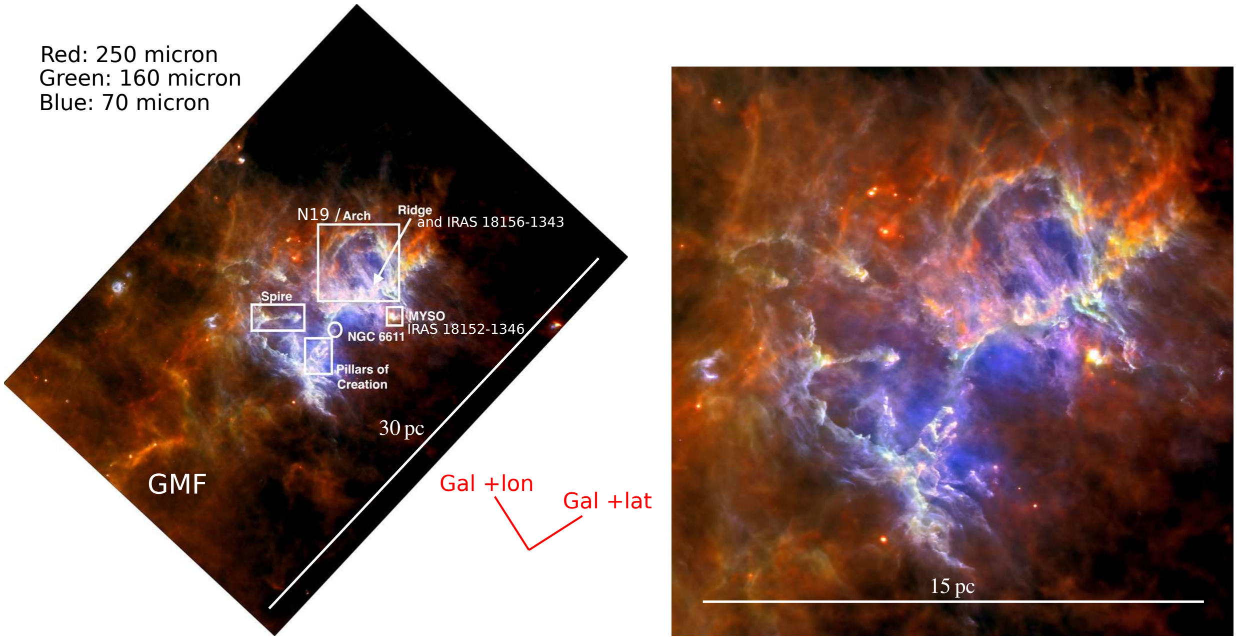

Figure 1.10 M16 at 70, 160, and 250 μm by Hill et al. (2012) (Fig. 1 in their paper). A number of features are labelled, and we added labels of our own in this reproduction. This figure is aligned in equatorial coordinates; Galactic axes are indicated in red.

called the Spire branches off and protrudes into the H II region. They also identify the "Northern filament," which we name in Chapter 3 the Bright Northern Ridge for its mid- and far-IR intensity, and the "Western filament," which is not pictured in their Figure 4 but is described in their Section 5.1. The Western Filament terminates in the Pillars of Creation and would, if extrapolated through the H II region, connect with the Northern filament. Hill et al. (2012) propose that NGC 6611 formed inside of a joint Western/Northern filament and created a cavity within it, while the Eastern filament remains largely undisturbed.

Xu et al. (2019) find that these filamentary structures are composed of three velocity components at 20, 22.5, and 25 km/s, which roughly match up with the velocities of the Pillars (Pound, 1998). According to the ^{13}CO(1$-$0) channel maps of Xu et al. (2019), the Northern filament includes components at all these velocities and exhibits the most extended structure around 20 km/s, while the Eastern filament is only present at $>$21 km/s. Chapter 3 in this thesis studies this in more detail.

1.6.3 The Cluster NGC 6611

The H II region associated with M 16 is powered by the early-type stars in the NGC 6611 cluster, a $\sim 2 \times 10^4\ M_\odot$ cluster whose most massive member is estimated to be $\sim 80\ M_\odot$ (Hill et al., 2012; Hillenbrand et al., 1993; Pfalzner, 2009). The cluster, at a heliocentric distance of ∼1740 pc (Kuhn et al., 2019), comprises a number of pre-main sequence (PMS) stars as well as stars surrounded circumstellar material, both signs of recent or ongoing star formation (Guarcello et al., 2009, 2007). The reddening law towards NGC 6611 is peculiarly high, $R_V = 3.75$ (Hillenbrand et al. 1993 and references therein), which is likely due to some combination of intracluster and foreground extinction dust within the H II region or the surrounding clouds. NGC 6611 members exhibit some age spread, as evidenced by several hundred PMS stars whose ages range from 0.25–1 Myr and a massive main sequence population about 2 Myr old lying alongside a handful of evolved massive stars, at least one of which is B2.5 I, which is around 6 million years old (Guarcello et al., 2010b; Hillenbrand et al., 1993). The O stars, the most massive stars, are all on the main sequence.

Guarcello et al. (2010b) find a stellar age gradient that is not in-to-outward, as it would be if the cluster's OB population triggered the younger stars, but moves from southeast (median 2.6 Myr) to northwest (median 0.3 Myr), based on the positions and ages of disk-less members of the cluster. They suggest that the catalyst for the southeastern star formation was the supershell described by Moriguchi et al. (2002) which arrived near M16 around 3 Myr ago and set off this most recent massive star forming event.

Guarcello et al. (2010a) notice that some stars appear too old (too blue) given the age estimates for NGC 6611. De Marchi et al. (2013) follow up on this and find two distinct populations of stars, bluer stars that they predict are at least 8 and no more than 30 Myr old (large error bars due to photometric uncertainty) and redder stars that are consistent with the previously determined ~ 1 Myr cluster age. They put this in context of the older southeastern population of age ~ 3 Myr, possibly triggered by the molecular shell from a 6 Myr old supernova; if these bluer stars are > 8 Myr old, then they must predate all this.

Indebetouw et al. (2007) and Guarcello et al. (2012) identify a small cluster of stars to the northeast of NGC 6611, slightly east (and outside) of N19. Most of the members of this association have disks or envelopes according to the mid-IR analysis by Indebetouw et al. (2007), and both teams of authors suggest that star formation in that association must have occurred in the last 0.3–0.5 Myr. The extinction towards these members is $A_V \sim 10$–20, so they must still be embedded within a dense cloud.

1.6.3.1 Young Stellar Objects in NGC 6611

We briefly define some terms regarding young stellar objects, or YSOs. YSOs are a broad category containing two major populations of sources: protostars and pre-main sequence (PMS) stars. The protostellar phase is the earliest phase in stellar evolution. The phase begins with the collapse of a dense molecular cloud fragment into a pressure supported core that pulls in more material as time goes on. As infalling gas shocks and heats up, it emits radiation that passes through interstellar dust, which absorbs and reradiates it in the millimeter and infrared, so the protostars are not optically visible. When the infall gas depletes or is blown away, the protostar becomes a pre-main sequence star. This type of star is optically visible and emits radiation via the Kelvin-Helmholtz mechanism, by which gravitational energy is liberated as radiation. When the star contracts enough for its internal temperature to reach a hydrogen burning threshold, it becomes a main sequence star and is placed on the zero-age main sequence, from which it continues to evolve.

Several notable YSOs have been identified in the region, and both are associated with remarkably bright mid-IR emission. One, a massive YSO (MYSO) named IRAS 18152–1346, lies slightly west of NGC 6611, towards the foreground/background "shell fragments" studied in Chapter 3 of this thesis, and was identified by Indebetouw et al. (2007) to be $\sim$8 $M_{\odot}$. This source is also associated with water maser emission (Braz & Epchtein, 1983), which signifies massive star formation. Another, IRAS 18156–1343, lies within the Eastern filament (Hill et al., 2012) / Bright Northern Ridge (Chapter 3) and is associated with very bright mid- and far-IR emission and the only detection of the [^{13}C II] line towards M16, which we discuss in Chapter 3. This bright IR region hosts a number of X-ray YSO candidates (Guarcello et al., 2012). Healy et al. (2004) detect water masers here, and Fontani et al. (2010) and Edris et al. (2007) looked for and did not detect methanol and OH masers, respectively, towards IRAS 18156–1343, which may indicate that the YSO is very young. Both of these IRAS sources are marked in Figures 1.9 and 1.10. IRAS 18159–1346, a third source associated with water maser emission (Braz & Epchtein, 1983; Healy et al., 2004; Valdettaro et al., 2005), lies towards SFO 30, a bright-rimmed cloud associated with the dark optical triangle close to NGC 6611 (Oliveira, 2008).

1.6.4 The H II Region M16

Much of the work on the M16 H II region and PDRs has centered on the bright and remarkable Pillars of Creation. Pound (1998) and Sofue (2020) study the molecular gas, Levenson et al. (2000) study the PDR, and Hester et al. (1996), García-Rojas et al. (2006), and McLeod et al. (2015) study the ionized gas towards the Pillars. Fewer studies have been made towards the wider M16 region or the diffuse gas surrounding the Pillars; Higgs et al. (1979) study the diffuse ionized gas and Flagey et al. (2011) study both ionized gas and PDRs. Flagey et al. (2011) detect a hot, 24 μm inner shell towards the center of the region, interior to the PDR, and this type of emission is commonly associated with the ionized gas in feedback-driven bubbles (Churchwell et al., 2006). They propose that the population of stochastically heated very small grains (VSGs) is enhanced in this shell due to dust grains being pulverized by collisions with the ionized gas. Given that Townsley et al. (2014) detect diffuse X-ray emission from the shocked-wind plasma bubble towards the center of the region, the 24 μm shell's well-defined edge may mark the contact discontinuity (Weaver et al., 1977) between the photoionized gas where the VSGs lie and the hot plasma.

Chapter 2: The Pillars of Creation in [C II] and Molecular Lines

2.1 Introduction

The Eagle Nebula, also known as M16, is a well-studied H II region lying above the Galactic midplane at $(l,\ b) = (16°9540,\ +0°7934)$, $(\alpha,\ \delta)_{J2000} = (18^{\mathrm{h}}18^{\mathrm{m}}48\overset{\mathrm{s}}{.}0,\ \text{-}13°48'24'')$. The H II region is illuminated by a $\sim$2 Myr old stellar cluster, NGC 6611 (Hillenbrand et al., 1993), born from the giant molecular cloud (GMC) W 37 (Zhan et al., 2016). Filaments primarily extended in the Galactic b direction, parallel to the larger scale elongation of W 37, lie within W 37 near the location of M16 (Hill et al., 2012; Xu et al., 2019).

The H II region associated with M 16 is powered by the early-type stars in the NGC 6611 cluster, a $\sim 2 \times 10^4\ M_\odot$ cluster whose most massive member is estimated to be $\sim 80\ M_\odot$ (Hill et al., 2012; Hillenbrand et al., 1993). The cluster, at a heliocentric distance of $\sim$2 kpc, comprises a number of pre-main sequence (PMS) stars as well as stars surrounded by circumstellar material, both signs of recent or ongoing star formation. NGC 6611 members exhibit some age spread, as evidenced by several hundred PMS stars whose ages range from 0.25–1 Myr and a massive main sequence population about 2 Myr old lying alongside a handful of evolved massive stars, at least one of which is B2.5 I, which is around 6 Myr old (Hillenbrand et al., 1993). Guarcello et al. (2009, 2010b, 2007) and De Marchi et al. (2013) delve into the star formation history of the region and characterize two different populations of stars: a group of >8 Myr old stars which likely existed before the formation of the M16 H II region, and a group of ∼1 Myr-old stars, broadly consistent with the ∼2 Myr age determination of NGC 6611 by other authors, whose formation event may have been triggered by a supernova shell's arrival ∼3 Myr ago. We adopt the distance of 1740 ± 130 pc determined using GAIA parallax observations (Kuhn et al., 2019) and a main sequence age of 2 Myr based on studies from the last two decades (Belikov et al., 1999, 2000; Dufton et al., 2006; Martayan et al., 2008; Stoop et al., 2023).

Within M16 lies an iconic pillar system whose Hubble Space Telescope (HST), and now JWST, images are well known to the public (Hester et al., 1996). The three main Pillars, extending towards a handful of bright O5–7 stars ~ 3 pc away in projection (Hillenbrand et al., 1993), are seen roughly parallel to the plane of the sky as in Figure 2.1. Spectroscopic studies by Pound (1998) and McLeod et al. (2015) have concluded that all the Pillars are inclined slightly towards or away from the observer, and the tallest pillar, called Pillar 1 (P1), is actually a superposition of two pillars: the northern half, called P1a, is actually behind the cluster and the southern half, called P1b, is in between the cluster and the observer (see Figure 2.1). Pound (1998) detects coherent molecular gas flows along the line of sight, which they conclude are projected motions along the pillar. They find that the observed radial velocity gradient along the pillar implies that the dynamical timescale for dissipation, $\sim 10^5$ yr, may be shorter than their estimated photoevaporation timescale $\sim 10^7$ yr. Both Pound (1998) and McLeod et al. (2015) suggest that Pillars 2 and 3 (P2 and P3) are between the cluster and the observer and that P2 points away from the observer towards the cluster (throughout this paper, "points" refers to the orientation of the head; i.e., the head of P2 is farther from the observer than the tail). The line-of-sight (LOS) velocity data collected by Pound (1998) and McLeod et al. (2015) indicate that P3 points towards the observer, and the illumination data from the HST observations presented by Hester et al. (1996)

and the MUSE observations analyzed by McLeod et al. (2015) are consistent with P3 lying between the cluster and the observer. Together, the velocity and illumination data imply that P3 does not point towards the cluster. P3 might point towards a cluster member displaced towards the observer along the line of sight (Section 2.4.2).

Due to the high spatial resolution of the JWST images, structures within the Pillar system are well-defined. We use the JWST images throughout this study to measure the on-sky angular widths of features.

2.1.1 The Photodissociation Region

The photodissociation region (PDR) is the region of far-ultraviolet (FUV; 6–13.6 eV) illuminated neutral atomic and molecular gas just behind the ionization front (see Tielens & Hollenbach 1985 and Wolfire et al. 2022 for detailed background). Due primarily to photoelectric heating from small grains and polycyclic aromatic hydrocarbons (PAHs) (Bakes & Tielens, 1994), the atomic region at the cloud surface is warmer ($T \sim 100$ K) than the molecular gas ($T \sim 10$ K) found deeper in the cloud. Most of the cooling in the atomic PDR is done through a small handful of fine-structure lines, principally the 158 μm [C II] line (singly-ionized carbon), and at $n \gtrsim 10^4$ cm^{-3}, the 63 μm and 145 μm [O I] lines (neutral oxygen) (Hollenbach & Tielens, 1999; Tielens & Hollenbach, 1985; Wolfire et al., 2022). Spectroscopically resolved observations of these lines, such as those we present here, allow us to probe the kinematics of the warmer, outer atomic region of the PDR. Observations of [C II] and [O I] are presented by Schneider et al. (2012, 2021) towards pillars and globules in Cygnus X.

At $A_V \gtrsim 5$, carbon is found primarily in the molecular phase as carbon monoxide (CO).

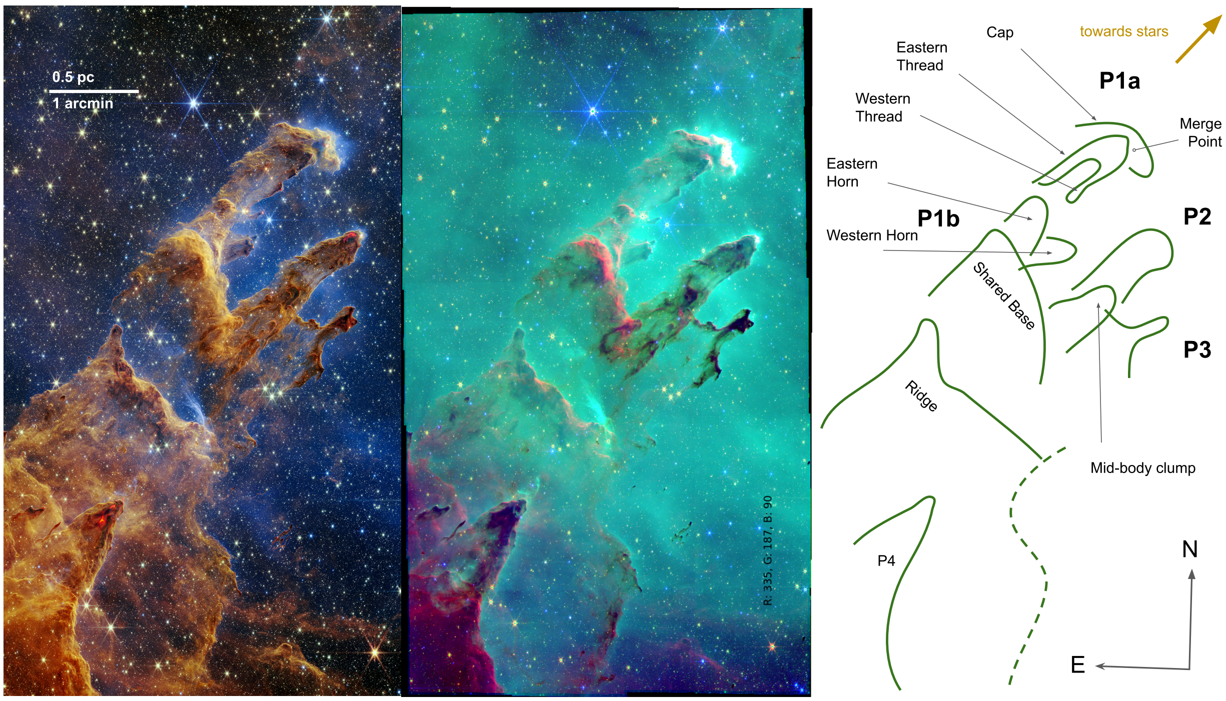

Figure 2.1 (*Left*) JWST color composite prepared by Joseph DePasquale (STScI), Anton M. Koekemoer (STScI), Alyssa Pagan (STScI). Colors are Purple: F090W, Blue: F187N, Cyan: F200W, Yellow: F335M, Orange: F444W, Red: F470N. The image was obtained from `https://webbtelescope.org/contents/media/images/2022/052/01GF423GBQSK6ANC89NTFJW8VM`. (*Center*) Three-color composite using JWST filters F090W (blue), F187N (green), and F335M (red). The stretches are nonlinear and limits have been adjusted. The 3.3 μm band, in red, includes a PAH feature and therefore indicates far-ultraviolet illumination. Section 2.2.4 includes a more detailed summary of the significance of these filters. (*Right*) Schematic diagram of the Pillars on the sky at the same angular scale as the two images to the left. Features are marked with labels which will be used throughout the paper. P1a refers to the northern half of Pillar 1, including the Cap and Eastern and Western Threads. P1b refers to the southern half and includes the Eastern and Western Horns and part of the Shared Base. The dashed line to the south marks a boundary which is kinematically discontinuous with the Ridge despite its apparent continuity in the visible and IR images; this is discussed in Section 2.3.6. The three images are nearly RA-Dec aligned; "up" in the image is 2.3° east of north. The scale bar in the top-left corner shows $1' \approx 0.5$ pc at 1740 pc line of sight.

From $A_V \sim$ 5–10, FUV radiation still warms the predominantly molecular gas, which we can probe with low- to mid-J CO lines. These lines, and particularly the bright ^{12}CO(J=1–0) line, should be optically thick and trace this molecular PDR layer as opposed to the colder, less illuminated molecular gas $A_V \gtrsim 10$.

Molecular lines more sensitive to dense gas ($n \gtrsim 10^5$ cm^{-3}) will probe the denser, colder layers beyond the PDR which are not heated by FUV radiation. By comparing observations of dense gas tracers, such as the HCO^+, HCN, and CS observed towards the Pillars by White et al. (1999), with the PDR tracers introduced above, we can explore not only the molecular gas inventory of the Pillars but also how mass moves between phases and leaves the Pillars through bulk flows (Pound, 1998) or photoevaporation (Hester et al., 1996; McLeod et al., 2015).

We present a multi-wavelength analysis using both velocity-resolved and continuum observations tracing a variety of gas phases within and around the Pillars, from the cold, dense layers deep within the pillar heads to the warm, outer layers illuminated by the bright members of NGC 6611. This study presents the first velocity-resolved [C II] and [O I] line observations of the Pillars of Creation which probe the conditions and kinematics of the FUV-illuminated PDR layer between the ionization front and the molecular gas within the Pillars. We describe the Pillars and surrounding features in all tracers in Section 2.3 and determine the location of major PDRs and discuss the illumination geometry in Section 2.4. Our derivation of column densities, number densities, and pressures in the atomic and molecular phases of the gas is discussed in Section 2.5, where we also discuss pressure equilibrium between these phases and the ionized gas. We discuss the photoevaporative timescale of the Pillars in Section 2.6 and include a summary of our work and some closing remarks in Section 2.7.

2.2 Observations

2.2.1 SOFIA

M16 was observed with upGREAT[1] on SOFIA on 9 flights between 2019 and 2022 from Palmdale, California and Tahiti in the [C II] $^2P_{3/2} \rightarrow {}^2P_{1/2}$ transition at 158 μm and in the [O I] 63 μm line in parallel with the upGREAT receiver (Risacher et al., 2018) onboard SOFIA. Note that we did not use the large undersampled [O I] map from the FEEDBACK mapping but instead, data from an earlier PI program (see below). An area of ~ 590 arcmin^2 was mapped in the on-the-fly (OTF) mode and atmospheric calibration was done with the GREAT pipeline (Guan et al., 2012). A Fast Fourier Transform Spectrometer (FFTS) with 4 GHz instantaneous bandwidth and a frequency resolution of 0.244 MHz serves as a backend (Klein et al., 2012).

The nominal angular resolution of the [C II] and [O I] data is 14.1$''$ and 6$''$, respectively, but here we use a [C II] data cube with a spatial resolution of 15.4$''$, a grid of 3.5$''$, and a spectral binning of 0.5 $\mathrm{km\ s^{-1}}$. The noise RMS in one channel is typically 1.0 K (Table 2.1). A 3rd order baseline was removed from the spectra, which were then averaged with 1/2 weighting (baseline noise). Spectra are presented on a main beam brightness temperature scale T_{MB} using an average main beam efficiency of 0.65. The forward efficiency is η_{f} = 0.97. See Schneider et al. (2020) for more observational details. These [C II] observations are made public through the NASA/IPAC Infrared Science Archive (IRSA)[2].

A smaller area of M16, covering mostly the Pillars of Creation, was observed during 2 flights in October 2016 (Cycle 5) with the GREAT receiver with two channels. The 7-pixel

[1] upGREAT and GREAT were developed by the MPI für Radioastronomie and the KOSMA/Universität zu Köln, in cooperation with the MPI für Sonnensystemforschung and the DLR Institut für Planetenforschung.

[2] `https://irsa.ipac.caltech.edu/Missions/sofia.html`

HFA was tuned to the [O I] $^3P_1 \rightarrow {}^3P_2$ line at 63 μm and the single pixel L2 channel to the CO(J=16–15) line at 1841.345506 GHz, which we do not discuss in this study. We employed the Fast Fourier Transform Spectrometer backend AFFTS. The center IF (intermediate frequency) was 1455 MHz for the [O I] line and 1000 MHz for the CO line. The map was obtained in beam-switched on-the-fly mapping mode. The stepsize of the map was 2.4$''$ which is at a higher sampling than the FEEDBACK large mapping. The angular resolution of the [O I] data is 6$''$. All line intensities are reported as main beam temperatures scaled with main-beam efficiencies of 0.69 and 0.68 for [O I] and CO, respectively, and a forward efficiency of 0.97. From the spectra, a 3rd order baseline was removed and spectra were then averaged with 1/2 weighting (baseline noise). We smoothed the [O I] data to a resolution of 0.4 $\mathrm{km\ s^{-1}}$.

2.2.2 CARMA and BIMA

We used the Combined Array for Research in Millimeter-wave Astronomy (CARMA, Bock et al., 2006) to map the Eagle Nebula pillars in four spectral lines that trace high H_2 volume density gas. The observations were obtained with the 15-element array comprised of the six 10.4 m antennas and nine 6.1 m antennas. Three E-array configuration tracks were obtained on August 8, September 8, and September 10, 2012, and one D-array configuration track was obtained on November 12, 2012. The antenna signals were transmitted to the eight-band spectral line correlator. Four bands were used to observe the spectral lines HCN(J=1–0), HCO^+(J=1–0), N_2H^+(J=1–0), and CS(J=2–1) in 7.8 MHz bandwidths with spectral resolution 24 kHz/channel (ΔV $\sim$0.08 $\mathrm{km\ s^{-1}}$). Four bands were used to measure continuum at $\sim$ 92 GHz, each with 490 MHz bandwidth and 12.5 MHz/channel. Combining the two sidebands gave a total continuum bandwidth of 3.84 GHz. (Continuum emission was detected at the level of $\sim$ 10 mJy; it is not discussed in this study.) The Eagle was observed with a 37-point hexagonal mosaic centered on $(\alpha,\,\delta)_{J2000} = (18^{\mathrm{h}}18^{\mathrm{m}}51\overset{\mathrm{s}}{.}29, -13°15'02.32'')$. The map was sampled at the Nyquist interval of the 10.4 m antennas at the CS rest frequency because it is the highest frequency and thus smallest interval. Finally, we also use in this paper the CO(J=1–0), ^{13}CO(J=1–0) and C^{18}O(J=1–0) archival Berkeley-Illinois-Maryland Array (BIMA) data of the Eagle pillars from Pound (1998) and Pound et al. (2007).

The data were reduced using the MIRIAD package (Sault et al., 2011, 1995). After phase, amplitude, passband, and flux calibration, and flagging of bad data, visibilities were inverted onto a 0.5$''$ spatial grid and 0.1 $\mathrm{km\ s^{-1}}$ channels using a robust weighting value of zero (Briggs, 1995). The inverted images were deconvolved with the MIRIAD task *mossdi* which uses CLEAN algorithm of Steer et al. (1984). Deconvolved maps were restored with a fitted 2D Gaussian beam. Details of the observations are provided in Table 2.1.

The N_2H^+(J=1–0) line splits into a series of hyperfine transitions, the two strongest of which, (J, F1, F) = (1–0, 2–1, 2–1) and (1–0, 2–1, 3–2), lie $\sim$1 $\mathrm{km\ s^{-1}}$ from each other. Since these are not well separated given the $\sim$1 $\mathrm{km\ s^{-1}}$ full-width at half-max (FWHM) of the lines, we only use spatial information from them and do not use their velocities. Our observations include a transition of N_2H^+ (J, F1, F) = (1–0, 0–1, 1–2) which is well-separated from other transitions given the typical FWHM, so we use velocity information from this line. The HCN(J=1–0) line is also split into hyperfine transitions, but the strong central transition is well separated from the others given the typical FWHM.

2.2.3 APEX

M16 was mapped on September 18-20, 2019, in good weather conditions (precipitable water vapor pwv = 0.6–0.9 mm) in the ^{13}CO(J=3–2) and ^{12}CO(J=3–2) transitions using the LAsMA spectrometer on the APEX[3] telescope (Güsten et al., 2006). LAsMA is a 7-pixel single polarization heterodyne array that allows simultaneous observations of the two isotopomers in the upper (^{12}CO) and lower (^{13}CO) sideband of the receiver, respectively.

The array is arranged in a hexagonal configuration around a central pixel with a spacing of about two beam widths ($\theta_{\mathrm{MB}} = 18.2''$ at 345.8 GHz) between the pixels. It uses a K mirror as de-rotator. The backends are advanced Fast Fourier Transform Spectrometers (Klein et al., 2012) with a bandwidth of 2×4 GHz and a native spectral resolution of 61 kHz. The mapping was done in total power on-the-fly mode using a reference position at $(\alpha,\, \delta)_{J2000} = (18^{\mathrm{h}}20^{\mathrm{m}}46\overset{\mathrm{s}}{.}3, -13°14'56'')$.

The mapped region, centered at $18^{\mathrm{h}}18^{\mathrm{m}}35\overset{\mathrm{s}}{.}7, -13°43'31.0''$ and of size $30' \times 22'$ at -40 deg angle (CCW against positive RA), was split into 2×2 tiles. Each tile was scanned with a spacing of 9″ (oversampling to 6″ in scanning direction), resulting in a uniformly sampled map with high fidelity. All spectra are calibrated in $\mathrm{T_{MB}}$ (main-beam efficiency $\eta_{\mathrm{MB}} = 0.68$ at 345.8 GHz). All linear baselines were removed and all data re-sampled to $0.1~\mathrm{km~s^{-1}}$ spectral bins. The final data cubes are built with a pixel size of $9.1''$ and an $18.2''$ beam after gridding.

M16 was mapped on May 3 and June 28, 2021, in reasonable weather conditions (pwv = 0.5–0.9 mm) in the ^{12}CO(J=6–5) transition using the SEPIA660 receiver and the FFTS1 backend spectrometer on the APEX telescope. The instrument was tuned so that the ^{12}CO(J=6–5)

[3] APEX, the Atacama Pathfinder Experiment is a collaboration between the Max-Planck-Institut für Radioastronomie, Onsala Space Observatory (OSO), and the European Southern Observatory (ESO).

line rest frequency 691.473 GHz lay in the upper sideband, whose bandwidth is 4 GHz and frequency resolution is 61 kHz. The OTF-mapped region is a $4.3' \times 4.3'$ square centered at $18^{\mathrm{h}}18^{\mathrm{m}}51\overset{\mathrm{s}}{.}2$, $-13°50'0''$. Spectra are calibrated in $T_{\rm MB}$ (main-beam efficiency $\eta_{\rm MB} = 0.45$). The final cube is gridded to 4.5″ pixels with a 9.6″ beam and has a channel width of 0.25 $\mathrm{km\ s^{-1}}$.

2.2.4 Ancillary Data

M16 was observed at 8 μm using the InfraRed Array Camera (IRAC, Fazio et al. 2004) on board *Spitzer* as part of the GLIMPSE program (Benjamin et al., 2003), and at 70 μm and 160 μm using the Photodetector Array Camera and Spectrometer (PACS, Poglitsch et al. 2010) and 250, 350, and 500 μm using the Spectral and Photometric Imaging REceiver (SPIRE, Griffin et al. 2010) aboard the *Herschel* Space Observatory (Pilbratt et al., 2010) as part of the Hi-GAL Galactic plane survey (Molinari et al., 2010). The IRAC image was obtained from the GLIMPSE website[4] and the PACS and SPIRE observations were obtained from the Herschel Science Archive (HSA), and they are accessible through the NASA/IPAC IRSA: GLIMPSE Team (2020) and Hi-GAL Team (2020a,b,c,d,e). Ultraviolet (UV) radiation, emitted in abundance from NGC 6611, excites large hydrocarbon molecules called polycyclic aromatic hydrocarbons, or PAHs, which fluoresce in the infrared (IR), and the 8 μm filter covers a particularly strong feature in the PAH spectrum (Tielens, 2008). Detailed studies by Indebetouw et al. (2007) and Flagey et al. (2011) discuss these and other *Spitzer* mid-IR images. Far-infrared (FIR) 70 and 160 μm emission traces warm dust illuminated with FUV radiation from the stars, with 70 μm relatively more sensitive to temperature than column density; M16 was studied in detail in the FIR by Hill et al. (2012).

The Pillars were observed using JWST NIRCam (Rieke et al., 2023) as part of the Cycle

[4] `https://irsa.ipac.caltech.edu/data/SPITZER/GLIMPSE/`

Species	Frequency (GHz)	Beam Size (″)	Beam PA (degrees)	dV ($\mathrm{km\ s^{-1}}$)	RMS (K)
Continuum	92	9.25×5.94	–5.34	⋯	0.0042
HCN	88.6318470	11.31×7.22	–6.57	0.10	0.52
HCO^+	89.1885180	11.30×7.15	–7.30	0.10	0.56
N_2H^+	93.1735050	10.59×6.76	–6.48	0.10	0.64
CS	97.9809680	10.12×6.45	–6.29	0.10	0.73
$C^{18}O$(J=1–0)	109.7821600	13.73×7.42	–9.55	0.267	0.60
^{13}CO(J=1–0)	110.2013530	6.80×4.29	–8.15	0.266	2.06
^{12}CO(J=1–0)	115.2712040	7.51×4.39	–1.38	0.254	5.03
^{13}CO(J=3–2)	330.5879653	20.0	0	0.111	0.68
^{12}CO(J=3–2)	345.7959899	19.2	0	0.106	0.55
^{12}CO(J=6–5)	691.4730000	9.6	0	0.25	1.65
^{12}CO(J=16–15)	1841.345506	15.9	0	⋯	⋯
[C II]	1900.536900	15.4	0	0.5	1.0
[O I]	4744.777490	6.7	0	0.4	1.9

Table 2.1 Beam PA is the position angle of the elliptical beam, measured in degrees east of north. dV is the velocity bin width used in this study. RMS is the root-mean-squared noise within each velocity bin for the given beam and dV. The 92 GHz continuum and CO(J=16–15) line were observed but are not used in this study.

1 outreach campaign (PI: Pontoppidan, PID #2739) and their data made publicly available via the Mikulski Archive for Space Telescopes (MAST): 10.17909/fbc0-1930. We use images in the filters F090W, F187N, and F335M, which trace 0.9 μm continuum and background emission from starlight, the 1.87 μm Pa-α recombination line from ionized hydrogen, and the 3.3 μm PAH feature. The 0.9 and 1.87 μm observations are particularly useful for locating areas of high near-IR (NIR) extinction towards the Pillars, and the 3.3 μm observation highlights illuminated PDR surfaces at $\sim$ 200 AU resolution.

2.3 Results

We present a rich collection of observations of the Pillars of Creation alongside publicly available archival data. Integrated intensity and continuum maps in Figure 2.2 show the Pillars in a variety of tracers, from warm atomic gas ([C II] and [O I]) and UV illuminated gas (8 μm PAH and 70 μm dust continuum) to warm (CO) and dense (HCO^+ and CS) molecular gas.

This data set is ripe for comparison between tracers of different physical conditions as well as between our velocity-resolved line maps and extremely high spatial resolution JWST images. Comparing integrated [C II] intensity to the F335M image in Figure 2.3 reveals myriad relationships between emission features both strong and weak, from the bright emission along the Pillars to the faint legs extending from the base of the Pillars down to the southeast (near $\alpha,\, \delta = 18^{\rm h}18^{\rm m}56\overset{\rm s}{.},\ -13^{\circ}51'20''$ in Figure 2.3), while the CS integrated intensity map overlaid in that figure unveils the density structure beneath.

Pillar 1 appears between $\rm V_{LSR} = 24\text{–}26\ km\ s^{-1}$ in the channel maps in Figure 2.4 and Pillars 2 and 3 appear between $\rm V_{LSR} = 20\text{–}23\ km\ s^{-1}$. The ~10 pc scale filaments observed by Hill et al. (2012) and Xu et al. (2019) lie at similar velocities $\rm V_{LSR} = 20$, 22.5, and $25\ \rm km\ s^{-1}$. Much of the [C II] emission in the channel maps is diffuse emission surrounding the Pillars between $\rm V_{LSR} \sim 24\text{–}27\ km\ s^{-1}$, and so the diffuse component line overlaps with and contaminates the P1 component line. We describe in Appendix B.2 the case and procedure for subtracting a background from [C II] spectra towards the Pillars to handle this contamination. The diffuse 3.3 μm haze, apparent by comparing the upper left corner of Figure 2.3 to the slightly dimmer lower right corner, may trace the same diffuse PDR as this $\rm V_{LSR} \sim 25\ km\ s^{-1}$ [C II] component. The pillar system connects towards the southeast to a ~10 pc scale system of emission features (only a small part of which is shown in Figure 2.4) at $\rm V_{LSR} \sim 25\ \ km\ s^{-1}$ which may be the illuminated edge of the H II region. At the lower velocities of P2 and P3, a different set of emission features extend towards the southeast, away from the stars, highlighted in blue in Figure 2.5. Higher velocity channel maps $\rm V_{LSR} \geq 29\ \ km\ s^{-1}$ reveal a faint, ring-like feature ~2 pc in diameter with a bright southern edge. Only the western side of this ring is included in the Figure 2.4 channel maps. Since it has a significantly different morphology than the pillar system, we deem it to be a foreground or background feature unrelated to the Pillars but likely part of the H II region and a candidate for future work.

The [C II] and [O I] line profiles (FWHM $\sim$ 2–3 $\mathrm{km\,s^{-1}}$) match the expected line width for atomic gas PDR emission. The peak main beam temperatures T_{MB} of [C II] reach $\sim$40 K towards the Pillars. The ^{12}CO line widths $\sim$ 2 $\mathrm{km\,s^{-1}}$ and peak T_{MB} (reaching $\sim$80 K in the (J=1–0) line) indicate their origin in the warm molecular gas in the PDR. The HCO^+, HCN, and CS line profiles are relatively thinner (FWHM $\sim$ 1–2 $\mathrm{km\,s^{-1}}$) and reach lower T_{MB} ($\sim$20 K in HCO^+ and HCN; $\sim$10 K in CS). All observed line widths are likely dominated by turbulent motions. No evidence of self-absorption in [C II] or [O I] is detected towards the bright Shared Base or any other location towards the Pillars (see Guevara et al. 2020a for a discussion of [C II] self-absorption in other Galactic star-forming regions).

Throughout the paper, we refer to Pillars 1, 2, and 3 as P1, P2 and P3. As was discussed in Section 2.1, P1 refers to the entire structure of Pillar 1 including both P1a and P1b (McLeod et al., 2015). The "head" of a pillar refers to the region of the pillar nearer to the illuminating stars, and the "tail" or "base" refers to the region farther from the stars. The "body" refers to the bulk midsection of the pillar. "Along" the body or "parallel" to the Pillars refers to the radial direction with respect to the stars, while "across" the body or "transverse" refers to the tangential direction with respect to the stars. We use the proper noun "Pillars" to refer to the system in M16 which is the subject of this work and the common noun "pillars" to refer to the generic structure found in other regions as well.

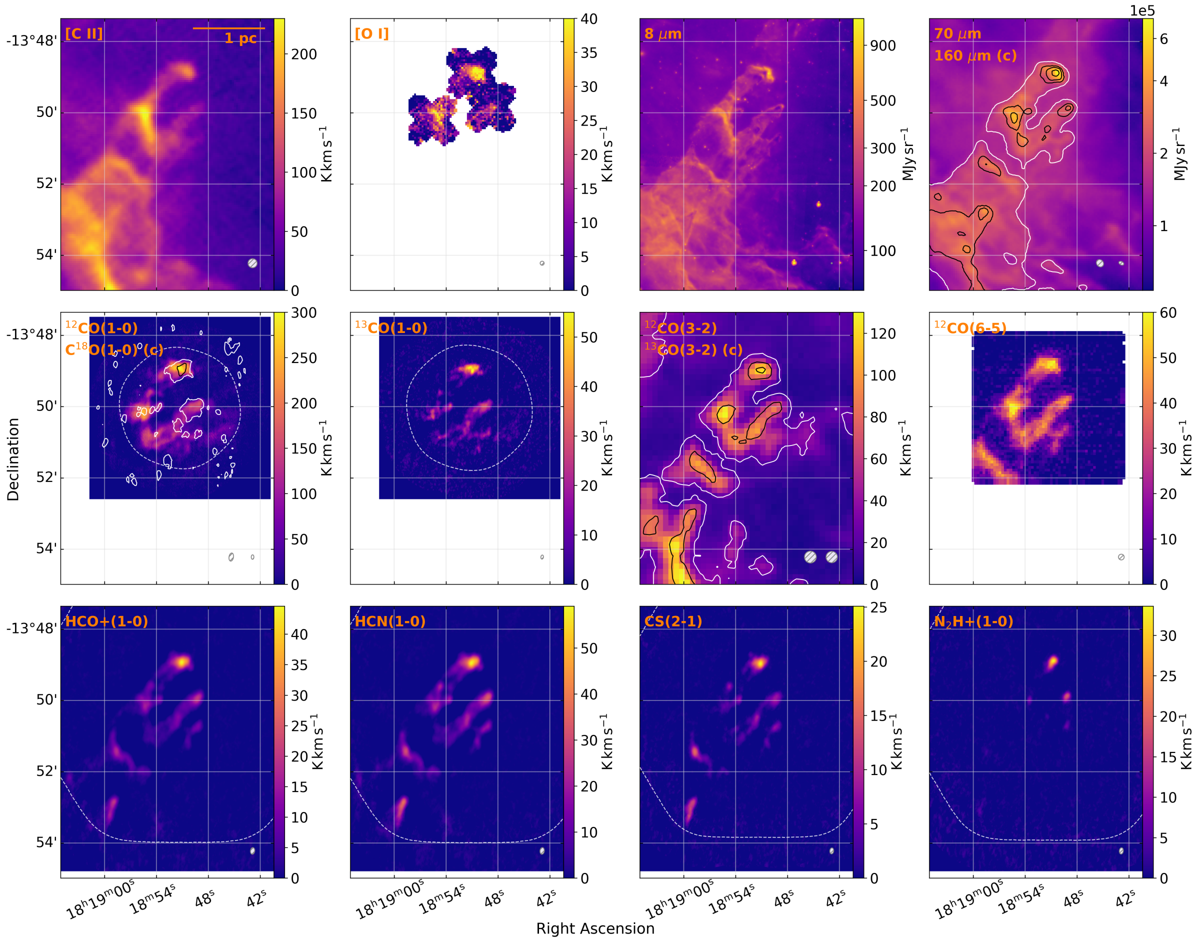

Figure 2.2 Integrated intensity and photometry centered on the Pillars. Contoured observations are marked with (c). The beam for each observation is shown in the lower right corner; the beam for the contoured observation, if present, is shown to the left of the color-scale observation's beam. All observations are shown at the same angular scale. [C II] and [O I] are integrated between $V_{LSR} = 18–27$ km s^{-1}, as they tend to have longer blue wings, and molecular lines not otherwise specified are integrated between $V_{LSR} = 19–27$ km s^{-1}. N_2H^+ and HCN are integrated between $V_{LSR} = 12.6–32$ km s^{-1} with respect to the rest frequencies given in Table 2.1 in order to include several satellite lines for each species (see Section 2.2). Contours are [0.5, 3.0] K km s^{-1} for C^{18}O(J=1–0); [4, 24, 44] K km s^{-1} for ^{13}CO(J=3–2); and [9, 18, 27, 45] $\times 10^5$ MJy sr^{-1} for the 160 μm image (the last contour spacing is intentionally uneven to increase visibility towards P1a). The contour colors are chosen to increase contrast with the image and have no further significance. The dashed white contour on the interferometric molecular line observations marks 50% gain from the primary beam mosaic pattern; outside this contour the sensitivity falls off (noise increases). Note the BIMA CO(J=1–0) maps are smaller than the CARMA maps of the other species and so cover the southeast Ridge with very low sensitivity. Nonetheless it is weakly detected.

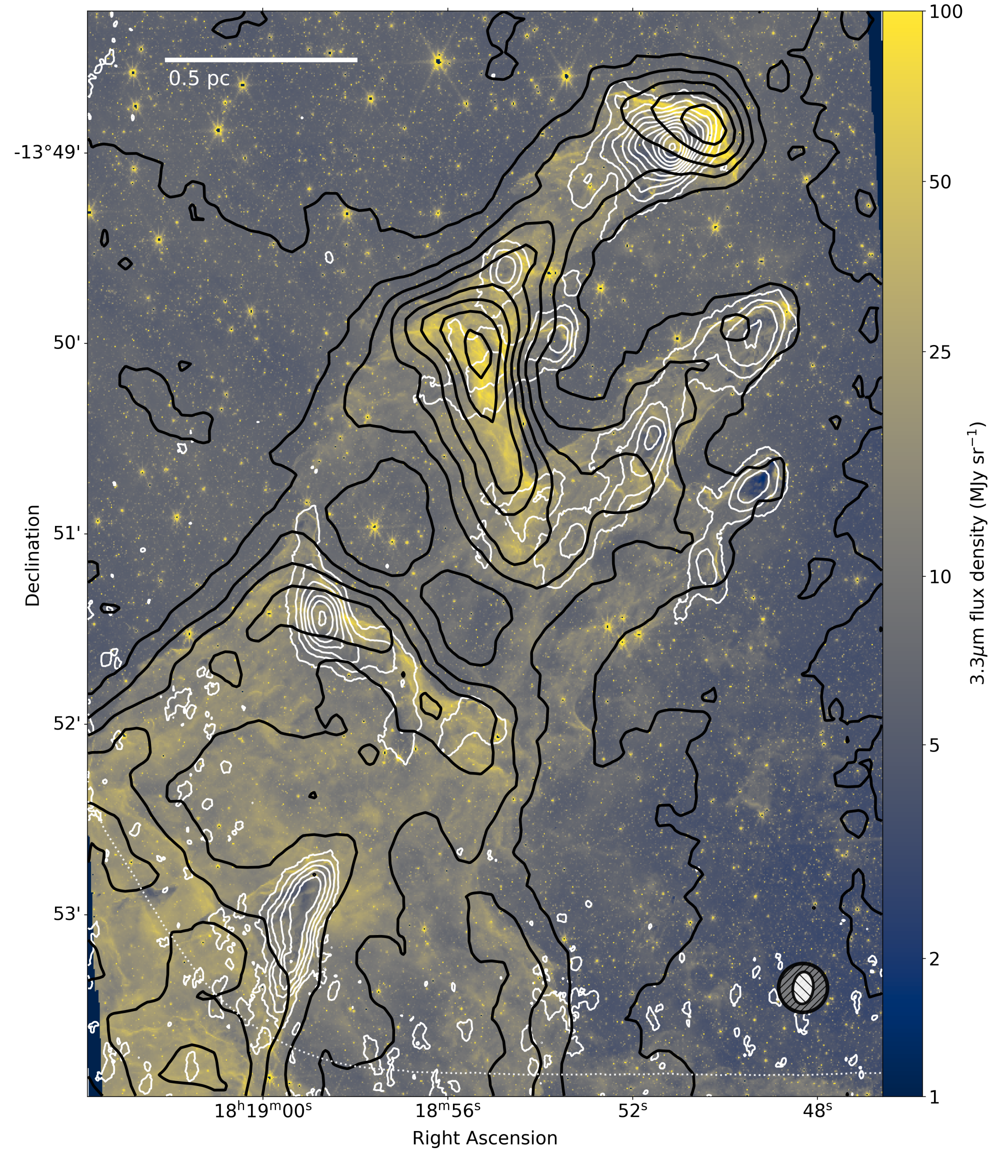

Figure 2.3 Integrated [C II] (black) and CS (white) line intensities between $\mathrm{V_{LSR}} = 19$–$27\ \mathrm{km\ s^{-1}}$ overlaid on the F335M image. [C II] integrated intensities are marked at the [25, 50, 75, 100, 125, 150, 175, 200, 225] K $\mathrm{km\ s^{-1}}$ levels, and CS at [0.8, 3.2, 5.6, 8, 10.4, 12.8, 15.2, 17.6, 20, 22.4, 24.8] K $\mathrm{km\ s^{-1}}$. The dotted white line marks the 50% gain contour for the CS observations; see the caption of Figure 2.2 for more detail. The [C II] beam is shown in grey in the lower right corner, and the CS beam superimposed in white. Note the spatial offsets between the two lines towards the Cap and the Threads, among other locations. The large-scale [C II] emission indicated by the lowest two contours is the $\mathrm{V_{LSR}} \sim 25\ \mathrm{km\ s^{-1}}$ background discussed in detail in Appendix B.2.

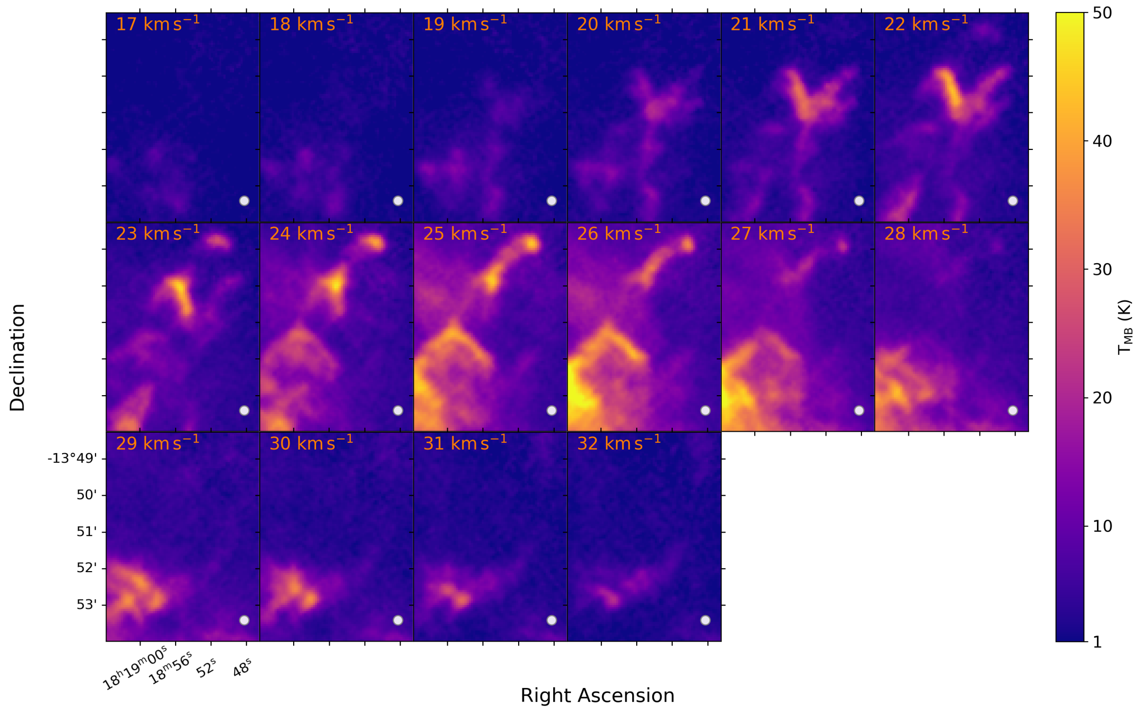

Figure 2.4 158 μm [C II] line channel maps binned to 1 $\mathrm{km\ s^{-1}}$ and centered on the Pillars. The beam is shown in the lower right corner of each map.

2.3.1 P1

The [C II] and [O I] lines, all observed molecular lines, and the 3–500 μm continuum peak in brightness twice along the length of Pillar 1: towards P1a and P1b. The peak brightness ratio of P1a to P1b is larger for denser gas tracers and smallest for [C II], in which P1b is brighter. We show spectra of [C II], [O I], CO(J=6–5), and CS towards these brightness peaks in Figure 2.6. Between the peaks, warm tracers like [C II] and 3–160 μm continuum are continuous and remain brighter than the background along the pillar, whereas the molecular lines trace the discontinuous, clumpy structure observed by Thompson et al. (2002) in near-IR images and White et al. (1999) in their radio, sub-mm, and IR observations (compare the [C II] and CS in Figure 2.3).

A bright rim of PAH and optical emission lies atop the molecular emission towards P1a due

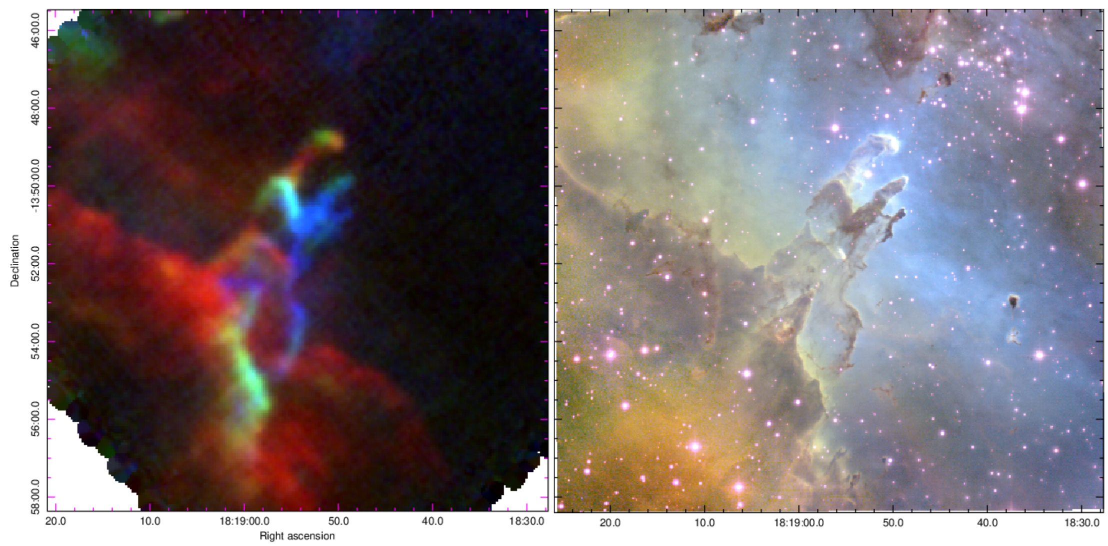

Figure 2.5 (*Left*) Color composite using [C II] line integrated intensities between $\mathrm{V_{LSR}} = 19$–$21.5\ \mathrm{km\,s^{-1}}$ (blue), 22–$23.5\ \mathrm{km\,s^{-1}}$ (green), and 24–$27.5\ \mathrm{km\,s^{-1}}$ (red). The color stretches are linear and start at 0 but have different upper limits. (*Right*) NOAO optical composite prepared by T.A. Rector (NRAO/AUI/NSF and NOIRLab/NSF/AURA) and B.A. Wolpa (NOIRLab/NSF/AURA) using observations from the WIYN 0.9 m telescope at the Kitt Peak National Observatory. The image was obtained from `https://noirlab.edu/public/images/noao-04086` and coordinate metadata applied using Astrometry.net[a] (Lang et al., 2010). The colors show the O III line at 499 nm (blue), the Hα line at 656 nm (green), and the S II line at 672 nm (red). [a]`https://astrometry.net`

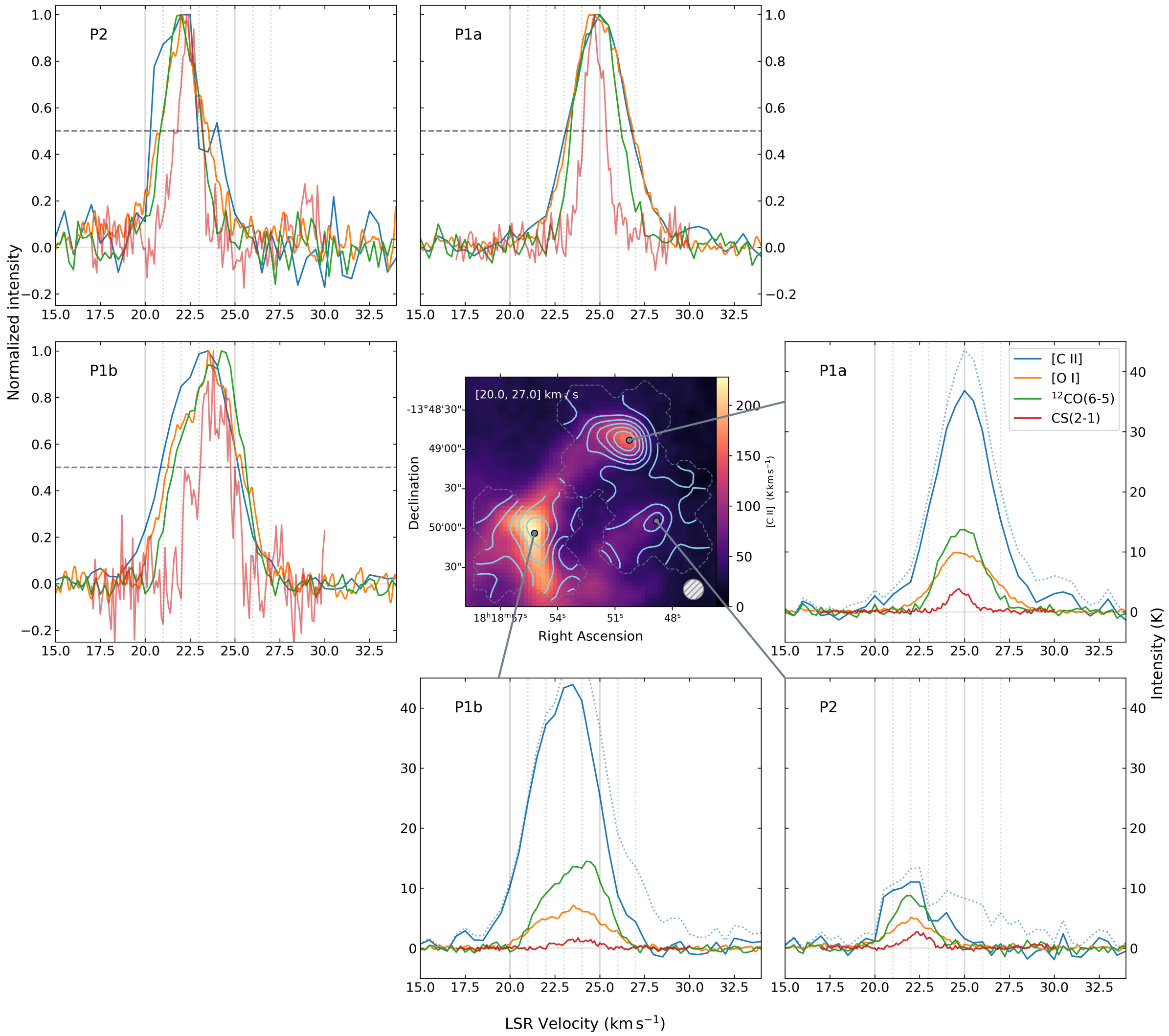

Figure 2.6 Spectra of the [C II], [O I], CO(J=6–5), and CS lines towards the three brightest [O I] positions. The lower-right three panels show the absolute spectra in Kelvins. The upper-left three panels show the same spectra normalized to their maxima. Half-maximum, for estimating the FWHM, is marked with dashed horizontal lines. The [C II] spectra are shown after the spectral background subtraction described in Appendix B.2, and the unsubtracted [C II] spectra are shown with dotted lines in the lower-right panels for context. Vertical lines mark every 1 $\mathrm{km\ s^{-1}}$ between 20–27 $\mathrm{km\ s^{-1}}$. The [O I], CO, and CS observations are all convolved to the [C II] beam, shown in the lower right corner of the central panel. The central panel shows [C II] (color) and [O I] (contour) emission integrated between 20–27 $\mathrm{km\ s^{-1}}$. The [O I] contours are placed at [0, 6, 12, 18, 24, 30] K $\mathrm{km\ s^{-1}}$. Dashed grey lines in the central panel show the area covered by these [O I] observations. Velocities are relative to the local standard of rest (LSR).

to direct illumination from NGC 6611 over a broad surface of neutral gas. An embedded source in the rim (Indebetouw et al., 2007; Sugitani et al., 2002) may contribute to the 8 μm emission. At the sub-arcsecond resolution of the 3.3 μm PAH image, the FUV-illuminated surfaces throughout the pillar appear as composites of the many illuminated surfaces of sub-0.01 pc clumps. The wavy surfaces are reminiscent of the ridges and waves detected by Berné et al. (2010) on the surface of Orion's shell or by Hartigan et al. (2020) along the edge of Carina's Western Wall. The gas is clumpy/porous at least down to this 0.01 pc length scale.

2.3.2 P1a: Threads and Cap

P1a appears composed of three morphologically and kinematically distinct features: the "Cap" oriented across the top of Pillar 1 and two filamentary structures (henceforth "Threads"; Figure 2.1) hanging down from the head of the pillar in the NIR images in absorption (JWST F090W and F187N in Figure 2.1 and the 1–2 μm images by Thompson et al. 2002) as well as in most molecular lines in emission. The HCO^+ and CS line channel maps in Figure 2.7 show that the Threads are more or less parallel to each other and have similar lengths of $\sim$0.3 pc. There are red-to-blue radial velocity gradients of order $-1~\mathrm{km\,s^{-1}}$ $\mathrm{pc^{-1}}$ along each Thread towards the pillar head (see between 70–100$''$ and $\mathrm{V_{LSR}} < 27~\mathrm{km\,s^{-1}}$ in the position-velocity diagram along P1 in Figure 2.8). The Eastern Thread is spatially broader, $\sim$0.15 pc wide in CO emission just below the head of the pillar, and is redshifted by $\sim 1~\mathrm{km\,s^{-1}}$ with respect to the thinner ($\sim$0.07 pc) Western Thread. The Eastern Thread has a transverse gradient in radial velocity, evident in the ^{12}CO position-velocity (PV) diagrams in Figure 2.9, redshifting to the west. [C II] emission towards the Threads is centered on the Eastern Thread and appears uniform

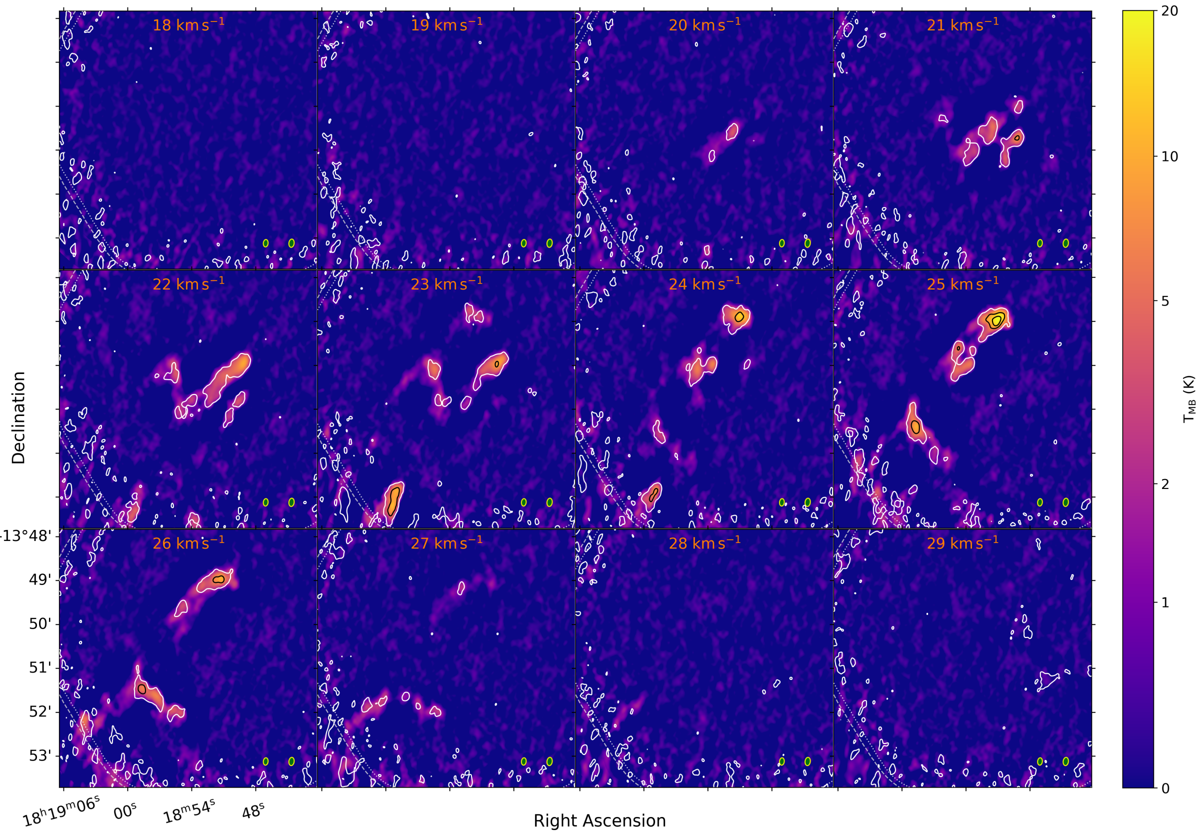

Figure 2.7 HCO^+ (color) and CS (contour) line channel maps binned to 1 $\mathrm{km\ s^{-1}}$ and centered on the Pillars. The HCO^+ images use an arcsinh colorscale to make low-level emission more visible. The CS contours mark [0.7, 4.7, 8.7] K. The contour colors are chosen to increase contrast with the image and have no further significance. The CS (left) and HCO^+ (right) synthesized beams are shown in the lower right corner of each map. The HCO^+ (CS) 50% gain contour is shown with a dashed (dotted) line.

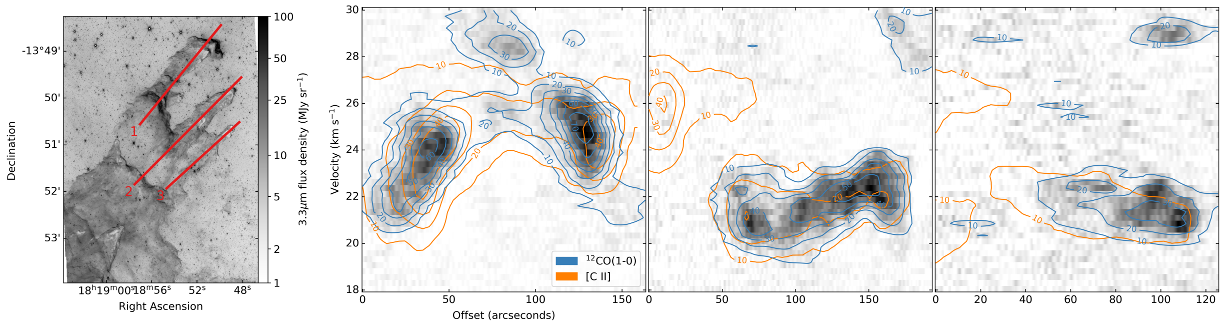

Figure 2.8 Position-velocity (PV) diagram along each pillar using the [C II] and ^{12}CO(J=1–0) line observations. The left panel shows the F335N image with the three paths overlaid. The paths are numbered and the labels are placed at the beginning of the path. The next three panels show, from left to right, the PV diagrams of P1, P2, and P3 along the numbered paths. In each PV diagram, the greyscale image is the CO PV diagram at the native CO spatial resolution, while the contours show both CO and [C II] at the [C II] resolution. Contour labels are main beam temperatures $T_{\rm MB}$ in Kelvins. Emission at $\rm V_{LSR} \gtrsim 27~km~s^{-1}$ is from background features not directly related to the Pillars. Velocities are $\rm V_{LSR}$.

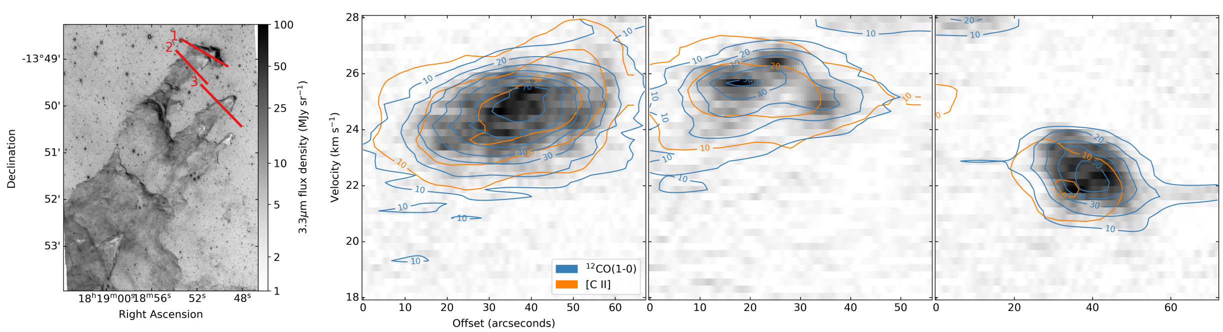

Figure 2.9 Same layout as in Figure 2.8, but with PV diagrams along different paths. The first path runs across the Cap and shows its peak velocity gradient. The second path crosses the two Threads and shows the differences in [C II] and CO velocity structure. The third path crosses the head of P2 and shows the spatial and kinematic offset of the [C II] peak with respect to CO as well as the velocity gradient across the head in both lines. Velocities are $\rm V_{LSR}$.

across that section of the pillar rather than threaded like the molecular gas; this difference is demonstrated in Figure 2.3 and is still evident when molecular lines are convolved to the [C II] beam. A detailed analysis of the velocity structure in [C II] and HCO^+ emission, described in Appendix B.3, reveals a kinematic detection of the Western Thread in [C II] spectra. Bonne et al. (2023c) observes filamentary features, which they termed "legs", extending from the IC 63 nebula away from the stars with similar velocity gradients.

The peak brightness temperatures of molecular lines towards each Thread are comparable. This implies one or both of 1) higher column density towards the Western Thread, which in turn implies higher density assuming cylindrical symmetry, or 2) higher temperature towards the Eastern Thread. The N_2H^+ line emission towards P1a around $\mathrm{V_{LSR}} = 23\text{–}26\ \mathrm{km\ s^{-1}}$ extends slightly towards the northernmost part of the Western Thread, indicating higher density.

The Cap is a lower velocity ($\mathrm{V_{LSR}} = 22\text{–}24\ \mathrm{km\ s^{-1}}$) [C II] component associated with P1a which extends east from the head and lies on top of the pillar like a cap. The Cap is observed in the lines of [C II], [O I], and all but the highest critical density molecular lines. A dark NIR feature indicating high extinction lies towards the Cap's molecular line emission, while the [C II] and [O I] are coincident with a bright NIR/illuminated-PAH rim spatially shifted towards the exciting stars.

There is a steep gradient in radial velocity along the Cap, with velocity increasing from east to west, in all lines in which the Cap is observed (see the first PV diagram in Figure 2.9). Line widths broaden significantly towards the center of the Cap where it meets the rest of P1a's associated velocity components. If we follow the Threads northwest into the pillar head, we find that they spatially merge just as their velocity gradients lead their line profiles to blend together in velocity and become indistinguishable. The line profiles of both Threads and the Cap blend together just northwest of the middle of P1a, where we detect the brightest molecular line and FIR continuum emission. Detection of the N_2H^+ line towards this "Merge Point", marked in Figure 2.1, indicates cold, shielded gas. The [C II] emission on the eastern side of the Eastern Thread has a particularly broad line profile with a lower velocity wing. A similar pattern is observed in ^{12}CO lines, and is present but significantly diminished in HCO^+ when compared to CS (see the spectra in Appendix B.1).

2.3.3 P1b: Base and Horns

P1b, the lower half of P1, includes features from the Horns down to the eastern half of the Shared Base. The complex of features is bright and continuous in warm tracers like [C II], PAH emission, and FIR dust continuum and discontinuous, particularly along the Shared Base, in molecular lines and other dense gas tracers. The two Horns extend northwest from P1b in all tracers with spatial resolution better than $\sim 10''$. These ~ 0.1 pc diameter clumps are particularly pronounced in the molecular line channel maps, indicating the presence of dense molecular gas, and the N_2H^+ and $C^{18}O$ lines are faintly detected towards the Western Horn but not the Eastern Horn. The Western Horn is brighter in longer wavelength ($> 160\ \mu$m) dust continuum, while the Eastern Horn is brighter in NIR ionized gas tracers and PDR tracers like [C II] and PAH features, consistent with a higher molecular gas column density through the Western Horn. A bright rim of optical, NIR, and PAH emission lies atop each Horn's molecular emission in the direction of NGC 6611. We discuss the illumination structure of P1b further in Section 2.4.

We observe velocity gradients along each Horn: the top of the Western Horn is more blueshifted than the gas below it, while the Eastern Horn is more redshifted than the gas below it. Interpreting these Horns as pillar-like structures along which gas is accelerated away from the stars (Pound, 1998), the observed gradients imply that the Western Horn faces towards us and the Eastern Horn faces away as we illustrate in Figure 2.10.

Below the Horns lies the Shared Base, a bright [C II]-emitting feature which is distinguishable from the rest of P1 by its darker appearance in the optical/NIR images (Figure 2.5). The high-resolution 3.3 and 8 μm PAH emission maps show extended emission all the way across the Shared Base between P1 and P2, indicating a broad illuminated surface. The Shared Base is the site of broad line emission in all observed lines and a strong radial velocity gradient ($\sim -3\ \mathrm{km\,s^{-1}}$ pc^{-1}) smoothly connecting P1 to P2. The [C II] and ^{12}CO lines contain excess low-velocity emission between $\mathrm{V_{LSR}} \approx$ 21–22 $\mathrm{km\,s^{-1}}$ compared to higher critical density molecular lines like HCO^{+}; we show example spectra in Appendix B.1.

2.3.4 P2

Continuum images from 3–500 μm show a cohesive column with a bright top. The 3.3 and 8 μm images resolve the head of P2 as a bright, $\sim$0.01 pc wide rim atop a dark clump about 0.08 pc in diameter and reveal a second similarly sized dark clump 0.4 pc below the head, about halfway down the pillar body. This clump along P2's body is outlined at its top by thin (0.006 pc at 3.3 μm) bright rim and coincides with a re-brightening in the 70–500 μm images.

Line emission peaks between $\mathrm{V_{LSR}} =$ 22–23 $\mathrm{km\,s^{-1}}$ towards the pillar head; high density tracers like N_2H^{+} peak closer to $\mathrm{V_{LSR}} = 23\ \mathrm{km\,s^{-1}}$ while warmer, lower density tracers like [C II] and ^{12}CO(J=1–0) are blueshifted by about 1 $\mathrm{km\,s^{-1}}$ and all ^{12}CO line profiles have low-velocity wings. This relative velocity shift of warm tracers to dense tracers, similar to low-velocity wings observed towards P1b and to lesser degree towards P3, persists throughout the northern half of the Pillar, but the pattern disappears as line widths increase towards the southern half. We discuss this behavior in Section 2.6.1.

Velocity gradients are detected in most lines both along and across the pillar body (Figures 2.8 and 2.9). Gradients across P1 and P2 were also observed by Sofue (2020). Line velocities are highest towards the northeastern side of the pillar head, and decrease both to the west across the head and to the south along the body. [C II], and [O I] where it is observed towards the head, trace a coherent column which gets almost monotonically brighter towards the base of the pillar in integrated intensity, with only a slight local brightness maxima at the head where the PAH tracers brighten. Molecular lines trace more substructure along P2 than [C II]. HCO^+, HCN, CS and the CO lines trace an elongated clump towards the head, the clump towards the middle of the body, and two filametary tails below the second clump. The $C^{18}O$ and N_2H^+ lines are only detected towards the head and the mid-body clump, where all molecular line profiles are broadest. Between these two features, molecular line emission is dim and lines are narrower (see for example the PV diagram along P2 in Figure 2.8).

The NIR and optical (Hester et al., 1996) images feature a bright "wisp" about midway along the pillar, just above the location of the clump. The wisp seems to originate from P3 and cross the body of P2, as we see some continuous edges in the optical images both towards and off P2. Emission from the HCO^+, CS, and ^{13}CO lines is dimmer where the wisp overlaps with P2 between the head and the clump. The wisp, where it passes over P2, is therefore coincident with a region of optically thinner lines of sight through P2. The southern edge of the wisp is very close (0.05 pc or $6''$, smaller than our molecular line beams) to the dark, dense clump mid-way down the pillar body.

2.3.5 P3

Pillar 3, the smallest of the three main Pillars, presents in our molecular line observations as a $\sim$0.38 pc long pillar oriented roughly parallel to P1 and P2 with two tails which extend $\sim$0.34 pc in either direction at $\sim$100° angles from the body in a "wishbone" shape also seen in optical images. The head of the pillar is brightest at $\mathrm{V_{LSR}} \approx 21.2\ \mathrm{km\ s^{-1}}$ in all molecular tracers. Using the line profile modeling described in Appendix B.3, we find that [C II] is blueshifted relative to the molecular lines by $\lesssim 0.3\ \mathrm{km\ s^{-1}}$ through the head. $C^{18}O$ and N_2H^+ are only observed towards the pillar head. The wishbone tails are reminiscent of the "ears" of cometary globules simulated by Lefloch & Lazareff (1994) in 2 dimensions, which they discuss in Sections 5.2 and 5.3.1 of their paper.

2.3.6 Ridge

The Ridge and P4 (Section 2.3.7) are detected in most molecular lines and are each associated with a compact clump of N_2H^+ line emission indicating enhanced gas density. The Ridge is outside of the half-power beam of the CO(J=1–0) observations, and P4 was not covered by the CO(J=6–5) observations and lies on the edge of the HCO^+, HCN, CS, and N_2H^+ half-power beam.

The Ridge, lying around 0.5 pc southeast of the main Pillars' tails and appearing in the same $\mathrm{V_{LSR}} \approx 25\ \mathrm{km\ s^{-1}}$ channel maps as P1 (Figure 2.7), is a 0.8 pc long and 0.08 pc thick bar of molecular and [C II] line emission oriented perpendicular to the direction of illumination. The Ridge spans nearly the same width as the three-pillar system. The integrated FIR dust emission from the Ridge (proxy for FUV radiation field; Section 2.4) is shifted towards NGC 6611 by

$\sim$0.03 pc with respect to dust column density (Section 2.5), and at higher resolution, the 3.3 and 8 μm PAH emission arise from the edge of the Ridge facing the cluster and decrease in brightness towards sites of enhanced molecular line emission along the Ridge. We do not detect a spatial shift of [C II] line emission with respect to molecular line emission.

Radial velocity increases from east to west along the Ridge in all lines in which it is observed. Below the Ridge, we observe diffuse PAH and dust emission between 3–500 μm as well as diffuse [C II] emission between $\mathrm{V_{LSR}} = 24$–$27\ \mathrm{km\ s^{-1}}$ (same velocity interval as the Ridge) clearly bounded to the northwest by the Ridge and to the northeast by another ridge of gas perpendicular to the Ridge. This diffuse emission appears bounded to the west/southwest by a curved stream of gas, represented by the dashed line in Figure 2.1, but this stream of gas is separated by a few $\mathrm{km\ s^{-1}}$ from the Ridge in [C II], CO(J=3–2), HCN, and HCO^+ line velocity. To the south, the diffuse emission continues into the bright, $\sim$10 pc scale feature associated with the edge of the H II region. We do not detect this diffuse emission in the molecular lines, but we do detect the Ridge, the perpendicular ridge to the northeast, and, faintly, the west/southwest stream. The Ridge and northeast ridge are comparably bright in [C II], while the northeast ridge is somewhat dimmer in ^{12}CO(J=3–2), much dimmer in HCO^+ and HCN, and not detected in CS.

Molecular gas column density is higher along the boundaries between the diffuse neutral gas and the ionized gas, particularly the Ridge, and all the neutral gas between the Ridge and northeast ridge is well illuminated. The west/southwest stream is closer in velocity to P2 and P3, while the Ridge is more kinematically similar to P1 as shown by the velocity RGB image in Figure 2.5. Figures 2.1 and 2.5 show optical and NIR counterparts to the Ridge, northeast ridge, and west/southwest stream.

2.3.7 P4

P4, a more triangular feature than the three main Pillars, has bright eastern and western edges in the 3.3 and 8 μm PAH maps. NIR continuum, like that in the central panel of Figure 2.1, shows extinction in all bands through the head and body. From the [C II] channel maps, we detect a radial velocity gradient along the edge of P4, from its southwestern corner ($V_{\rm LSR} \sim 21\ {\rm km\,s^{-1}}$) up its western side to its point ($\sim 23\ {\rm km\,s^{-1}}$) and back down its northeastern corner ($\sim 25\ {\rm km\,s^{-1}}$). [C II] line emission outlines the (upper two) triangular edges of P4 and is around 30% dimmer towards the middle of the pillar. The blueshifted western edge corresponds with the dark ridge in the NIR images. We do not resolve much spatial structure in the CO(J=3–2) observations but do detect some variability in radial velocity along the feature. P4 lies towards the edge of the H II region, which is a brighter [C II] source with a complex line profile that is not well separated from P4's line emission.

2.3.8 Summary and Geometry

The overall picture that emerges from this wealth of data is schematically represented in Figure 2.10. The PAH emission traces surface structures illuminated by the stellar cluster and can be used to derive the geometry of the Pillars and their orientation relative to the stellar cluster. The Pa-α emission originates mostly from diffuse ionized gas filling the H II region surrounding the Pillars. The relative strength of this line helps in placing structures such as P4 and the Ridge more on the near side or far side of the ionized cavity. Peak [C II] and molecular line velocity gradients along each pillar trace bulk motions of the gas pushed away from the stars and can indicate whether pillars are inclined towards or away from the observer (McLeod et al., 2015;

Pound, 1998). This analysis places P1b, P2, and P3 in the foreground and, while P1b and P2 point toward the illuminating stars, P3 is backlit. P1a is in the background and points toward the illuminating stars as well. P1b and P2 are connected by the Shared Base, while a connection between P1a and P1b is implied by the kinematically continuous [C II] emission between them and their on-sky projected alignment. Warm gas tracers are blueshifted by $\sim$0.5 $\mathrm{km\ s^{-1}}$ towards P1b and the head of P2. Since these pillars are both facing away from us, we interpret this to mean that the less dense outer layers are accelerated down the pillars more quickly than the dense interior layers; this is discussed in detail in Section 2.6.1. We note that we determine the sign of the pillar inclination (towards or away from the observer), but not its magnitude, from the kinematic analysis; the particular inclinations depicted in Figure 2.10 are but one possible configuration. Sofue (2020) calculates the absolute values of the inclinations to be 47°, 40°, and 40° for P1a, P2, and P3, respectively; each may be towards or away from the observer.

The Threads' radial velocity gradients, redshifting away from the head, are consistent with material being accelerated away from the dense head along a pillar which is on the far side of the illuminating stars and points towards both the stars and the observer, consistent with the LOS position of P1a suggested by Pound (1998) and McLeod et al. (2015). The Eastern Thread is redshifted with respect to the Western Thread; if material flows down both Threads with a similar velocity, then the Eastern Thread may be more inclined, as drawn in Figure 2.10, so that it has a greater projected velocity than the Western Thread. The Cap's radial velocity gradient blueshifts away from the head, which would imply that it lies between the stars and the observer and faces away from us. The velocity gradient may be due to unknown kinematic interactions in the pillar head, or it is possible that the head is extended along the line of sight so that parts of it are on either side of the cluster with respect to the observer. This second explanation is not so unreasonable if we expect that P1's head is almost right below the cluster with very little line-of-sight offset; in this case, the line-of-sight separation between the nearest and farthest parts of the head, on opposite sides of the cluster with respect to us, wouldn't be that large. We elect to place P1a directly below and only slightly behind the stars in our geometric model in Figure 2.10, in accordance with the second explanation for this velocity gradient.

The Shared Base is depicted in Figure 2.10 extending a significant distance between P1 and P2. Our analysis of column density towards the Shared Base versus average number density elsewhere implies a LOS width $\gtrsim$0.5 pc (see Sections 2.4.1.2 and 2.5.1), and our analysis of the FUV radiation field places the heads of P1a and P2 $\sim$1 pc from each other along the LOS (see Section 2.4.2). Both of these analyses depend on the geometry and optical depth of the Pillars, and the latter is sensitive to the LOS geometry of the cluster members and extinction of FUV radiation between the cluster and the Pillars, though relative distances (such as between P1a and P2) via the latter method are not affected by uniform extinction between the cluster and all features. Figure 2.10 represents our analysis-based educated guess of LOS widths and separations of the Shared Base and other features, but these uncertainties prevent us from making precise estimates.

The positions of P4 and the Ridge are more uncertain than those of the three main Pillars. We place P4 closer to the observer along the LOS based on its relative darkness in Pa-α, and the Ridge farther from the observer based on its relative brightness in Pa-α (Figure 2.1). FIR emission towards both of these features, but particularly P4, is brighter than we expect given the projected distances of the selected stars, so the assumptions about the cluster which we use to estimate incident FUV radiation field for the three primary Pillars are not appropriate for features farther away from the cluster. Additionally, some of P4's FIR emission might originate from

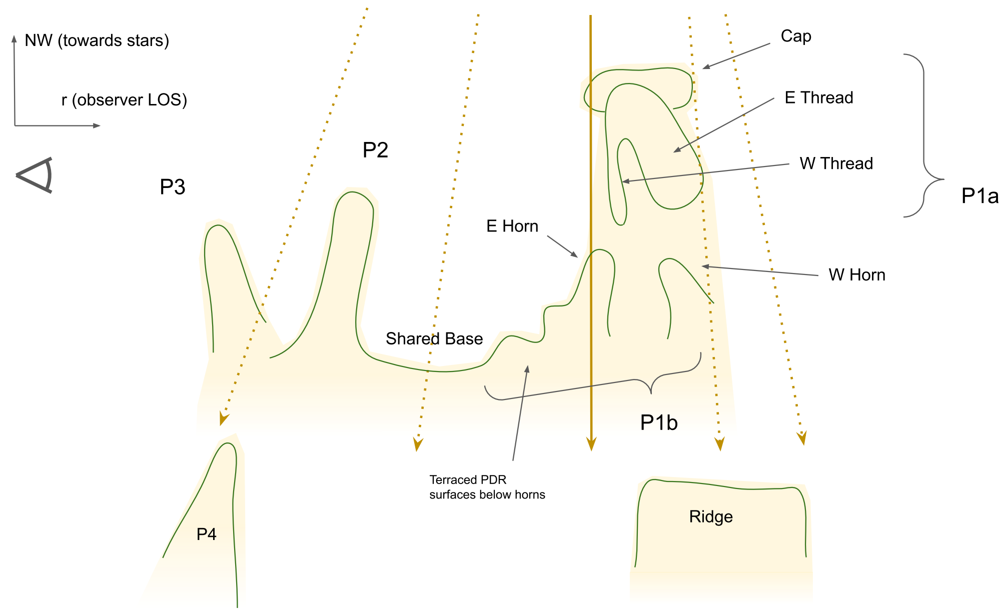

Figure 2.10 Schematic diagram of the pillar system as viewed from the southwest, so that the observer's line of sight runs horizontally across the figure. The green lines mark molecular gas structures and the yellow highlight marks atomic gas structure, which forms an envelope around the molecular gas (Section 2.4.1.1). The gold rays originating from the top of the figure mark the direction of illumination, with the solid central line marking the "perpendicular" ray and the assumed line-of-sight position of the stars. P1a and P1b are both collections of features. The Shared Base and P1b overlap in definition, and the distinction between them is not particularly relevant because they are both approximate labels for (sets of) observed features. We estimate that the heads of P1a and P2 are separated by $\sim$1 pc along the line of sight; see Section 2.3.8 for more detail.

1) an embedded young stellar object (YSO) and/or 2) internal heating by that YSO, rather than solely from reprocessed FUV radiation from the main cluster. We discuss this in more detail in Section 2.4.2.

2.4 Photodissociation Regions

2.4.1 Morphology and Geometry of the Major PDRs

Any bright [C II]-emitting feature is likely the site of a PDR, and our [C II] observations show that M16 is rich in PDR emission. The vast majority of the [C II] emission is indeed from atomic gas, with a line width of $\sim$1 $\mathrm{km\,s^{-1}}$ rather than from ionized gas which would have a turbulence-dominated line width closer to 10 $\mathrm{km\,s^{-1}}$ (Cuadrado et al., 2019, and see Appendix B.2 for discussion about [C II] from the H II phase). Throughout P1 and the rest of the pillar system, sub-arcsecond resolution optical and near-IR maps trace bright rims which are $\sim$5–20 times brighter than their surroundings. We interpret these areas, which include the Cap, Eastern Horn, and Shared Base in P1, the bright rim atop the head of P2, and parts of the head of P3 and the Ridge, to be limb-brightened edge-on PDRs. We interpret the dimmer, "average brightness" emission to originate from poorly illuminated PDRs or PDRs viewed face-on or through dust extinction.

The remainder of this section highlights some of the bright PDRs throughout the Pillars with a focus on their orientation with respect to the observer and implications about the overall geometry of the system. In order to discuss the geometry of some of these structures, we must consider the atomic and molecular gas column densities through them. Column densities are discussed in depth in Section 2.5, but the results of that section inform the following discussions.

2.4.1.1 P1a

Bright PDRs are associated with three distinct sets of features along the body of P1: the Cap, the Horns, and the Shared Base. The head of P1 features a prominent PDR across the top of the Cap, observed as a bright rim in 8 μm and [C II], and [O I] sitting atop the molecular emission (Figure 2.3), which we are viewing edge-on (Levenson et al., 2000). Below the Cap, we see relatively bright PAH emission towards a sort of "shoulder" atop the Western Thread, but only moderate PAH emission between the Cap and the Horns indicating that there are few edge-on illuminated surfaces towards the Threads.

Most of the [C II] and molecular spectra towards the head of P1a are not fit well by a single Gaussian component. Since we observe several morphologically distinct components in the channel maps presented in Section 2.3.2, we determine that P1a contains multiple components which are separated by less than their individual linewidths. In a detailed kinematic analysis of P1a described in Appendix B.3, we find that the HCO^+ spectra towards P1a are fit well with 3 components corresponding to the Cap, Eastern Thread, and Western Thread, while the [C II] spectra towards P1a are fit well with 2 components corresponding to the Cap and a combined-Thread component. The [C II] spectra towards the Threads are dominated by the Eastern Thread component, which lies at a higher velocity than the Western Thread component based on their molecular line velocities, but we detect a weak signature of the Western Thread component in the [C II] spectra. As the [C II] emission does not exhibit the threaded morphology found in the molecular emission, even at matched spatial resolution, we determine that the [C II] likely originates from a more uniform, extended envelope of atomic gas surrounding the dense molecular gas features.

Unlike the P1a spectra discussed above, the [C II] and molecular spectra towards the Merge Point in P1a, marked in Figure 2.1, are fit well with a single component. Based on our analysis in Appendix B.3, we suggest that the Cap and two Threads are physically joined together as one component towards this position. N_2H^+ line emission detected towards the Merge Point indicates cold, shielded molecular gas buried deep within the cloud. Our proposed geometry in Figure 2.10 envisions the Cap as a compressed rim or globule-like structure and the two Threads as legs trailing down from that cloud.

2.4.1.2 P1b

The Horns, the warm gas below them, and the Shared Base are all capped with bright rims of PAH emission and form a terraced arrangement of edge-on PDRs. These rims lie atop sites of molecular emission which are spread out in velocity. Molecular line emission towards the Horns lies at $\mathrm{V_{LSR}} = 23$–$25\ \mathrm{km\ s^{-1}}$. The bases of the Horns are connected by warm, low column density ^{12}CO-bright gas between $\mathrm{V_{LSR}} = 23$–$24\ \mathrm{km\ s^{-1}}$ (White et al., 1999). The Shared Base lies at $\mathrm{V_{LSR}} = 22$–$23\ \mathrm{km\ s^{-1}}$. The Shared Base and the Horns are spatially and dynamically connected but are separated by about 0.13 pc and $1\ \mathrm{km\ s^{-1}}$ and appear as distinct features in molecular line channel maps. These observations are consistent with the Horns and Shared Base being distinct, but connected, sites of strong PDR activity. P1b and the Shared Base host multiple clumps of illuminated gas and behave in some ways like pillar heads.

Table 2.3 in Section 2.5 lists a high atomic column density $N(\mathrm{H})$ derived from C^+ towards the Shared Base compared to what we expect based on the PDR modeling described in Section 2.4.3. Either the atomic gas density towards the Shared Base is $\sim$2 times higher than other regions or there is a long line-of-sight length through this gas structure. We prefer the second explanation since we do not expect P1b to be the site of enhanced atomic gas density, particularly since there is little molecular gas. If we expect the density to be closer to the median atomic gas density in Table 2.3, then the Shared Base may extend $\gtrsim$0.5 pc along the line of sight like a “valley” between P1b and P2 as pictured in Figure 2.10. This can explain the strong observed gradient in peak velocity along the Shared Base, as the projected gradient would be larger than the physical gradient. The terraced arrangement of illuminated surfaces along P1b as well as the position of P1a below NGC 6611 while P1b and P2 are closer to the observer (McLeod et al., 2015; Pound, 1998) suggest that P1b continues to extend away from the observer along the LOS above the Shared Base, towards the Horns.

The emission characteristics of the Eastern and Western Horns described in Section 2.3 indicate that the Eastern Horn is associated with more illuminated surface, either in total or facing us. Some, but not all, of the Eastern Horn's brightness compared to the Western Horn can be explained by two geometric phenomena. First, the Western Horn's illuminated surface must be mostly on the far side of the feature so that its $<$8 μm emission is extincted by dust within the Horn. Second, the Eastern Horn is superimposed on the body of P1, which can still be viewed through the Horn at longer wavelengths (dust continuum $\geq$70 μm and the [C II] line) and must be responsible for the Eastern Horn's brightness at those wavelengths. This line-of-sight relationship is easiest to see in the optical images where it is clear that there is extra pillar emission surrounding the Eastern Horn. The observed radial velocity gradients (Section 2.3) along the Horns suggest that the Western Horn faces towards us and the Eastern Horn faces away.

2.4.1.3 P2

All PDR tracers (PAH, 70–160 μm, [C II]) are dimmer towards P2 and P3 than towards the PDR-heavy P1. The brightest [C II] emission along P2 lies around $\mathrm{V_{LSR}} = 20$–$22\ \mathrm{km\ s^{-1}}$ and is associated with the Shared Base. The emission further up the body of P2 is roughly 60% as bright as the emission towards its base and remains roughly constant in brightness even towards the head of P2. We attribute these observations to P2 hosting a smaller illuminated PDR surface than the various locations along P1. Towards P2, we observe PDR tracers through a limited column density and thus they appear less bright than towards P1. Bright PAH emission is observed along the edge of the P2 head, which is not as flat in projection as the Cap in P1a and may present 1) less surface area in total and 2) a larger fraction of surface area illuminated at higher inclination (greater angle from the normal). Below the head of P2, we see a rim of enhanced PAH emission atop the dark clump mid-way down the body and atop several cometary clumps towards the base. P1 and P2, despite a clear difference in the brightness and abundance of PDRs along their bodies, both contain numerous small illuminated surfaces between their heads and tails.

2.4.1.4 P3

P3 is even dimmer in [C II] than P2 (see spectra in Appendix B.1) and is not as well resolved in [C II] or 70 μm since its projected width ($\sim$14$''$, 0.1 pc) is comparable to their beams. At 3.3 μm, the head of P3 is capped by a thin ($\approx$0.008 pc) rim of PAH emission. The two tails of P3 which give it its wishbone shape are brighter along their cluster-facing edges in 3.3 and 8 μm emission, indicating that the tails host PDRs. As P3 and its tails are small compared to the beams of most of our observations, we will not be able to study them in as much detail as P1 and P2.

2.4.1.5 Ridge

The fact that the Ridge is approximately perpendicular to the direction of illumination and spans the width of the three-pillar system lying above it suggests that it may have formed in the shadow of the Pillars. It is at least somewhat illuminated by the cluster at present, as it hosts an extended PDR surface along its 1 pc long surface facing NGC 6611. The derived C^+ column density towards the Ridge is higher than expected given its projected width ($\approx$0.1 pc), similar to what we described for the Shared Base in Section 2.4.1.2, so it must have a LOS size of $\gtrsim$0.3 pc.

The rim of PAH emission is brighter and thicker where molecular line emission is weak along the Ridge, which could be due either to extinction through the dense clumps if the Ridge faces slightly away or gas density variations along the Ridge altering the physical PDR width if the Ridge is viewed nearly edge-on.

2.4.1.6 P4

The two sides of the angular P4 both host edge-on PDRs at their surfaces. We assume the low 1.87 μm Pa-α emission towards P4 (green in the central panel of Figure 2.1) is due to a low foreground column density of diffuse ionized gas, indicating that P4 is relatively close to the observer within the pillar system. The low intensity PAH emission towards the face of P4 may then originate from the illuminated far side and be extincted by dust inside the structure. We cannot determine the orientation of P4 based on kinematics or extinction, but we orient it in Figure 2.10 pointing away from the observer towards the main cluster. One must consider the possibility that it faces towards the observer similar to P3.

The source driving the Herbig-Haro object HH 216 lies at the tip of P4 (Andersen et al., 2004; Flagey et al., 2020; Indebetouw et al., 2007). Indebetouw et al. (2007) suggest that it is one of two Class I YSOs identified towards the tip of P4, while Flagey et al. (2020) identify a third nearby point source which may be responsible. We discuss the possible effect of this source on the FUV radiation field at P4 at the end of Section 2.4.2.

2.4.2 Sources of Illumination

The brightest members of NGC 6611 are ~ 2.5 pc from the Cap in P1a and ~ 5 pc from P4, meaning that illumination varies by a factor of ~ 4 along the pillar system. We use the catalog of NGC 6611 published by Hillenbrand et al. (1993) to estimate the FUV radiation field G_0 throughout the pillar system. The process is described in Tiwari et al. (2021) and the software is publicly available as `scoby`[5]. We link the spectral types of early-type NGC 6611 members published by Hillenbrand et al. (1993) to T_{eff} and $\log\, g$ values using the tables of Martins et al. (2005), and then use the T_{eff} and $\log\, g$ values to select stellar models from the PoWR suite (Hainich et al., 2019; Sander et al., 2015). The PoWR stellar models provide theoretical spectra, which we combine with the catalog coordinates to estimate the FUV (6–13.6 eV) intensity at a given location from a single star assuming the projected distance and no intermediate extinction. We estimate the total FUV intensity at the given location by summing across the contribution from all, or a subset of, stars in the catalog. There are a handful of early-type stars within ∼1 pc of the Pillars in projection which cause our G_0 estimate to exceed 5000 Habing units towards the Pillars. This is unreasonable given the FIR-based estimates described later in this section, so these stars must lie ≳1 pc away along the line of sight. We restrict our sample to stars within 2 pc in projection of the approximate cluster core $(\alpha,\, \delta)_{J2000} = (18^{\mathrm{h}}18^{\mathrm{m}}35\overset{\mathrm{s}}{.}9543,\ -13°45'20.364'')$, which includes 30 stars with types B2.5 and earlier. We additionally restrict stars to have $\log_{10}(L_{\text{FUV}}/L_{\odot}) > 4.5$ since the largest cluster members should dominate the feedback; 8 stars remain after the filtering. We find that including all 30 stars increases G_0 by ∼50% near the Pillars. The FUV radiation field calculated from our final list of 8 stars (# 161, 166, 175, 197, 205, 210, 222, 246 in the

[5] The code is archived at `http://hdl.handle.net/1903/30441`; `scoby` is also developed on GitHub

catalog of Hillenbrand et al. 1993) is $G_0 \sim 2500$ Habing units towards the heads of P1a and P2, ~ 1700 towards P3, ~ 1500 Habing units towards the Shared Base, and < 1000 Habing units below the Ridge.

We can also estimate the FUV radiation field based on FIR thermal emission from dust, assuming that dust is re-radiating absorbed FUV radiation (Wolfire et al., 2022). The FUV radiation field values are derived from the FIR dust emission at 70 and 160 μm using the methodology described in Schneider et al. 2016 and corrected for a background sampled from the regions described in Appendix B.2. Through this method, we estimate $G_0 \sim 2000$, 700, and 300 Habing units towards the heads of P1a, P2, and P3, respectively; and 800–1200 Habing units towards the Shared Base, the Ridge, and P4.

The stellar estimates of G_0 should be strict upper limits as they assume that all stars and features lie at their projected distances on the plane of the sky and that all starlight reaches every feature without extinction. The discrepancy between the higher stellar estimate and lower FIR estimate of G_0 towards P2 and P3 could be a result of 1) line-of-sight separation on the order of a few parsecs, consistent with their positions on the near side of the cluster with respect to the observer, 2) intermediate extinction by gas/dust within the cavity, and/or 3) beam dilution by the $\sim 14''$ beam at 160 μm, as the PDR surfaces at the heads of these two smaller pillars cover a smaller solid angle than the PDR towards the Cap in P1. Allowing for some line-of-sight spread among the cluster members, the FIR-based estimates of G_0 towards the Cap, Shared Base, Ridge, and P4 are fairly consistent with the stellar estimates. These features must lie close to their projected distances from the stars; this is most significant for the Cap, which lies fairly close in projection and so must lie approximately directly below the brightest cluster members.

The Pillars' FUV illumination is dominated by the massive cluster members near the cluster core. The handful of early-type stars which are close in projection (within $\sim$1 pc) to the Pillars are not significant contributors to the FUV field at the Pillars and thus must be separated from the Pillars by $\gtrsim$1 pc along the line of sight, though they may still be important contributors to the FUV field below the Ridge and to off-axis illumination. These near-Pillar stars may shine on parts of the pillar bodies that would otherwise be shadowed by the pillar heads with respect to the cluster core; that said, off-axis illumination is probably dominated by the diffuse extreme ultraviolet (EUV, $h\nu > 13.6$ eV) field created by recombinations directly to the ground state.

P3 appears not to face the bright cluster core, as explained in Section 2.1. It is possible that it faces a different star than the rest of the pillars, one which lies on the outskirts of the cluster. P3 is the nearest of the Pillars to the observer (McLeod et al., 2015, and see schematic in our Figure 2.10), so a star displaced closer to the observer along the LOS could have a significant impact on the evolution of P3 while having little impact on P1 or P2. We do not have sufficient information to identify a candidate star, but suggest that it could be among stars # 166, 197, 205, and 210 (O8.5 V, O7 V((f)), O5 V((f*)), and B1 III, respectively), which lie $\sim$2 pc away in projection from P3 in the direction it points. P1 and P2 are well aligned with the expected morphology and kinematics of the radiative interaction of the NGC 6611 cluster with the molecular shell; we consider it unlikely that P3's orientation away from the cluster is evidence that P3 was sculpted by a different phenomenon than the other Pillars, such as ablative Rayleigh-Taylor instability (Mizuta et al., 2006), given its similarity in morphology and close proximity. Since we cannot constrain the orientation of P4, we must consider the possibility that it faces us like P3, in which case this same discussion would apply.

2.4.2.1 Line-of-Sight Pillar Geometry from G_0

We can roughly estimate the line-of-sight geometry of the Pillars using our two G_0 estimates, assuming that the catalog-based $G_{0,\,\mathrm{star}}$ is the emitted FUV radiation field and the FIR-based $G_{0,\,\mathrm{dust}}$ is the apparent FUV radiation field seen by the features. The stars are assumed to be at their projected distances, lying on the plane of the sky, and all optical paths between the cluster and the features are assumed to be free of extinction. This model attributes all differences between $G_{0,\,\mathrm{star}}$ and $G_{0,\,\mathrm{dust}}$ to the line-of-sight displacement of each feature from the plane on which the cluster stars lie. To simplify the calculation, we further assume that all the stellar radiation originates from the center of the cluster using the same coordinate as earlier. The catalog-based estimate assumes that all features are at their projected distances, so $G_{0,\,\mathrm{star}} = L/4\pi r^2$, where r is the projected distance from a given position to the cluster center and L is the FUV luminosity of the cluster. The FIR-based estimate measures the apparent radiation field, so $G_{0,\,\mathrm{dust}} = L/4\pi(r^2 + z^2)$, where z is the displacement of the feature from the cluster plane. The ratio of the two G_0 estimates can be solved for the absolute value of z.

$$\frac{G_{0,\,\mathrm{star}}}{G_{0,\,\mathrm{dust}}} = \frac{r^2 + z^2}{r^2} = 1 + (z/r)^2 \;\rightarrow\; |z| = r\left(\frac{G_{0,\,\mathrm{star}}}{G_{0,\,\mathrm{dust}}} - 1\right)^{1/2} \tag{2.1}$$

The heads of P1a and P2 are estimated to lie ∼0–1 pc and ∼2–3 pc, respectively, from the plane of the cluster; higher values are obtained when the background subtraction is applied to $G_{0,\,\mathrm{dust}}$. The head of P3 is close to the size of the 160 μm beam, so beam dilution may slightly reduce $G_{0,\,\mathrm{dust}}$ and inflate separation; we estimate a separation of ∼2–5 pc from the plane. The absolute separations for each feature are sensitive to the background subtraction, which is in turn sensitive to the 70 μm opacity through the head, and also the underlying assumption of extinction-free optical paths. The relative separation between features is less sensitive to these. Given the assumptions and uncertainties involved, we conclude that P1a/P2 and P2/P3 are each separated on the order of $\sim$1 pc along the line of sight, so that the three primary Pillars span a few pc along the LOS.

We compare to the distances calculated by Sofue (2020) using peak radio continuum brightness. LOS separations from the plane of the cluster $z = 1.8$, 2.5, and 2.8 pc for P1a, P2, and P3 are calculated as $z = D\cos(i)$ from the true distances $D = 2.6$, 3.2, and 3.6 pc and inclinations $i = 47°$, 40°, and 40° presented by Sofue (2020). In both their and our estimates, P1a is nearest and P3 is farthest from the plane of the cluster. Our estimate, from both G_0 and kinematic clues (Section 2.3.8), positions P1a closer to the plane of the cluster than the estimate by Sofue (2020).

Line of sight displacement z can only be calculated when $G_{0,\,\mathrm{star}} \geq G_{0,\,\mathrm{dust}}$, which is the case for the three primary Pillars but not towards the Ridge or P4. Stars $>$ 2 pc from the cluster core in projection may contribute more significantly to the radiation field at those two features since they are farther from the cluster core. The LOS displacements of the Ridge and P4 therefore cannot be estimated using this method. The Shared Base is extended along the LOS (Section 2.4.1.2), so $G_{0,\,\mathrm{dust}}$ is likely overestimated there and LOS distance cannot be determined.

At the tip of P4 lie two Class I YSOs, HH-N and HH-S, identified by Indebetouw et al. (2007) in NIR and mid-IR images, and a third source of unknown type $\sim$3″ from HH-N identified by Flagey et al. (2020) in the NIR. Any one of these sources may drive HH 216. A point source appears at the tip of P4 in both the 70 and 160 μm observations near the location of HH-N and the NIR point source. The source emission is $\sim$50% brighter than the diffuse P4 emission in both bands and likely affects the $G_{0,\,\mathrm{dust}}$ estimate towards that position. It is unclear whether radiation from the source heats or otherwise affects P4. Indebetouw et al. (2007) noted that the YSOs appear extincted by tens of A_V, but the NIR source's luminosity and extinction are not known. If P4 is heated internally, the derived $G_{0,\,\mathrm{dust}}$ is unsuitable for the LOS separation estimate.

2.4.3 Modeling PDRs Towards the Pillars

We model observations towards several PDRs associated with the Pillars to measure densities and FUV radiation fields at those locations (see Wolfire et al. 2022 for an overview of PDR modeling). We use the Wolfire-Kaufman 2020 models available in the PDR Toolbox which we access via the `pdrtpy`[6] software (Kaufman et al., 2006; Pound & Wolfire, 2008, 2023). This particular model set assumes a plane-parallel, face-on PDR geometry most appropriate for PDRs at the surface of non-clumpy clouds. The observed intensities of [C II], [O I], ^{12}CO(J=1–0), ^{12}CO(J=3–2), and ^{12}CO(J=6–5) at selected locations towards the PDRs are integrated over the relevant velocity intervals for each PDR and convolved to the [C II] resolution. We do not convolve ^{12}CO(J=3–2), which has a slightly larger beam. The higher resolution of the other observations is more valuable than keeping all the beams matched.

The on-sky widths of the modeled features are close to the [C II] beam width, so we assume that 1) the beam filling factor is 1 for all observations except ^{12}CO(J=3–2), 2) there is zero emission outside the features and 3) the ^{12}CO(J=3–2) beam filling factor is the ratio of the beam areas $\Omega_{\mathrm{[C\ II]}}/\Omega_{\mathrm{CO}}$. We scale the ^{12}CO(J=3–2) intensities up by the ratio $\Omega_{\mathrm{CO}}/\Omega_{\mathrm{[C\ II]}}$ to account for beam dilution.

For pairs of these integrated intensities, the PDR Toolbox takes ratios and plots them on a grid of density n and FUV radiation field G_0 using precalculated models. This procedure cancels

[6] `https://dustem.astro.umd.edu`

out the beam filling factor to first order. The resulting diagrams, shown in Figure 2.11, are called overlay plots and their usage is described in detail in Tiwari et al. (2022) and Pound & Wolfire (2023). The ratios appear as lines curving across the grid. In principle, all lines should intersect at a density and radiation field consistent with the observations. In practice, our overlay plots generally do not converge at one specific location but rather a region of the n vs. G_0 grid around $n \approx 2 \times 10^4$ cm^{-3} and a few 10^2 Habing units, which we take to be the physical conditions consistent with our observations under the Wolfire-Kaufman 2020 PDR models. The results of the PDR Toolbox fitting routine for the four sample locations from Figure 2.11 are listed in Table 2.2.

Density is fairly well bounded under this model, with our observations fitting between $\sim$1–4 $\times 10^4$ cm^{-3}. We estimate this uncertainty using a contour of a few times the minimum χ^2 and confirm that this region of parameter space doesn't change much between lines of sight which should have similar density and illumination. This density estimate is consistent with the estimates made by Pound (1998) and Levenson et al. (2000) as well as broadly consistent with our estimate based on the [C II] column density and assumed line-of-sight geometry (Section 2.5.1.2; Table 2.3).

Radiation field is much more loosely bound, as we can only place an upper limit of $G_0 \sim 1000$ Habing units and no realistic lower limit under this model. The PDR models used here assume face-on geometry, which may produce slightly inaccurate results, so we rely on independent estimates of density and radiation field to gauge how accurate the PDR model-based estimates might be.

We can further bound the radiation field seen by the Pillars using our independent estimates of G_0 from stellar catalogs and FIR dust emission which we described in Section 2.4.2 The

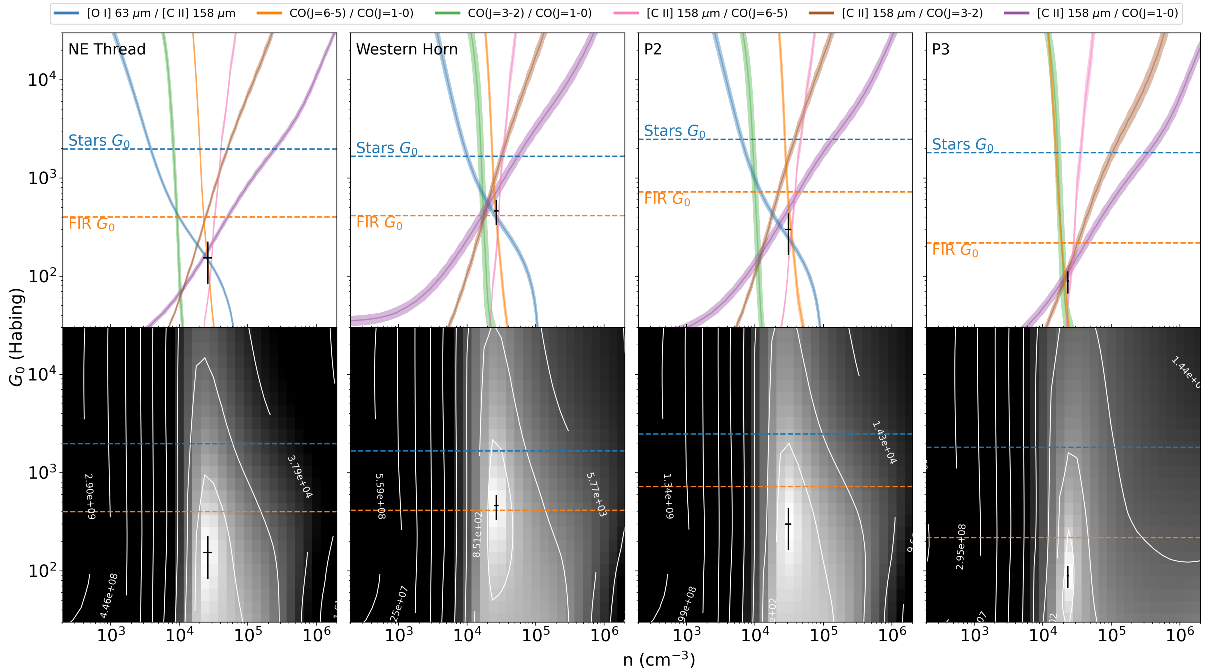

Figure 2.11 *(Top row)* Overlay plots made using `pdrtpy` which show observed line ratios towards 4 locations which are labeled in the top left corner of each plot. The black cross shows the automatically fitted solution and associated uncertainty; these values are listed in Table 2.2. *(Bottom row)* The reduced χ^2 associated with the automatic fit, with overlaid labeled contours. Radiation field values estimated via stellar catalog and FIR emission are plotted as horizontal dashed lines in each figure.

stellar method, as previously discussed, yields estimates of $G_0 \sim$ 1–2 $\times 10^3$ Habing units in the neighborhood of the Pillars. These estimates mark the upper end of the PDR model estimate of radiation field, so we assume that the radiation field seen by the Pillars is somewhere between 500–2000 Habing units depending on local geometry.

We are unable to make substantial claims about spatial variation in the density and radiation field based on the PDR models, as the uncertainties in our modeling techniques are greater than the local variation. We find that the densities and radiation fields are generally self-consistent across all modeled regions towards the Pillars.

Location Name	G_0 (Habing)	n (cm^{-3})	χ^2/dof	dof
NE-thread	150	2.6×10^4	150	5
W-Horn	460	2.7×10^4	14	5
P2	300	3.1×10^4	58	5
P3	89	2.3×10^4	6.3	4

Table 2.2 The G_0 and n values are those fitted to the observed line ratios overlayed on the top row of Figure 2.11. These correspond to the minimum χ^2 location, in color on the bottom row of Figure 2.11, which is indicated with a black cross in all panels of that figure.

2.5 Mass and Physical Conditions

2.5.1 Molecular and Atomic Hydrogen Column Densities

Molecular and atomic gas column densities are estimated using the ^{13}CO(J=1–0) and [C II] lines, respectively, as well as with dust emission. Column densities are summed pixel-by-pixel to estimate the total pillar masses, and line-of-sight distances are assumed to estimate densities in each gas phase. Table 2.3 lists column and number densities and Table 2.4 lists pillar masses.

2.5.1.1 ^{13}CO Column Density

We estimate the molecular gas column density assuming optically thin ^{13}CO(J=1–0) emission following Tiwari et al. (2021) (their Appendix E) and Mangum & Shirley (2015). We assume that the J=1–0 lines of ^{12}CO and ^{13}CO share the same excitation temperature along each line of sight, that ^{12}CO(J=1–0) is optically thick everywhere, and that the beam filling factor is unity. We adopt an isotopic ratio $^{12}\mathrm{CO}/^{13}\mathrm{CO} =^{12} \mathrm{C}/^{13}\mathrm{C} = 44.65$ based on the galactocentric radius-dependent expression given by Yan et al. (2019) using a galactocentric radius of 6.46 kpc calculated using Equation 2 by Brand & Blitz (1993). We convert ^{12}CO column density to molecular hydrogen column density $N(\mathrm{H}_2)$ using the abundance ratio $^{12}\mathrm{CO}/\mathrm{H}_2 = 8.5 \times 10^{-5}$ (Tielens, 2021). Hydrogen is assumed to be entirely in the molecular phase where CO is detected, so that total hydrogen column density (defined as $N_{\mathrm{H}} = N(\mathrm{H}) + 2N(\mathrm{H}_2)$) is $N_{\mathrm{H}} = 2N(\mathrm{H}_2)$. Gas mass is calculated by summing N_{H} over the boxes shown in Figure 2.12 and converting to mass using a mean molecular weight $\mu = 1.33$.

We estimate line-of-sight-averaged densities by assuming cylindrical symmetry, so that line-of-sight distance through the feature is equal to the angular width of the features, and dividing column density by that distance. H_2 column densities and gas masses are listed in Tables 2.3 and 2.4, respectively. Uncertainties are estimated by propagating the channel RMS noise of the ^{12}CO and ^{13}CO(J=1–0) observations and, for conversion of column density into mass, the heliocentric distance uncertainty, into the procedure described above.

2.5.1.2 C^+ Column Density

We do not detect the [^{13}C II] line towards the Pillars, so we estimate an upper limit on the C^+ column density using the [C II] channel noise T_{rms} as a detection limit. We estimate an upper limit on the [^{13}C II] hyperfine component at +11.2 $\mathrm{km\ s^{-1}}$ with respect to the [^{12}C II] line (see Table 1 in Guevara et al. 2020a) since it is sufficiently far from the [^{12}C II] line center given the observed linewidths, and we assume that the isotopic ratio $^{12}\mathrm{C}^+/^{13}\mathrm{C}^+ = {}^{12}\mathrm{C}/^{13}\mathrm{C}$ and use the same value as in Section 2.5.1.1. Equation 4 in the paper by Guevara et al. (2020a) relates the observed line brightness of [^{12}C II] to [^{13}C II] given the [^{12}C II] optical depth. We find an upper limit of $\tau_{12} \lesssim 1.3$ using the brightest [^{12}C II] spectrum which lies towards P1b. Bonne et al. (2023a) find a similar upper limit on [C II] optical depth towards the DR21 ridge using the same

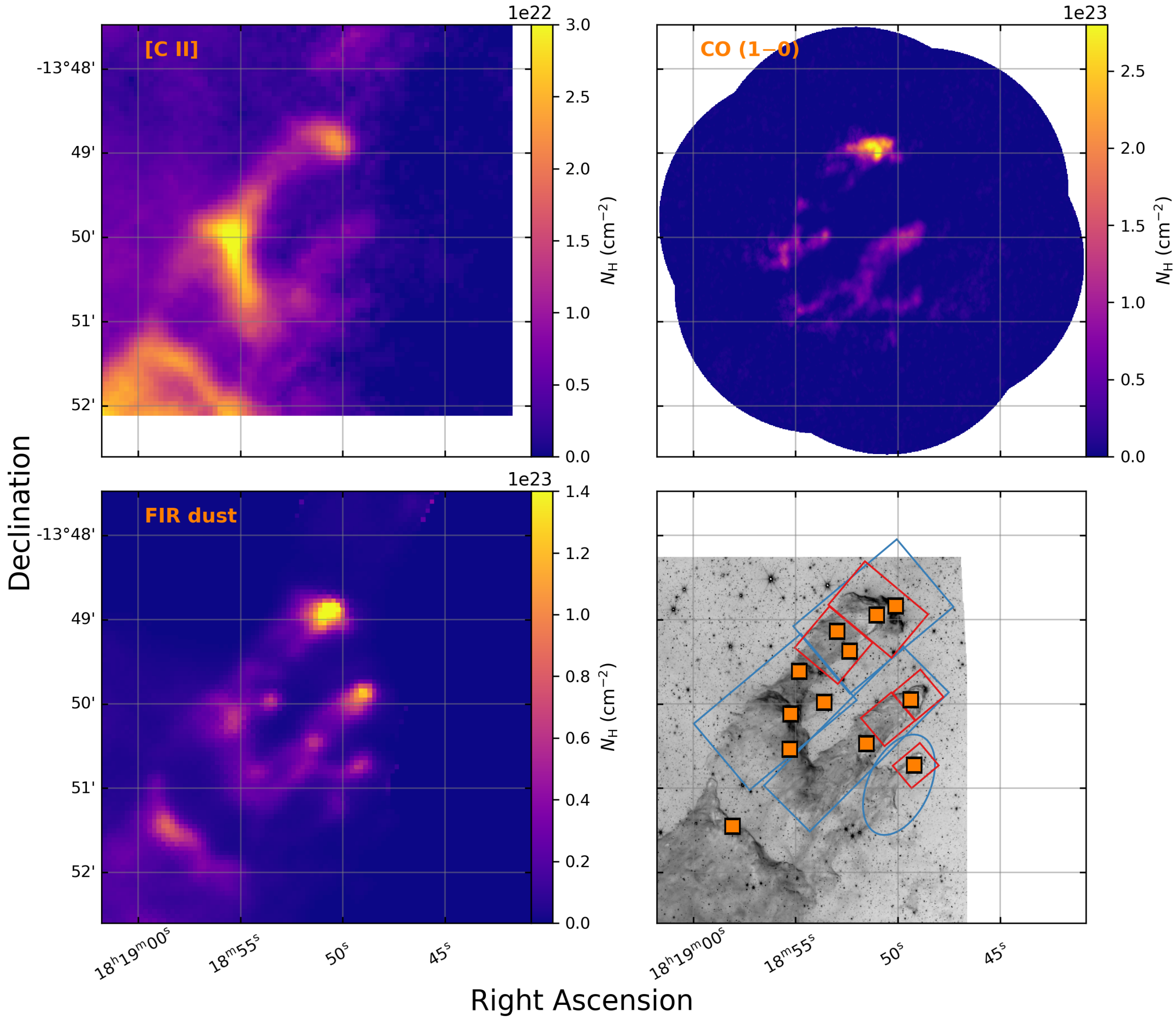

Figure 2.12 The top-left, top-right, and bottom-left panels show hydrogen column densities $N_{\rm H}$ derived from C^+, CO(J=1–0), and FIR dust emission. The bottom-right panel shows the JWST F335M image in greyscale as a reference. All four plots are on the same size scale and the grey gridlines are in the same place. On the bottom-right panel, blue boxes show the integration areas for the pillar masses in Table 2.4, and red boxes show the same for Table 2.6. Orange squares mark the locations from which column densities are sampled in Table 2.3. In Table 2.3, from P1a-edge to Shared-Base-Mid, locations are listed in order of decreasing declination along P1. The P2 locations are also in order of decreasing declination along P2.

method.

We use the method of estimating $^{12}C^{+}$ column density without a detected [^{13}C II] line described by Okada et al. (2015), and we assume a constant $T_{\rm ex}$ rather than a constant optical depth. The adopted $T_{\rm ex} = 107$ K is calculated using the highest [C II] line brightness towards the Pillars and our upper limit of $\tau \leq 1.3$, and $T_{\rm ex}$ is therefore a lower limit towards that location (considering the emitted radiation temperature $T_{\rm R}$ constant, τ and $T_{\rm ex}$ have an inverse relationship in the optically thin and $\tau \sim 1$ regimes). Assuming a fixed $T_{\rm ex}$ across the field is equivalent to assuming that density and kinetic temperature are fixed across the map, so that only the column density influences the observed line brightness. Kinetic temperature is determined by the density n and radiation field G_0 according to PDR models. Both n and G_0 may be slightly higher at the heads of the three Pillars which contain dense molecular gas and are closer to the stars, but the column densities there are not high enough to probe $T_{\rm ex}$. $T_{\rm ex}$ must therefore be sampled from the higher column density P1b location. We will overestimate column density towards dense, highly irradiated locations like the pillar heads, and we will underestimate column density towards less dense, poorly illuminated locations along pillar bodies. If $T_{\rm ex} \sim 150$ K, column densities would be approximately halved around the map, and it is unlikely that $T_{\rm ex}$ is considerably lower than 100 K. We convert $N(\mathrm{C}^{+})$ to atomic hydrogen column density $N(\mathrm{H})$ using the abundance ratio $\mathrm{C/H} = 1.6 \times 10^{-4}$ (Sofia et al., 2004) and calculate column densities assuming a filling factor $\eta = 1$. We assume hydrogen to be entirely in the atomic phase where C^{+} is present so that $N_{\rm H} = N(\mathrm{H})$, but we note that some [C II] emission may originate from CO-dark molecular gas (Pabst et al., 2017).

The spatially variable [C II] background discussed in Appendix B.2 contributes to the total column density derived in the region. To determine just the contribution to the Pillars requires subtracting a background. We calculate column densities with the total intensities (no background spectrum subtraction) and subtract out a column density background sampled from the same locations as the spectral background. Within these background sample regions, we take the mean column density to be the background and the standard deviation to be a systematic uncertainty on both target and background column density due to the variability of the background. Statistical uncertainty from the RMS channel noise is propagated through the process described above, though this source of uncertainty is reduced by the sum over pixels to obtain mass. Background-corrected column densities are listed in Table 2.3. Estimates of the systematic uncertainties and the 1-σ statistical uncertainties are given in the table's caption.

We find the highest C^+ column density towards P1b rather than P1a despite the higher molecular gas column density towards P1a. Mass is calculated as described in Section 2.5.1.1. The atomic hydrogen mass is typically $\sim$30% of the molecular gas mass.

2.5.1.3 Column Density from Dust Emission

We calculate column densities from FIR dust emission to compare to the molecular and atomic gas column densities derived from CO and C^+. Optical depth at 160 μm is calculated directly using the 70 and 160 μm observations and the method described by Tiwari et al. (2021). The $\geq$250 μm maps have lower spatial resolution and do not resolve some Pillar features. We obtain $\sim$14$''$ resolution in our final map by using only 70 and 160 μm. We subtract the flux background in each band, sampled from the background regions described in Appendix B.2 (Figure B.3), prior to calculation of dust properties in order to isolate the Pillar emission. We divide the dust optical depth at 160 μm by the dust extinction cross section per H nucleus at 160 μm,

Location Name	Width ($''$)	(pc)	C$^+$ $N_{\rm H}$	$n_{\rm H}$	CO $N_{\rm H}$	$\sigma_{\rm stat}$	$n_{\rm H_2}$	Dust $N_{\rm H}$	$\sigma_{\rm stat}$
P1a-edge	17	0.14	20.9	4.7×10^4	31	8	3.5×10^4	59	12
P1a-center	45	0.38	13.9	1.2×10^4	286	21	1.2×10^5	139	24
E-Thread	20	0.17	8.2	1.6×10^4	31	9	3.0×10^4	22	7
W-Thread	10	0.08	3.8	1.4×10^4	29	9	5.5×10^4	24	9
E-Horn	13	0.11	14.8	4.4×10^4	80	14	1.2×10^5	22	6
W-Horn	14	0.12	1.7	4.6×10^3	125	15	1.7×10^5	54	15
Shared-Base-E	33	0.28	29.2	3.4×10^4	59	13	3.4×10^4	59	10
Shared-Base-Mid	22	0.19	18.0	3.1×10^4	$\leq$6	6	...	24	7
P2-head	18	0.15	5.0	1.1×10^4	114	14	1.2×10^5	95	22
P2-clump	9	0.08	6.3	2.7×10^4	65	11	1.4×10^5	59	16
P3-head	13	0.11	3.6	1.1×10^4	67	11	9.8×10^4	58	22
Ridge	13	0.11	19.2	5.7×10^4	...	...	...	63	13

Table 2.3 Column and number densities derived from C$^+$, CO, and dust emission measurements; the species is indicated above each column density column. Column densities are sampled towards each location, shown in Figure 2.12, and given in units of 10^{21} cm^{-2}. The standard conversion between column density and A_V is $A_V = N_{\rm H}/1.9 \times 10^{21}$ cm^{-2} (Bohlin et al., 1978), so the column densities listed in the table can be divided by 1.9 to estimate A_V. Column densities derived using the [C II] line have statistical uncertainty $\sigma_{\rm stat} = 0.6$ (table units) except for location Shared-Base-E, which has $\sigma_{\rm stat} = 0.7$, and an additional systematic uncertainty of 1.5 or 1.7 (table units) for the northern and southern background samples, respectively (see Appendices B.1 and B.2), which estimate the spatial variability of the C$^+$ background (Section 2.5.1.2). Atomic and molecular gas number densities $n_{\rm H}$ and $n_{\rm H_2}$ are estimated using the C$^+$ and CO measurements of column density by dividing $N(\rm H)$ and $N(\rm H_2)$, respectively, by the assumed LOS width of each feature. We assume $N_{\rm H} = N(\rm H)$ in the atomic gas and $N_{\rm H} = 2N(\rm H_2)$ in the molecular gas in order to estimate density and pressure in each phase independently; however, some of the [C II] emission could arise from CO-dark molecular gas. On-sky angular widths are estimated using the JWST images and are adopted as the LOS widths through the features assuming cylindrical symmetry.

Feature Name	C$^+$ M$_{\rm H}$	$\sigma_{\rm stat}$	$\sigma_{\rm sys}$	CO M$_{\rm H_2}$	$\sigma_{\rm stat}$	dust M$_{\rm H}$	$\sigma_{\rm tot}$	M$_{\rm tot}$
P1a	24	1	7	79	3	83	23	103
P1b	41	2	8	37	2	64	20	78
P2	34	2	7	70	3	95	33	103
P3	4.2	0.6	2.7	14	1	15	7	18

Table 2.4 Gas mass M derived for the pillars from [C II], ^{13}CO(J=1–0), and dust emission. Masses are given in $M_\odot$ and rounded; sums are calculated from exact numbers. Statistical and systematic uncertainty estimates are given where applicable. Total masses are considered to be the sum of atomic gas mass from C$^+$ and the molecular gas mass from CO.

$C_{\rm ext,160}/{\rm H}$. We take the $R_V = 3.1$ value of $C_{\rm ext,160}/{\rm H} = 1.9 \times 10^{-25}$ cm^{-2}/H from Draine (2003), following the method of Tiwari et al. (2021). This yields $N_{\rm H}$, the column density of H nuclei or total column density, directly. These column densities are, in theory, equal to the sum of hydrogen column densities derived from C^+, C, and CO as dust is present at all phases, but they should be dominated by the relatively larger molecular gas column. Column densities are listed in in Table 2.3 and masses, calculated as described in Section 2.5.1.1, are listed in Table 2.4.

We measure dust temperatures ranging from 25 K in the cold clumps, such as the pillar heads and the Western Horn, to 30 K along the lower column density pillar bodies. Since we are using the 70 and 160 μm measurements for this estimate, we are more sensitive to warm dust. Dust temperature varies along the line of sight through the Pillars, with colder gas and dust embedded within the dense pillar heads and other clumps, shielded from radiative heating. Assuming a constant temperature along a line of sight with real temperature variation can cause column density to be underestimated (Howard et al., 2019; Storm et al., 2016). Including the 250 μm band increases sensitivity to cold dust at the expense of spatial resolution and raises the mass estimates by about 10% (these larger estimates are not included in the table), which is within our uncertainty estimates described below.

The PACS handbook quotes a 5% calibration uncertainty on the 70 and 160 μm measurements; this dominates the total uncertainty towards the pillar heads. We estimate an uncertainty on our flux background subtraction in each band, which is about 15% of the background and dominates total uncertainty outside the bright pillar heads. The PACS observations include a statistical uncertainty map; this is the smallest relative contribution to the total uncertainty, but we include it anyway since including additional sources of uncertainty is trivial using a Monte Carlo sampling method. Using such a method, we estimate the total uncertainties on column density and mass by computing N_{H} and M_{H} for 1000 realizations of the three uncertainties added to the observations and adopting the 1-σ uncertainties to be the difference between the 84$^{\mathrm{th}}$ and 16$^{\mathrm{th}}$ percentile values divided by 2. To these uncertainties, we add in quadrature the 15% uncertainty from the heliocentric distance (Kuhn et al., 2019). The median N_{H} and M_{H} values are consistent with the values calculated without considering uncertainty, so we record the latter values in the tables.

The dust-derived column densities tend to be closer to the CO-derived column densities than to those from C^{+}, satisfying our expectation that the dust column is dominated by contribution from the molecular gas phase. The dust-derived N_{H} values tend to be lower than the CO-derived values, with the largest difference observed towards the bright center of P1a. This is likely due to significant dust temperature variation along the line of sight, which causes the average temperature to be higher and the optical depth to then be underestimated. For this reason, we take the CO values as the better gauge of molecular gas column density. Towards the northern edge of P1a, where [C II] is brightest, the dust-derived N_{H} is larger than the CO-derived value; we attribute this to the line of sight passing primarily through warm atomic gas with less LOS temperature variation, as the sum of the C^{+}-derived and CO-derived column densities is consistent with the value from dust.

2.5.2 Density

Line-of-sight averaged densities are derived by dividing the column density measurements by estimated line-of-sight feature widths. We estimate the angular size across each feature in Table 2.3 using the high-resolution JWST NIR images and assume cylindrical symmetry to adopt the same width along the line of sight. We use this width for both the atomic gas and the molecular gas, even though they would be layered along lines of sight passing through molecular gas. Densities $\sim 10^5$ cm^{-3} are derived from the CO- and dust-based column densities. These densities are broadly consistent with the observed HCO^+, HCN, CS, and N_2H^+ brightness temperatures (listed in Appendix B.1) according to estimates from the RADEX[7] radiative transfer software (van der Tak et al., 2007). Densities $\sim 10^4$ cm^{-3} are derived from C^+-based column densities, which are consistent with those estimated using the PDR Toolbox.

We adopt $n_{\rm H} = 1.8 \times 10^4$ cm^{-3} as the atomic gas density by taking the average $n_{\rm H}$ in Table 2.3. From this average we exclude the Shared Base and Ridge positions, since their line-of-sight size depends strongly on the adopted geometry which is very uncertain, and the Eastern Horn, since we cannot isolate its [C II] emission from P1 emission behind it. We adopt $n_{\rm H_2} = 1.3 \times 10^5$ cm^{-3} as the molecular gas density by taking the average $n_{\rm H_2}$ towards dense features (heads, Horns, and the P2 clump) in Table 2.3. The molecular gas density we derive is consistent with the estimates by Pound (1998), White et al. (1999), and Levenson et al. (2000).

The critical density of [C II] in the presence of either H or H_2 ranges from 3–5 $\times\, 10^3$ cm^{-3} at ∼100 K, so our adopted atomic gas density implies that the kinetic temperature $T_{\rm K}$ should be similar to the excitation temperature $T_{\rm ex}$. Recalling that our $T_{\rm ex}$ is a lower limit due to optical depth, we place a lower limit on atomic gas $T_{\rm K} > 100$ K. The derived molecular gas densities are greater than the critical density of ^{12}CO(J=1–0) by a factor of ~ 50, so the radiation temperature $T_{\rm R}$, assumed equal to the observed $T_{\rm MB}$, of the optically thick ^{12}CO(J=1–0) line should be similar to the kinetic temperature of the gas it probes. The kinetic temperature of the warm, outer layers of molecular gas probed by ^{12}CO must therefore be $T_{\rm K} \sim$ 50–70 K for most of the

[7] `http://var.sron.nl/radex/radex.php`

pillar bodies and reach $T_{\mathrm{K}} \sim 100$ K towards brightly illuminated regions in P1a and P1b. The derived molecular gas density is close to the critical densities $\sim 10^5$ cm^{-3} of HCO^+ and HCN and slightly below the critical densities $\sim 3 \times 10^5$ cm^{-3} of N_2H^+ and CS. The HCO^+ and HCN lines are optically thick according to RADEX given their assumed abundance (Tielens, 2021) and the CO-derived column density $N(\mathrm{H}_2)$, so their observed $T_{\mathrm{MB}} = T_{\mathrm{R}} \sim$ 15–20 K likely traces $T_{\mathrm{K}} \sim 20$ K molecular gas towards P1a.

2.5.3 Pressure Balance

We estimate pressures for the ionized, atomic, and molecular gas phases of gas and comment on the possibility of pressure equilibrium. Pressures are listed in Table 2.5. We follow White et al. (1999) in using the presence of pressure equilibrium between the ionized and molecular gas as a proxy for whether or not the ionization-driven shock has already been driven through the pillar heads.

2.5.3.1 Ionized Gas

Our observations do not probe directly the physical conditions of the ionized hydrogen (H II) phase, so we take values $n_{\mathrm{e}} \sim$ 1120–1800 cm^{-3} and $T_{\mathrm{e}} \approx$ 8000–10,000 K from optical ion line studies of the pillar surface by García-Rojas et al. (2006) and McLeod et al. (2015). Levenson et al. (2000) note that temperature may be higher near the PDR-H II interface due to photoelectric heating, a harder radiation field, and high density. We estimate thermal pressure in the ionized gas flowing from the surface of the pillar $P_{\mathrm{i}}/k_{\mathrm{B}} = 2n_{\mathrm{e}}T = 1.8\text{–}3.6 \times 10^7$ K cm^{-3}. We neglect any sources of non-thermal pressure in the ionized gas near the pillar surface; magnetic fields should not be important in the ionized phase due to low densities and, while a turbulent linewidth was detected in the ambient H II region (far from the pillar surface, where the photoevaporative flow does not dominate gas kinematics) in M16 by Higgs et al. (1979), the radial striations evident in the optical images presented by Hester et al. (1996) indicate that the photoevaporative flow near the pillar surface is not turbulent.

2.5.3.2 Molecular Gas

Pattle et al. (2018) discuss the pressures originating within the molecular gas phase. We follow their discussion and recalculate pressures using our observations of the molecular gas. We determined $n_{\mathrm{H}_2} = 1.3 \times 10^5$ cm^{-3} in Section 2.5.2. Molecular gas temperature should be coupled to dust temperature T_d at densities $n \gtrsim 10^5$ cm^{-3} (White et al., 1999). We find $T_{\mathrm{d}} \sim 25$ K towards the dense gas (Section 2.5.1.3), comparable to the value $T \sim 20$ K found by White et al. (1999) using 350–2000 μm photometry, which is more sensitive to cold dust but less sensitive to warm dust than the 70 and 160 μm photometry used for our estimate. Thermal pressure in the molecular gas is $P_{\mathrm{H}_2,\,\mathrm{therm}}/k_{\mathrm{B}} = n_{\mathrm{H}_2} T \approx 3.2 \times 10^6$ K cm^{-3}. We estimate the pressure from turbulent support using the molecular line velocity dispersion $\sigma_{\mathrm{obs}} \approx 0.6 \mathrm{~km~s^{-1}}$ (thermal velocity dispersion, $\sigma_{\mathrm{therm}} \sim 0.1 \mathrm{~km~s^{-1}}$, contributes less than 2% of σ_{obs}) to be $P_{\mathrm{H}_2,\,\mathrm{turb}}/k_{\mathrm{B}} = \rho\sigma^2 = (2 n_{\mathrm{H}_2} \mu m_{\mathrm{H}}) \sigma^2 \approx 1.5 \times 10^7$ K cm^{-3} ($\mu = 1.33$), consistent with pressure derived from the line widths observed by White et al. (1999).

Pattle et al. (2018) estimate the plane-of-sky magnetic field strength $B = 170$–320 μG within the Pillars, calculated using the Davis-Chandrasekhar-Fermi method (Chandrasekhar & Fermi, 1953; Davis, 1951) and therefore assuming that the turbulent velocity field is isotropic, which implies magnetic pressure $P_{\mathrm{H_2,B}}/k_{\mathrm{B}} \approx 0.9$–$3.0\times10^7$ K cm^{-3}. The factor of 3 range in their pressure value seems to be driven mostly by variation in the molecular line widths observed by White et al. (1999); our observations indicate that some of this line width can be attributed to line-of-sight confusion rather than turbulent velocity dispersion and we observe single-component line widths near the lower end of their range. We use the Equation 1 in the paper by Pattle et al. (2018) to estimate $B_\perp \sim 320$ μG and $P_{\mathrm{H_2,B}}/k_{\mathrm{B}} \approx 3.0 \times 10^7$ K cm^{-3} from our observed molecular gas velocity dispersion $\sigma_v \approx 0.6$ km s^{-1} along lines of sight with limited line-of-sight confusion. The magnetically-dominated total pressure within the molecular gas is $P_{\mathrm{H_2}}/k_{\mathrm{B}} \approx 4.8 \times 10^7$ K cm^{-3}.

The total pressure in the molecular gas is slightly higher than the pressure in the ionized gas. The molecular and ionized gas phases are likely in pressure equilibrium, with the extra pressure supporting the molecular gas against self-gravity. We assume that the ionization-driven shock has already passed through the molecular gas.

We observe a velocity gradient across the head of P2, which could indicate an additional mode of rotational support in the pillar head. For comparison, we estimate a rotational "pressure" $P_{\mathrm{H_2,rot}} = \rho\omega^2 r^2$ where $\omega r \approx 0.5$ km s^{-1} based on the CO line velocities (see the PV diagram in Figure 2.9), finding $P_{\mathrm{H_2,rot}}/k_{\mathrm{B}} \approx 10^7$ K cm^{-3} (not included in our total pressure). This is comparable to turbulent pressure and less than magnetic pressure (3×10^7 K cm^{-3}, see above), and could contribute $\sim$20% of the total support to the pillar head, but we would expect the head to be extended in the plane of rotation across the pillar if that were so. Since we do not observe oblateness, we find it unlikely that rotational support is a significant support mechanism in the pillar heads. Pillar rotation is further discussed by Sofue (2020).

2.5.3.3 Atomic Gas

We determined the density of the warm, atomic gas to be $n_{\rm H} \approx 1.8 \times 10^4$ cm^{-3}. The lower limit on the $T_{\rm ex}$ of the [C II] line indicates a kinetic temperature $T_{\rm K} > 100$ K (Section 2.5.2), and temperatures up to 250 K are consistent with the approximate n and G_0 in the PDR models (Pound & Wolfire, 2023). This results in a thermal atomic gas pressure $P_{\rm H}/k_{\rm B} = n_{\rm H}T \sim 2$–$5 \times 10^6$ K cm^{-3}. The atomic gas phase is likely hydrostatically supported by turbulence similar to the molecular gas. We remove the thermal velocity dispersion of [C II] $\sigma_{\rm therm} \sim 0.5\ {\rm km\ s^{-1}}$ given the assumed $T_{\rm K}$ from the observed [C II] velocity dispersions $\sigma_{\rm obs} \sim$ 1.1–1.4 ${\rm km\ s^{-1}}$ to find $\sigma_{\rm turb} = (\sigma^2_{\rm obs} - \sigma^2_{\rm therm})^{1/2} \sim$ 1.0–1.3 ${\rm km\ s^{-1}}$. Adopting the turbulent velocity dispersion $\sigma_{\rm turb} \approx 1.3$ yields a turbulent pressure of $P_{\rm H,\,turb}/k_{\rm B} \sim 5 \times 10^6$ K cm^{-3} in the atomic gas. This is an upper limit since the photoevaporative flow velocity $\sim 0.5\ {\rm km\ s^{-1}}$ projected along the line of sight should contribute to the observed width of the [C II] line, but we cannot disentangle these contributions in our observations. We discuss the impact of this flow velocity on the photoevaporative lifetime of the Pillars in Section 2.6.2. Ultimately even the highest estimate of turbulent pressure in the atomic gas allowed by the observations is an order of magnitude smaller than the total pressures in the ionized and molecular phases in Table 2.5.

It is likely that ionization-driven shocks have already passed through the Pillars, so the atomic gas should be in pressure equilibrium with the ionized and molecular gas phases surrounding it. However, our estimate of the total atomic gas pressure falls significantly short of the ionized gas pressure by $P/k_{\rm B} \sim 1 \times 10^7$ K cm^{-3}. The missing pressure is likely from the magnetic field in the atomic gas whose strength must be $B \sim 200\mu$G. Pellegrini et al. (2009, 2007) estimate comparable magnetic field strengths in the PDRs in M17 and the Orion Bar and determine that the magnetic field is important to the structure, particularly the width, of the PDR. We don't have an independent estimate of the field strength in the atomic layer, but scaling the molecular phase B field by the ratio of the molecular to atomic gas densities gives a field strength of $B_{\perp} \sim 85\ \mu$G and a corresponding $P_{\mathrm{B}}/k_{\mathrm{B}} \sim 2 \times 10^6$ K cm^{-3}, which is insufficient for pressure equilibrium.

We conclude that ambipolar diffusion, the flow of neutrals past ions, has weakened the magnetic field in the molecular gas faster than in the atomic gas because the molecular gas has a lower ionization fraction. The pillar heads are still magnetically supported now, but the magnetic field in the molecular gas must have been larger in the past. The ambipolar diffusion timescale $\tau_{\mathrm{AD}} \sim 10^6$ yr in the molecular gas is similar to the age of the cluster, as we demonstrate in the next section. Carbon is ionized in the atomic gas, so the ionization fraction there is $\chi_{\mathrm{ion}} \sim 10^{-4}$ and $\tau_{\mathrm{AD}} \sim 10^9$ yr.

2.5.4 Ambipolar Diffusion and Molecular Cloud Collapse

Mouschovias (1991) determined that the reduction in magnetic support due to ambipolar diffusion could precipitate the collapse of molecular cores into stars. We estimate the possibility of such a collapse in the Pillars before they are photoevaporated. Critical mass under magnetic field support can be expressed as

$$M_{\mathrm{c,B}} = 9.7\left(\frac{R}{0.1\ \mathrm{pc}}\right)^2\left(\frac{B}{100\ \mu\mathrm{G}}\right)M_{\odot} \tag{2.2}$$

The magnetic critical masses, calculated using the assumed radii in Table 2.6, for the heads of P1a, P2 and P3 are 83, 21, and 10 $M_{\odot}$, respectively, while the estimated H_2 masses are 72, 14, and 6 $M_{\odot}$. For all the pillar heads, but particularly P1a whose geometry is complex (see Section 2.3.2), the R^2 dependence carries significant uncertainty into the critical mass determination from our assumptions about line-of-sight width, but we can conclude that all the heads are nearly critical. Lefloch & Lazareff (1994) present calculations to determine the gravitational stability of magnetically supported globules in Section 5.9 of their paper, and these suggest that the pillar heads are unstable given their current magnetic field strengths.

For magnetically subcritical clouds, gravitational collapse is controlled by the process of ambipolar diffusion of the supporting magnetic field. The ambipolar diffusion timescale is

$$\tau_{\rm AD} \approx 2 \times 10^5 \left(\frac{\chi_{\rm ion}}{10^{-8}}\right) \text{ yr} \tag{2.3}$$

$$\chi_{\rm ion} \approx 2 \times 10^{-7} \left(\frac{10^4 \text{ cm}^{-3}}{n_{\rm H_2}}\right)^{1/2} \tag{2.4}$$

where the degree of ionization $\chi_{\rm ion}$ is calculated for a typical cosmic ray ionization rate $\zeta_{\rm CR} = 3 \times 10^{-17}$ s^{-1} (Elmegreen, 1979). For the adopted $n_{\rm H_2} = 1.3 \times 10^5$ cm^{-3}, we find $\chi_{\rm ion} \sim 6 \times 10^{-8}$ and $\tau_{\rm AD} \sim 1$ Myr which is similar to both the age of the cluster and Pillars as well as the estimated photoevaporative lifetime of the Pillars (Section 2.6.2). The models by Bergin et al. (1999), which use physical conditions similar to those observed towards the pillar heads, indicate that $\chi_{\rm ion} < 10^{-8}$ is more typical of these massive cores; this would mean ambipolar diffusion weakens the magnetic field more quickly than expected. Adopting this lower ionization fraction would yield $\tau_{\rm AD} \sim 0.2$ Myr, smaller than both the age of the system and the photoevaporative lifetime. It is possible that any of the pillar heads may collapse to form stars before they are photoionized as ambipolar diffusion weakens the magnetic fields supporting them against

Component	P_{therm}	P_{turb}	P_B	P_{tot}
Molecular gas	3	15	30	48
Atomic PDR gas	2–5	5	2*	9–12
Ionized flow	18–36			18–36

Table 2.5 Pressures in the molecular, atomic, and ionized gas near P1a. Pressures are expressed as $P/k_{\rm B}$ in units of (10^6 K cm^{-3}). Total pressures are calculated by summing across lower and upper estimates, respectively. The value ranges are intended as approximate estimates of our uncertainty in the pressures due to uncertain, or multiple, estimates of density or other properties. The atomic gas magnetic pressure (*) in this table is calculated by scaling down the magnetic field in the molecular gas by the ratio of mass densities in the two phases, but we suspect it is much larger as discussed in the text.

gravitational collapse. Protostars have been observed towards the heads of P1a and P2, so fragmentation and local collapse may have already taken place (Indebetouw et al., 2007; Linsky et al., 2007; Sugitani et al., 2002).

The interplay between gravity, magnetic fields, and turbulence in context of cloud collapse is a complicated one which we simplify in our discussion here; see the review by Hennebelle & Inutsuka (2019a). The ambipolar diffusion timescale is slow compared to the dynamic timescales of clouds. Quicker alternatives for overcoming magnetic support are available, such as turbulence or other methods of locally enhancing the mass-to-magnetic-flux ratio (Bailey & Basu, 2014; Vázquez-Semadeni et al., 2011). If magnetic support were overcome more quickly, the magnetically supported and critical Pillar heads would be even more likely to fragment and collapse into stars before they evaporate.

2.5.5 Constraints on Pillar Age

Simulations by Williams et al. (2001) indicate that the shock can pass through the dense, molecular pillar head in 10^5 yr while the ionization front takes $\sim 0.5 \times 10^6$ yr to photoevaporate the pillar, comparable to the $\sim 10^6$ yr age of the system. Our observations are consistent with a shocked, equilibriated pressure structure, in which the shock passed through long ago and left the ionization front behind. This relieves us of the tight upper limit of $\sim 10^5$ yr on the pillar age required for unshocked pillar heads (White et al., 1999; Williams et al., 2001). Our estimated photoevaporation timescales $\sim 10^6$ yr (Section 2.6.2) and the NGC 6611 cluster age $\sim 2 \times 10^6$ yr also favor the post-shock, $\sim$$10^6$-yr-old Pillars scenario. See also the discussion of timescale tension by Williams et al. (2001).

2.6 Discussion

2.6.1 Warm Gas Dynamics

Along lines of sight towards the Shared Base and the head of P2, the peak [C II], [O I], and CO line velocities are blueshifted by $\sim$0.5 $\mathrm{km\ s^{-1}}$ with respect to the denser molecular gas tracers. The [C II] line, but not the CO, is similarly blueshifted towards the head of P3. This is inconsistent with a photoevaporative flow from an illuminated surface that is mostly facing away from us, but is consistent with gas flowing down these pillars away from the star (towards us in projection along the LOS).

Simulations by Lefloch & Lazareff (1994) predict that less dense, outer layers of gas move down the pillar bodies more quickly than denser gas (see their Figure 4c–f). These simulations also predict blue line wings towards the head of a globule (oriented away from us, as P1b and P2 are) at two different evolutionary stages: a wing due to compressed gas on the far side of the head moving towards the observer during the first $\sim$0.1 Myr while the cloud is collapsing into a globule, and a wing during the stable cometary phase at an age of $\sim$1 Myr as small clumps are ejected and accelerated along the globule. As we mention in Section 2.3.5, the wishbone tails of

P3 resemble the "ears" which emerge in these simulations; comparisons could be drawn between the later stages of these ears and the Threads. Observational comparisons could be made between the Threads, ears, and tails and the "legs" observed by Bonne et al. (2023c) towards IC 63.

Since [C II], [O I], and ^{12}CO should all trace warmer, outer layers of gas, the observed velocities can be explained if these layers are moving faster down the pillar than the colder, denser gas deeper in the pillar heads. We, in our [C II] and molecular lines, and Pound (1998) in CO and McLeod et al. (2015) in optical ion lines, have observed radial velocity gradients along the Pillars which are thought to trace gas accelerated away from the star as it flows down the pillar. Flow of gas away from the head down the body is predicted in simulations of certain pillar configurations by Mackey & Lim (2010) and of cometary globules by Lefloch & Lazareff (1994). To explain our blueshifted outer layers gas, we need only require that the phenomenon acts more strongly on less dense gas, accelerating it more quickly near the head so that we see a relative velocity shift there but not further down the pillar body where all phases have been accelerated. The driving force is unknown, but we suggest a few possibilities. This could be a shearing flow generated by the action of stellar photons on the slanted pillar structure. The action is transmitted in the warm PDR surface layers, so they respond first. Deeper self-gravitating layers will be slowly carried along through shearing action. Other candidates for the driving force could be the rocket effect or shocks driven by the ionization front, perhaps in combination with surface geometry. Stellar winds, while a good candidate for transferring momentum radially away from the exciting stars, do not reach the surface of the pillars. The striations detected in optical images by Hester et al. (1996) indicate that photoevaporated material flows away from the ionization front uninterrupted for at least a few tenths of a parsec, so the winds must terminate against the H II region further away towards the stars (see the diagram in the left panel of Figure 19 in the

Feature Name	R(, H) ($''$)	R(, H) (pc)	A (pc^{-2})	M_H ($M_\odot$)	M_{H_2} ($M_\odot$)	$M_{\rm tot}$ ($M_\odot$)	$\dot{M}$ ($M_\odot$ Myr^{-1})	t (Myr)
P1a Head	20	0.17	0.18	15	72	86	54	1.6
P1a Neck	20, 38	0.17, 0.32	0.34	8	7	15	103	0.1
P2 Head	10	0.08	0.04	2	14	16	14	1.2
P2 Neck	10, 28	0.08, 0.24	0.13	3	21	24	38	0.6
P3 Head	7	0.06	0.02	1	6	7	7	1.0

Table 2.6 Pillar heads are modeled as hemispheres and necks as cylinders; the R(, H) columns give radius and, if applicable, height. The adopted height for each pillar neck matches the height of the box used to sum over column density. Mass values are rounded to the nearest whole number. Adopted atomic gas density at the base of the photoevaporative flow is $n_{\rm H} = 1.8 \times 10^4$ cm^{-3}. Adopted flow velocity is 0.5 $\rm km\ s^{-1}$.

paper by Westmoquette et al. 2013).

Towards the Eastern Thread, the [C II] and ^{12}CO lines are blueshifted with respect to CS and other molecules. P1a faces towards, not away from, the observer, so this velocity shift is not well explained by these mechanisms. The velocity shift towards the Eastern Thread may be due to an entirely different phenomenon than the velocity shifts towards the Shared Base, P2, and P3.

2.6.2 Pillar Lifetimes

We estimate the photoevaporative lifetime of the pillars based on our observations. We adopt the equation for mass loss rate $\dot{M} = A v_f \rho_{\rm H}$ from Gorti & Hollenbach (2002), where A is the total evaporative surface area, v_f is the photoevaporative flow velocity from the surface, and $\rho_{\rm H}$ is the mass density at the base of the flow.

Warm atomic gas should flow along the pressure gradient through the PDR towards the ionization front at a v_f comparable to, but no greater than, the sound speed in the atomic gas $c_{\rm H} = (P_{{\rm H},therm}/\rho_{\rm H})^{1/2} \sim 1\ \rm km\ s^{-1}$. The observed [C II] velocity dispersion gives an upper limit $v_f \lesssim \sigma_{\rm obs} \approx 1.4\ \rm km\ s^{-1}$, though we attribute most of the observed velocity dispersion to turbulence (Section 2.5.3). We adopt $v_f \sim 0.5\ \mathrm{km\ s^{-1}}$.

Mass density at the base of the flow $\rho_{\rm H} = \mu m_{\rm H} n_{\rm H}$, where we use $\mu = 1.33$ and the atomic gas density $n_{\rm H} = 1.8 \times 10^4\ \mathrm{cm^{-3}}$ from Section 2.5.2. Evaporative surface area A is estimated based on the on-sky sizes of the Pillars in high-resolution optical and NIR images. In order to better understand the evolution of the Pillars, we estimate the evaporative lifetimes of the heads and bodies separately. Evaporation of low column density regions towards the pillar bodies is of particular interest, since we detect significant [C II] line and PAH emission from these regions. We define the pillar "necks" as the lower column density segments of the body between the head and any dense clumps along the body. We use the lack of detected N_2H^+ emission to distinguish the neck from the head and rest of the body. For P1a, the neck comprises both Threads, and for P2 the neck extends between the pillar head and the clump. We do not resolve P3 well enough to define a neck. The boxes used to integrate the head and neck masses are shown in the rightmost panel of Figure 2.12. We model pillar heads as hemispheres and necks as cylinders, and we select a single typical radius for both components of each pillar based on the angular sizes in Table 2.3. The height of the neck is the length of the box used to integrate its mass. The adopted dimensions and corresponding mass loss rates are listed in Table 2.6. The surface area is the only variable changed from region to region, as the number densities in Table 2.3 do not vary by more than a factor of a few and the total [C II] velocity dispersion only varies by $\sim$50%. Column densities calculated using C^+ and CO are summed pixel-by-pixel within the boxes to find the atomic and molecular gas masses, and the total mass of each feature is considered to be the sum of the mass in both phases. The photoevaporative lifetime of each feature is the mass divided by the mass loss rate. The masses and photoevaporative lifetimes are listed in Table 2.6.

The pillar heads will evaporate in $\sim$1–2 Myr by our estimate, consistent with the estimate by McLeod et al. (2015) of ∼3 Myr for these pillars as well as the estimate by Westmoquette et al. (2013) of ∼2 Myr for the pillars surrounding NGC 3603. This is similar to the ∼2 Myr age of the NGC 6611 system, so the Pillars likely formed with roughly a few times as much mass as they have now and have photoevaporated over the last ∼Myr down to their present-day masses. As we discussed in Section 2.5.3, the photoevaporative lifetime is at least as large as τ_{AD}, so the heads of the Pillars may still collapse to form stars before they are completely photoevaporated.

The pillar necks appear to evaporate on a shorter timescale of ∼0.1 Myr due to their much larger surface areas. If we have overestimated their mass loss rates, the culprit could be a diminished flow velocity which is obscured in the observed velocity dispersion by the more dominant turbulent velocity dispersion. In the case of Pillar 1, the flow velocity would have to be diminished by a factor of ∼10. We do observe thinner (by $\lesssim$0.5 $\mathrm{km\ s^{-1}}$) line profiles towards the Threads in P1a and the neck of P2, so this order of magnitude decrement in flow velocity between the head and the neck is possible and must be observationally confirmed with, for example, velocity resolved radio recombination lines or optical ion lines. G_0, measured from FUV emission, is diminished only by ∼60% from the Head to the Neck of P1a, and by ∼30% in P2.

We briefly consider the possibility that the necks do evaporate ∼10x more quickly: either they will evaporate and cause the dense clumps towards the heads to appear as cometary globules like those observed towards Cygnus X (Schneider et al., 2016) or at the 0.01 pc scale elsewhere in M16, or they are being replenished by bulk gas flows from the head like those discussed in Section 2.6.1, which may hasten the dissipation of the pillar heads by a factor of ∼2. The meaningful difference between the two evolutionary scenarios is whether the Pillars are observed as globules or coherent pillars for the last ∼1 Myr of their lives; the work of Schneider et al. (2016) suggests the former.

2.7 Conclusion

We observed the Pillars of Creation in M16 in velocity-resolved [C II] and [O I] for the first time and detected PDRs which are spatially and kinematically associated with the molecular gas. We combine these data with observations of APEX, CARMA, BIMA, *Herschel*, *Spitzer*, and JWST to obtain a multi-layer view of these gas structures.

The largest pillar, P1, is the site of the brightest emission from both molecular gas and PDR tracers. It is separated into two substructures, P1a and P1b, which roughly correspond to its head and its base, respectively. These substructures are somewhat separated along the line of sight, though still linked by kinematically continuous [C II] emission. In P1a, the molecular tracers CO, HCN, HCO^+, and CS reveal two dense filamentary structures which we term the "Threads" running parallel to the pillar body and terminating in a dense "Cap" at the head of the pillar. Our kinematic modeling indicates that these three distinct components are connected towards a region of high column density in the pillar head. Below the Threads past a region of low column density lies P1b, which is linked to the base of P2 by a bright, high column density PDR called the Shared Base. P2, a $\sim$1 pc long pillar which lies closer to the observer than P1, features a dense clump at its head and another halfway down its body. P2 and P3 are dwarfed in brightness by the PDRs towards P1. We include in our studies a handful of nearby PDR host structures, namely the Ridge and P4, which are kinematically related to the Pillars.

This wealth of data allows us to develop a geometric model for the structure of this pillar system, summarized by the schematic in Figure 2.10. Velocity gradients along the Pillars indicate that P1a and P3 point towards the observer while P2 points away. The relative strength of diffuse foreground ionized gas emission places P1a farthest from the observer, and P2 and P3 on the near side with respect to the bright O stars. P2 and P3 are darker optical sources and so their illuminated sides must face away from the observer. All of this is consistent with the conclusions of Pound (1998) and McLeod et al. (2015). We establish from kinematic and column density information that P2 and P1b are connected by the Shared Base, a PDR which is significantly extended along the line of sight.

The [C II] line traces the same parsec-scale spatial and dynamic patterns as the molecular lines, exhibiting the same velocity gradients along P1 and P2 (P3 is too dim in [C II] and not well enough resolved to confirm or rule out a gradient). At smaller scales, [C II] and [O I] emission is generally smoother and more continuous than molecular emission, particularly towards the Threads in P1a, so we conclude that a PDR layer can manifest as a common envelope around dense features like the Threads. The [C II] and ^{12}CO(J=1–0) lines are blueshifted by ∼0.5 $\mathrm{km\ s^{-1}}$ w.r.t. the rest of the molecular lines towards the Shared Base and the heads of P2 and P3. We suggest that this is caused by the same process as the observationally established acceleration of gas away from the stars down the bodies of pillars (McLeod et al., 2015; Pound, 1998) and that the process acts more strongly on the less dense gas in the outer layers of pillars. These motions are similar to those simulated by Lefloch & Lazareff (1994) and Mackey & Lim (2010) and may be a shear flow of the outer layers down the surface of the pillars.

We study the illumination based on both cataloged cluster members and FIR dust emission and constrain the FUV intensity to $G_0 \sim 10^3$ Habing units towards the Pillars. The head of Pillar 1 is characterized by a relatively high $G_0 \sim 2000$ Habing units and good agreement between the stellar and FIR estimates, indicating that it is directly illuminated and the projected distance to the stars is close to the true distance.

We determine the average molecular gas density in the Pillars to be $\sim 1.3 \times 10^5$ cm^{-3} and the average atomic gas density to be $\sim 1.8 \times 10^4$ cm^{-3}. The integrated column densities towards the Pillars yield total masses of 103, 78, 103, and 18 $M_\odot$ for P1a, P1b, P2, and P3 respectively. The atomic gas is typically ∼25% of the total mass, with the exception of P1b which contains about half its mass in the atomic phase. The masses of the Pillars are concentrated in the heads and occasional clumps along the bodies, such as the Horns atop P1b and the clump halfway down P2. These clumps are illuminated, as we detect PDR emission from their cluster-facing surfaces.

Based on pressures derived from our number densities, we assume that the pillars are in pressure equilibrium with the ionized gas around them and that the PDRs associated with the Pillars are magnetically supported. In addition, the magnetic pressure of the dense molecular gas seems to be supporting the Pillar heads and clumps against gravity, but we infer that ambipolar diffusion is reducing the magnetic field support over a ∼1 Myr timescale.

We estimate that the heads of each pillar will be photoevaporated by radiation from NGC 6611 in ∼1–2 Myr. Whether they remain coherent pillars or evolve into free-floating globules as they evaporate may indicate whether or not flows of gas from the head into the body are a significant mass loss pathway compared to photoevaporation. Improved understanding of the evolutionary phases of pillars will reveal their relationships to cometary globules and other categories of observed features.

The Pillars' column shapes are to some extent a shadow of the concentrated mass at their heads, but it is clear from our observations and analysis that there are pre-existing density enhancements all along their bodies. The structure and orientation of the Pillars are affected by the pre-existing structure in the molecular cloud which is sculpted by the radiation field when massive stars turn on.

Chapter 3: SOFIA FEEDBACK Survey: The Eagle Nebula in [C II] and Molecular Lines

3.1 Introduction

Massive stars form in massive complexes of dense gas (Motte et al., 2018), and upon illumination they inject vast amounts of radiative and mechanical energy back into those cloud complexes. Interest in pre-supernova feedback has increased as it has become evident that a few million years of ionizing radiation can dissipate a cloud (He et al., 2019) or that a cluster can inject more than a supernova's worth of energy ($\sim 10^{51}$ erg) in winds over its lifetime (Tiwari et al., 2021). Protostar, main-sequence, and evolved stellar feedback all set the stage for the effect the first supernova has on the surrounding cloud and intercloud environment, and understanding their effects is key to a complete understanding of the energetic life cycle of the interstellar medium.

The massive members of a cluster quickly reach their main sequence luminosities (Zinnecker & Yorke, 2007) and ionize the gas around it which causes rapid pressure-driven Spitzer expansion (Spitzer, 1978). These stars also blow supersonic winds which collide with the photoionized H II region, injecting momentum directly through collision (Geen & de Koter, 2022), and adding further pressure as the shocked winds form a million-degree plasma and fill an interior cavity inside the H II region (Weaver et al., 1977). These three phenomena work together to inflate a multi-phase cavity around the cluster, and there has been much debate and study as to whether winds or photoionization dominate this action (Bonne et al., 2022; He et al., 2019; Pabst et al., 2019, 2021; Tiwari et al., 2021).

Just beyond the edge of the H II region lies a layer which receives no H-ionizing extreme ultraviolet (EUV; $h\nu > 13.6$ eV) radiation but still receives abundant far ultraviolet (FUV; $6 < h\nu < 13.6$ eV) radiation which can dissociate molecules like H_2 and CO and ionize carbon. The influence of FUV radiation upon these photodissociation regions (PDRs) sets them apart chemically from the further-away and un- or poorly-illuminated neutral and molecular phases (Hollenbach & Tielens, 1997; Wolfire et al., 2022). PDR gas is heated photoelectrically as FUV radiation knocks electrons off large, complex organic molecules called polycyclic aromatic hydrocarbons (PAHs; Tielens 2008). Fine-structure lines of neutral oxygen ([O I] 63 and 146 μm) and ionized carbon ([C II] 158 μm) are collisionally excited and radiatively de-excited, cooling the gas. It is with these far-infrared (FIR) tracers that the PDR can be viewed directly and even spectroscopically resolved. Due to Earth's atmosphere's far-infrared opacity and nearby water features, these PDR lines can only be detected from high above the atmosphere, either from far-infrared space observatories like Herschel or from high altitude using balloons or airborne observatories such as SOFIA.

PDR tracers such as [C II] are used to determine the conditions in the FUV-illuminated interface between the photoionized H II region and the largely unilluminated molecular gas and can shed light on whether feedback energy from within the cavity is coupling with the neutral and molecular gas. This leads to the greater question of how efficiently and in what particular ways stellar feedback is injected back into its environment.

This work focuses on M16, the Eagle Nebula, an H II region driven by the $\sim 10^4\ M_\odot$

(Pfalzner, 2009) cluster NGC 6611 with a most massive member of type O3.5 V((f)) (Stoop et al., 2023). The region, at a heliocentric distance of 1740 pc (Kuhn et al., 2019), is surrounded by several giant molecular clouds and filaments (GMCs, GMFs; Xu et al. 2019; Zhan et al. 2016), at least one of which seems to have birthed the cluster (Hill et al., 2012; Nishimura et al., 2021). M16 is well studied across the electromagnetic spectrum, in part because it harbors the iconic Pillars of Creation, whose Hubble Space Telescope (HST) and JWST images are widely recognized (Hester et al., 1996). The bright PDRs associated with the Pillars were studied in [C II], [O I], and molecular lines by Karim et al. (2023), and in this work we extend the same general methods to the wider M16 region.

We present a multiwavelength analysis using velocity resolved and continuum observations of the M16 massive star forming region, tracing multiple phases of gas from the 10^6 K shocked wind plasma to the FUV-irradiated PDRs to cold, dense molecular gas. Our velocity-resolved analysis centers on the brightest $\sim$30′-wide (15 pc) region of M16, and we contextualize these using archival degree-scale continuum images which reveal the faint outer reaches of NGC 6611's influence. We present observations in Section 3.4 and derive column densities from the [C II] and CO lines in Section 3.6. We numerically estimate the feedback capacity of NGC 6611 based on observed catalogs of its members in Section 3.7 and we compare these to the energies and pressures in various phases of gas in Section 3.8 to evaluate how well stellar feedback has coupled to the gas. We conclude the paper with a discussion in Section 3.9 of region morphology and contextualize the results of our feedback analysis within a proposed 3-dimensional geometric picture of the region.

3.2 Observations

3.2.1 SOFIA

The [C II] line was observed towards M16 between 2019 and 2023 on flights from Palmdale, California and Tahiti. The 158 μm $^2P_{3/2} \rightarrow {}^2P_{1/2}$ transition was mapped on-the-fly using upGREAT[1] (Risacher et al., 2018), a 7-pixel heterodyne receiver with a fast Fourier transform spectrometer (FFTS) backend with 4 GHz instantaneous bandwidth and 0.244 MHz frequency resolution (Klein et al., 2012). Atmospheric calibration was done with the GREAT pipeline (Guan et al., 2012)

The nominal angular resolution of the [C II] data is 14.1″, but here we use a [C II] data cube with a spatial resolution of 15.5″, a grid of 5″, and a spectral binning of 0.5 $\mathrm{km\,s^{-1}}$. The noise RMS in one channel is typically 1.0 K. All spectra are presented on a main beam brightness temperature scale T_{MB} using an average main beam efficiency of $\eta_{\mathrm{MB}} = 0.65$. The forward efficiency is η_{f} = 0.97. Further observational details are available in the paper by Schneider et al. (2020).

The map used in this study contains 6 more tiles (squares with 8′ sides into which observations were divided) than the map presented by Karim et al. (2023). The observations for one of these tiles, to the west of the Pillars of Creation, were not fully completed due to SOFIA's decommissioning in the summer of 2023. The affected tile has a higher RMS noise, typically 2.5 K, and contains stripe artifacts along the scanning axis. This tile is coincident with the region within M16 where we search for an expanding shell signature. The [C II] signal from the shell is

[1] upGREAT and GREAT were developed by the MPI für Radioastronomie and the KOSMA/Universität zu Köln, in cooperation with the MPI für Sonnensystemforschung and the DLR Institut für Planetenforschung.

detected at $\sim$2–3 σ due to the increased noise.

3.2.2 APEX

M16 was mapped in the J=3–2 transition of ^{12}CO and ^{13}CO using the LAsMA spectrometer on the APEX[2] telescope (Güsten et al., 2006). We use data cubes with a 9.1″ pixel and an 18.2″ beam after gridding and 0.1 $\mathrm{km\,s^{-1}}$ spectral bins. Spectra are calibrated in T_{MB} with a main-beam efficiency $\eta_{\mathrm{MB}} = 0.68$ at 345.8 GHz. Further observational details are given by Karim et al. (2023).

The OFF position is slightly contaminated near $\mathrm{V_{LSR}} = 21.1\ \mathrm{km\,s^{-1}}$. It makes a small divot in the spectra but does not affect our analysis and conclusions.

3.2.3 CO (1–0) Line Observations

We use the publicly available ^{12}CO(J=1–0), ^{13}CO(J=1–0), and C^{18}O(J=1–0) line observations made by Xu et al. (2019) using the 13.7 m radio telescope at the Purple Mountain Observatory (PMO) in Delingha. The observations have a 53″ beam, about 3$\times$ the size of the SOFIA [C II] and APEX CO (J=3–2) beams. The 0.3 $\mathrm{km\ s^{-1}}$velocity resolution, 0.2 K sensitivity, and half square degree field of view make it a valuable compliment to our observations.

We use the publicly available ^{12}CO(J=1–0), ^{13}CO(J=1–0), and C^{18}O(J=1–0) line observations from the FUGIN survey (Umemoto et al., 2017) made with the 45 m Nobeyama[3] radio telescope. The observations have a 20″ beam, 0.65 $\mathrm{km\ s^{-1}}$ velocity resolution, and $\sim$1 K sen-

[2]APEX, the Atacama Pathfinder Experiment is a collaboration between the Max-Planck-Institut für Radioastronomie, Onsala Space Observatory (OSO), and the European Southern Observatory (ESO).

[3]The 45-m radio telescope is operated by the Nobeyama Radio Observatory, a branch of the National Astronomical Observatory of Japan.

sitivity. Scanning artifacts appear over the M16 region due to weather conditions during some of the observations. The FUGIN survey covers $|b| < 1^\circ$, and M16 extends up to $1\overset{\circ}{.}2$. However, the nearly 4 square degree field of view spanning all the way to the Galactic plane makes this a valuable asset alongside our wide-field continuum images. The observations and their analysis are described in detail by Nishimura et al. (2021).

We use both sets of CO (J=1–0) observations because the PMO observations cover the central M16 region but do not cover the extended area including the rest of the GMF towards the Galactic plane, while the FUGIN observations cover a larger area including the GMF, but do not cover $b > 1^\circ$.

3.2.4 Ancillary Data

To analyze the shock-ionized plasma within wind-blown bubbles, we obtain the diffuse X-ray spectra and maps extracted by Townsley et al. (2014) from the Chandra ACIS-I mosaics by Linsky et al. (2007) and Guarcello et al. (2010b).

We use a collection of publicly available continuum images in our analysis to trace a variety of other cold and warm phases of gas associated with H II region bubbles. We obtain 70–500 μm Herschel PACS and SPIRE images from the Herschel Science Archive; the GLIMPSE 8 μm Spitzer IRAC image and the 24 μm Spitzer MIPS image from the NASA/IPAC Infrared Science Archive (IRSA); the WISE 3.4, 4.6, 12, and 22 μm images from the IRSA; 90 cm VLA observations from the MAGPIS survey website[4]; 850 μm observations from the Atlasgal survey using APEX; and the DSS2 red optical image from the ESO Online interface to the DSS archive[5].

[4]https://third.ucllnl.org/gps
[5]https://archive.eso.org/dss/dss

3.3 Structure of M16

We review the structure of M16 as seen in wide-field images and spectra from archival sources.

3.3.1 GMC W 37 and the GMF

The 160–850 μm images (Figure 3.1) and large-field FUGIN CO (J=1–0) observations (Figure 3.2) trace a $\sim$40 pc long giant molecular filament (GMF) running perpendicular to the Galactic plane. The upper part $0.^{\circ}5 \lesssim b \lesssim 1^{\circ}$ of the GMF widens out into a giant molecular cloud (GMC) W 37 Westerhout (1958); Zhan et al. (2016). This GMF, hereafter "the GMF," intersects with M16 and is likely the birthplace of the cluster (Hill et al., 2012). It was suggested by Moriguchi et al. (2002), Guarcello et al. (2010b), and Comerón & Torra (2018) to be the remnant shell of an old, distant supernova which may have triggered the formation of both M16 and M17 $\sim$3 million years ago.

The GMF runs down towards the Galactic plane from W 37, between $0^{\circ} \lesssim b \lesssim 0.^{\circ}5$, in the CO as well as in 500 and 850 μm. The GMF, traced with blue lines in Figure 3.1, was grouped together with GMF 18.0–16.8 to the east[6]/$+l$ by Ragan et al. (2014) and Li et al. (2016), but Zhan et al. (2016) relates GMF 18.0–16.8 to another GMF 16.5–15.8 to the west/$-l$ of the W 37 GMC, leaving the GMF running down from W 37 with the label "dense ridge" in their paper. GMF 18.0–16.8 appears in the FUGIN CO observations in Figure 3.2B to the left of W 37 at $\mathrm{V_{LSR}} = 21\text{–}23\ \mathrm{km\,s^{-1}}$ and is not traced by the 160, 500, or 850 μm. The GMF, on the

[6]"East" here refers to equatorial coordinates, while $+l$ refers to Galactic coordinates. In reality, of course, these gas clouds are not aligned with either coordinate system, so we give these multiple descriptors of their relative positions and orientations to be more descriptive.

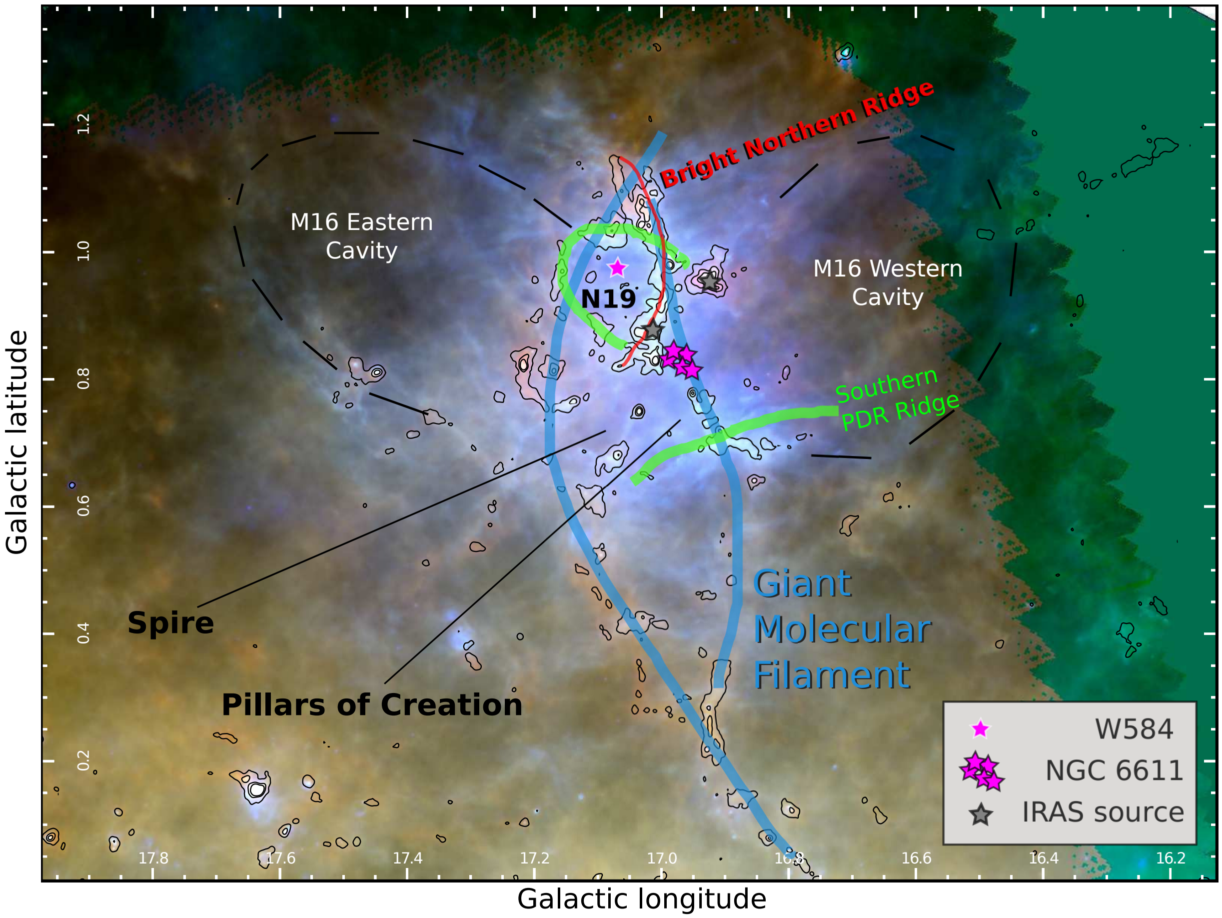

(A)

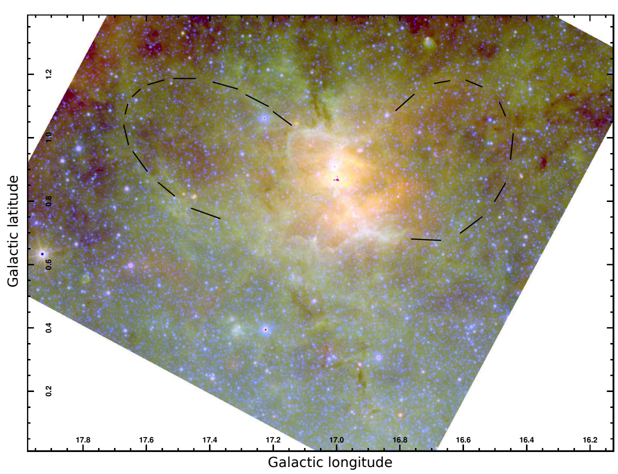

(B)

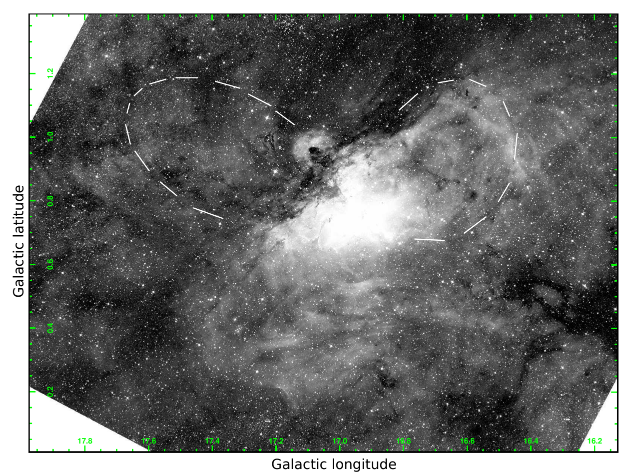

(C)

Figure 3.1 (A) Herschel 500, 160, 70 μm in red, green, and blue, and 850 μm in black contours. Features are marked with colored lines. (B) WISE 22, 12, and 4.6 μm in red, green, and blue, and (C) optical DSS2 R-band. Dashed black or white lines in all images outline the infrared lobes.

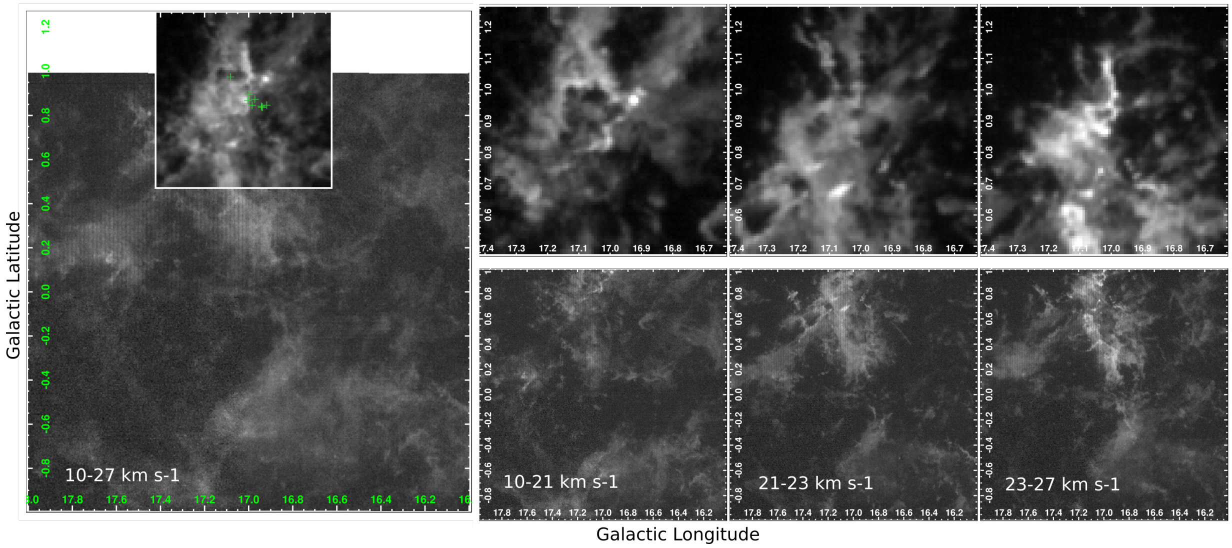

Figure 3.2 ^{12}CO(J=1–0) integrated intensities in 4 different velocity intervals. The leftmost panel shows the PMO and FUGIN observations overlaid. The FUGIN observations cover $|b| < 1°$, but M16 extends slightly above $b = 1°$. The PMO observations cover a smaller area but reach up to $b \approx 1.°3$. Green crosses show early-type members of NGC 6611. The two rows to the right show PMO observations on top and FUGIN observations on the bottom. The velocity intervals used for each column are marked on the bottom row. Observations are from PMO and are at a 55″ beam. Observations are from the FUGIN survey using Nobeyama and are at a 20″ beam.

other hand, is nearly perpendicular to GMF 18.0–16.8 and is clearly traced in the FIR/sub-mm in Figure 3.1 where it is marked in blue. The GMF lies in the interval $\mathrm{V_{LSR}} = 21\text{–}27\ \mathrm{km\ s^{-1}}$ based on CO line velocities. Parts of the GMF are seen in absorption in the mid-IR images in Figure 3.1 below the bright H II region. These dark lanes are included in catalogs by Rygl et al. (2010), Peretto et al. (2016), and Eden et al. (2019) and do not appear to be illuminated by the NGC 6611 cluster.

3.3.2 Filaments within M16

The GMF widens into GMC W 37 and splits into two subfilaments where it intersects with M16. This $\sim 1.5 \times 10^5\ M_\odot$ GMC (Nishimura et al., 2021; Zhan et al., 2016) dominates the CO observations between $\mathrm{V_{LSR}} = 10\text{–}27\ \mathrm{km\ s^{-1}}$ shown in Figure 3.2. W 37 connects with the GMF between $V_{LSR} = 21$–$27\ \mathrm{km\,s^{-1}}$, while the lower velocity $V_{LSR} = 10$–$21\ \mathrm{km\,s^{-1}}$ interval is dominated by northern/$+b$ CO emission. The same degree-scale cloud structure appears in W 37 throughout 21–27 $\mathrm{km\,s^{-1}}$, though the 23–27 $\mathrm{km\,s^{-1}}$ emission is arranged into thinner, clumpier filaments compared to the more diffuse 21–23 $\mathrm{km\,s^{-1}}$ emission. Hill et al. (2012), who studied the region using Herschel HOBYS observations, identified several subfilaments associated with the GMF within M16. The GMF branches into two subfilaments $\sim$10 pc below M16, which they call the Eastern and Western filaments. The Western filament terminates at the southern boundary of the H II region, the PDR ridge marked in green in Figure 3.1. The Pillars of Creation extend from the filament into the H II region and point towards what Hill et al. (2012) call the Northern Filament. The Spire, another pillar in M16, branches off from the Eastern filament. The Eastern filament, they point out, is relatively unperturbed by stellar feedback while the Western and Northern filaments were once perhaps connected and have been severed by stellar feedback as NGC 6611 formed within them. The Pillars of Creation lie atop the Western filament where it protrudes into the H II region. Hill et al. (2012) identify the Ridge, a part of the Northern filament which we call the Bright Northern Ridge for additional specificity, north of NGC 6611 (Figure 3.1, marked in red). The Bright Northern Ridge is bright across the IR, from mid-IR PDR and ionized gas tracers like 8, 12, 22, and 70 μm to high column density dust and molecular gas tracers like 160, 500, and 850 μm in Figure 3.1 and CO in Figure 3.2 (top right panel, high velocity). It seems to lie behind the lower velocity Northern Cloud (described below), as it does not appear in the optical, and is kinematically associated with the higher velocity filamentary emission. Guarcello et al. (2012) detected a young population of X-ray sources within the Bright Northern Ridge. A particularly bright piece of the region hosts the source IRAS 18156–1343, which is associated with water maser emission (Codella et al., 1994).

We hereafter refer to the 23–27 $\mathrm{km\ s^{-1}}$ gas whose emission peaks around 25–26 $\mathrm{km\ s^{-1}}$ as the "natal cloud" of NGC 6611. This is the same velocity at which Karim et al. (2023) identify a diffuse [C II] component around/behind the Pillars. The natal cloud includes the filaments described by Hill et al. (2012) as well as the Pillars, Spire, and Bright Northern Ridge and is kinematically associated with the GMF.

3.3.3 N19 and the Northern Cloud

The northern, low velocity emission between 10–21 $\mathrm{km\ s^{-1}}$, peaking in CO around $\sim$19 $\mathrm{km\ s^{-1}}$, appears in absorption in the optical (compare the optical in Figure 3.1 to the 10–21 $\mathrm{km\ s^{-1}}$ CO map in Figure 3.2, top left panel) indicating that it lies in front of the H II region with respect to the observer, while the higher velocity emission associated with the GMF must lie in the background. We hereafter refer to the northern, low velocity cloud as the "Northern Cloud." Together, the natal cloud and the Northern Cloud constitute the GMC W 37, consistent with the definition implied by the diagrams of Zhan et al. (2016).

Within the Northern Cloud lies a bright infrared ring filled with optical emission. Known as N19 (Churchwell et al., 2006) or G0170780+0095101 (Jayasinghe et al., 2019) and called the "Arch" by Hill et al. (2012), the ring is bright at 8, 12, 70, and 160 μm, heavily obscured by nearby bright emission in the 24 μm images, and faint $\geq$250 μm. The N19 ring is likely the projected shell of a bubble driven by the O9 V star called W584 (Guarcello et al., 2010b; Hillenbrand et al., 1993), though it has also been suggested to be the compressed remnant of a cloud-cloud collision (Nishimura et al., 2021). N19 is spatially and kinematically connected to the rest of the Northern Cloud as traced by CO, seen in the top-left panel of Figure 3.2.

From the bottom edge of the Northern Cloud extends a dark optical triangle that protrudes into the bright H II region near NGC 6611. Within this region, which is sometimes called the "north bay", lies the bright-rimmed cloud (BRC) SFO 30 (Oliveira, 2008; Sugitani et al., 1991) and the source IRAS 18159–1346, towards which water maser emission, indicating early stage star formation, has been detected (Braz & Epchtein, 1983; Healy et al., 2004; Valdettaro et al., 2005).

A CO source is associated with another IR source IRAS 18152–1346, identified as an $\sim$8 $M_{\odot}$ massive young stellar object (MYSO) by Indebetouw et al. (2007). Zhan et al. (2016) and Xu et al. (2019) identified it as a bright CO source, and Codella et al. (1995) detected water maser emission toward it. It has a wide, asymmetric line profile with a long low velocity tail extending to around $\mathrm{V_{LSR}} \sim 0\ \mathrm{km\,s^{-1}}$ in both the PMO and FUGIN observations Its $\mathrm{V_{LSR}} \sim 19\ \mathrm{km\,s^{-1}}$ peak associates it with the Northern Cloud.

3.3.4 Bright PDR and H II Interior of M16

The 8 and 12 μm maps trace PDRs around M16 and are similar to the velocity-integrated [C II] line emission. Emission at 24 μm, 70 μm, and 90 cm trace similar structures and are particularly bright towards the Pillars, Spire, and Bright Northern Ridge. The 24 μm and 90 cm images are particularly similar and are shown in Figure 3.3. The 70 μm emission traces hot dust in the PDR, 90 cm traces ionized gas via free-free emission, and 24 μm traces hot dust in both neutral and ionized gas (Churchwell et al., 2009). The tight correlation between the brightest PDR emission and H II region indicates that the H II region emission is dominated by high-density ionized gas very close to the neutral gas. Compared to the 8, 12, and 70 μm, the

24 μm and 90 cm trace more emission inside the H II region. Flagey et al. (2011) identified a 24 μm inner ring, interior to the PDRs, and suggested that the action of wind-driven shocks within the photoionized gas may grind dust into very small grains. This inner shell can be seen at 22 μm in red in our Figure 3.1, but is clearly shown in Figure 1 in the paper by Flagey et al. (2011). M16 is very bright and extended at 24 μm; emission drops off gradually from the center out to $\gtrsim$10 pc away as shown in Figure 3.3.

3.3.5 Extended Infrared Lobes

To the $\pm l$ sides of that bright central region lie $\sim$15 pc (approximately half-degree) diameter infrared lobes. These two large, elongated rings have faint infrared edges and dark interiors in 8, 12, and 70–500 μm images. They are identifiable in the FIR color-composites in Figure 3.1 by the blue 70 μm emission along their edges and in the mid-IR WISE composite by their green 12 μm edges. They are marked with dashed lines in the panels of Figure 3.1 and are slightly tilted towards higher Galactic latitude. The left $(+l)$ lobe has a clear bottom edge $(-b)$ in the 8, 12, 24, and 70–500 μm images. Two pillars with IR point sources within them sit along this edge, and their bright rims point back toward NGC 6611, indicating that there is dense gas along the edges which is influenced by the cluster. These pillars, along with the entire left lobe, are completely obscured in the optical, probably by extinction from the Northern Cloud. The right $(-l)$ lobe's edge appears to be a collection of a few concentric infrared ring fragments. The right lobe is filled with optical emission (Figure 3.1) which truncates where the edge fragments appear in the infrared. Parts of the right lobe's interior are darker at 8 μm than the left lobe's interior, but this effect is not present at 12 and 24 μm.

Relative brightness of the lobe edges compared to their interiors is greater at shorter mid-IR wavelengths, like 8 μm, compared to 22-24 μm. The lobe edges are illuminated in the FUV but are not particularly warm. The 22–24 μm intensity decreases with distance from NGC 6611, and this effect is weaker at the shorter mid-IR wavelengths where PAH emission dominates. This might indicate a temperature gradient in the dust associated with the lobes. The 12 μm band shows both effects, as its wide bandpass covers PAH features as well as continuum from small grains. The FUGIN CO observations trace emission along the bottom edge of the left lobe including the two pillars. The rest of the lobe edges must be fairly low column density so that FUV reaches most of, if not all, the way through.

3.3.6 Summary of Structure

The GMF is traced by CO at $\sim$25–26 $\mathrm{km\ s^{-1}}$ and 850 μm continuum and extends all the way through W 37 and M16 to the Galactic plane. NGC 6611 likely formed from this filament, as dense gas features hosting bright PDRs such as the Bright Northern Ridge, the Pillars, and the Spire share this velocity and are located along its subfilaments. The cavity generated by feedback from NGC 6611 appears to have blown out of the sides of the filament in which the cluster formed. The combined IR and sub-mm observations reveal a well-expanded H II region consisting of two lobes bright in ionized medium tracers (e.g., 24 μm dust emission) while lobe edges light up in PDR tracers like 70 μm from warm dust and 8 and 12 μm PAH emission.

The bright PDR edges indicate limb brightening from a $\sim$40 pc diameter shell surrounding a cavity. Radiation from NGC 6611 influences gas far from the bright $\sim$10 pc wide center of the H II region, where gas and dust are hot and dense and shine brightly. Within the central region, dense molecular gas is sculpted into parsec-scale pillars such as the Pillars of Creation and the Spire. Bright PDR covers the surface of the Bright Northern Ridge, a dense molecular gas ridge which lies only a few parsecs in projection from the NGC 6611 cluster. Diffuse X-ray-emitting plasma surrounds the cluster and also appears above and perhaps behind the surrounding molecular gas (Townsley et al., 2014), indicating that shocked-wind plasma has escaped the central region.

The H II region has expanded along $\pm l$, perpendicular to the GMF which extends along $\pm b$. Simulations show that H II regions expand non-uniformly in the presence of dense gas, seeking out lines of sight with lower densities (Fukuda & Hanawa, 2000; Whitworth & Priestley, 2021; Zamora-Avilés et al., 2019). The M16 H II region's expansion is constrained along the filamentary axis and seems to have expanded out wherever the filament is not.

We introduce in the next Section our new [C II] and CO (J=3–2) observations of the bright central region of M16. These velocity-resolved observations offer the capability to distinguish features kinematically as well as spatially, like we did with the CO (J=1–0) spectra. The (J=3–2) transition is more sensitive than the (J=1–0) to dense gas and highlights gas structures which either retain high primordial densities or have been shock-compressed by feedback from the cluster. The [C II] observations unlock the capability to kinematically resolve PDRs. The [C II] transition traces similar FUV-illuminated gas as FIR dust or mid-IR PAH tracers (Pabst et al., 2017, 2021), but can be spectroscopically resolved. The combination of [C II] and CO observations is a powerful tool for determining the structure and kinematics of illuminated and un-illuminated gas in a star formation system and evaluating the effects of stellar feedback on the surrounding gas.

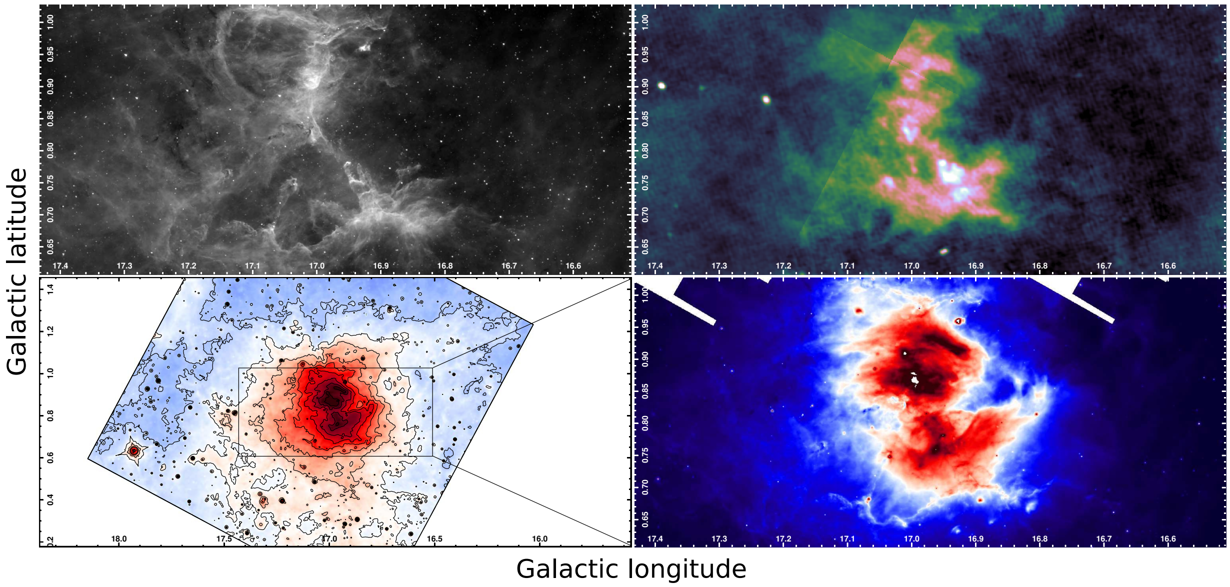

Figure 3.3 PDR and ionized gas tracers toward M16. Clockwise from top-left, they are the 8 μm, 90 cm, 24 μm, and 22 μm. The 22 and 24 μm essentially trace the same gas (via dust); the 22 μm observations cover a wider field at a lower resolution. The first three images all show the same field toward the bright center of M16. We show a larger field at 22 μm, and the black box in the center of that panel shows the field for the other three images.

3.4 Results from [C II] and CO

3.4.1 Spectra and Channel Maps

The typical [C II] spectrum towards M16 is a combination of two velocity components: a bright component at the natal cloud velocity $\mathrm{V_{LSR}} \approx 25$–$26~\mathrm{km~s^{-1}}$, and a secondary peak at $\mathrm{V_{LSR}} \approx 17$–$18~\mathrm{km~s^{-1}}$, close to the $\sim$19 $\mathrm{km~s^{-1}}$ Northern Cloud velocity. These components appear in the large-area average [C II] spectrum at the top of Figure 3.4. Channel maps of [C II] in Figure 3.5 and CO in Figure 3.6 show that the 25–26 $\mathrm{km~s^{-1}}$ emission traces the filamentary structure of the natal cloud and the $\sim$17–18 $\mathrm{km~s^{-1}}$ emission traces N19 and the Northern Cloud. The natal cloud [C II] emission includes CO-emitting features like the Bright Northern Ridge,

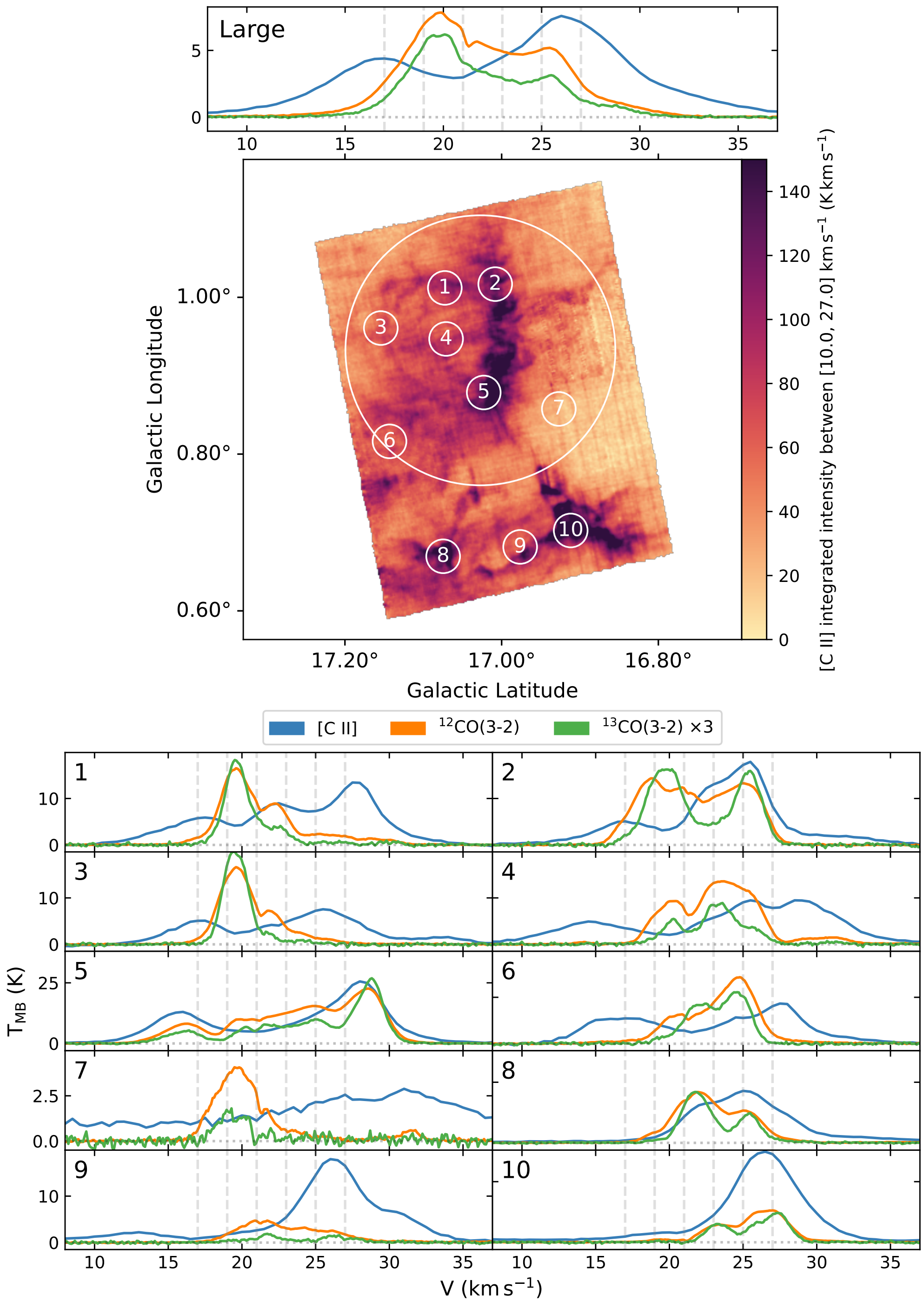

Figure 3.4 Averaged [C II], ^{12}CO(J=3–2), and ^{13}CO(J=3–2) spectra from within regions outlined on the integrated [C II] intensity image in the center. Spectra from the largest circle are shown above the image, and spectra from the numbered regions are shown in the panels below the image. ^{13}CO spectra are shown multiplied by 3 for better visibility. Vertical lines mark every 2 $\mathrm{km\ s^{-1}}$ between 17–27 $\mathrm{km\ s^{-1}}$. This conveniently marks the Northern Cloud near 19 $\mathrm{km\ s^{-1}}$, the diffuse CO component at 21–23 $\mathrm{km\ s^{-1}}$, and the natal cloud emission near 25 $\mathrm{km\ s^{-1}}$.

the Spire, the Pillars of Creation, and the southern PDR ridge at the base of the Pillars (where region 10 is marked in Figure 3.4) as well as diffuse [C II] emission with no CO counterpart that extends to $+l$ from the Bright Northern Ridge (behind N19, for example where region 4 is marked in Figure 3.4).

We overlay [C II] and CO intensity maps integrated within the same velocity intervals in the red-blue images in Figure 3.7 and the velocity red-green-blue (RGB) images in Figure 3.8 to emphasize similarities and differences in what is traced by these transitions.

3.4.1.1 [C II] Channel Maps

The lowest velocity [C II] emission in the channel maps in Figure 3.5 appears around 7–11 $\mathrm{km\,s^{-1}}$ to $-l$ and traces the gas along the interior of the right IR lobe as seen at 8–12 or 70–500 μm. From 13–21 $\mathrm{km\,s^{-1}}$, [C II] emission highlights the Northern Cloud and N19. The Northern Cloud and N19 fade into confusion with the line wings of the diffuse emission behind the Bright Northern Ridge around 23 $\mathrm{km\,s^{-1}}$; their spatial coincidence and distinctness is emphasized in the [C II] RGB image in Figure 3.8. Morphology clearly distinguishes the Northern Cloud and natal cloud components as separate features in [C II], and though they are confused in in their line wings, their peaks are well separated by $> 5\ \mathrm{km\,s^{-1}}$ as seen in regions 1–4 in Figure 3.4, greater than the typical line width of 2–3 $\mathrm{km\,s^{-1}}$ in individual spectra.

The filamentary structure of the natal cloud—Pillars, Spire, and Bright Northern Ridge—appears in bright [C II] emission between 23–27 $\mathrm{km\,s^{-1}}$. Beyond 27 $\mathrm{km\,s^{-1}}$, a few bright spots of emission remain on the Bright Northern Ridge, and the southern PDR ridge below the Pillars spreads out and highlights a different set of small ridges along the same lines of sight, indicating that the southern PDR ridge is a complex PDR surface viewed edge-on. The highest velocity [C II] emission $\mathrm{V_{LSR}} \gtrsim 35\ \mathrm{km\,s^{-1}}$ appears toward the same region inside the right IR lobe as the lowest velocity emission.

3.4.1.2 Comparison of [C II] to CO

The CO (J=3–2) line generally traces the same components as CO (J=1–0) but with different relative intensities. The same is true between CO (J=3–2) and [C II] at the Northern cloud and natal cloud velocities, but not between $\mathrm{V_{LSR}} = 21\text{–}23\ \mathrm{km\,s^{-1}}$ where the CO lines trace a diffuse W 37.

CO (J=3–2) channel maps in Figure 3.6 show low velocity emission appearing along the flat bottom of the Northern Cloud between $\mathrm{V_{LSR}} = 13\text{–}17\ \mathrm{km\,s^{-1}}$. One clump of CO emission at 9 $\mathrm{km\,s^{-1}}$ is coincident with [C II] emission and traces a mid-IR and FIR clump, but besides that, we do not detect CO from the inside of the right IR lobe as we do [C II]. The spot of CO (J=3–2) emission visible from 5–19 $\mathrm{km\,s^{-1}}$ is associated with the MYSO IRAS 18152–1346 and has a similar wide, asymmetric profile as in the CO (J=1–0) observations.

N19 appears in CO from 17–21 $\mathrm{km\,s^{-1}}$ and its ring is wider and has a clumpier inner edge in CO than in [C II]. Spectra towards the edge of the N19 ring in Figure 3.4 (regions 1–4) show that the [C II] emission is blueshifted with respect to the CO emission. CO (J=3–2) and (J=1–0) emission from the Northern Cloud extends further north/up than [C II]; [C II] emission here is faint, indicating that the far reaches of Northern Cloud are a poorly illuminated reservoir of dense gas.

At 19 $\mathrm{km\,s^{-1}}$, the diffuse background component begins to appear in the CO channel maps below the Northern Cloud. This component is strongest and most widespread between 21–23 $\mathrm{km\,s^{-1}}$. We detect faint [C II] emission in this interval towards some of the CO-bright locations, but this component is largely undetected in [C II](see regions 5–7 in Figure 3.4). The CO (J=1–0) observations show that much of the surrounding W 37 CO emission lies at $\mathrm{V_{LSR}} \sim 21\text{–}23\ \mathrm{km\,s^{-1}}$. The Galactic Sagittarius-Carina arm crosses around this velocity (Kuhn et al., 2021), so some of this diffuse emission may also be unrelated foreground or background gas and therefore may not have a strong [C II] counterpart.

From 23–27 $\mathrm{km\,s^{-1}}$, CO channel maps trace the Pillars, Spire, and Bright Northern Ridge. The Bright Northern ridge appears as a thin, bright filament in CO, in contrast to its more diffuse appearance in [C II]. The $-l$ side of the Bright Northern Ridge connects spatially and kinematically to a diffuse cloud of gas. This diffuse molecular cloud, apparent in the 25 $\mathrm{km\,s^{-1}}$ channel map, is spatially separated from the diffuse [C II] emission behind the Bright Northern Ridge. There is [C II] emission towards this molecular cloud at 25 $\mathrm{km\,s^{-1}}$, but [C II] and CO do not clearly trace the same morphology. This is the natal cloud velocity interval, so there are likely many small clouds and filaments associated with W 37 and the GMF along these lines of sight.

The high velocity CO channel maps show a scattering of bright emission spots, many of which are spatially coincident with [C II] emission in the same channels. [C II] and CO both trace a particularly bright clump along the Bright Northern Ridge close to the location of NGC 6611 around the 29 $\mathrm{km\,s^{-1}}$ channel; we show spectra towards the clump in region 5 in Figure 3.4. Just like in the low velocity channels, we do not detect high-velocity CO inside the right lobe like we do [C II].

3.4.1.3 Summary of Channel Maps

In summary, [C II] and CO trace the natal cloud and Northern Cloud, demonstrating that these two distinct molecular cloud substructures of W 37 are illuminated. Pockets of CO-dark [C II] emission and [C II]-dark CO emission as well as some differences in traced morphology indicate that the PDR and molecular gas structures are similar but not one-to-one. The red-blue images in Figure 3.7 reveal a complex interplay between the phases. Gas behind the Bright Northern Ridge and along the southern PDR ridge is mostly atomic, and there are reservoirs of unilluminated molecular gas attached to illuminated structures like the Bright Northern Ridge and Northern Cloud. There is also a large reservoir of unilluminated molecular gas between 21–23 $\mathrm{km\,s^{-1}}$ which generally lacks a [C II] counterpart and may be a significant chunk of W 37 which NGC 6611 has not influenced.

As we saw in CO (J=1–0) in Section 3.3 and show here in Figure 3.9, the [C II] and CO emission from the Northern Cloud is coincident with the dark optical absorption feature which obscures the left IR lobe. This places the Northern Cloud in between the observer and NGC 6611/the natal cloud. The dark optical triangle extending into the bright H II region, towards SFO 30, is traced in [C II] and CO around 21 $\mathrm{km\,s^{-1}}$ and associated in the channel maps with Northern Cloud emission. Spectra from both lines toward this location, which is near the source IRAS 18159-1346, include many velocity components between 17–28 $\mathrm{km\,s^{-1}}$. The edge of this triangle which faces NGC 6611 is arch-like and opens towards the cluster. This strongly suggests that the Northern Cloud is illuminated and influenced by NGC 6611. N19 is a separate ring driven into the Northern Cloud by W584, the O9 star inside it (Guarcello et al., 2010b; Hillenbrand et al., 1993). The bottom edge of the Northern Cloud, which contains PDR and molecular gas, may be compressed between opposing feedback from W584 and NGC 6611.

3.4.2 M16 Expanding Shell

High ($\mathrm{V_{LSR}}$ ~35–40 $\mathrm{km\ s^{-1}}$) and low (~10–15 $\mathrm{km\ s^{-1}}$) velocity [C II] emission relative to the bulk 19–26 $\mathrm{km\ s^{-1}}$ emission is detected towards the western opening of the M16 cavity, just west of the Pillars of Creation. High velocity emission, shown in red in Figure 3.10, is diffuse and fills part of the western opening while low velocity emission shown in blue in the Figure is concentrated in a few clumps. Figure 3.11 shows the 9 $\mathrm{km\ s^{-1}}$ [C II] and CO clump mentioned in Section 3.4.1.2 which traces a small IR ridge. The 8 and 160 μm maps show that this small ridge is nestled within a network of other faint PDR structure near the northern end of the western cavity opening. The PDR emission does not extend all the way across the opening.

The western opening overlaps with the [C II] map tile affected by the truncated observations mentioned in Section 3.2.1, which cause the striped artifacts in Figure 3.10 near the red and blue emission. The noise RMS increases to ~2.5 K in this tile so that the redshifted emission is typically detected at $\sim 2\sigma$ and the blueshifted clump at $\sim 4\sigma$.

We conclude that this faint PDR area on the northern edge of the western opening is a composition of limb brightened foreground and background shell expanding at no less than ~10 $\mathrm{km\ s^{-1}}$, the LOS-projected velocity separation from the $\mathrm{V_{LSR}} \sim 25\ \mathrm{km\ s^{-1}}$ natal cloud emission. We do not detect significant high or low velocity emission in the [C II] spectra towards the middle of the western opening, shown in orange in Figure 3.10, so the emission is faint if present at all.

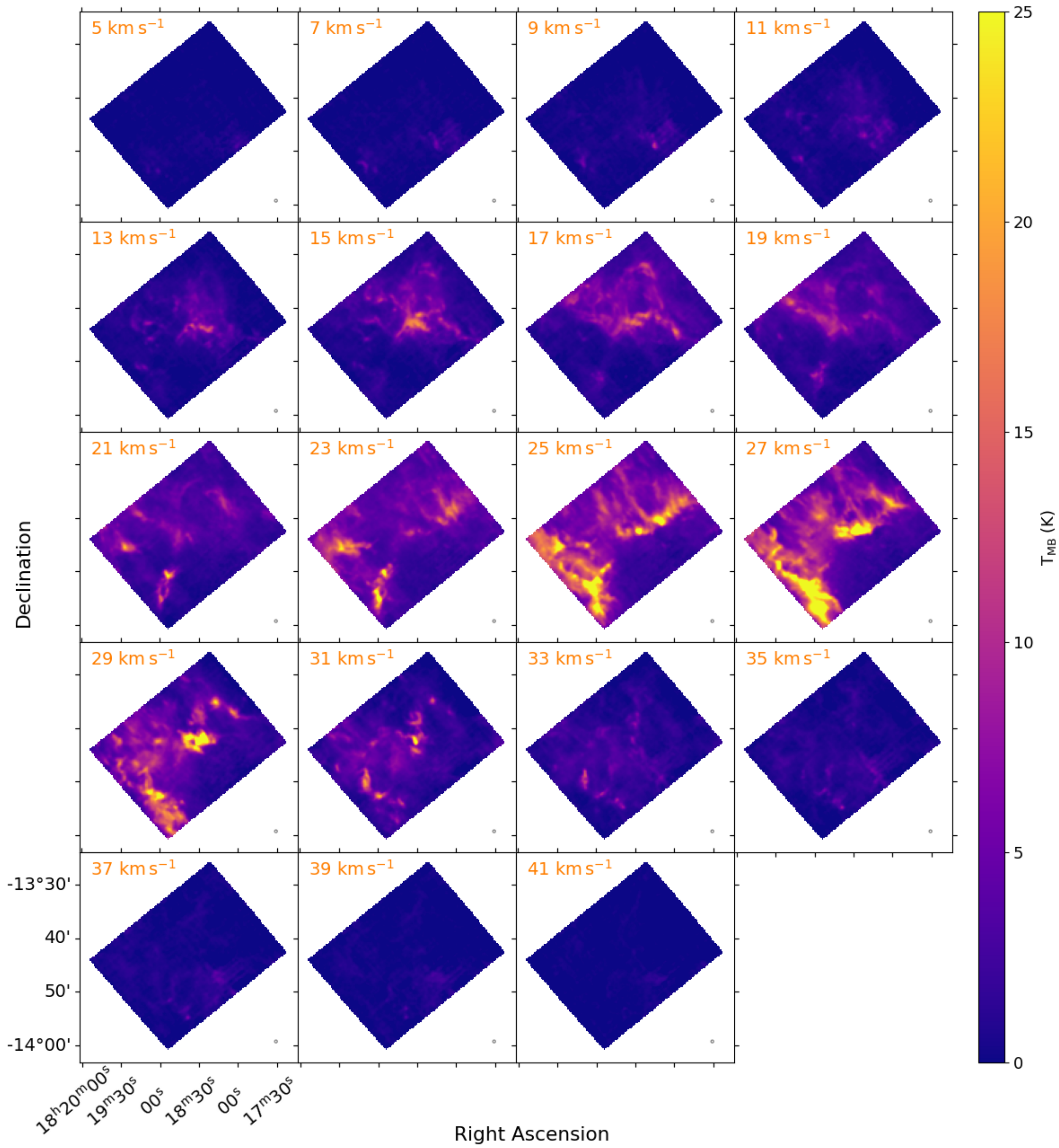

Figure 3.5 [C II] line channel maps. All maps are on the same linear scale shown on the colorbar to the right. The beam is shown in the lower right corner of each map. The data are convolved here to a 30″ beam and binned to 2 $\mathrm{km\ s^{-1}}$ channels to increase the signal to noise ratio.

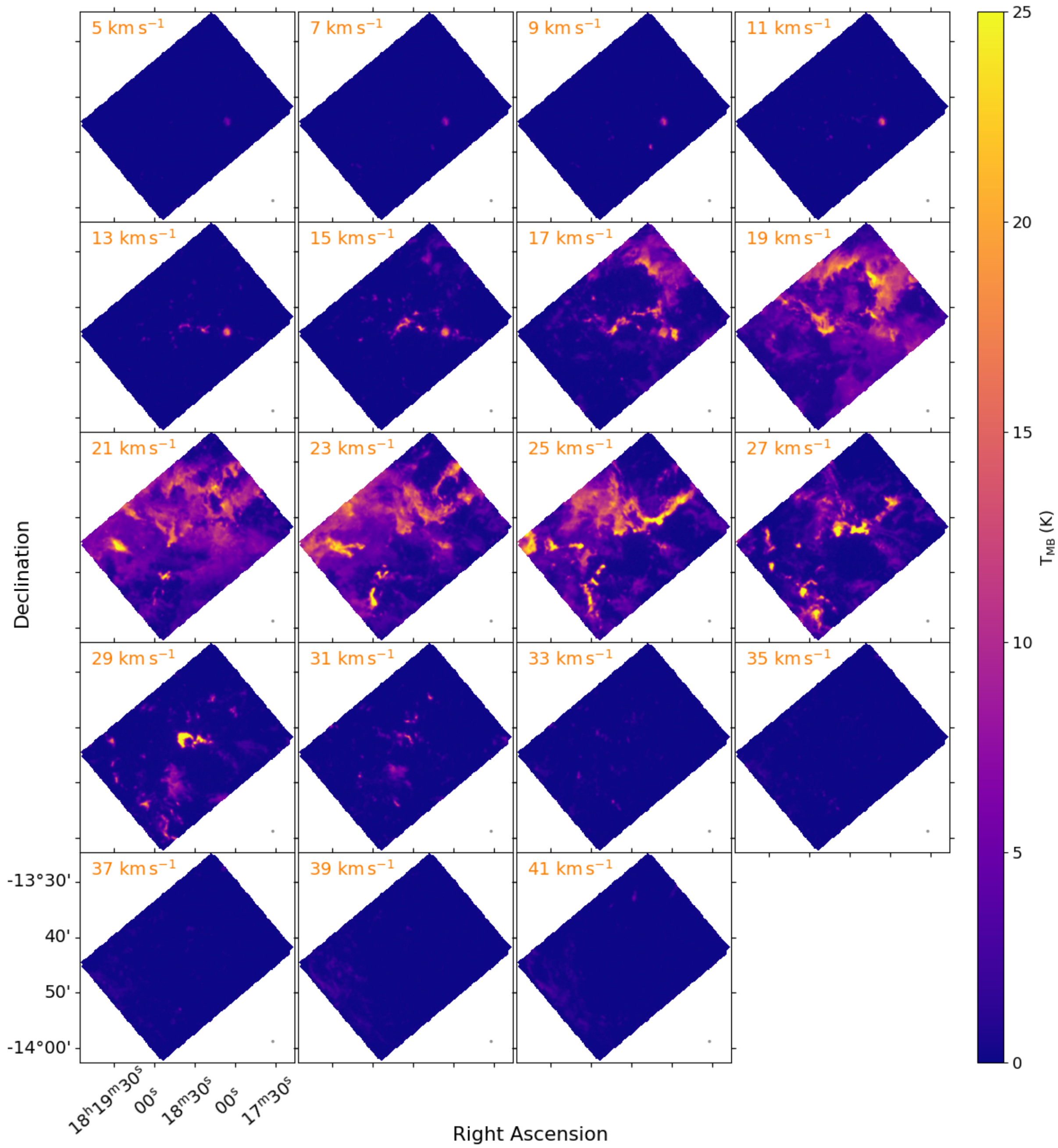

Figure 3.6 ^{12}CO(J=3–2) line channel maps. Similar setup to Figure 3.5. Data are presented at the original $\sim$20$''$ resolution and binned to 2 $\mathrm{km\ s^{-1}}$ channels.

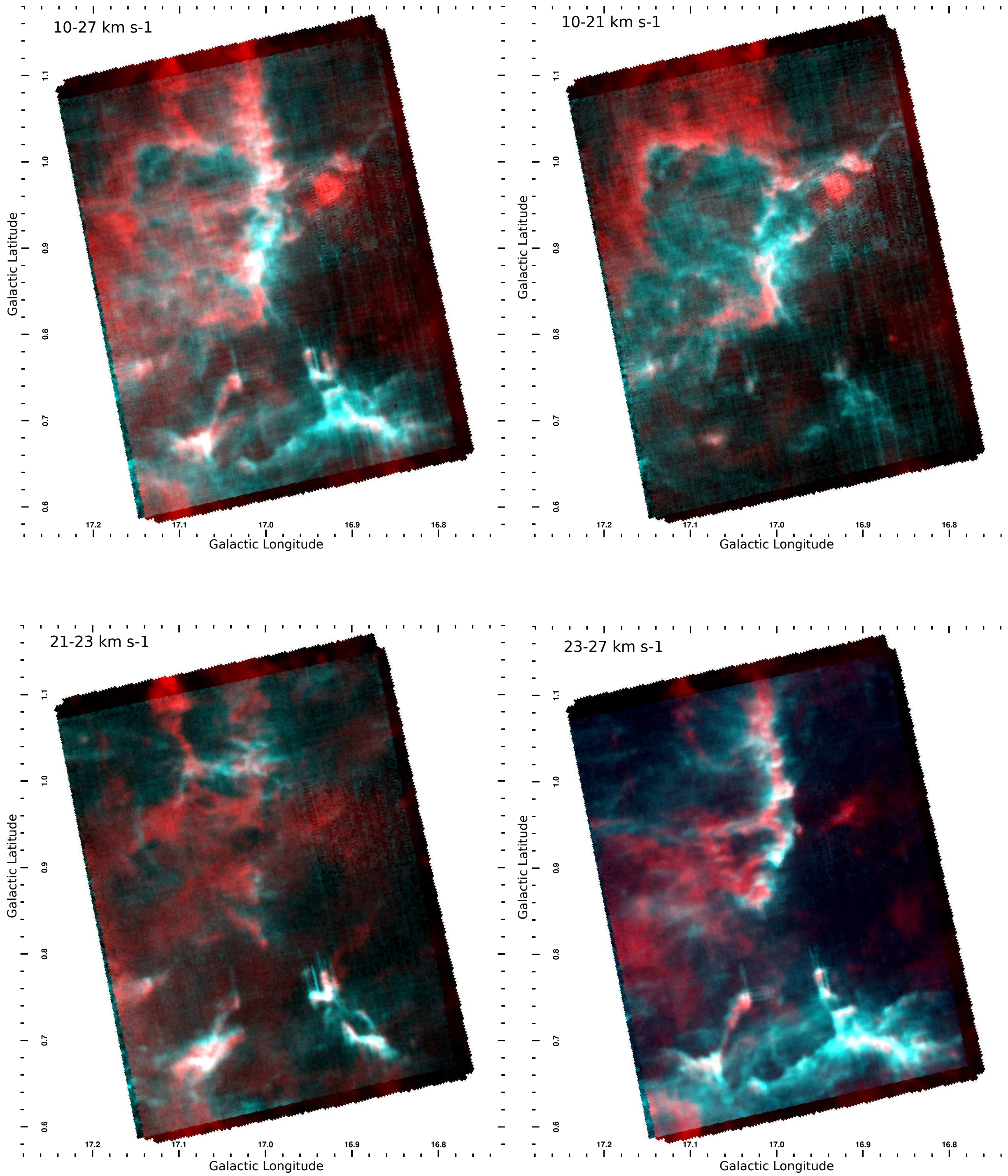

Figure 3.7 Color composites showing [C II] and ^{12}CO(J=3–2) integrated within four different velocity intervals. Velocity intervals are labeled in the top-left corners. CO is shown in red and [C II] in cyan.

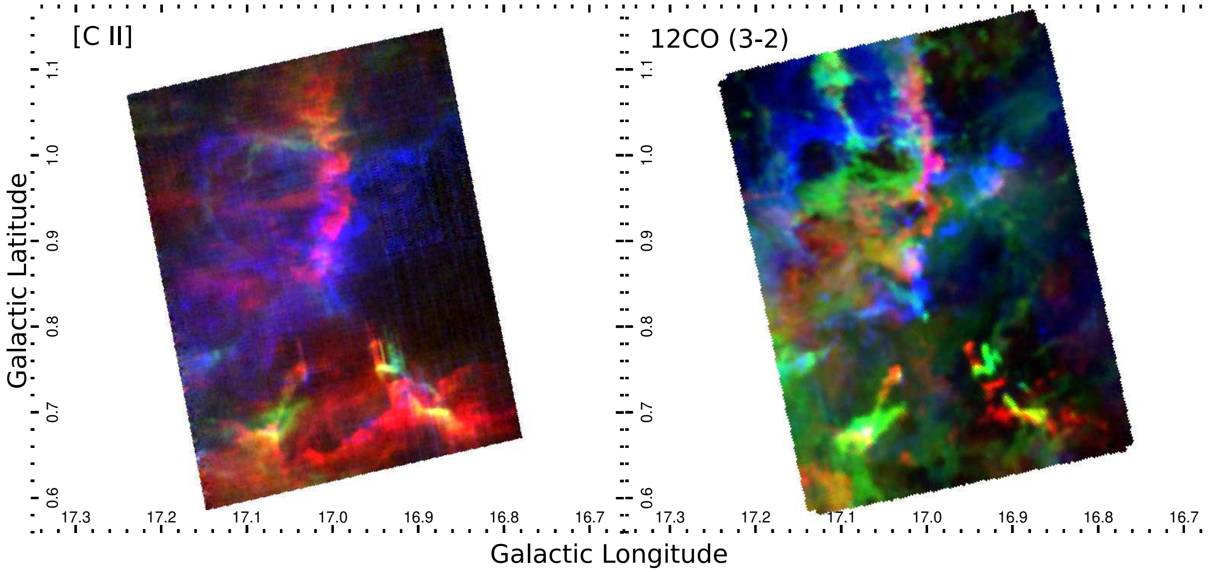

Figure 3.8 Velocity RGB composites made from [C II] (left) and ^{12}CO(J=3–2) (right) observations. Blue, green, and red show $\mathrm{V_{LSR}} = 10$–21, 21–23, and 23–27 $\mathrm{km\ s^{-1}}$ respectively.

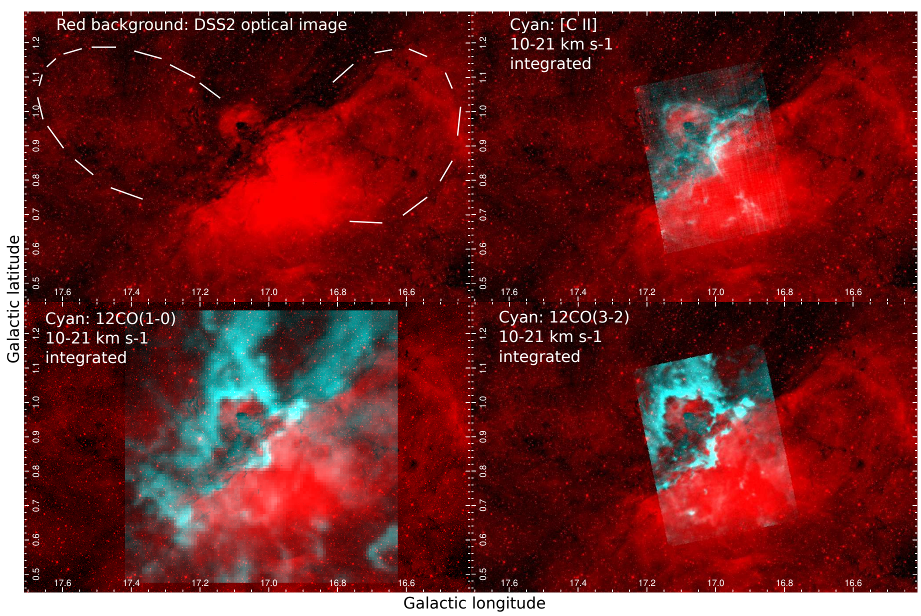

Figure 3.9 Optical DSS2 red filter in the red color in all four panels. Images are aligned to Galactic coordinates with $+b$ up and $+l$ to the left and all four panels are matched to the same angular scale. The dashed white lines in the top left panel outline the lobes seen in the infrared images. The right lobe is filled with optical emission, and the left lobe is optically dark. The cyan overlays show the [C II] in the top right, ^{12}CO(J=1–0) in the bottom left, and ^{12}CO(J=3–2) in the bottom right panels. The overlays show each line integrated between $\mathrm{V_{LSR}} = 10$–$21\ \mathrm{km\ s^{-1}}$ to highlight the Northern Cloud's coincidence with the optical absorption blocking the left lobe.

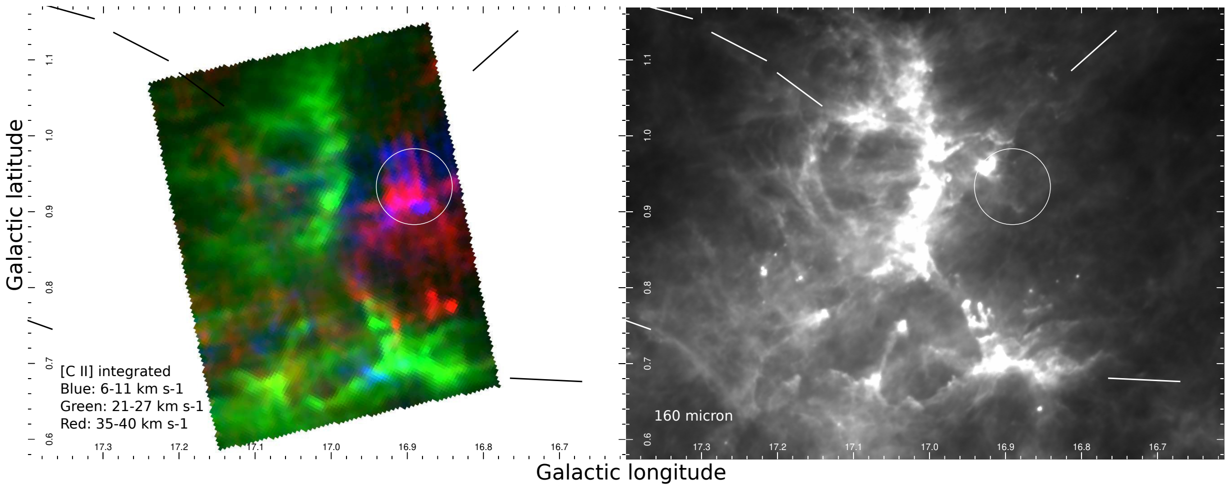

Figure 3.10 Left panel: Color composite showing [C II] integrated intensities in three velocity intervals. Blue, green, and red show $\mathrm{V_{LSR}} = 6$–11, 21–27, and 35-40 $\mathrm{km\ s^{-1}}$, respectively. The blue and red velocity intervals highlight the detected foreground and background fragments of the expanding shell. Right panel: the same field at 160 μm for reference. The lobes, which extend outside the field shown here, are marked in both panels with white or black dashed lines near the corners of the field. The white circle in both panels shows the area from which the spectrum in Figure 3.16 is extracted.

3.4.3 N19

The N19 ring appears as a thin ∼2 pc radius ring with a smooth interior in the mid-to-far IR, out to 160 μm, and in [C II]. CO and 250–850 μm trace a thicker ring with a jagged, clumpy interior with a radius ∼0.5 parsec larger than the mid-IR ring. The wider molecular ring appears in absorption in the mid-IR (Figure 3.12) and must be cold.

The infrared ring is traced by the [C II] line between $\mathrm{V_{LSR}} = 17$–18.5 $\mathrm{km\ s^{-1}}$ and reappears at ∼21.5 $\mathrm{km\ s^{-1}}$. Spectra towards the northeast part of the ring show a self-absorption signature at 19 $\mathrm{km\ s^{-1}}$ as seen in Figure 3.13, so there must be a temperature gradient in the PDRs around N19 and the Northern Cloud. Figure 3.13 shows a [C II] spectrum from a nearby part of the Northern Cloud which peaks at 19 $\mathrm{km\ s^{-1}}$. The CO ring peaks around 19–20 $\mathrm{km\ s^{-1}}$ and may be associated with colder PDR.

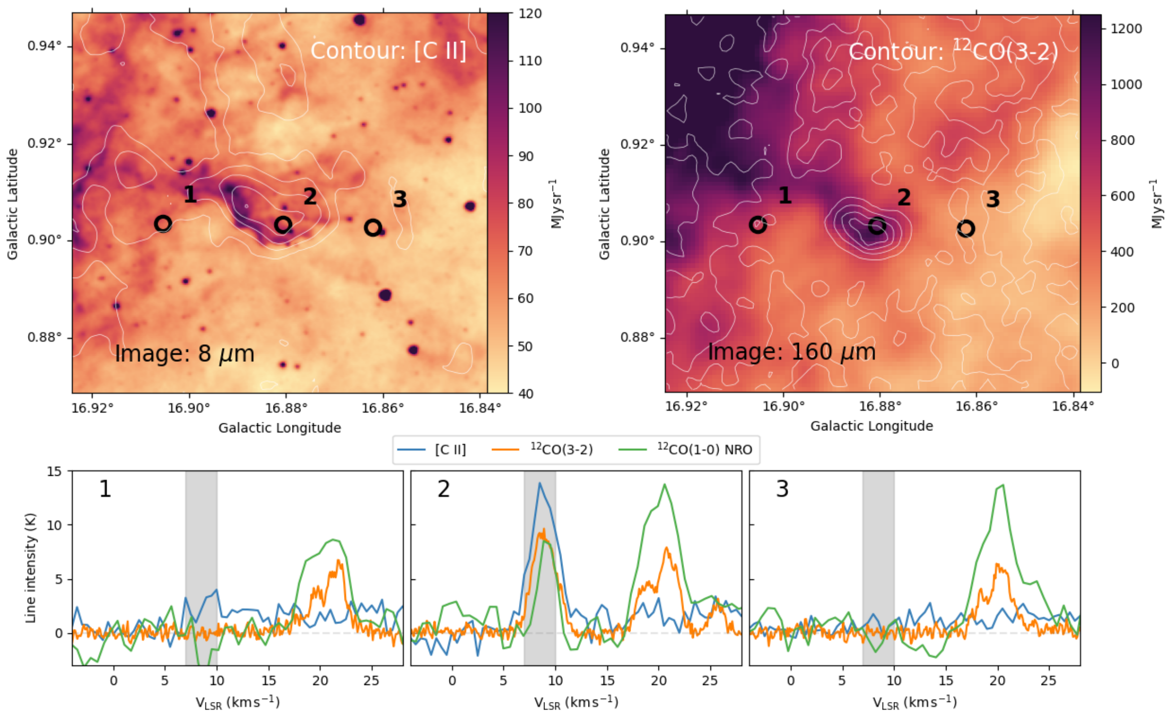

Figure 3.11 Infrared images and [C II] and CO spectra highlighting the blueshifted clump, the only shell fragment detected in CO, on the edge of the opening of the western cavity. The two images on top show a zoom-in on the blueshifted clump at 8 and 160 μm. The three circles mark three positions from which we extract spectra. One position lies towards the clump and two lie to each side for comparison. The contours are [C II] (left) and ^{12}CO(J=3–2) (right) intensities integrated between $\mathrm{V_{LSR}}$ = 7–10 $\mathrm{km\ s^{-1}}$. The spectra on the bottom are extracted at the positions numbered 1–3. [C II] spectra and ^{12}CO (J=1–0) and (J=3–2) spectra are shown. We show the Nobeyama CO (J=1–0) observations since the 20$''$ beam is similar to that of the APEX CO (J=3–2) data. The [C II] contours and spectra are both shown at the CO (J=3–2) beam. A clear line associated with the blueshifted clump appears around 8–9 $\mathrm{km\ s^{-1}}$, well separated from the diffuse 20–25 $\mathrm{km\ s^{-1}}$ emission.

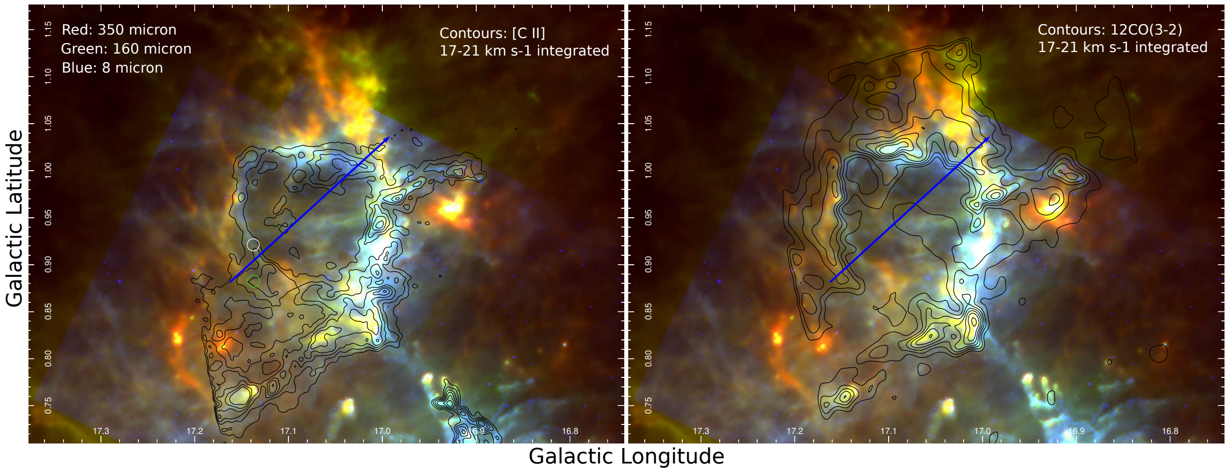

Figure 3.12 Infrared and millimeter view of the N19 ring. The color composite shown in both panels is 350 μm in red, 160 μm in green, and 8 μm in blue. Contours show [C II] (left) and ^{12}CO(J=3–2) (right) integrated between $\mathrm{V_{LSR}} = 17$–$21\ \mathrm{km\,s^{-1}}$. [C II] contours mark 18, 24 30, 36, 42, and 48 K $\mathrm{km\,s^{-1}}$. CO contours mark 20, 30, 40, 50, 60, 70, and 80 K $\mathrm{km\,s^{-1}}$. The white and green circles in the left panel mark the areas from which the spectra in Figure 3.13 are taken. The blue arrow in both frames shows the path for the PV diagram in Figure 3.14.

The signature of half an expanding shell moving towards the observer appears inside the ring in [C II] at $\mathrm{V_{LSR}} \lesssim 17\ \mathrm{km\,s^{-1}}$ and reaches a velocity of $\sim$13 $\mathrm{km\,s^{-1}}$ at the center of the ring. It appears in the position-velocity (PV) diagram in Figure 3.14 as an arc deflecting downward, marked with a line. A redshifted counterpart is not confirmed in either [C II] or CO, but due to the confusion with the Bright Northern Ridge and other natal cloud emission, we cannot rule out its existence. The PV diagram shows a high velocity $\mathrm{V_{LSR}} \gtrsim 28\ \mathrm{km\,s^{-1}}$ feature co-located with the foreground shell which may be interpreted as the red-shifted side of the shell, but the channel maps in Figure 3.5 reveal the feature to be $\sim$0.5 pc across, smaller than the shell, and likely unrelated.

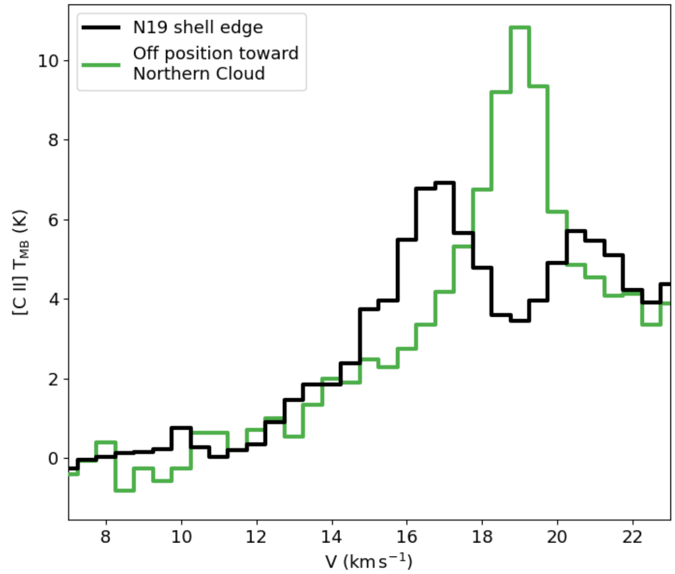

Figure 3.13 [C II] spectra towards and off the edge of the N19 PDR shell showing possible signs of self-absorption. The black spectrum towards the shell edge dips near 19 $\mathrm{km\ s^{-1}}$, and the nearby Northern Cloud spectrum in green peaks close to that velocity. The black and green spectra are taken from the white and green circles, respectively, marked in Figure 3.12.

3.5 Geometry

3.5.1 The Natal Cloud and M16 Cavity

In Section 3.3 we discuss the infrared structure of M16 and its appearance as an expanded H II region which is constrained along the axis of the GMF; this is summarized in the annotated chart in Figure 3.1. This projected appearance may arise from either a 3-dimensional bipolar H II region with two separate cavities or a single large ellipsoidal cavity, and we argue here for the latter case. Bipolar H II regions have been observed and studied throughout the Galaxy and form within molecular gas sheets. A separate cavity bursts out of each side of the sheet, while the H II region expansion is constrained in the plane of the sheet (see the diagrams in Figures 1 and 2 in Deharveng et al. 2015). Deharveng et al. (2015) describe one of the characteristic features of

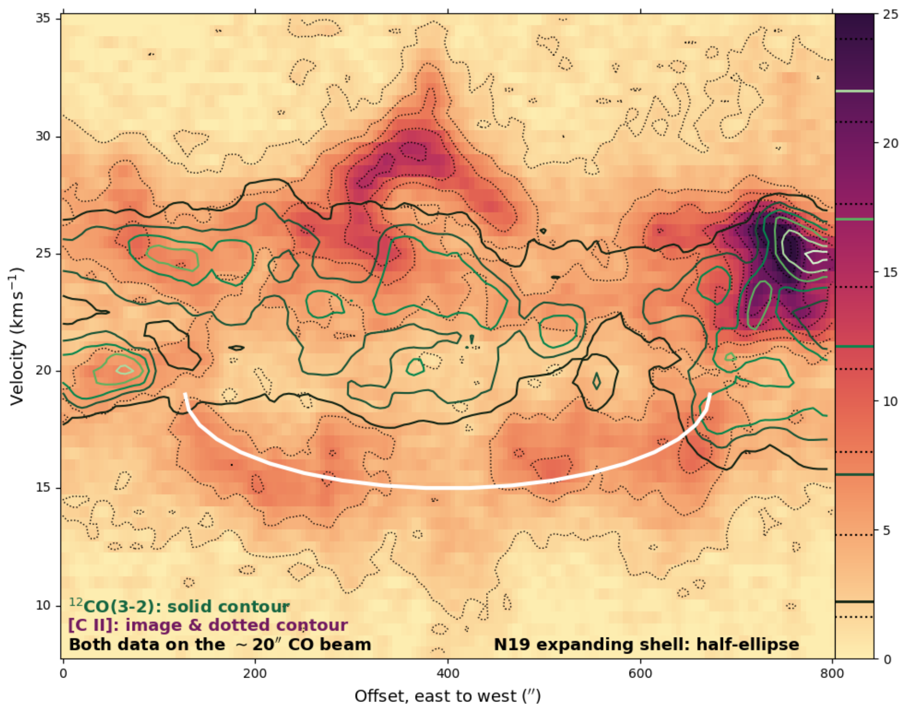

Figure 3.14 PV diagram showing [C II] in color image and ^{13}CO(J=3–2) in contours. The N19 ring appears in [C II] $\mathrm{V_{LSR}} < 21\ \mathrm{km\ s^{-1}}$ and the expanding $4\ \mathrm{km\ s^{-1}}$ foreground shell signature is marked with a white half-ellipse. The path along which this PV cut is taken is shown as a black arrow in Figure 3.12. Emission $\mathrm{V_{LSR}} > 23\ \mathrm{km\ s^{-1}}$ is mostly associated with the Bright Northern Ridge, and the $\mathrm{V_{LSR}} > 30\ \mathrm{km\ s^{-1}}$ emission is unrelated to N19, as discussed in the text.

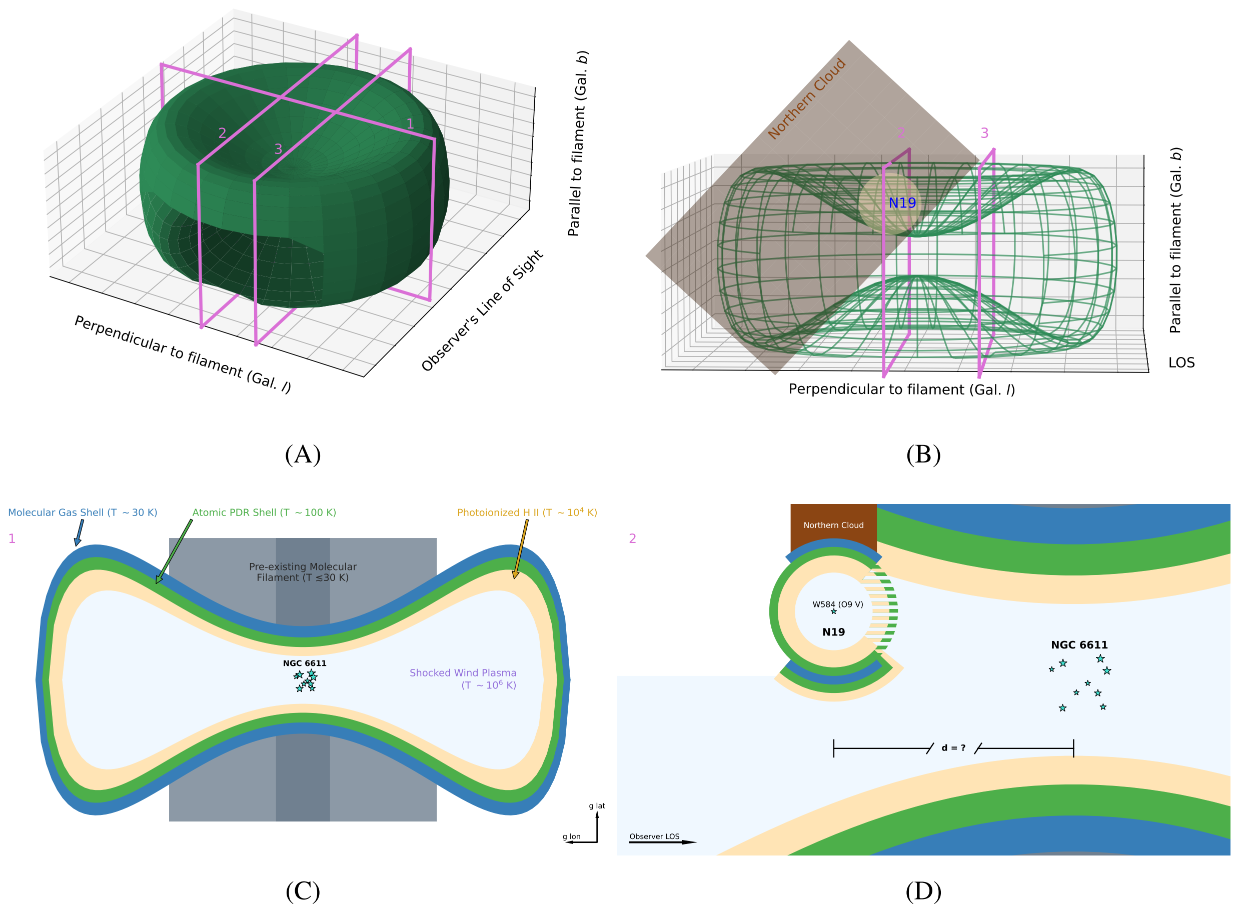

Figure 3.15 Four diagrams describing a simplified geometric picture of the shell. The top-left and top-right panels show a 3-dimensional schematic of the “biconcave disc” shape viewed from two different angles and with a solid and transparent wireframe surface respectively. The front side has been opened to show the inside of the shape as well as model how M16 may be broken open; observations suggest it is either broken or very thin towards the front and back. Pink frames numbered 1–3 outline the cross-cuts which are diagrammed in the lower-right (1) and lower-left (2) panels of this Figure and in the top panel of Figure 3.16 (3). The top-right panel shows the shell viewed approximately face-on from the observer’s perspective and includes a semi-transparent rectangular overlay representing the Northern Cloud, which obstructs the left lobe of the cavity, and a circle representing N19, both of which appear in the #2 cross-cut. The bottom-left panel shows cross-cut #1 marked in the top-right panel, along the plane of the sky. Gas phases and the exciting cluster, NGC 6611, are labeled. The bottom-right panel shows cross-cut #2, marked in the top two panels, which includes the Northern Cloud and N19. It is not determined whether N19 has an intact background shell, so that side is represented by a hashed surface. We do not detect a foreground or background molecular gas shell, so these are excluded from the diagram. The scale bar indicates that the physical separation between NGC 6611 and the Northern Cloud/N19 is unknown.

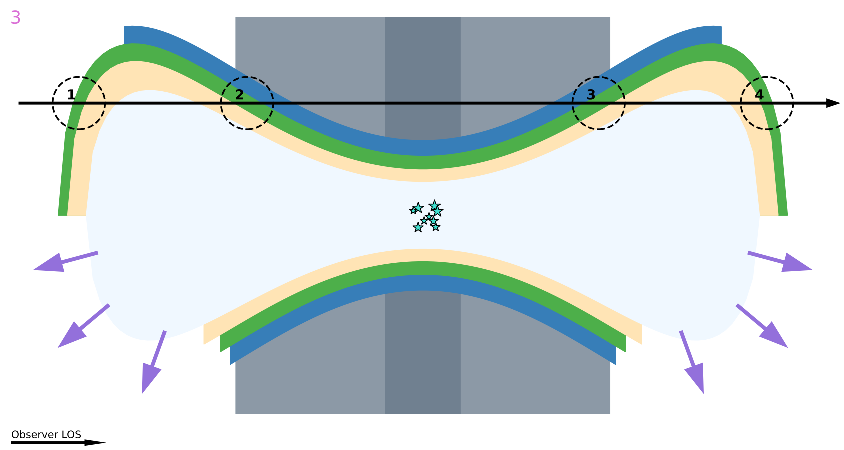

(A)

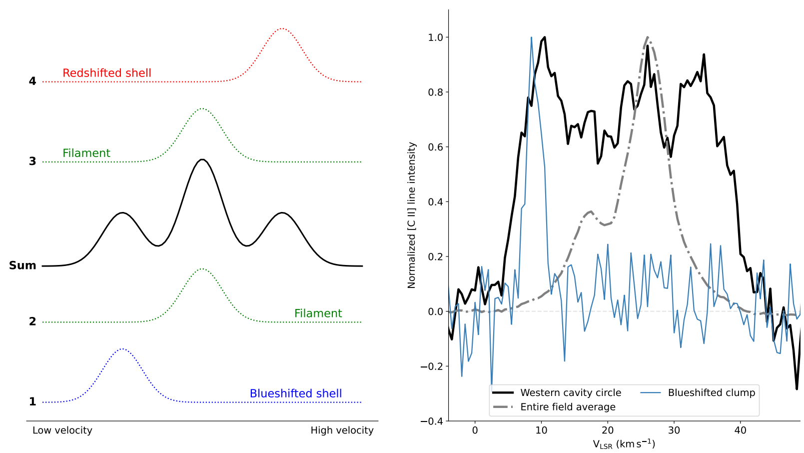

(B)

Figure 3.16 The top panel shows an observer's line of sight cross-cut through the M16 shell and cavity, marked as #3 in the 3-dimensional diagrams in Figure 3.15. The front and back of the shell are depicted as broken open. The black horizontal arrow through the top of the shell shows an observer's line of sight, and numbered black dashed circles mark where the line of sight crosses neutral PDRs which would radiate [C II] line emission. The bottom panels show a cartoon spectrum on the left and observed [C II] spectra on the right. The line of sight PDR crossings circled in the top panel would contribute the colored dashed-line spectrum components, numbered accordingly, in the cartoon spectrum. The solid black cartoon spectrum is the sum of the four component spectra, representing what would be observed. This is described in more detail in Section 3.5.1. The observed spectrum labeled "Western cavity circle" is from the circular region shown in Figure 3.10 towards the shell fragments. A spectrum towards the blueshifted clump, a notable shell fragment described in Section 3.4.2, is included. The average [C II] spectrum from the entire field is shown in dash-dotted gray to emphasize the natal cloud component near $\mathrm{V_{LSR}} = 25$—$26\ \mathrm{km\ s^{-1}}$. The observed spectra are consistent with our model.

bipolar H II regions as a ring of molecular gas in the plane of the sheet surrounding the cluster. Bonne et al. (2022) observes such a ring in CO in the bipolar H II region RCW 36.

Should we interpret the GMF as a sheet viewed nearly edge-on, we would expect a similar CO ring running vertically ($\pm b$) through the bright central region in front of and behind NGC 6611. This ring would be viewed nearly edge on so that it appears as two spatially overlaid but kinematically distinct filaments in projection. The foreground side of the ring would appear as an optical dark lane. We detect no such ring towards M16. Instead, the observer's line of sight is relatively unobstructed towards the exciting cluster. While the 19 $\mathrm{km\ s^{-1}}$ Northern Cloud lies in front of the cluster, it is too spatially extended to be the foreground half of a ring created by NGC 6611 and must instead be a separate cloud of gas, as described in Section 3.5.2. The GMF is more likely a true filament, not a sheet, based on these observations.

We propose the following 3-dimensional model, shown in Figure 3.15, for the large cavity created by feedback from NGC 6611. The GMF constrains cavity expansion towards and away from the Galactic plane, while relatively lower column density towards all other angles allows expansion. The result is an ellipsoidal or toroidal cavity. For the purpose of our diagram, we adopt a shape called the "biconcave disc," used in cell biology to describe the shape of the typical red blood cell (An et al., 2022) because it resembles our observations and has an analytical description that is easily plotted. Figure 3.15(C) shows a plane-of-sky cross-cut through the biconcave disc so that the cross-cut resembles on-sky observations of the infrared lobes. The full horizontal width of the cavity is $\sim$40 pc based on our observations, while the height of the cavity (at its tallest, off-center) is $\sim$12 pc; the diagrams are not to scale.

The simulations of star formation within a filament by Fukuda & Hanawa (2000) (see Figures 1 and 3 in their paper) show a similarly shaped cavity compressed along one axis by the filament. The simulations by Whitworth & Priestley (2021) indicate that recombinations at the surface of a dense filament can slow an encroaching ionization front and may even trap it if there is still accretion onto the filament, which may have been the case earlier in M16's history. Zamora-Avilés et al. (2019) find in their simulations that H II regions expand anisotropically, seeking out low density lines of sight and avoiding dense cores.

We describe in Section 3.4.2 the [C II] signature from the foreground and background PDR shell fragments. [C II] emission traces fragments rather than a complete shell, so the foreground shell surface must be thin ($A_V \lesssim 0.5$; Section 3.8.1) or broken. We illustrate the 3-dimensional shell model as broken open in the front in Figure 3.15 and we diagram an observer's line-of-sight cross-cut through the western cavity, where the [C II] shell fragments are detected, in Figure 3.16. Purple arrows show escaping shocked-wind plasma in Figure 3.16, whose large sound speed allows it to wrap around the region quickly compared to the dynamical timescale of the cavity. The background side of the cavity is obscured in the spectroscopically unresolved images by the bright mid-ground emission, and it is faint in [C II] like the foreground side. For lack of more detailed information, we assume symmetry in our model.

A black arrow representing an observer's line of sight passes through the partial foreground/background of the shell in the top panel of Figure 3.16. This line of sight passes through the neutral atomic PDR, colored green in the diagram, 4 times, marked with black dashed circles and numbered. The #1 and #4 PDR crossings should be blueshifted and redshifted, respectively, since the cavity can easily expand in those directions. The #2 and #3 PDRs are on the surface of the dense filamentary gas of the natal cloud and should not be so easily accelerated by stellar feedback due to the mass behind them, so we argue that both of these sections of PDR should share the velocity of the filament and therefore be kinematically indistinguishable from each other. We diagram the resulting spectrum from these four PDR crossings in the bottom-left panel of Figure 3.16 and compare to the observed [C II] spectrum through the western cavity in the bottom-right panel. The observed spectrum has a middle velocity component at $\mathrm{V_{LSR}} \sim 25\ \mathrm{km\,s^{-1}}$ which matches the natal cloud component which dominates the dash-dotted grey line in the same Figure. We show integrated [C II] intensity maps of the blue- and red-shifted shell fragments compared to the central component in the color composite in Figure 3.10, and we mark the lobes on the [C II] composite and the 160 μm image for reference. The [C II] shell fragments appear inside the cavity, but do not fill it, consistent with our conclusion that it has broken open.

The DSS2 red optical image in Figure 3.1 shows optical emission running down from the center of the H II region towards the Galactic plane approximately along the filament. Should optical emission be able to escape the cavity from the foreground break in the shell in Figure 3.16, it could illuminate and reflect off filament-associated gas below the cavity. The real filament would not terminate at a sharp edge as drawn in the diagram, but instead density would continue to drop off for some distance comparable to the extent of the cavity.

The Pillars of Creation, Spire, and a handful of other pillars are not depicted in our diagrams. Their presence fits well into this model: gas near the central axis of the filament is dense and clumpy. As dense-enough clumps within the filament are revealed by the ionization front, they are sculpted into pillars whose tails face away from the illuminating stars. Since these are remnants of the dense natal cloud, they are more likely to be found along the filamentary axis like the Pillars of Creation and the Spire, both of which are connected to branches of the dense filament. Close inspection of the 8 μm map reveals a number of pillar-like structures which all point back towards the stars and are kinematically associated with larger associations of gas.

3.5.2 Northern Cloud and N19

The Northern Cloud lies between the filament and the observer, obstructing optical emission from the H II region as demonstrated in Figure 3.9. It spans some tens of parsecs, much of which is un-illuminated by NGC 6611, as indicated by the PMO CO observations compared to the 8 μm. The CO (J=1–0) observations, which cover a larger area than the [C II] and CO (J=3–2), show that it extends towards higher Galactic latitude. The Northern Cloud, at $\sim$19 $\mathrm{km\,s^{-1}}$, forms a curtain of molecular gas which blocks much of the H II region from view in the optical but does not obstruct [C II], 8 μm, 24 μm and radio free-free emission, which trace PDRs and H II gas behind the Northern Cloud. The edge of the Northern Cloud facing the NGC 6611 cluster is itself a PDR, which indicates that the Northern Cloud is close to the cluster and influenced by its feedback as explained in Sections 3.3 and 3.4.1.3.

We summarize this geometry in panels B and D of Figure 3.15. In panel B, we represent the Northern Cloud as a rectangle in front of the left lobe of M16. We diagram a cross-cut through M16, the Northern Cloud, and N19 in panel D. The Northern Cloud is simultaneously illuminated from within by N19's central star and from below and behind by NGC 6611; it is not a distant foreground feature, but rather an additional cloud influenced by NGC 6611 feedback.

We detect a foreground expanding shell towards N19, but we are prevented by confusion with the Bright Northern Ridge and natal cloud emission from detecting or ruling out a background expanding shell or any PDR which could be the back face of the bubble. We represent the back face of the bubble in Figure 3.15D with a hashed line. The influence of NGC 6611 on the shape of N19 is clear from observations as the on-sky projected N19 ring is flat on the side facing the cluster, as shown in Figure 3.9. The line-of-sight separation between NGC 6611 and the Northern Cloud/N19 is not constrained by our observations but they must be close enough (within ∼10 pc or so) that NGC 6611's influence is felt. We indicate this uncertainty using the scale bar in the left panel of Figure 3.15B.

3.6 Column Densities and Masses

3.6.1 CO Column Densities

We estimate ^{13}CO(J=1–0) column densities using the observations of Xu et al. (2019) and the same method as Tiwari et al. (2021) and Karim et al. (2023), in which excitation temperature is obtained from the peak ^{12}CO(J=1–0) brightness in the relevant velocity interval. We adopt the isotopic ratio $^{12}\mathrm{CO}/^{13}\mathrm{CO} = 44.65$ derived for the galactocentric radius $D_{\mathrm{GC}} = 6.46$ of M16 by Karim et al. (2023), use the abundance ratio $^{12}\mathrm{CO}/\mathrm{H}_2 = 8.5 \times 10^{-5}$ Tielens (2021) to convert CO column densities to $N(\mathrm{H}_2)$, and convert to mass using a mean molecular weight $\mu = 2.66$.

The N19 ring and the Bright Northern Ridge are particularly bright in CO(J=3–2) and must be dense, so we use both CO transitions to derive both column density and number density here. As the CO J=3–2 and J=1–0 transitions have very different optical depths and critical densities, column densities require a coupled excitation and radiative transfer treatment. We have used the Radex radiative transfer software (van der Tak et al., 2007) to model line emission from the ^{13}CO (J=3–2) and (J=1–0) and C^{18}O(J=1–0) transitions. This method frees us from the assumption of local thermodynamic equilibrium (LTE), which is implicit in the technique described above. We apply a method which relies on the assumption that excitation conditions are constant throughout a given feature, so we must use this method on coherent gas features. Since we use C^{18}O, there is an additional constraint that this faint line must be detected. The

Feature Name	n Radex (cm^{-3})	$N(\mathrm{H_2})$ Radex (cm^{-2})	$N(\mathrm{H_2})$ ^{13}CO(J=1–0) LTE (cm^{-2})	$N(\mathrm{H_2})$ 70, 160 μm (cm^{-2})	$N(\mathrm{H_2})$ 160–500 μm (cm^{-2})
Bright Northern Ridge	$8.9^{+3.7}_{-3.3} \times 10^3$	$7.1^{+5.5}_{-2.1} \times 10^{21}$	$1.0 \pm 0.5 \times 10^{22}$	$3.1 \pm 2.2 \times 10^{22}$	$2.2 \pm 1.3 \times 10^{22}$
N19	$5.6^{+2.3}_{-1.6} \times 10^3$	$1.1^{+0.7}_{-0.4} \times 10^{22}$	$1.6 \pm 0.5 \times 10^{22}$	$2.2 \pm 1.5 \times 10^{22}$	$1.9 \pm 0.9 \times 10^{22}$

Table 3.1 Density and column density for the Bright Northern Ridge and N19. Density and the leftmost column density are derived using Radex. Uncertainties from the Radex fit are asymmetric so the upper and lower error bars are given as superscripts and subscripts, respectively. The remaining columns list the mean $\pm$ standard deviation of the column densities derived toward each feature using the other methods discussed in the text. The mean and standard deviation are calculated from within the same mask as the Radex fits. All column densities are expressed as $N(\mathrm{H_2})$. The Radex and CO LTE measurements are made at the PMO resolution, while the two FIR dust emission measurements are made at higher resolutions and so vary more within the mask.

N19 CO ring and Bright Northern Ridge fulfill these criteria, so we derive column density and number density towards these two features using our Radex analysis. We use the LTE ^{13}CO(J=1–0) column density method everywhere else.

We use Radex to calculate emission for these transitions using assumed excitation conditions: kinetic temperature T_{K}, total hydrogen column density $N(\mathrm{H_2})$, and gas density n. The transformations from $N(\mathrm{H_2})$ to ^{12}CO and ^{13}CO column density are given above. We adopt the isotopic ratio ^{12}CO/C^{18}O $= 417$ (Wilson & Rood, 1994). We compare an ensemble of measurements from the gas feature (either the N19 ring or the Bright Northern Ridge) at the appropriate velocity interval to modeled emission at a variety of excitation conditions. A solution is determined for each set of measurements (the three CO transitions toward one line of sight, i.e. one pixel), and the median solution is taken from the ensemble of measurements (all pixels towards the gas feature). The method is described in detail in Appendix C.2.

The two ^{12}CO transitions are inconsistent with each other at any given kinetic temperature; T_{K} can be tuned to make either one agree with the three other measurements, but never both. ^{12}CO(J=1–0) measurements require T_{K} to be $\sim$5 K higher than ^{12}CO(J=3–2), which in turn means that ^{12}CO(J=1–0) leads to lower $N(\mathrm{H_2})$ and n solutions than ^{12}CO(J=3–2). A combination of line-of-sight variability and differing optical depths cause the two optically thick transitions to be sensitive to different layers of gas with different excitation conditions. Instead of choosing one of the optically thick ^{12}CO lines to set the temperature, we maintain $T_{\mathrm{K}} = 30$ K for all solutions. We tested the stability of the solutions under temperature variation between 20–40 K and find an inverse relationship between assumed T_{K} and the n solution. The column density solution is less sensitive. Temperature-driven variation in both solution parameters is comparable to their estimated uncertainties when $T_{\mathrm{K}} = 30$ K is assumed.

Column densities derived from the ^{13}CO(J=1–0) transition under LTE tend to agree with the column densities derived using the Radex grid method. Both of these agree within a factor of $\sim$2 with column densities derived from FIR dust emission; dust-derived $N(\mathrm{H_2})$ are larger than CO-derived $N(\mathrm{H_2})$. Average column densities from each of these techniques are given for N19 and the Bright Northern Ridge in Table 3.1.

3.6.2 C$^+$ Column Densities

We calculate the column density of N_{H} associated with C$^+$ using the [C II] line using the method described by Karim et al. (2023).

We detect the $F = 2 - 1$ [^{13}C II] line ($+11.2\ \mathrm{km\ s^{-1}}$ relative to the [C II] line; Cooksy et al. 1986; Guevara et al. 2020b; Ossenkopf et al. 2013) only toward IRAS 18156–1343 within the Bright Northern Ridge. The integrated [^{13}C II] intensities are shown in contour in Figure 3.17 and spectra are shown in red in Figure 3.18. The [^{13}C II] spectra are scaled up by the factor α/s_F, where α is the assumed carbon isotopic ratio 44.65 (Karim et al., 2023) and s_F is the hyperfine transition strength coefficient 0.625 for the $F = 2-1$ line (Guevara et al., 2020b, in their Table 1). Estimated $T_{\rm ex}$ (described below) reaches nearly 150 K in a small area surrounding the source.

Since [^{13}C II] is only detected toward the IRAS source, that spectrum is likely not representative of the entire region. The source is associated with higher optical depth [C II] emission, up to $\tau = 2.2$ as shown in Figure 3.18. For the rest of the [C II] emission, we apply the methodology developed by Okada et al. (2015) and used by Karim et al. (2023). To calculate $T_{\rm ex}$, we use the same $\tau < 1.3$ upper limit on optical depth as Karim et al. (2023). This is close to the typical upper limit calculated toward bright lines of sight south of the Pillars and along the Bright Northern Ridge.

We calculate $T_{\rm ex}$ for the Northern Cloud and natal cloud velocity intervals separately. For the $\rm V_{LSR} \sim 23$–$27\ \rm km\,s^{-1}$ natal cloud emission, we assign $T_{\rm ex} = 120$ based on the maximum $T_{\rm ex}$ calculated using $\tau = 1.3$ towards the southern PDR ridge as well as the Bright Northern Ridge. We let $T_{\rm ex}$ exceed 120 K in the small area surrounding the IRAS source, assigning to each pixel the $T_{\rm ex}$ calculated from its peak line intensity assuming $\tau = 1.3$. We assign $T_{\rm ex} = 67$ K for gas between $\rm V_{LSR} = 10$–$21\ \rm km\,s^{-1}$ based on the maximum observed brightness towards the Northern Cloud and N19.

Column densities of $\rm C^+$ are converted to $N_{\rm H}$ using the C/H abundance ratio 1.6×10^{-4} Sofia et al. (2004). We find typical column densities $N_{\rm H} \sim 3$–6×10^{21} cm^{-3} towards most places and $N_{\rm H} \sim 1$–2×10^{22} cm^{-3} towards sites of bright [C II] emission, including around IRAS 18156–1343.

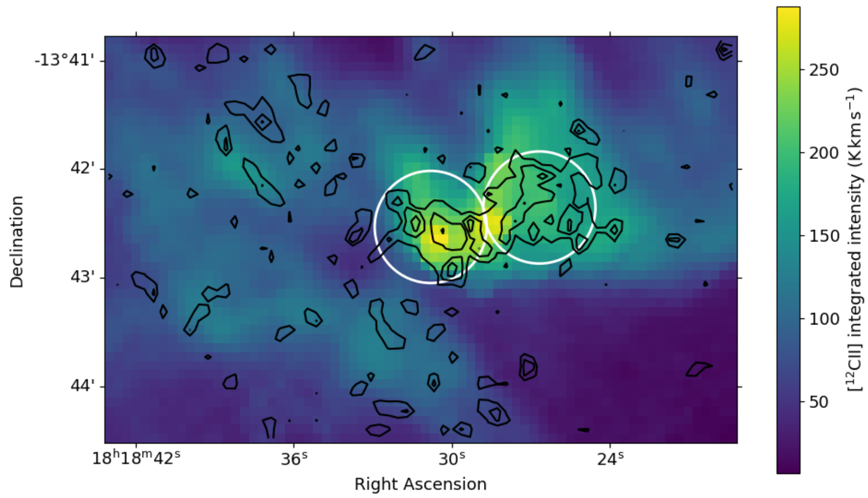

Figure 3.17 Color image shows the [C II] intensities integrated between $\mathrm{V_{LSR}} = 26$–$31\ \mathrm{km\,s^{-1}}$. Contours show the [^{13}C II] emission integrated within the same interval. Circles show the two regions in which spectra are averaged for Figure 3.18. Each circle is 4 [C II] beams across. The emission from within the left circle is $\sim 1\ \mathrm{km\,s^{-1}}$ higher velocity than that from the right circle. The brightest [C II] emission locations are slightly offset from the [^{13}C II] emission locations.

Feature Name	Atomic ($M_\odot$)	Molecular ($M_\odot$)	Molecular Entire field ($M_\odot$)
Natal cloud	4.1×10^3	1.3×10^4	2.4×10^4
Bright Northern Ridge	6.2×10^2	1.3×10^3	...
Intermediate molecular gas	...	1.5×10^4	2.7×10^4
Northern Cloud	1.9×10^3	1.7×10^4	3.3×10^4
N19	6.5×10^2	4.2×10^3	...

Table 3.2 Mass estimates towards features in M16 within their relevant velocity intervals. Atomic gas column density is derived using [C II] and molecular gas is derived from ^{13}CO(J=1–0) using the LTE method. The Northern Cloud is defined between $\mathrm{V_{LSR}} = 10$–$21\ \mathrm{km\,s^{-1}}$. The natal cloud is defined between 21–27 $\mathrm{km\,s^{-1}}$ for the atomic gas and between 23–27 $\mathrm{km\,s^{-1}}$ for the molecular gas. Intermediate gas is defined between 21–23 $\mathrm{km\,s^{-1}}$ for molecular gas only, as [C II] emission in that interval is from line wings of Northern Cloud or natal cloud emission. The N19 and Bright Northern Ridge masses are integrated from within appropriate masked regions, while natal cloud, intermediate gas, and Northern Cloud masses are all integrated over the entire observed [C II] field. The CO (J=1–0) observations cover a wider field than the [C II], so we give molecular masses integrated over the [C II] field only (third column) and over the entire CO observed field (fourth column).

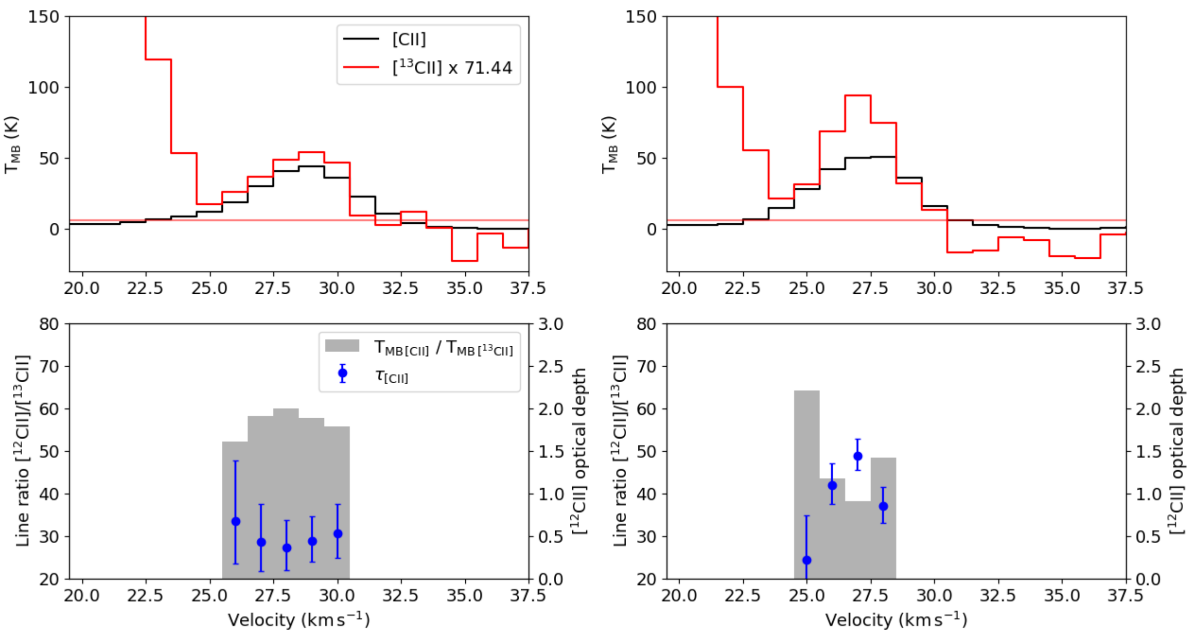

Figure 3.18 The top two panels show [C II] (black) and [^{13}C II] (red) spectra averaged within the two circles in Figure 3.17; the left circle's spectra are on the left here. The step plots show spectra binned to 1 km s^{-1} channels. The [^{13}C II] spectra are scaled up by the factor α/s_F, described in the text, and shifted by -11.2 km s^{-1} to account for the [^{13}C II] rest frequency. The horizontal line shows the 1 σ level for [C II] scaled up by α/s_F and adjusted for the number of averaged spectra. Note that the lower velocity side of the [^{13}C II] line overlaps with the relatively bright high velocity line wing of the [C II] line. The bottom panels show the [C II]/ [^{13}C II] ratio (grey bars) and the [C II] optical depth and associated uncertainty (blue points). We exclude channels where [^{13}C II] is below 1 σ or where [C II] $T_{\rm MB}$ exceeds the adjusted [^{13}C II] $T_{\rm MB}$. This figure is based on those by Guevara et al. (2020b).

Selected stars	$L_{\rm bol}$ ($L_\odot$)	$L_{\rm FUV}$ ($L_\odot$)	$L_{\rm mech}$ ($L_\odot$)	Q ($\rm s^{-1}$)	$M_{\rm total}$ ($M_\odot$)
NGC 6611 S	2.33×10^6	1.04×10^6	4.06×10^3	8.43×10^{49}	385
NGC 6611 H	1.53×10^6	9.06×10^5	1.94×10^3	6.25×10^{49}	235
N19 O9 V	5.25×10^4	3.14×10^4	1.84	7.43×10^{47}	18

Table 3.3 The first two rows give the estimates of the NGC 6611 cluster feedback capacity using the Stoop et al. (2023) and Hillenbrand et al. (1993) catalogs under the filter criteria described in the text. The "NGC 6611 S" row in this table uses stars marked "S" in the last column of Table C.1, and so for "H" The third row gives the estimates for the O9 V star driving N19. Columns list bolometric, FUV (6–13.6 eV), and mechanical (wind kinetic) luminosities, H-ionizing photon emission rate Q, and total stellar mass.

3.7 NGC 6611 Feedback Capacity

The NGC 6611 cluster, with a handful of O-type stars at its core, powers the M16 H II region. In order to estimate the ionizing radiation and stellar wind output of the cluster, we apply the `scoby` code, described by Karim et al. (2023), to observed catalogs of NGC 6611. These feedback capacity estimates can be compared to observed gas motions to gauge the feedback coupling efficiency.

Table 3.3 gives the total mass loss rate, mechanical energy injection, momentum transfer rate, FUV luminosity, and ionizing photon flux for the selected stars from each catalog. Feedback capacity estimates from the two NGC 6611 catalogs agree fairly well. The catalog compiled by Stoop et al. (2023) produces slightly larger mechanical and radiative luminosities on account of the earlier spectral types. Binarity has a lesser effect since the companions tend to be late-O or B types. We adopt the spectral types from the Stoop et al. (2023) catalog and the resulting feedback capacity values for the remainder of this study.

The total NGC 6611 cluster mass is approximately $\sim 2 \times 10^4$ $M_\odot$ (Pfalzner, 2009), about half as massive as the Westerlund 2 cluster which powers RCW 49 (Tiwari et al., 2021; Zeidler et al., 2021). Westerlund 2, over its similar ∼2 Myr lifespan, has emitted $\sim 6 \times 10^{51}$ ergs in its winds (or as little as 1/10$^{\rm th}$ if clumpy; Puls et al. 2008) and has a total FUV brightness of $\sim 4 \times 10^6\ L_\odot$.

N19 is driven by a single O9 V star named W584 (Guarcello et al., 2010b) whose type is given in the catalogs by Hillenbrand et al. (1993) and Evans et al. (2005) (via Stoop et al. 2023). This star is outside the 2.5 pc search radius from NGC 6611 and so is not double-counted in our feedback estimates. Table C.1 lists its position and catalog identification and Table 3.3 lists feedback capacity estimates.

3.8 Energetics

3.8.1 M16

The western lobe of the M16 cavity, which opens up west of the Pillars of Creation, is associated with shell fragments traced by [C II] and expanding at ± 10 km s^{-1} with respect to the natal cloud $V_{\rm LSR} \approx 25$–26 km s^{-1} emission. Integrated [C II] emission maps in Figure 3.10 show these fragments located inside the infrared lobes. We assume that the infrared lobes and the ± 10 km s^{-1} [C II] shell fragments all trace the same large shell based on our geometrical picture of the region discussed in Section 3.5.1. These fragments are detected in [C II] but not in CO, with the exception of the ∼20 $M_\odot$ blueshifted clump.

The line-of-sight expansion velocity estimate of ∼10 km s^{-1} suggests that, over the ∼2 Myr lifespan of the cluster, the cavity could have expanded ∼20 pc from the cluster core. Since the inclination of these shell fragments is not known, their projected line-of-sight velocities are lower limits. Nevertheless, this matches the ∼20 pc on-sky projected $\pm l$ widths of the infrared lobes.

The lobes are smaller in the $\pm b$ direction, $\sim$10 pc; this is also the direction along which the GMF extends. We suggest that the cavity is expanding at $\sim$10 $\mathrm{km\ s^{-1}}$ in all directions perpendicular to the $\pm b$-extended filament and is restricted along the filament.

We place an upper limit on the mass in this large cavity shell using our non-detection of [C II] and CO towards the western cavity and an assumption about its geometry. [C II] is only detected towards a few fragments in this area, so we use the 1 K sensitivity limit to estimate a column density detection limit. This limit is $N_{\mathrm{H}} \sim 10^{21}\ \mathrm{cm^{-2}}$ ($A_V \sim 0.5$) assuming a typical line width of 3 $\mathrm{km\ s^{-1}}$ and $T_{\mathrm{ex}} = 60$ K based on the shell fragment emission. To estimate surface area, we use a 3-dimensional compressed ellipsoidal cavity rather than a biconcave disc (Section 3.5.1) for simplicity; the difference between the surface area of these shapes is not important for an order-of-magnitude estimate. We use two equal semimajor axes of 20 pc and a semiminor axis of 6 pc, and we assume that $N(\mathrm{H_2})$ through any part of the shell surface is $< 10^{21}\ \mathrm{cm^{-2}}$. The mass in the shell must be $\lesssim 10^4\ M_{\odot}$. This is similar to the mass of the cluster ($\sim 2 \times 10^4\ M_{\odot}$, Pfalzner 2009) and large gas clouds in M16 such as the Northern Cloud or the natal cloud gas near M16 (Section 3.6), and is smaller than the $\sim 10^5\ M_{\odot}$ GMC W 37 (Zhan et al., 2016).

We estimate the shell thickness using the $\sim$0.5 pc on-sky width of the edges of the lobes in the 8 and 160 μm images. There are multiple overlaid edges, probably from a wavy shell surface viewed edge on. Our 0.5 pc estimate is the width of the smallest resolved edges and is consistent at both wavelengths. Using the $10^{21}\ \mathrm{cm^{-2}}$ upper limit on the column density through the foreground shell, we place an approximate upper limit $\lesssim$700 $\mathrm{cm^{-3}}$ on the average shell density.

3.8.1.1 M16 X-Ray Plasma

M16 was observed with Chandra ACIS between 0.5–7 keV (Guarcello et al., 2010b; Linsky et al., 2007), and the diffuse emission spectrum separated from the point source emission and extracted by Townsley et al. (2014). We analyze the spectrum extracted from the region outlined in white in Figure 3.19 using the SPEX package (Kaastra et al., 1996), applying optimal binning (Kaastra & Bleeker, 2016) and optimizing the model fit using C-statistics (Kaastra, 2017). The best-fit model requires one "hard" ($T \sim 10^7$–10^8 K) and two "soft" ($T \sim 10^6$–10^7 K) collisionally-ionized components and a foreground absorption of $N_{\rm H} \sim 1.1 \times 10^{22}$ cm^{-2} $\sim$ $5\ A_V$, which is comparable to the optical extinction towards the cluster stars (Stoop et al., 2023). The softest component, $T = 1.7 \times 10^6$ K, is associated with an emission measure $\mathrm{EM} = 1.4 \times 10^{58}$ cm^{-3} over the 246 square arcminute (63 pc^2) extraction area (Figure 3.19). Following Tiwari et al. (2021), we assume the emitting plasma fills a sphere whose projected (circular) area is equal to the extraction area. Electron density, assuming $n_e = n_{\rm H}$, relates to emission measure and emitting volume as $\mathrm{EM} = n_e n_{\rm H} V = n_e^2 V$, and we derive $n_e = 1.1$ cm^{-3} which is similar to the values found for RCW 49 by Tiwari et al. (2021) and RCW 36 by Bonne et al. (2022). Thermal pressure in the plasma is $P_{\rm therm}/k_{\rm B} = 1.9 \times 10^6$ K cm $^{-3}$. We estimate the observed thermal energy $E_{\rm therm} = 3 \times 10^{48}$ erg using the same volume used to derive density. Figure 3.19 shows X-ray emission towards the interiors of the eastern and western lobe cavities at the edges of the ACIS fields, so we expect that plasma fills these lobes, though there would be a negative gradient in density away from the cluster. We use the ellipsoidal cavity dimensions (two equal 20 pc semimajor, one 6 pc semiminor) to estimate the volume in the M16 cavity and place, using the thermal plasma pressure measured towards the center, an upper limit

$E_{\rm therm,\,tot} < 8 \times 10^{49}$ erg on the thermal energy in plasma inside the entire cavity. This is ∼1/10$^{\rm th}$ the available mechanical wind energy from NGC 6611, though it may approach the total wind energy if winds are clumpy.

3.8.1.2 M16 Pressure and Energetics

We estimate the pressure and energy within the PDR shell. Using our upper limit on number density, the upper limit on thermal pressure for a typical 100 K PDR is $P_{\rm therm}/k_{\rm B} \lesssim 6 \times 10^4$ K cm $^{-3}$. To properly estimate turbulent pressure, we would need a [C II] line width towards the shell. While we detect [C II] emission towards the few shell fragments shown in Figure 3.10, their properties may not be representative of the entire shell and we do not detect emission towards the center of the cavity as shown in that Figure. We also do not have observations constraining the magnetic field in the PDRs in the greater M16 region, and magnetic fields tend to provide a significant amount of nonthermal support within PDRs (Hennebelle & Inutsuka, 2019b; Karim et al., 2023; Nakamura & Li, 2008; Pellegrini et al., 2009, 2007). Therefore we assume pressure equipartition so that $P_{\rm therm} = P_{\rm turb} = P_{\rm B}$. The total pressure in the shell would be $P_{\rm tot}/k_{\rm B} = (P_{\rm therm} + P_{\rm turb} + P_{\rm B})/k_B =\lesssim 2 \times 10^5$ K cm $^{-3}$. Magnetic support, typically approximated as a pressure, is $P_{\rm B} = B^2/8\pi$. Under our assumptions, $B \lesssim 15~\mu$G in the M16 PDR shell.

The upper limit on the kinetic energy associated with the $\lesssim 10^4~M_\odot$ shell expanding at $10~{\rm km~s^{-1}}$ is $\lesssim 10^{49}$ erg. We also estimate an upper limit on the thermal energy inside the shell $E_{\rm therm} < \frac{3}{2}\, k_B T\ (M/\mu m_{\rm H}) \sim 10^{48}$ erg. Our analysis of stellar feedback capacity of NGC 6611 places its mechanical wind luminosity over the last 2 Myr at $\sim 10^{51}$ erg (or 10^{50} erg if winds

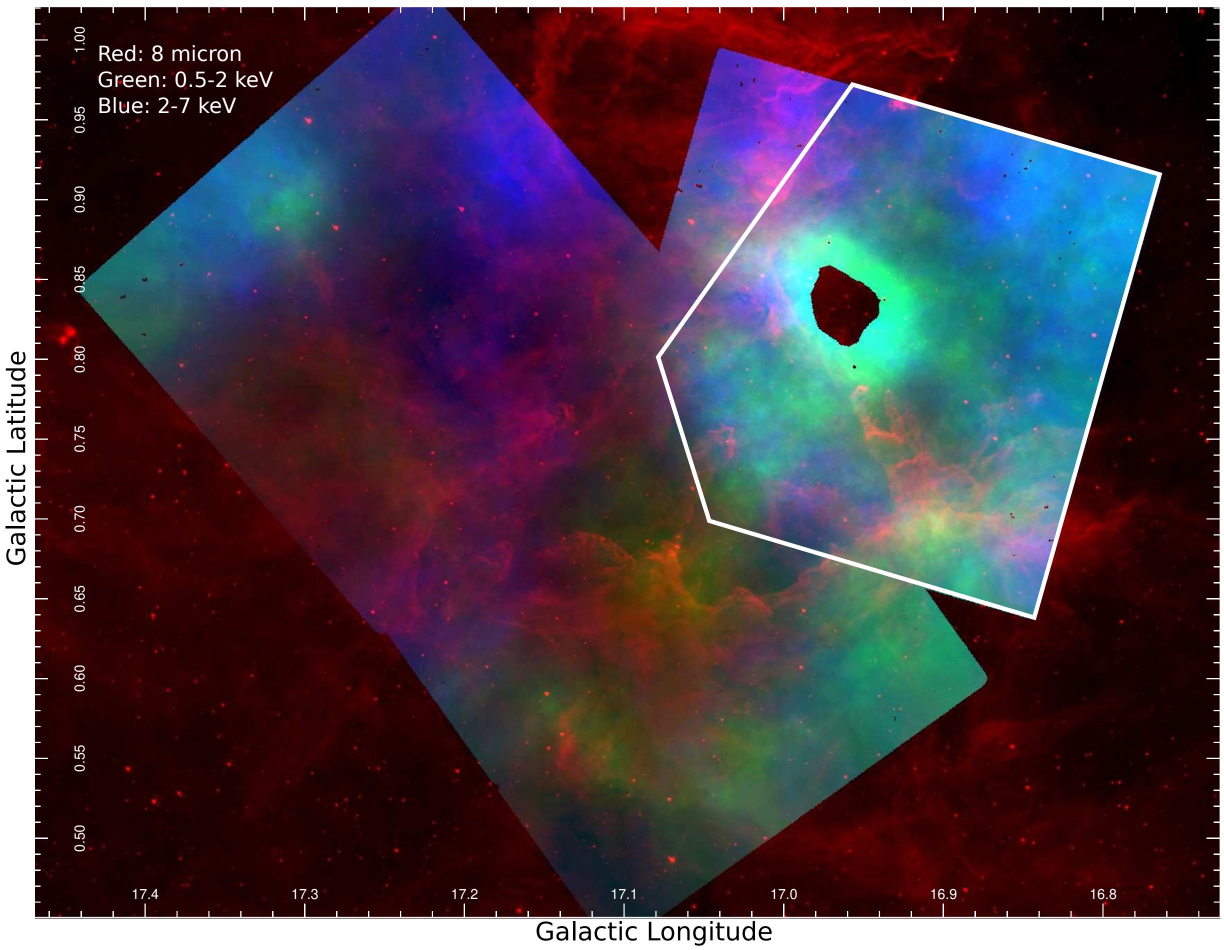

Figure 3.19 Color composite showing the diffuse emission extracted from Chandra ACIS X-ray observations over the 8 μm image. 8 μm is shown in red, the 0.5–2 keV band in green, and the 2–7 keV band in blue. The extraction region for the analyzed spectrum is outlined in white. The harder band is less susceptible to extinction. The brightest X-ray emission surrounds NGC 6611, whose immediate area is masked out since it is dominated by point sources. The X-ray-dark region to the left of NGC 6611 is spatially correlated with Northern Cloud CO emission. The X-ray emission at the top-left lies towards the inside of the eastern lobe and emission to the right of the Pillars lies inside the western lobe.

are clumpy; Puls et al. 2008). The column densities of the detected shell fragments are low ($N_{\rm H} \lesssim 10^{21}$ cm^{-2} and only a few tens of $M_\odot$, equivalent to $\lesssim 10^{47}$ erg at 10 $\rm km\ s^{-1}$) and so their kinetic energy is insignificant compared to the feedback capacity of NGC 6611.

The ionized gas pressure analysis by Pattle et al. (2018) is appropriate for the ambient ionized gas within the M16 cavity. Hester et al. (1996) used photoevaporative flows from the Pillars of Creation to estimate the density in the ambient (not part of the flow) ionized gas $n_{\rm H} \approx 29$ cm^{-3} within a few parsecs from the Pillars, and we assume that $n = n_{\rm H} + n_e = 2n_{\rm H} = 58$ cm^{-3}. We adopt the same $T_{\rm K} = 8000$ K as Hester et al. (1996) and Pattle et al. (2018), so $P_{\rm therm}/k_{\rm B} = 4.6 \times 10^5$ K cm $^{-3}$. Higgs et al. (1979) derives the three-dimensional turbulent velocity $\sigma_{\rm v,\,3d} \approx 12\ \rm km\ s^{-1}$ from H recombination lines towards the bright center of the M16 region; there is some risk that these measurements are biased towards the dense gas, but Karim et al. (2023) found it unlikely that the high-density photoevaporative flow, whose bright emission can dominate the line of sight, is turbulent. At least one of the individual positions observed by Higgs et al. (1979) does not include emission from the Pillars or Bright Northern Ridge, and the linewidth does not vary significantly. We estimate turbulent support in the ionized gas $P_{\rm turb}/k_{\rm B} = 2.3 \times 10^5$ K cm $^{-3}$ using the one-dimensional turbulent velocity $\sigma_{\rm v,\,1d} = \sigma_{\rm v,\,3d}/\sqrt{3} \approx 7\ \rm km\ s^{-1}$. In regions close to where the bubble has broken open, pressure will be smaller because the gas is flowing out. We neglect magnetic support in the ionized gas.

3.8.2 N19

The N19 cavity has an associated foreground expanding shell moving at $\sim$4 $\rm km\ s^{-1}$ towards the observer projected along the line of sight. The on-sky projected radius of N19 is $\sim$2 pc

(Churchwell et al., 2006; Jayasinghe et al., 2019). The dynamic age of the cavity is ~0.5 Myr. This is less than the estimated ~2 Myr age of NGC 6611, so either the N19 bubble has accelerated so that its average expansion velocity over time has been 1–2 $\mathrm{km\,s^{-1}}$, or the N19 cavity was formed after NGC 6611.

3.8.2.1 N19 PDR Shell

Since we detect only the foreground half of an expanding PDR shell associated with N19, we model the PDR shell as a hemispherical shell of inner radius 1.8 pc and outer radius 2.3 pc based on its on-sky projected size in the 8 μm image. The integrated [C II] column densities between $\mathrm{V_{LSR}} = 10$–$21\ \mathrm{km\,s^{-1}}$ toward the N19 ring suggest 650 $M_\odot$ of PDR gas (Table 3.2).

The column density of the limb brightened edge of the PDR shell is $N_\mathrm{H} \sim 10^{22}\ \mathrm{cm^{-2}}$ based on the [C II] line measurements. The limb brightened path tangent to the inner sphere through a simple concentric-sphere configuration is $l = 2(r_2^2 - r_1^2)^{1/2}$ for inner and outer radii $r_1,\ r_2$; for the hemispherical shell model, we remove the factor of 2 and estimate a 1.4 pc limb brightened path through the shell. Using the limb brightened column density through the PDR shell, we estimate number density $n \sim 2300\ \mathrm{cm^{-3}}$. We also estimate number density using the 650 $M_\odot$ PDR mass and the estimated shell volume ~13 pc^3, which yields $n \sim 1500\ \mathrm{cm^{-3}}$.

The [C II] line brightness towards the N19 cavity is just a few Kelvin. Our estimated RMS noise of 1 K suggests a column density detection threshold $\sim 1 \times 10^{21}\ \mathrm{cm^{-3}}$ for a typical $3\ \mathrm{km\,s^{-1}}$ linewidth and $T_\mathrm{ex} \sim 60\ K$ (same assumptions as for the M16 shell). If we take a column density upper limit of $N_\mathrm{H} < 5 \times 10^{21}\ \mathrm{cm^{-2}}$ through the assumed 0.5 pc thick foreground shell, density is implied to be $n \lesssim 3200\ \mathrm{cm^{-3}}$. Should the shell density be the $n \sim 1500\ \mathrm{cm^{-3}}$

estimated above, then column density through the foreground shell is $N_{\rm H} \sim 2.3 \times 10^{21}$ cm^{-2} which is consistent with our observations. This is equivalent to $A_V \sim$ 1–2 (Bohlin et al., 1978).

A measured $E(B-V) = 1.55$ is listed for W584 within N19; this yields $A_V = 5.5$ for assumed reddening $R_V = 3.56$ (Kumar et al., 2004; Stoop et al., 2023), which is ∼1–2 standard deviations ($\sigma_{A_V} \approx 1.1$) greater than the mean $A_V \approx 3.8$ of the NGC 6611 core early-type members listed in Appendix C.1 using A_V values from Stoop et al. (2023). The extra $A_V \sim$ 1–2 towards the N19 star is consistent to order-of-magnitude with the $A_V \sim$ 1–2 that we estimate through the N19 foreground shell; however, this is assumes (1) the cluster-core members see no additional extinction and (2) that the N19 foreground shell is uniform, and integrated [C II] intensity maps suggest that it is not uniform. We determine that all observations are consistent with a PDR shell density $n \sim 1500$ cm^{-3} and mass 650 $M_\odot$.

3.8.2.2 N19 Molecular Gas Shell

We use the CO and 160–500 μm images to estimate a molecular gas shell inner radius ∼2 pc and outer radius ∼3 pc; the overlap with the PDR shell outer radius is not important in this approximation. Although we do not detect a foreground or background molecular gas shell in CO, we assert that the ring is associated with the N19 shell on account of the spatial and kinematic coincidence.

Column densities calculated from ^{13}CO(J=1–0) observations and integrated around the N19 ring indicate the presence of ∼4200 $M_\odot$ of molecular gas. Line diagnostics described in Section 3.1 suggest column density $N(\mathrm{H_2}) \sim 1.1 \times 10^{22}$ cm^{-2} and density $n \sim 5600$ cm^{-3} towards the molecular shell.

The line of sight path $N(\mathrm{H_2})/n \approx 0.6$ pc is smaller than the 4.5 pc limb brightened path through the edge of a spherical shell with our adopted dimensions. We suggest that the filling factor varies along the line of sight through the limb-brightened shell. This could be caused by a wavy surface, so that the line of sight repeatedly passes in and out of the shell, or density variation along the line of sight. The projected shell we see has a wavy surface, as seen in the CO and the FIR in Figure 3.12, and the higher resolution FIR in that image shows plenty of clumpiness not resolved in the PMO CO observations.

3.8.2.3 N19 Pressure and Energetics

A typical PDR temperature $T \sim 100$ K and our estimated PDR density $n \sim 1500\ \mathrm{cm}^{-3}$ imply a pressure $P_{\mathrm{therm}}/k_{\mathrm{B}} \sim 1.5 \times 10^5$ K cm $^{-3}$. Using a typical [C II] line width of 3–4 $\mathrm{km\ s}^{-1}$, the turbulent pressure is $P_{\mathrm{turb}}/k_{\mathrm{B}} \sim 5 \times 10^5$ K cm $^{-3}$. Assuming equal turbulent and magnetic pressures, the magnetic field strength may be ∼40 μG. The sum of the thermal, turbulent, and magnetic pressures in the PDR is $P_{\mathrm{tot}}/k_{\mathrm{B}} \sim 10^6$ K cm $^{-3}$. Kinetic energy in the $650\ M_\odot$ PDR shell expanding at 4 $\mathrm{km\ s}^{-1}$ is $\sim 1 \times 10^{47}$ erg. Thermal energy is $\sim 1.2 \times 10^{46}$ erg.

For our CO line diagnostics, we assumed a kinetic temperature $T \sim 30$ K in the molecular gas, giving thermal pressure $P_{\mathrm{therm}}/k_{\mathrm{B}} \sim 1.7 \times 10^5$ K cm $^{-3}$. CO line velocity dispersions are $\sigma \approx 1\ \mathrm{km\ s}^{-1}$ towards N19, so turbulent pressure $P_{\mathrm{turb}}/k_{\mathrm{B}} \sim 1.8 \times 10^6$ K cm $^{-3}$ and magnetic field strength may be 80 μG. The sum of the thermal, turbulent, and magnetic pressures in the molecular gas is $P_{\mathrm{tot}}/k_{\mathrm{B}} \sim 4 \times 10^6$ K cm $^{-3}$, which is in agreement with the total pressure in the PDR given the approximate nature of these estimates. We do not detect the expansion of the molecular shell along the line of sight, so it may be moving in the plane of the sky anywhere from

0–4 $\mathrm{km\ s^{-1}}$, since its mass may slow expansion in those directions, and may carry 0–7 $\times\ 10^{47}$ erg of kinetic energy.

We do not have direct measurements which probe photoionized gas conditions toward N19. The ionized gas is expected to be in pressure equilibrium with the PDR and the molecular cloud and the derived pressure $\sim$1–4 $\times\ 10^6$ $\mathrm{K\ cm}^{-3}$ of these implies an electron density $\sim$200 cm^{-3} in the ionized gas and therefore $\sim 10^{47}$ erg in thermal energy, disregarding any bubble volume occupied by a shock-ionized plasma phase. This thermal energy is comparable to the kinetic energy in the shell.

3.8.2.4 N19 Expansion Timescales

Given the wind luminosity and kinetic energy listed in Table 3.4 for N19, the bubble may be driven either by mechanical energy from winds (Weaver et al., 1977), thermal pressure from photoionized gas (Spitzer, 1978), or a combination of both. We use observed parameters to estimate the age of the bubble using analytical expressions describing these two expansion solutions. The simple dynamic age approximation $R(t)/v(t) = 0.5$ Myr calculated at the beginning of Section 3.8.2 for time-dependent radius and velocity $R(t)$ and $v(t)$ does not account for acceleration.

The expression for the bubble age under thermal expansion can be derived from Tielens (2010) given initial density n_0, ionized gas sound speed c_i, ionizing photon emission rate $Q_0 = 7.4 \times 10^{47}$ s^{-1}, recombination coefficient to the first excited electronic state $\beta_B = 2.6 \times 10^{-13}$ cm^3 s^{-1}, and shell radius $R_s(t)$:

$$t = \frac{4}{7}\frac{R_0}{c_i}\left[\left(\frac{R_s(t)}{R_0}\right)^{7/4} - 1\right]$$

where the Strömgren radius $R_0^3 = (3/4\pi)Q_0/(n_0^2\beta_B)$. We adopt $c_i = 10\ \mathrm{km\ s^{-1}}$. We can express the shell velocity $v_s(t)$ as

$$v_s(t) = c_i \left(\frac{R_0}{R_s(t)} \right)^{3/4}$$

and use the age derived above from observed radius to estimate the velocity for purely thermal expansion and compare to the observed 4 $\mathrm{km\ s^{-1}}$. The initial density may have been as high as 10^3 cm^{-3} in the past, and we estimate from pressure equilibrium above that the photoionized gas must be ∼200 cm^{-3} at present. Using these numbers as limits, we estimate that the age of N19 is between 0.2–0.5 Myr assuming a purely thermally-driven expansion, with higher density yielding greater age. Initial densities $\lesssim$300 cm^{-3} produce velocities $> 4\ \mathrm{km\ s^{-1}}$ and $n_0 = 1000\ \mathrm{cm^{-3}}$ yields ∼2.5 $\mathrm{km\ s^{-1}}$ expansion.

The expression for bubble age under wind-driven expansion given the same initial density n_0, mechanical luminosity from W584 $L_{\mathrm{mech}} = 7 \times 10^{33}$ erg s^{-1}, and shell radius $R_s(t)$ can be rearranged from Eq. 51 by Weaver et al. (1977):

$$t_6 = (27)^{-5/3} n_0^{1/3} L_{36}^{-1/3} R_s(t)^{5/3}$$

where age t_6 is expressed in Myr, L_{36} in 10^{36} erg s^{-1}, n_0 in cm^{-3}, and $R_s(t)$ in parsecs. Shell velocity is given by Eq. 52 by Weaver et al. (1977):

$$v_s(t) = 16 n_0^{-1/5} L_{36}^{1/5} t_6^{-2/5}$$

where $v_s(t)$ is in $\mathrm{km\ s^{-1}}$. Using the same 200–1000 cm^{-3} initial density range as above, we find wind-driven expansion ages of 0.4–0.7 Myr given the observed radius, where higher density yields greater age. Expansion velocities would be 2–3 $\mathrm{km\ s^{-1}}$, with higher density yielding lower velocity. We discuss implications in the following Section.

3.9 Discussion

3.9.1 Wind-Driven or Thermally Expanding?

3.9.1.1 Thermal Expansion

The description of the expansion of an H II region follows the discussion in Chapter 12.2 in Tielens (2010). We consider a massive star with an ionizing photon luminosity Q_0 turning on in a homogeneous hydrogen cloud with density n_0. Initially, the ionization front will race through the cloud ionizing a region with size R_0 given by the Strömgren relation

$$Q_0 = \frac{4\pi}{3} R_0^3 n_0^2 \beta_B$$

with β_B the recombination coefficient to all levels with principle quantum number ≥ 2. Ionization will raise the temperature to some 10^4 K and the overpressure will drive a shock into the surrounding cloud that sweeps the cloud up into a shell. High shell density allows the shell to cool rapidly and remain thin. As the H II region expands, H II gas density will drop and the ionization front will eat into the swept-up shell, increasing the mass of ionized gas. At time t, the expansion velocity and radius of the H II region are given by

$$v_s(t) = \frac{dR_s(t)}{dt} = c_i \left(\frac{R_0}{R_s(t)} \right)^{3/4}$$

$$\frac{R_s(t)}{R_0} = \left(1 + \frac{7}{4} \frac{t}{t_0} \right)^{4/7}$$

Property	M16	N19	Unit
Q_0	8.43×10^{49}	7.43×10^{47}	s^{-1}
$E_{\rm wind}$	9.82×10^{50}	1.12×10^{47}	erg
Age	2	~0.5	Myr
Neutral shell			
Mass	$< 10^4$	650	$M_\odot$
n	< 700	1500	cm^{-3}
T	100*	100*	K
$P_{\rm th}$	$< 6 \times 10^4$	1.5×10^5	K cm^{-3}
$P_{\rm turb}$	...	5×10^5	K cm^{-3}
$P_{\rm tot}$	$< 2 \times 10^5$	1×10^6	K cm^{-3}
$E_{\rm th}$	$< 10^{48}$	1.2×10^{46}	erg
$E_{\rm kin}$	$< 10^{49}$	1×10^{47}	erg
Molecular shell			
Mass	...	4200	$M_\odot$
n	...	5600	cm^{-3}
T	...	30	K
$P_{\rm th}$	...	1.7×10^5	K cm^{-3}
$P_{\rm turb}$	...	1.8×10^6	K cm^{-3}
$P_{\rm tot}$	...	4×10^6	K cm^{-3}
Photoionized gas			
n	58	~200	cm^{-3}
T	8000	...	K
$P_{\rm th}$	4.6×10^5	...	K cm^{-3}
$P_{\rm turb}$	2.3×10^5	...	K cm^{-3}
$P_{\rm tot}$	6.9×10^5	...	K cm^{-3}
X-ray plasma			
n	1.1	...	cm^{-3}
T	1.7×10^6	...	K
$P_{\rm th}$	1.9×10^6	...	K cm^{-3}
$E_{\rm th}$ (observed)	3×10^{48}	...	erg
$E_{\rm th}$ (est.)	$< 8 \times 10^{49}$	...	erg

Table 3.4 Top rows give star/cluster H-ionizing photon emission rate, wind energy injection over the age of the system, and the age. Gas pressures are expressed as P/k_B, as indicated by their units. Due to lack of relevant measurements, no molecular gas estimates are given for the M16 shell and no ionized gas estimates are given for N19. The atomic gas temperatures marked with (*) are assumed based on typical atomic PDR temperatures. See Section 3.8 for further details.

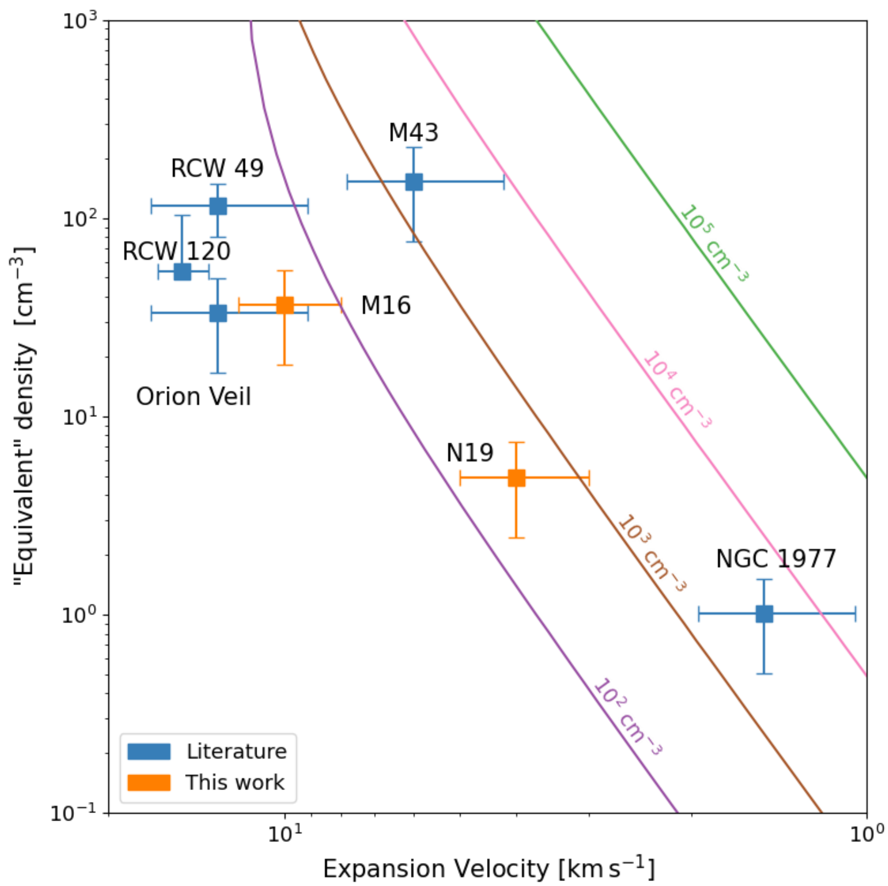

Figure 3.20 Equivalent shell density plotted against shell expansion velocity for a few H II regions including M16 and N19 from this work. The mass of the shell is translated to an "equivalent" density $\frac{Q_0}{\beta_B}\frac{\mu m_{\mathrm{H}}}{M_{\mathrm{shell}}}$ where the recombination rate coefficient $\beta_B = 2.3 \times 10^{-13}$ cm^3 s^{-1} (Tielens, 2010). We use PDR shell masses for N19 and M16, neglecting any molecular gas. The equivalent density and expansion velocity are related through the initial density of the medium. Contours show several initial, pre-bubble densities (cm^{-3}) (Spitzer, 1978). Regions which fall to the left of all contours have expanded too rapidly to be purely thermally driven and must have been wind-blown.

where $t_0 = R_0/c_i$ and c_i is the sound speed in the ionized gas. Assuming that the shell of swept up gas is very thin, the mass of the shell is given by

$$M_{\rm shell}(t) = \frac{4\pi}{3} R_s(t) \mu m_{\rm H} (n_0 - n(t))$$

where $n(t)$ is related to the radius of the H II region through the Strömgren relation. Realizing that

$$\left(\frac{R_s(t)}{R_0}\right)^3 = \left(\frac{n_0}{n(t)}\right)^2$$

and

$$\frac{v_s(t)}{c_i} = \left(\frac{n(t)}{n_0}\right)^{1/2}$$

we can rewrite this as

$$M_{\rm shell}(t) = \frac{\mu m_{\rm H}}{\beta_B Q_0} \left(\frac{c_i}{v_s(t)}\right)^4 \left(1 - \left(\frac{v_s(t)}{c_i}\right)^2\right)$$

We can then define an "equivalent" density as

$$N(t) = \frac{Q_0}{\beta_B} \frac{\mu m_{\rm H}}{M_{\rm shell}(t)}$$

which allows us to compare the results for H II regions powered by stars with very different ionizing luminosities. With some rearranging, we can show that

$$\frac{n_0}{n(t)} = \frac{1}{2}\left(1 + \sqrt{1 + 4n_0/N(t)}\right)$$

At late times, the "equivalent" density will scale as

$$N(t) \approx \left(\frac{n(t)}{n_0}\right)^2 n_0$$

The "equivalent" density links the observed shell mass to a reduction in the density of the ionized gas due to the thermal expansion of the H II region.

Figure 3.20 shows the relation between expansion velocity and the mass of the shell translated to this equivalent density, as defined above, for a few relevant initial densities of the medium. The expansion velocity drops rapidly with time as the mass of the swept-up shell increases. We note that H II regions powered by earlier spectral types than approximately O9 have observed expansion speeds which exceed the sound speed in the ionized gas and these cannot be driven by thermal expansion of the ionized gas in a homogeneous medium.

3.9.1.2 Wind-Driven Expansion

The diagram in Figure 3.21 groups H II regions together by the similarity between their time-integrated mechanical luminosities and the kinetic energy carried by their expanding shells. A perfect coupling between gas motion and mechanical input from stellar wind would yield $E_{\mathrm{kin}}/E_{\mathrm{W}} = \mathrm{constant}$ for all time and make a horizontal track in this diagram. Weaver et al. (1977) finds that more than half the mechanical energy ends up as thermal energy in the collisionally-ionized plasma and that, at later times, thermal conduction between the collisionally-ionized plasma and the photoionized H II gas causes the mechanical-to-kinetic energy transfer to reduce over time; this means that the evolutionary track will start lower ($E_{\mathrm{kin}}/E_{\mathrm{W}} < 1$) on the diagram. Other expansion drivers not accounted for in this diagram, such as thermal pressure from the

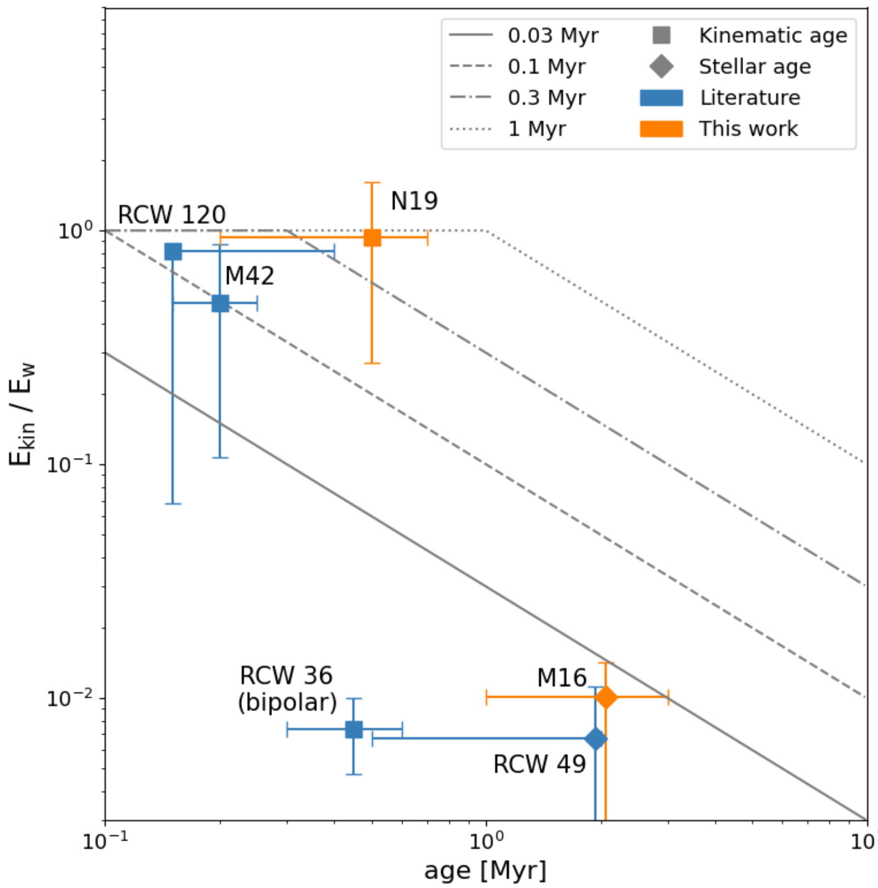

Figure 3.21 Ratio of the shell kinetic energy to the cluster's mechanical energy (mechanical luminosity × age) plotted against the age of the cavity for a few H II regions including M16 and N19 from this work. Lines represent idealized evolutionary tracks following a burst, and subsequent decoupling of gas motion from mechanical input, at the age given in the legend. The diagram and evolution within it are discussed further in the text of Section 3.9.1.

ionized gas or radiation pressure, would increase E_{kin}.

Should the mechanical input completely decouple from the gas motion so that E_{kin} is constant, such as during a burst which releases pressurized gas into the environment, a region would evolve in time down the diagram as E_{W} grows linearly with time while E_{kin} does not. The tracks in Figure 3.21 assume that E_{kin} remains constant after the burst. In reality, a burst may not cause the coupling to change so abruptly, and instead change over a few 10^5 years if limited by the sound speed in the photoionized gas. Other expansion drivers may soften this decline, though a burst would also reduce the coupling between gas motion and thermal pressure from photoionized H II.

The shell's total kinetic energy will decline after the burst during the momentum-conservation phase as more gas is swept up into the shell, which we do not model in the evolutionary tracks in Figure 3.21. The shell kinetic energy in this Figure only accounts for neutral gas mass, so any kinetic energy carried by gas which becomes photoionized on the interior of the shell is not accounted for and will also represent "removal" of E_{kin}.

In summary, the evolutionary trend of bubbles on the diagram in Figure 3.21 is to the right while the bubble is intact and then to the bottom right after the bubble bursts. Other avenues through which kinetic energy is added to the shell, such as radiation pressure, will push the region upwards on the diagram, and kinetic energy losses push the region downwards. An earlier burst has a similar effect to an inefficient coupling phase (in which the pre-burst horizontal evolution occurs at $E_{\mathrm{kin}}/E_{\mathrm{W}} < 1$) in regions can end up lower on the diagram at earlier times.

We include in Figure 3.21 other Galactic H II regions using shell masses, velocities, and ages from the literature (M42: Pabst et al. 2020; RCW 36: Bonne et al. 2022; RCW 49: Tiwari et al. 2021; RCW 120: Luisi et al. 2021). Kinematic shell ages are used where possible, and stellar cluster ages used otherwise. The kinematic shell ages tend to be $\gtrsim 10^5$ yr younger than the stellar ages, which suggests that shells "break out" of the dense gas and expand on a multi-parsec scale after a few hundred thousand years. In the cases of M16 and RCW 49, the asymmetric expansion or clear burst signatures make kinematic ages difficult to determine. In M16, the anisotropic expansion renders the spherical-expansion analytical models used for N19 in Section 3.8.2.4 no more accurate than a simple constant-velocity assumption of $r/v = t = 20 \text{ pc}/10 \text{ km s}^{-1} \approx 2 \text{ Myr}$ which is consistent with the age of the cluster. In RCW 49, Tiwari et al. (2021) estimate a kinematic age of 0.5 Myr and conclude that it is too incongruous with the ~2 Myr stellar age, so expansion must have accelerated more recently, perhaps due to increased mechanical feedback from evolved stars. Uncertainty on the M16 shell kinetic energy is driven primarily by the uncertain shell mass, upon which we have placed the upper limit of $10^4\ M_\odot$, and also by uncertainty of order $\sim 2 \text{ km s}^{-1}$ on the expansion velocity. We use a 50% uncertainty on the mass and a 1 km s^{-1} uncertainty on the shell expansion velocity of N19. The uncertainty on the kinematic age of the N19 shell is dominated by the assumption of initial density n_0.

3.9.1.3 Comparison to Observations of the Eagle Nebula

NGC 6611 has swept up a thin, extended shell of some $10^4\ M_\odot$ and imparted up to 1% of its available wind energy to this neutral shell and up to 10% to the plasma which fills the cavity inside the shell. A considerable $\sim 10^5\ M_\odot$ (Zhan et al., 2016) of molecular gas and a few $10^4\ M_\odot$ of PDR gas remains within a few parsecs of the cluster, while the shell has expanded in some directions out to nearly 20 pc away and broken open towards others. Wind energy is largely channeled away from the nearby reservoir of dense gas (see Table 3.4).

Shell expansion of 10 $\mathrm{km\ s^{-1}}$ at an age of 2 Myr is too fast for a thermally-driven Spitzer expansion according to Figure 3.20 (Spitzer, 1978), and there is plenty of wind energy available from the cluster, so the greater M16 shell must be wind-driven. Its location on the diagram in Figure 3.21 places it in the company of RCW 49, a region powered by another high-mass cluster with even more wind and radiative energy available, and RCW 36, a bipolar H II region. RCW 49 and RCW 36 have both broken open (Bonne et al., 2022; Tiwari et al., 2021), as we suspect M16 has.

W584, the O9.5 V star powering the N19 bubble, has swept up a shell of $\sim 650\ M_\odot$ of PDR gas and $\sim 4200\ M_\odot$ of molecular gas. Its winds have carried a modest $\sim 10^{47}$ erg over the last 0.5 Myr. The PDR shell, expanding at 4 $\mathrm{km\ s^{-1}}$, contains a very similar $\sim 10^{47}$ erg in kinetic energy.

No expanding foreground or background molecular gas shell is detected towards N19, and the $4200\ M_\odot$ molecular shell we see in projection must not cover the entire bubble. The shell may expand faster toward the observer, unburdened by dense gas in this direction, than it does on the plane of the sky where we see plenty of dense gas. The expansion velocity of the dense molecular gas is therefore unknown, but we can logically bound it between 0–4 $\mathrm{km\ s^{-1}}$ as discussed in Section 3.8.2.3. On the low end, it adds little kinetic energy to the total budget and the available wind energy is sufficient to drive shell expansion. On the high end, kinetic energy is $\sim 7\times$ the available wind energy. The molecular shell must be constraining the expansion velocity of N19 in the plane of the sky. We place N19 in Figure 3.20 under the assumption that the dense gas has hardly accelerated and kinetic energy is only imparted on the observed expanding PDR shell.

The analysis in Section 3.8.2.4 of N19's observed radius and expansion velocity using the thermal pressure-driven and wind-driven expansion analytical calculations (Spitzer, 1978; Weaver et al., 1977) indicate that expansion is consistent with thermally-driven expansion due to pressure from the photoionized gas for an initial cloud density ∼300–400 cm^{-3} and an age of ∼0.5 Myr. However, the mechanical energy input from W584 is similar to the kinetic energy in the shell and the thermal energy in the photoionized gas, so it is likely that winds contribute to the expansion. Winds on their own are insufficient to accelerate the shell to the observed 4 $\mathrm{km\ s^{-1}}$ for a reasonable (not too low) initial cloud density. N19's expansion must be driven by a combination of both thermal and wind energies.

3.9.1.4 Comparison to Observations of Other H II Regions

In Figure 3.21, the six regions are grouped into two distinct groups of 3. One group, including N19, is typically younger and has a ratio $E_{\mathrm{kin}}/E_{\mathrm{W}}$ close to unity while the other group, which includes M16, is typically older and has a ratio $E_{\mathrm{kin}}/E_{\mathrm{W}} \sim 0.01$. There are a handful of characteristics which might create these groups.

First, this may be an evolutionary track. The diagonal overlays show idealized evolutionary tracks through the diagram assuming that the bubble around the star or cluster bursts and mechanical energy input decouples from the kinetic energy of the swept-up shell. It is possible that the younger group represents intact or very recently burst regions while the older group represents evolved burst regions.

Second, RCW 120, M42, and N19 are all driven by a small number of O stars. N19 is driven by a single O9 V, M42 is driven by θ^1 Ori C which is an O7 V along with a couple early B-type stars (Pabst et al., 2020), and RCW 120 is driven by a single O8 V (Luisi et al., 2021).

In contrast, M16 and RCW 49 are both driven by massive clusters of multiple O-type stars; the earliest member of NGC 6611 is an O3, while RCW 49 hosts >30 O stars and a WR binary of two 80 $M_\odot$ members (Tiwari et al., 2021; Zeidler et al., 2015). RCW 36 is driven by an O9.5 V and an O9 V (Bonne et al., 2022), which would associate it more with the former group.

Third, the environment in which each region formed could affect the coupling. We show in this work that M16's cavity is shaped by the filament in which NGC 6611 was born and that N19 formed in a nearby cloud externally illuminated by NGC 6611. M42 is a blister H II region expanding out of the surface of the OMC1 core (Pabst et al., 2020). RCW 36 formed in a sheet and broke out of either side of the sheet almost simultaneously (Bonne et al., 2022). RCW 120 moves through a cloud at 4 $\mathrm{km\ s^{-1}}$ and creates a bow shock and cometary H II region (Luisi et al., 2021).

Given the small number of regions, it is premature to conclude what primarily governs the energetic coupling efficiency between stellar feedback and the kinetic energy of the shell. From this short discussion, we suggest that all three of these factors (age, central stars, and gas environment) may be important. More studies are needed to fill in this diagram and build statistics.

3.9.2 Effectiveness of Feedback on Clearing Away Gas

Feedback from the NGC 6611 cluster was effective in clearing a cavity within its natal molecular cloud. However, this cavity was significantly constrained by the dense filament embedded in the molecular cloud. Though ionizing radiation reaches outside of the cluster and we find evidence that the photoionized H II gas and collisionally-ionized wind-shocked plasma have escaped the region, there is plenty of dense molecular gas within a few parsecs of the cluster which has survived the intense feedback.

We consider the large-scale feedback of NGC 6611. The $\sim$2 Myr old cluster has vented 10^4 K and 10^6 K gas into the wider environment. Ionizing and FUV radiation freely escapes tens of parsecs away in multiple directions. The feedback is directionally constrained by surrounding dense gas. We note the slight upturn to $+b$ of the infrared lobes, which might arise from a Galactic plane density gradient acting as a second-order effect to the local molecular cloud density structure. The vented gas might preferentially escape upwards; sensitive, degree-scale observations of diffuse X-ray emission around M16 may be able to determine whether such a gradient influences plasma distribution.

NGC 6611, after 2 Myr, has not evaporated or dispersed all the molecular gas that surrounds it. Rather, we find a number of dense ridges which may harbor future generations of stars. Karim et al. (2023) estimated that the Pillars of Creation would survive for another $\sim$1 Myr and may fragment and collapse to form more stars due to weakening magnetic support. We extend this conclusion to the other dense clouds surrounding M16, such as the Spire and the Bright Northern Ridge. There are also sections of unilluminated filament to $\pm b$, traced by 500 μm and 850 μm but not 70 μm or 160 μm in Figure 3.1. N19 appears to be a younger cavity, so it may have formed when NGC 6611 was already a Myr old. At least two active star forming regions (SFO 30/two IRAS sources in Bright Northern Ridge, and MYSO/IRAS source in Northern Cloud; Section 3.4) are observed towards M16, and one is embedded within dense, hot molecular gas and PDR rings inside the Bright Northern Ridge, between M16 and N19. It is possible that compression from either/both M16 and N19 created a dense, massive clump from which this YSO formed. We cannot determine if star formation was triggered by feedback from NGC 6611, but we conclude that NGC 6611 left plenty of dense gas intact for future generations of stars.

M16 lies above the Galactic plane and does not appear to have broken open towards the plane. Feedback from M16, such as ionizing radiation, is probably not very impactful to star formation within the plane. As mentioned earlier, the rest of the filament from which NGC 6611 formed is unilluminated and therefore also not impacted by feedback. We predict that the inevitable sequence of supernovae will similarly expand cylindrically outwards and be constrained along the filament (bipolar HII region studies show this for sheets). The cavity has already been evacuated, but the explosions may still impact the nearby clouds such as the one which obscures the optical $+l$ half of M16.

N19 is driven by a single O9 V star, so its capacity for large-scale feedback is limited compared to the nearby NGC 6611 powering M16. N19's relative youth compared to M16 means that it may represent the future of either of the YSOs observed towards M16.

3.10 Conclusion

We determine, by analyzing velocity-resolved [C II] and CO line observations and wide-field continuum images, the geometry and physical conditions in the Eagle Nebula and the response of the gas to energetic feedback from the massive NGC 6611 cluster. The dense gas structure of the region is dominated by a $\sim 10^5\ M_{\odot}$ filament near $\mathrm{V_{LSR}} \sim 25\ \mathrm{km\ s^{-1}}$. From this filament the $\sim$$10^4\ M_{\odot}$ cluster was born and displaced no more than $\sim$$10^4\ M_{\odot}$ of gas in the form of a wind-blown shell. The shell is highly elliptical and extends away from the filament's major axis, indicating that the filament significantly constrained the evolution of the cavity. The shell's projected size ($\sim$20 pc radius) is consistent with its $\sim$$10\ \mathrm{km\ s^{-1}}$ expansion velocity as traced by foreground and background shell fragments detected in [C II]. Unobstructed optical emission indicates that the shell is very thin or broken open towards the observer.

A smaller cloud hangs in the foreground a few parsecs in front of NGC 6611 and the filament. This Northern Cloud hosts an independent H II region cavity, N19, powered by a single O9 V star. The cavity is surrounded by a bright PDR shell and, displaced radially outwards, a molecular gas shell. The signature of an expanding foreground shell toward N19 is detected in the [C II] observations. The Northern Cloud is also illuminated from below and behind by NGC 6611. The few $\sim 10^5$ yr old N19 cavity is dynamically younger than M16 by at least one million years and is likely driven by a combination of mechanical wind energy and thermal pressure from photoionized gas.

Significant gas mass has been displaced by stellar feedback within the Eagle Nebula, but its massive filamentary skeleton holds firm against the erosion caused by multiple generations of star formation. It shows, at multiple size scales from its collection of 0.1 pc scale pillars to the 10 pc scale filament, that the pre-existing density structure of the interstellar medium has significant influence on how energy is put back into the gas and how long dense gas remains in the presence of massive stars. A new generation of young stellar objects has been observed in the region, some of them with the capability to drive more energetic feedback, and plenty of dense gas remains to form future generations should the conditions be right.

Chapter 4: Scoby: Spectra from Catalogs of OB Stars

4.1 Introduction

A key asset to studies of massive stellar feedback is an accurate estimate of the radiative and mechanical energy output of each star within the central cluster. Estimates must be made for each star in regions driven by one or two stars (like N19 or M42; Pabst et al. 2020) to regions driven by many (like M16 or RCW 49; Tiwari et al. 2021). These estimates should be standardized, so that comparison across regions does not depend on the particular models used by each author, and the method for calculating them should scale well for up to a few tens of stars.

Observed stellar spectral types are determined using spectroscopic classification methods (see, for example, Hillenbrand et al. 1993). Sternberg et al. (2003) and Martins et al. (2005) provide maps from spectral types to physical stellar parameters such as effective temperature $T_{\rm eff}$, surface gravity $\log g$, and bolometric luminosity L. These parameters are specific and descriptive and can be used to model the star's radiative and mechanical feedback outputs.

Software which estimates stellar feedback properties using observed spectral types in a standard and scalable manner is crucial to efficient and reproducible feedback studies. There exists software, Starburst99 (Leitherer et al., 2014), which estimates feedback from a generic cluster of a given mass, but if observed stellar types are available, they should be used for more accuracy. In addition, projected radiation field maps can be created from the on-sky positions of known stars.

I developed a Python software library called `scoby` to meet these goals. `scoby` uses a network of tables to determine feedback properties from observed spectral types in service of massive stellar feedback studies like those in Chapters 2 and 3 in this thesis. The library provides classes and functions designed to be imported into an existing Python workflow. This Chapter describes the basic operations of `scoby`

4.2 Description of `scoby` Software

The software begins by loading and linking together internally-stored tables in a convenient format. We use the spectral type calibrations in Tables 1–3 by Martins et al. (2005), the stellar wind models in Tables 1 and 2 by Leitherer et al. (2010), and the O and B star spectra from the PoWR models by Sander et al. (2015) and Hainich et al. (2019). These tables are loaded into memory from text files and reorganized into lookup tables using a combination of Python dictionaries and pandas DataFrames (McKinney, 2010).

4.2.1 Tabular Data

We use the theoretical spectral type calibration by Martins et al. (2005). This provides a map from O-type classifications (letter type, numerical sub-type, and luminosity class) to $T_{\rm eff}$, $\log\, g$, and L. The set of all these types forms a surface in this 3-dimensional parameter space such that unique interpolations[1] can be made from any two parameters to the third. The tables by Martins et al. (2005) cover O3 to O9.5 in sub-type steps of 0.5 for luminosity classes I, III,

[1]We use the 2-dimensional cubic Clough-Tocher interpolator to interpolate from $(T_{\rm eff},\ \log\, g)$ to $\log\, L$ or $(T_{\rm eff},\ \log\, L)$ to $\log\, g$. We use 1-dimensional linear interpolation/extrapolation to map stellar spectral type, converted to a number as described in the text, to any of $T_{\rm eff}$, $\log\, g$, or $\log\, L$.

and V. When searching this table for parameters for a given spectral type, we first look for an exact match to the search query. If the query is for B3 or earlier, we extrapolate parameters using the O3–O9.5 data for that parameter for the given luminosity class. For extrapolation, the spectral type is converted to a number by converting "O" to 0 and "B" to 10 and adding this number to the sub-type following the method of Vacca et al. (1996) (who also provides a separate calibration). We implement a "memoization" scheme to avoid repeated extrapolations. Other calibrations, including those by Vacca et al. (1996) or Sternberg et al. (2003), could be used here behind the abstraction barrier of the lookup table class. In this way, `scoby` is flexible to future developments in spectral type calibration without needing to be completely rewritten. The diagram in Figure 4.1 shows the Vacca et al. (1996) calibration (which were also used by Sternberg et al. 2003) alongside the Martins et al. (2005) calibration which we use.

We note that some catalogs we have used actually list the $T_{\rm eff}$ and bolometric luminosity values as observationally measured quantities in addition to spectral types. For these cases, `scoby` has the flexibility to prefer these values to those obtained via calibration tables.

We use stellar wind properties from the models and tables by Leitherer et al. (2010), which are the same data used for the widely adopted Starburst99 software (Leitherer et al., 2014). The PoWR models, which we will describe shortly, assume the mass loss rate for all stars. The Leitherer et al. (2010) tables of wind properties provide mass loss rate $\dot{M}$ and wind terminal velocity v_∞ for O and B stars of type B3 and earlier and of class I, III, and V. The models are gridded in $T_{\rm eff}$ and L, but the coverage of parameter space is not even and, while spectral types are tabulated for each model, some types are assigned to multiple models. Instead, we take $T_{\rm eff}$ and L values from the spectral type calibration and select the closest wind model using a 2-dimensional interpolation in $(T_{\rm eff},\ \log\ L)$ parameter space. We derive mechanical luminosity as $1/2\ \dot{M} v_\infty^2$

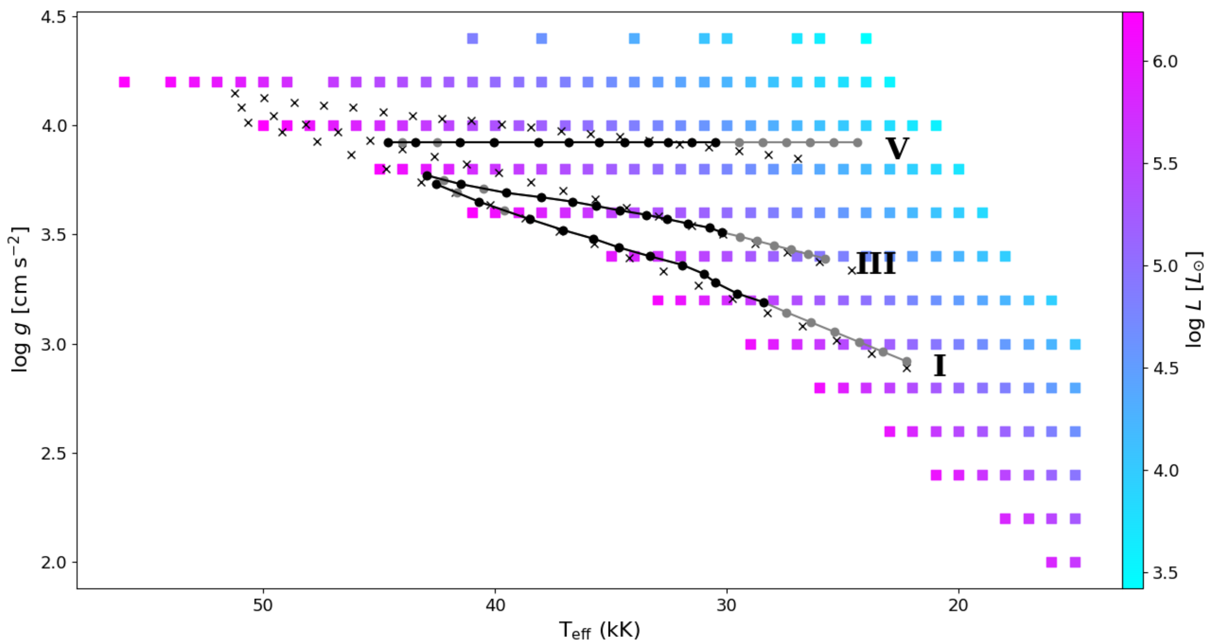

Figure 4.1 Colored squares show the model coverage of the PoWR stellar atmosphere models, which are gridded in $T_{\rm eff}$ and log g. The color of the square represents the bolometric luminosity associated with that model. The black circles connected with lines show O3–O9.5 stars (from left to right) according to the models by Martins et al. (2005). The grey circles which extend each track to the right show B0–B2.5 extrapolated (and O3.5 and O4.5 interpolated) from the Martins et al. (2005) values as described here in the text. Black Xs show O3–B2.5 using the calibration by Vacca et al. (1996); note that these are somewhat hotter and have higher surface gravity, as explained by Martins et al. (2005). Each track represents a luminosity class labelled on the right.

and momentum flux as $\dot{M}v_\infty$.

We obtain calibrated theoretical stellar spectra from $\lambda \sim 10\ \mu$m up to $\lambda \sim 120$ Å (0.1 keV) from the PoWR grid of OB stellar atmosphere models (Hainich et al., 2019; Sander et al., 2015). These models are gridded in $T_{\rm eff}$ and $\log g$ and their distribution in this parameter space is shown in Figure 4.1. We take the parameters from the spectral type calibration and interpolate onto a grid of $(T_{\rm eff},\ \log g)$ to select the nearest model. Each PoWR model is also associated with a bolometric luminosity L, so we can effectively re-index the PoWR grid in terms of $(T_{\rm eff},\ \log L)$. In the case that $T_{\rm eff}$ and L are available as measured quantities, we interpolate from the known $(T_{\rm eff},\ \log L)$ to the nearest model using the re-indexed grid. The model spectrum can be integrated or manipulated in a variety of ways; most commonly, we integrate the FUV radiation field between 6–13.6 eV or the ionizing photon flux $>$13.6 eV.

We demonstrate with Figure 4.1 that the disparity between different sets of calibrations is larger than the distances between a calibrated spectral type (black circle on the diagram) and the nearest PoWR model (colored square). This means that the uncertainty introduced by any of our interpolations or extrapolations is insignificant compared to calibration uncertainty based on stellar atmosphere theory.

After linking together the calibration tables, wind property models, and atmosphere models, we have a complete map of OB spectral types to radiative and mechanical feedback properties.

We demonstrate the agreement of `scoby` with alternate methods of deriving feedback properties in Figure 4.2. We compare the FUV luminosity, which is used to find G_0 around the star/cluster, of OB spectral types from `scoby` to those derived using the method by Schneider et al. (2023) in which the blackbody function at the star's effective temperature is integrated between 6–13.6 eV, divided by $\sigma_{\rm SB}T^4/\pi$, and multiplied by the total luminosity of the star. We obtain the effective temperature and total luminosity from the Martins et al. (2005) calibration, though as we point out above, these can be obtained observationally. We compare the ionizing photon emission rate Q_0 from `scoby` , computed by integrating the flux density divided by $h\nu$ above 13.6 eV, to values from both the Martins et al. (2005) and Sternberg et al. (2003) models. We find that `scoby` generally agrees well with the other methods and models. The FUV luminosities from `scoby` include all the spectral features that cause the spectrum to deviate from an ideal blackbody. The ionizing photon rates from `scoby` agree more closely with the models by Martins et al. (2005) than the models by Sternberg et al. (2003) do.

4.2.2 Interpretation of Spectral Type Strings

`scoby` contains a sophisticated string parsing engine for interpreting spectral types from published catalogs. We typically access catalogs through Vizier or published as supplementary material accompanying a paper. Catalog access is independent of `scoby` and challenging to automate; we discuss this in Section 5.2.4. Spectral types are given as a text column and may include markers of uncertainty, such as dashes representing type or sub-type ranges or slashes, as well as peculiarity markers, such as the "((f))" in the type of the O3.5 V((f)) star which is the most massive member of NGC 6611 (see Appendix C.1 for some examples). None of the models we use handle any sort of spectral peculiarities, so we rid the spectral type strings of any peculiarity designations.

Our parsing engine handles uncertainty in spectral types with great care. While it would be simple to choose the first letter or number which appears and remove the uncertainty, we are

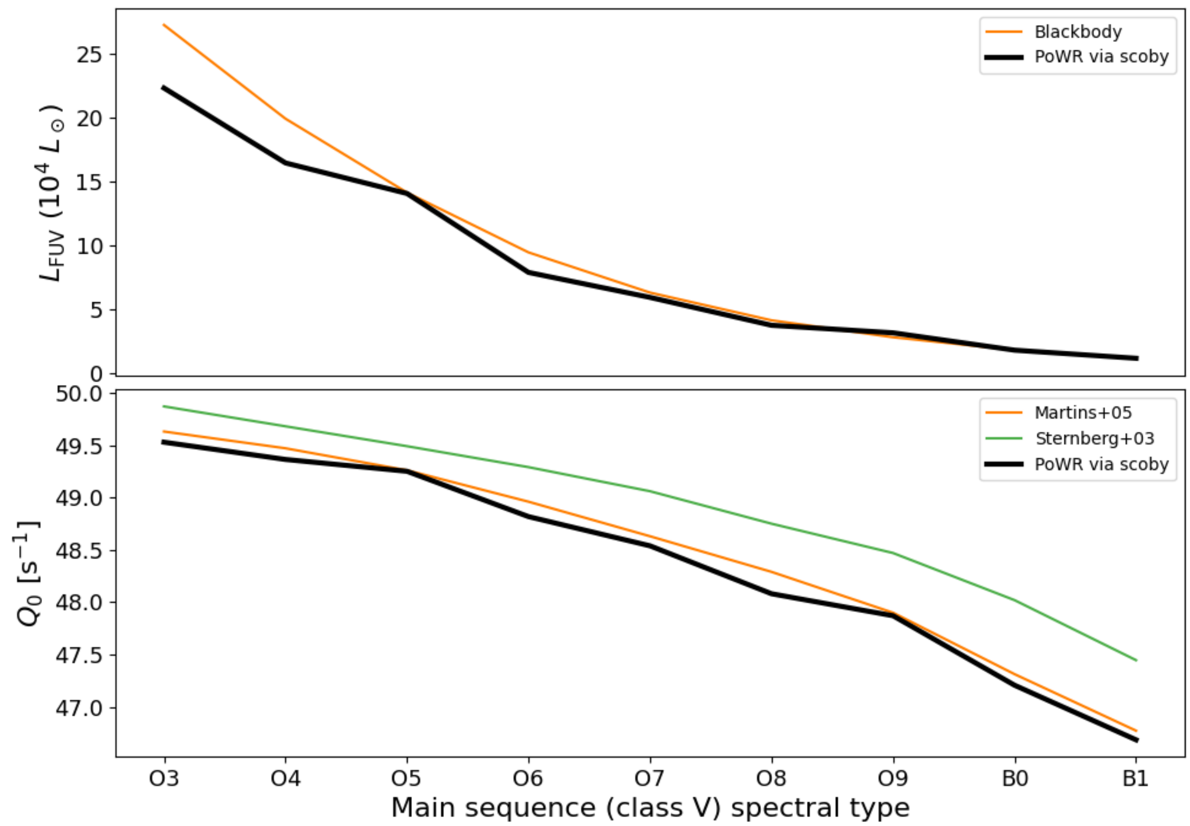

Figure 4.2 Two comparisons of stellar feedback properties from `scoby` to the same feedback properties derived other ways. The top panel shows FUV (6–13.6 eV) luminosity $L_{\rm FUV}$ and the bottom panel shows H-ionizing photon emission rate Q_0. Both are shown as a function of OB spectral type for luminosity class V (main sequence). More detail about the derivations of each property are given in the text at the end of Section 4.2.1.

interested in the propagation of this uncertainty into the feedback properties. The catalog authors published uncertain types as their most faithful interpretation of the data, and we should use their types as stated as best as possible rather than arbitrarily choosing a type from a list or range.

We begin by splitting up multiple systems (binaries, etc) and creating a list of each member of the system containing the single star spectral type. The list contains a single item for a single system and two items for a binary system, but can theoretically be arbitrarily long—NGC 6611 contains a triple system according to the catalog by Stoop et al. (2023). For each single star type in the list, we then interpret the uncertainty markers. We interpret slashes (e.g. O3/4 or O3 III/V) to mean "or," and so we create a list of "possibilities" for each single star type and add both options to the list. For example, a type of O3/4 V would produce the possibilities O3 V and O4 V, and a type of O5/5.5 V/III (MSP 18 in Westerlund 2; see #743 in the Table 3 by Mohr-Smith et al. 2015) would produce four possibilities: O5 V, O5.5 V, O5 III, and O5.5 III. We interpret dashes as ranges between the two types or sub-types in half-type steps and add them to a list of possibilities as described above. A type of O3-4 V would produce possibilities of O3 V, O3.5 V, and O4 V. Only luminosity classes of I, III, and V are resolved, so a type of O5 III-V would be interpreted the same as O5 III/V and produce O5 III and O5 V, for example. Combinations of slashes and dashes on different parts of the type can be interpreted (e.g. O4-6 I/III) as can dashes which "cross" letter types (e.g. O9-B1 would produce O9, O9.5, B0, B0.5, B1) and multiple slashes (e.g. O9/O9.5/B1), but multiple slashes or dashes referring to the same component of the type are not supported (e.g. O4-5/7-8) nor would we expect these to appear.

Our parsing engine is designed to handle a variety of cases which we have encountered in the handful of catalogs we have processed, but unforeseen cases may arise and can be handled manually by, for example, replacing the string before `scoby` processes it. Our interpretation of uncertainties and the examples we give are based on a straighforward logical understanding of the spectral type system rather than a complex physical interpretation. For example, we interpret the series of O and B types and luminosity classes I, III, V as linear sequences in which the relationship between, e.g., class I and III is the same as the relationship between class III and V.

The parsing engine produces, for each star system[2] in the cluster, a list of system members (one for single system, two for binary, etc). For each system member, there is a list of possibilities based on type uncertainties. An original type of O5 V will be processed into a single member with one possible type of O5 V, while a binary type O4/5 V + O9.5/B0 V will be processed into possibilities (O4 V, O5 V) and (O9.5 V, B0 V). The individual types in each possibility list do not contain peculiarities, refer to 1 single star, and are not uncertain. Each of these can be unambiguously assigned stellar properties using the calibration tables.

4.2.3 Assignment of Stellar Properties

For each individual star in each system, and for each possible type that star may have, we calculate the FUV luminosity, ionizing photon flux, mechanical luminosity, stellar mass, and any other desired properties which can be derived from the models. When a property of a system is queried, a random possibility is chosen from each possibility list for each member 1000 times and the median is used as the result. The 16$^{\mathrm{th}}$ and 84$^{\mathrm{th}}$ percentile values are used as the lower and upper uncertainty limits, respectively. Properties are then summed across binary/multiple systems.

[2]Terms here may be confusing as there are several hierarchical levels at this point. A cluster contains a number of star systems. A system contains one or more stars. A star is a component of a system and may have multiple possible types depending on uncertainty signifiers assigned by the catalog author. A possibility, or possible type, refers to a discrete type for a single star.

scoby is typically run for an entire cluster of stars simultaneously. When a property is queried of the cluster, the cluster is "realized" 1000 times using the possibility lists of its members and the property is summed over the entire cluster for each realization. The median and uncertainties are calculated for the cluster-wide distribution of results. The cluster realization process overrides the individual star system realization process, so there is only ever one "realization" loop.

The process for aggregating cluster-wide properties follows a "map-reduce" framework such that an external "map" function can be inserted into the workflow. The main use case for this is creating a spatial image of the projected G_0 radiation field. scoby does not track star coordinates, so the coordinates must be handled externally by the user. A relatively simple function manipulating the FUV luminosity based on each star's sky coordinates can be written by the user and sent as an argument into a scoby method. scoby will use that function as a map function and does not need to "know" how it works as long as adheres to the scoby application programming interface. scoby can still realize the cluster multiple times (in this case, realize the map of G_0 1000 times) and obtain an uncertainty at each pixel in the G_0 map without needing to know that it is working with a 2-dimensional image for each star instead of a single value. To create a useful G_0 image realized 1000 times from all members in the cluster, scoby must work with intermediate arrays of $X \times Y \times 1000 \times N \sim 10^8$–$10^9$ elements where the size of the image $X,\ Y$ may be $\gtrsim 100,\ 100$ and the cluster may contain $N \sim 10$–100 members. Considering that a Python float is 64 bits or 8 bytes, this internal array can approach a few Gigabytes in size, and may exceed this if the image contains more pixels. Since this approaches the amount of RAM on a typical laptop, scoby implements an efficient memory management system using the numpy (Harris et al., 2020) library's memory mapping capabilities to prevent the Python kernel from using much slower swap memory or crashing when all memory is consumed. This framework and its flexibility, along with our strong abstraction barriers, ensure that `scoby` can be used for a variety of processes without needing to be modified internally to handle each one.

The `scoby` library is tested using the Python `unittest` framework. Each segment of the computational pipeline can be tested individually to ensure the entire system is working as expected. We compare final derived properties to other models or methods of calculation when possible, as shown in Figure 4.2 and described at the end of Section 4.2.1.

4.3 Software Usage

`scoby` has supported a number of studies: Tiwari et al. (2021), Emig et al. (2022), Slaughter et al. (2023), Karim et al. (2023), and Chapter 3 of this thesis. The code is publicly available on GitHub[3] with installation instructions. We have also made publicly available Jupyter notebooks[4] which show examples of how to use `scoby` including how to use it to make G_0 images.

4.4 Conclusion

The `scoby` library standardizes and automates a significant amount of work in the process of deriving feedback properties from observed clusters of massive stars. The software is written for flexibility and can expand its capacity in the future. `scoby` carefully handles uncertainty in spectral types, and the effects of uncertainty as it propagates into cluster-wide feedback properties are relatively unexplored. `scoby` offers plenty of potential for future feedback studies, and in the next Chapter, we detail one possible project.

[3]https://github.com/ramseykarim/scoby
[4]https://github.com/ramseykarim/scoby-nb

Chapter 5: Summary and Outlook

5.1 Summary of this Thesis

A central theme of this thesis is the importance of gas density structure to the coupling efficiency of stellar feedback to the dense gas. In Chapter 1 we outline the state of knowledge and what is at stake: to understand the impact of stellar feedback on the star formation environment, e.g. the nearby dense gas, we need to observe these systems in detail and study their PDRs to determine how energy is transferred across that threshold.

In Chapter 2, we start at the small scale and study the Pillars of Creation, parsec-scale columns and globules of dense gas left behind by the ionization front some Myr ago. We determine that they will remain for another Myr, evolving into free-floating globules (Schneider et al., 2016), before they are photoevaporated. Considering that the most massive stars in the $\sim$2 Myr old cluster may evolve into Wolf-Rayet stars or even supernovae in another one or two million years, before the Pillars are fully evaporated, the Pillars are relatively long-lived structures within the region.

The molecular gas in the Pillars is magnetically supported, but that gas has slowly slipped past field lines for a long time now and should collapse into dense cores, potentially stars, before the Pillars evaporate. Already, several YSO candidates are observed towards the heads of P1a and P2. Dense gas is shielded from rapid photoionization within the heads of the Pillars long enough to form more stars; this echoes the theoretical conclusions of Zamora-Avilés et al. (2019) and Whitworth & Priestley (2021).

Whether the Pillars would have formed stars had they not been compressed by ionization-driven shocks is difficult to say, since we don't know what that primordial pre-SF gas structure looked like. Studies of the YSOs at the tips of the Pillars (Indebetouw et al., 2007) suggest that some, but not all, are younger than the massive cluster and could have been formed due to feedback interactions with their natal clouds. Whether the Pillars would have formed the same kind of stars is even trickier to answer. It is very likely that the Pillars evolved from some primordial dense gas association; observing so many pillars and globules in such a small region indicates that there was probably a larger scale overdensity such as a filament which was evaporated head-on and not quite dense enough to ward off the ionization front like in the model by Whitworth & Priestley (2021). The dense gas there might have accreted more gas and formed stars anyway, had NGC 6611 not turned on, so it is tough to make the case that feedback from NGC 6611 facilitated more star formation. Two avenues of future work are necessary to tackle these sorts of questions. First, we need observations of a diverse array of pillars and other dense gas structures (filaments, swept-up shells, BRCs, globules, etc.) at different evolutionary stages and then we need to categorize or link them together with a theory of dense gas evolution near/within H II regions; see the project outlined in Section 5.2.1. Second, we need to develop simulations informed by these observations which can trace gas and star formation through evolutionary stages and address what-if questions about stellar feedback.

We zoom out into the larger Eagle Nebula in Chapter 3. Here we find a $\sim$10 pc filament with the M16 H II region erupting out of the sides. The PDR shell is seen 20 pc away in either direction, and low visual extinction towards the cluster as well as starlight leaking out of the front side of the bubble suggests that the foreground shell is very thin or broken open. The M16 bubble has expanded anisotropically, seeking out the low density lines of sight away from the filament, in accordance with the simulations of Fukuda & Hanawa (2000) and Zamora-Avilés et al. (2019) and the observations of NGC 7538 by Beuther et al. (2022) or G316.75 by Watkins et al. (2019).

On the sky, the double-lobe shape of the shell is reminiscent of bipolar H II regions (Bonne et al., 2022; Deharveng et al., 2015). However, bipolar H II regions form from sheets (Whitworth et al., 2022) and should have a visible dense gas ring where dense gas is swept up into a compressed ring-shell in the plane of the sheet. There is no such ring configuration observed towards the central H II region in M16, so we conclude that M16 is not a bipolar H II region. We propose in Chapter 3 that the cavity is shaped like a "biconcave disc," which also resembles the cavity formed in the simulations by Fukuda & Hanawa (2000). The simulations by Zamora-Avilés et al. (2019) show a turbulent medium not particularly swept up into a single shell anywhere, but certainly indicate that the H II region advances in every direction other than along the filamentary axis. This biconcave cavity, pinched between the remains of the dense natal filament, is novel to the H II region literature. Other than its implication in the simulations of Fukuda & Hanawa (2000), this natural conclusion to star formation within a ridge has not been explored. It must be observed in other regions and verified by simulations, and if it cannot be, then M16 must be carefully revisited to develop an alternative theory.

The particular shape of M16 notwithstanding, it is clear that plasma has vented out of the region and that the considerable stellar wind energy has not been efficiently transferred to the neutral gas. Dense gas structures like the Bright Northern Ridge, Pillars of Creation, and Spire remain neutral and have been potentially compressed further by stellar feedback. There is unilluminated filamentary gas above and below the H II region, so stellar feedback will probably not deplete the dense gas reservoir. Stellar feedback has, however, evacuated a large cavity around the filament, which must have put a stop to any further accretion like in the case of G316.75 (Watkins et al., 2019).

This thesis significantly advances the state of knowledge regarding both the Pillars of Creation as well as the greater M16 H II region and the N19 bubble. To push our knowledge even further, we need deep, detailed observational studies of handfuls of representative regions like these and the rest of the FEEDBACK survey paired with broad statistic-building surveys of different aspects of star formation and stellar feedback.

5.2 Future Work

We propose several relevant projects which extend or complement the work of this thesis.

5.2.1 Pillar Survey

The evolution of pillars must be studied to understand whether they can harbor significant next-generation star formation and what their presence indicates about the pre-SF dense gas structure. Studies have been conducted on multiple pillars in other regions, such as Carina by Klaassen et al. (2020) or Cygnus X by Schneider et al. (2016), but a cross-region pillar survey has not been made. Pillars, globules, and other similar features like bright rimmed clouds (BRCs) should be studied across multiple regions to look for similarities in morphology (double-tails like P3, helical bodies like Carlqvist et al. (2002) sees in the Rosette pillar, or velocity gradients along/across the pillar bodies), association (whether there are several pillars close together or if they are isolated), dense gas context (whether pillars seem to extend from unilluminated filament like in M16), or absence (what do regions with no pillars have in common).

I propose that the Pillars of Creation and the Spire in M16 were formed from density enhancements embedded within filaments or accretion flows, as indicated by the unilluminated filaments seen underneath them in the FIR (Hill et al., 2011). If this were the case for some class of pillars, their presence in other H II regions could indicate pre-SF density structure. That would indicate in M16 that NGC 6611 may have formed from a small hub-filament system (HFS) embedded within the larger GMF. There are other less obvious pillars in M16 to be studied as well which could support this hypothesis. A multi-region pillar survey would also test this theory by revealing whether this pattern is seen in other regions.

An additional question that a pillar survey can tackle is whether all pillars represent the same physical mechanism, or if they are instead set up by a few different types of conditions and coaxed into a column shape by common instabilities. For example, above we suggest that the pillars in M16 may have formed from dense clumps once embedded in filaments or accretion flows. However, the many small filaments observed near the Wd 2 cluster in RCW 49 are not aligned with any particular (resolved) dense gas structures and are not "grouped up" like the M16 pillars are; these may represent some other formation conditions or mechanism, such as RT instabilities or turbulent density perturbations shaped into pillars. The shaping mechanisms may be similar, like RDI, so that the end result is a common pillar shape. This question must be addressed with detailed attention paid to each pillar in a survey. The existence of single or multiple formation pathways impacts how pillars are interpreted as remnants of pre-SF gas structure, as discussed above.

The observations necessary to support this project are velocity-resolved molecular and atomic line maps, high-resolution mid- and far-IR images tracing cold and warm dust and PDRs, and photoionized gas tracers like 24 μm, radio recombination lines, or Hα, if it is not too extincted. These sorts of probes enabled the study in Chapter 2. Single-dish CO maps paired with archival IR data will reveal the molecular gas kinematics with some information about temperature and illumination. Observations of the [C II] line like those used in our research are ideal for disentangling the illuminated PDR phase from un-illuminated molecular gas.

5.2.2 Biconcave H II Regions

In Chapter 3, we propose that the M16 cavity is shaped like a biconcave disc with a diameter of $\sim$40 pc. Besides the simulations of Fukuda & Hanawa (2000), this is an unexplored H II region morphology. Further examples should be sought out to verify whether this is a common morphological outcome.

The FEEDBACK survey targets are good candidates for this, but even more candidates can be selected from spectroscopically unresolved images. M16's morphology could be deduced from optical/NIR, mid-IR, and FIR images. FIR shows both warm and cold dust, which trace PDRs and molecular gas. The ISM is generally optically thin in the FIR, so dust is detected all along the line of sight. Dense gas behind the H II region would be traceable. The Herschel archive holds a large quantity of suitable FIR data. Mid-IR images tracing PAH emission or ionized gas via hot dust (i.e. $\sim$24 μm) will highlight PDRs, and the considerable volume of high spatial resolution data in the Spitzer archive would be suitable. Most of the ISM is optically thin to mid-IR continuum, save for very high column density gas or bright mid-IR emitting gas. This can be useful for identifying whether certain dense gas features lie in front of or behind PDR emission, but also generally means that PDRs can be seen through moderate foreground extinction. Finally, optical or NIR data from a variety of telescopes is plentiful and publicly available. Any optical/NIR band will be sensitive to foreground extinction, which can be very helpful for identifying foreground and background sources (i.e. placing the Northern Cloud in front of M16 in Chapter 3). Optical images may prove tricky to use if there is considerable foreground extinction along the line of sight from dust unrelated to the H II region complex which obscures the entire region wholesale; it may be possible to use NIR images in these cases instead.

The key identifying features of a biconcave H II region would be similar to the bipolar H II region characteristics outlined by Deharveng et al. (2015): two PDR lobes separated by a perpendicular filament of dense gas. The major difference would be the ring of dense gas around the H II region in the plane of the filament, which would be present in the bipolar H II region but not in the biconcave H II region. The front half of the ring should absorb optical and potentially some mid-IR emission in front of the H II region, and both the front and back halves should appear in FIR emission. The ring should line up with the filament, as in RCW 36. The presence of a ring implies that the filament is really a sheet viewed edge-on, and the ring is the small, swept up shell in the plane of the sheet. This means that the H II region is a true bipolar H II region. The lack of a ring would corroborate our biconcave H II region theory, suggesting that the filament is a true filament in 3 dimensions and that the H II region has expanded everywhere along the plane to which the filament is normal.

Using the wealth of archival optical, mid-IR, and FIR images, candidates for other biconcave H II regions can be identified or the morphology can be ruled out as unlikely due to lack of candidates. Since the general observable characteristics mostly match those of bipolar regions, catalogs of bipolar regions would be a good place to start.

Follow-up evaluation of M16's morphology could include large-scale velocity-resolved [C

II] line observations to determine whether other shell fragments can be found outside the area observed by SOFIA. These observations would need to be at least as sensitive as our upGREAT observations and resolve the [C II] line to at least 1–2 $\mathrm{km\,s^{-1}}$ to identify line components separated by $\sim$10 $\mathrm{km\,s^{-1}}$, but spatial resolution need not be better than $\sim$1–5$'$ since the cavity is large. This sort of moderate spatial resolution [C II] data might be useful for evaluating other biconcave H II region candidates and may be achievable with balloon-borne experiments.

5.2.3 Bubble Morphology Census

The work of the FEEDBACK Survey must be continued so that we have a catalog of 11 instances of H II region and bubble morphology. Each study must be as detailed as those completed so far, since details are critical and looks can be deceiving. For example, it would have been easy to declare M16 a bipolar H II region on account of the two lobes, or even neglect them altogether since they are faint. In NGC 7538, Beuther et al. (2022) found multiple bubbles, but suspected that rather than each holding their own source, they were the anisotropic expansions of the same cavity into an inhomogeneous medium. This H II region catalog will help us understand common star formation outcomes and what sorts of broad classifications into which they fit. This can extend the bipolar H II region studies by Deharveng et al. (2015) and Samal et al. (2018) and fold in spectroscopically-resolved lines like CO and [C II]. The kinematic information held in the [C II] line is critical to the accuracy of these classifications, as it will break degeneracies such as whether a ring projection on the sky is a 3-dimensional ring or bubble in the sky, or whether clouds which are spatially connected in projection are kinematically related (i.e. P3 and the blueshifted stream in Chapter 2 or the Northern Cloud and filament in Chapter 3).

5.2.4 Cluster feedback capacity analysis with `scoby`

Among the key questions that can be answered by the FEEDBACK survey is how feedback effects and efficiency scale with the mass of the central cluster. Already we see that a bubble driven by one or two B stars tends to expand from thermal pressure from photoionized gas while O-type clusters inflate bubbles with winds. These findings are preliminary, and the main issue now is that there is no standardized approach to estimating stellar feedback.

Accurately quantifying the feedback capacity of the stars is essential to evaluating the effect of stellar feedback on the surrounding gas. It is established that the most massive stars dominate the stellar feedback, but it was found that in clusters with many O stars such as Wd 2 in RCW 49 (Tiwari et al., 2021), the mid-to-late O stars were plentiful enough to contribute significantly, but still not dominantly, to the feedback. The studies in the FEEDBACK survey take various approaches to selecting the relevant OB stars and use a variety of literature methods to derive feedback properties from spectral types. A more systematic approach to determining cluster masses is necessary.

The `scoby` software I developed to estimate stellar feedback is described in Chapter 4. The input to the software is a list of spectral types (and their coordinates, for some outputs) which must be obtained from a literature catalog of OB spectral types. There is no standard format for stellar catalogs in the literature. Online table/catalog synthesis software like VizieR attempts to address this, but the non-uniformity of the tables they aggregate means that they are at best an online interface to a literature table. Object identification inconsistencies exacerbate this problem. Most importantly, not all the stars in a given projected area are associated with a cluster; cluster membership must be confirmed with extinction and kinematic information, which is best obtained from literature. To state this more clearly: if you want a catalog of cluster members, you must find one or more papers in the literature which have studied and made a dedicated catalog of cluster membership.

Once a catalog has been identified for a source, the spectral types must be extracted. This may be relatively simple, if the catalog is accessed via the VizieR API in `astropy`, or slightly more involved if a text table must be machine-read in Python. For one catalog, this could take a few to few tens of minutes, depending on how much text comprehension must be done. Since, as explained above, there is no standard format for catalogs, this work must be manually repeated for catalogs from other sources.

The two steps outlined above make feedback estimation a labor-intensive process which must be conducted manually. The manual work produces a list of OB spectral types and positions. The `scoby` software I developed automates the rest of the process. The resulting feedback estimates should be systematically compared to estimates of thermal and kinetic energy in the gas and region mechanics (i.e., wind-driven, thermal expansion, etc.) and morphology (broken open, single bubble, inhomogeneous expansion, etc.). Imposing the same spectral type cutoff is important to comparing between FEEDBACK sources. An informative meta-study would investigate the particular choice of cutoff and its effect on the conclusions. Aggregating cluster catalogs for FEEDBACK sources and running them through the `scoby` software would make a good project for Master's student or an enterprising undergraduate.

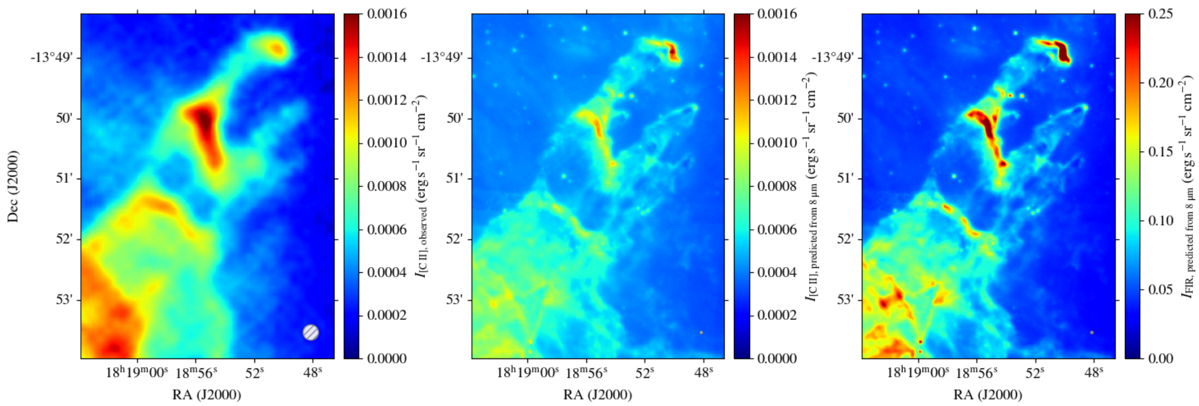

Figure 5.1 The left panel shows integrated SOFIA upGREAT [C II] towards the Pillars of Creation with its 15″ beam. The middle and right panels show scaled 8 μm emission using the correlations from Pabst et al. (2021) which models [C II] and FIR 40–500 μm at 1.5″ spatial resolution, revealing rich detail. The hypothetical [C II] map at the central panel, with all the spatial detail, can be kinematically resolved with an appropriate future observatory.

5.3 Distant Outlook

The future of far-IR PDR observation was rocked by the discontinuation of SOFIA and, with it, our ability to map and resolve the [C II] and [O I] lines at high spatial and spectral resolution. There is hope with balloon-borne missions like GUSTO and ASTHROS and the potential for an IR "probe" class space mission. GUSTO, which successfully landed after its flight over Antarctica, will shortly deliver a survey of ∼50 square degrees of the Galactic plane in [C II], covering ∼100 H II region bubbles which will greatly increase sample statistics (Walker et al., 2022). ASTHROS will observe the [N II] fine-structure line, which traces ionized gas within the H II region and will complement [C II] studies with information about the overall kinematics of the ionized phase and its response to feedback from massive stars. High spatial resolution [C II] observations, like those modeled in Figure 5.1 based on 8 μm data using the observed correlation provided by Pabst et al. (2021), would provide a wealth of detail for studies of parsec-scale Galactic gas structures within these bubbles.

In the meantime, there is still plenty of scientific potential left in the SOFIA upGREAT observations, even those which have been published. In my study of M16, I noted plenty of minor peculiarities whose pursuit did not fit well into my projects and time frames, such as the [^{13}C II] spectrum towards the MYSO in the Bright Northern Ridge.

The future of near- and mid-IR PDR observation will thrive with JWST online. Its spectroscopic coverage of PAH emission bands, H_2 lines, and ionized gas lines will facilitate deeper study of these components at high spatial resolution. Ground-based spectroscopically resolved CO rovibrational line mapping is another key ingredient for star formation studies, as evidenced by its importance to both projects in this thesis. While much attention in the radio and submillimeter has been rightfully devoted to pushing the limits of spatial resolution with ALMA and the ngVLA, there is great utility in single-dish mappers such as APEX and GBO, and many other international observatories such as PMO or Nobeyama, in tracing the dense gas structure of these star forming regions. We extend the same argument for the [C I] line, which can also be observed from the ground. Together, [C I] and CO probe the deep PDR and underlying unilluminated molecular gas and, with multiple molecular line transitions, the physical conditions in those phases. These velocity-resolved maps can enable detailed studies of feedback in individual sources or statistic-building surveys of many star forming regions.

It is not clear when we will next be able to put a far-infrared spectrometer on a steerable observatory above Earth's atmosphere. In the meantime, there is plenty of work to be done in preparation.

Appendix A: Facilities and Software used in this Thesis

A.1 Facilities

1. SOFIA / GREAT, upGREAT
2. APEX / LAsMA, LABOCA
3. CARMA
4. BIMA
5. Spitzer / IRAC, MIPS
6. Herschel / PACS, SPIRE
7. WISE
8. JWST / NIRCam
9. Purple Mountain Observatory
10. Nobeyama Radio Observatory
11. VLA
12. Chandra / ACIS

13. DSS2

A.2 Software

1. Scoby (`https://github.com/ramseykarim/scoby`; snapshot archived at `http://hdl.handle.net/1903/30441`)
2. Astropy (Astropy Collaboration et al., 2013, 2018, 2022)
3. Spectral Cube (Ginsburg et al., 2019)
4. PVextractor (`https://github.com/radio-astro-tools/pvextractor`)
5. Regions (Bradley et al., 2022)
6. Numpy (Harris et al., 2020)
7. Scipy (Virtanen et al., 2020)
8. Pandas (McKinney, 2010)
9. Matplotlib (Hunter, 2007)
10. PDRT (Pound & Wolfire, 2023)
11. POWR (Hainich et al., 2019; Sander et al., 2015)
12. SPEX (Kaastra et al., 1996)

Appendix B: Regarding the Study of the Pillars of Creation

B.1 Measured Main Beam Temperatures and Spectra

Table B.1 lists coordinates and Table B.2 lists measured main beam temperatures for the 12 locations for which we give column and number densities in Table 2.3. Their positions are shown in the leftmost panel of Figure 2.12. The Table B.2 measurements are all given at their native resolutions. Figures B.1 and Figure B.2 show most line spectra towards these locations. The spectra are all shown convolved to the [C II] beam (15.4″), except for the CO(J=3–2) lines which are shown at their native resolutions (∼20″).

B.2 Systematic Velocity and [CII] Background

Key to understanding the [C II] line spectra through the Pillars is understanding the atomic gas that surrounds the them. Foreground and background elements may appear in the spectra towards the Pillars, and must be acknowledged and accounted for in any meaningful interpretation of Pillar spectra. Around the velocity of P1, $\mathrm{V_{LSR}} \sim 25\ \mathrm{km\,s^{-1}}$, the surrounding area is also bright in [C II], particularly east of the Pillars as seen in the channel maps in Figure 2.4. The spatial extent of this component indicates that $\mathrm{V_{LSR}} \sim 25\ \mathrm{km\,s^{-1}}$ may be a region-scale "systematic velocity" related to the bulk velocity of the clouds from which the star cluster was

Location Name	Right Ascension (hh:mm:ss)	Declination (dd:mm:ss)	Background
P1a-edge	$18^{h}18^{m}50^{s}.1147$	-13°48′50.286″	N
P1a-center	$18^{h}18^{m}51^{s}.0331$	-13°48′56.830″	N
P1a-E-thread	$18^{h}18^{m}52^{s}.9684$	-13°49′08.407″	N
P1a-W-thread	$18^{h}18^{m}52^{s}.3583$	-13°49′22.366″	N
E-Horn	$18^{h}18^{m}54^{s}.8134$	-13°49′36.870″	S
W-Horn	$18^{h}18^{m}53^{s}.6043$	-13°49′58.878″	S
Shared-Base-E	$18^{h}18^{m}55^{s}.2294$	-13°50′07.362″	S
Shared-Base-Mid	$18^{h}18^{m}55^{s}.2857$	-13°50′32.292″	S
P2-head	$18^{h}18^{m}49^{s}.3745$	-13°49′57.146″	N
P2-clump	$18^{h}18^{m}51^{s}.5274$	-13°50′28.378″	N
P3-head	$18^{h}18^{m}49^{s}.2048$	-13°50′43.792″	N
Ridge	$18^{h}18^{m}58^{s}.0793$	-13°51′27.241″	S

Table B.1 Coordinates are J2000. Background column lists whether the northern or southern background sample was used for column density (Section 2.5.1.2) and spectral (Appendix B.2) subtraction.

Location Name	[C II]	[O I]	CO (1–0)	^{13}CO (1–0)	C^{18}O (1–0)	CO (3–2)	^{13}CO (3–2)	CO (6–5)	HCN	HCO^{+}	CS	N$_2$H^{+}
P1a-edge	43.6	13.4	43.8	12.0	0.7	26.9	11.2	9.5	6.1	6.2	2.2	1.8
P1a-center	37.1	11.5	104.2	27.5	3.3	41.7	23.1	19.5	22.6	22.1	12.8	3.6
P1a-E-thread	27.8	7.1	51.0	13.9	0.5	28.3	10.4	13.1	6.6	5.6	3.2	1.6
P1a-W-thread	18.1	7.5	52.8	18.3	0.9	19.5	9.2	5.1	6.9	4.9	2.8	1.1
E-Horn	39.3	7.6	81.1	16.3	0.4	20.1	6.3	16.7	9.1	7.1	6.4	1.3
W-Horn	15.8	10.8	82.9	28.7	1.5	15.7	9.1	11.5	12.8	10.7	7.9	2.2
Shared-Base-E	47.9	8.6	80.7	11.7	1.3	31.4	10.5	17.0	6.5	6.1	2.9	1.3
Shared-Base-Mid	38.1	6.0	33.7	5.4	0.6	28.9	9.6	11.5	1.7	2.0	1.9	1.2
P2-head	18.2	8.0	68.6	20.9	1.8	24.5	13.5	17.3	14.6	14.1	7.0	3.7
P2-clump	22.2	···	47.8	17.4	1.3	35.4	15.4	15.9	7.3	7.0	5.3	1.3
P3-head	11.5	···	59.2	26.6	1.3	18.8	8.9	9.7	11.8	10.3	8.1	1.4
Ridge	40.7	···	···	···	···	30.6	19.0	20.4	5.7	5.5	2.5	1.4

Table B.2 Peak main beam temperatures in Kelvins from lines at their native resolutions, which are listed alongside RMS temperatures in Table 2.1. The positions are shown in the leftmost panel of Figure 2.12. Since these are calculated as the maximum value from each spectrum, a measurement 1 or 2 times the RMS noise in Table 2.1 should be regarded as a potential nondetection; the spectra in Figures B.1 and B.2 provide additional context. The N_2H^+ measurements are from the satellite line (J, F1, F) = (1–0, 0–1, 1–2) since the brightest lines at the center of the bandpass overlap (see Section 2.2). The Ridge is outside the half-power level of BIMA's primary beam, so the CO(J=1–0) measurements there are not given. The listed [C II] measurements have not had any background subtracted from them.

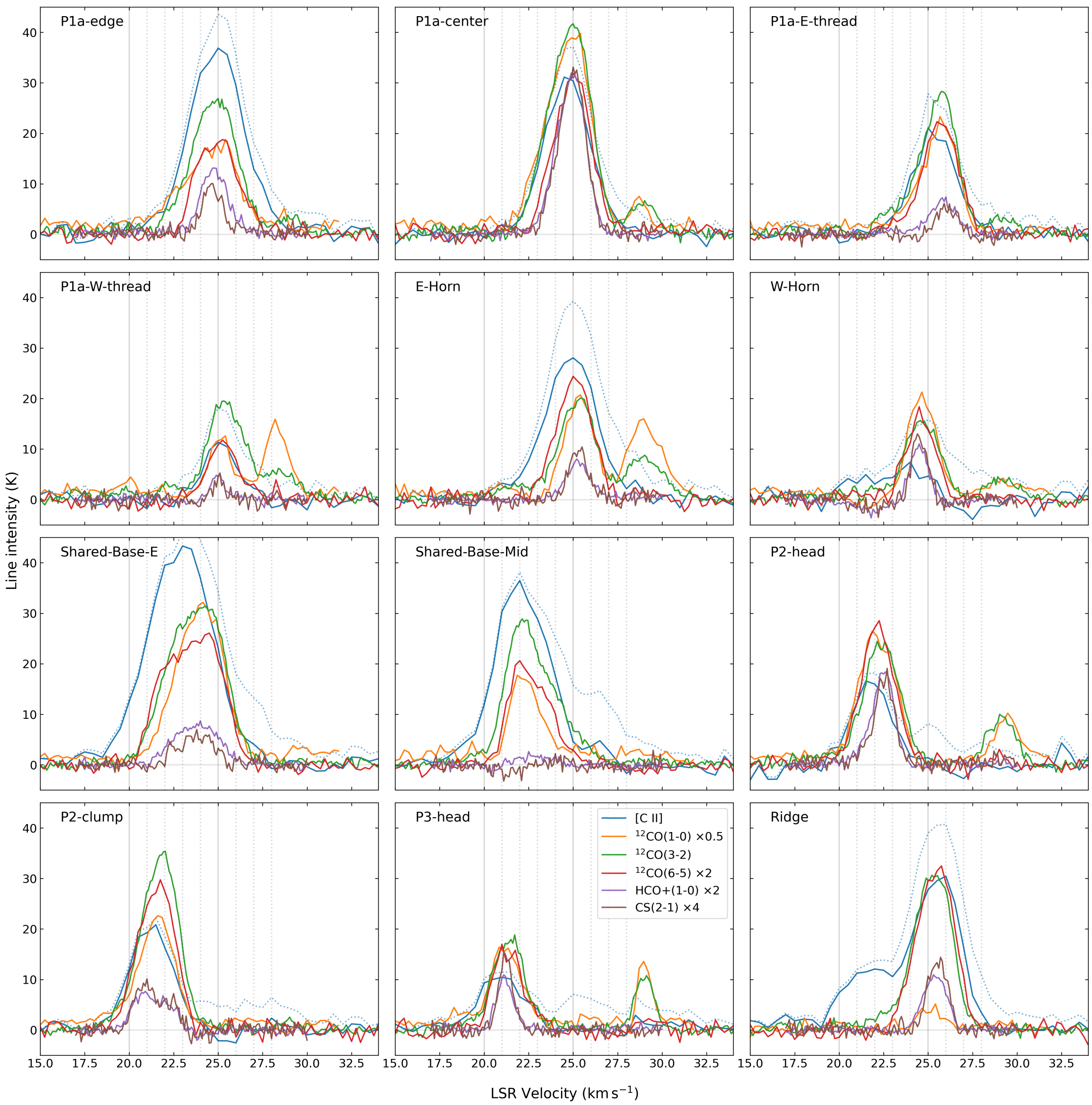

Figure B.1 Spectra observed towards the pillars in several lines. All data are convolved to the [C II] resolution, except CO(J=3–2) which is shown at its native resolution. Locations are those shown in the leftmost panel of Figure 2.12 and listed by name in Tables 2.3 and B.2. The [C II] line spectra are shown with a dotted line before and a solid line after subtracting out the background as described in Appendix B.2; the second column in Table 2.3 lists whether the northern or southern background was subtracted. Vertical lines mark every 1 $\mathrm{km\ s^{-1}}$ between 20–28 $\mathrm{km\ s^{-1}}$. Several lines/locations show additional components separated from the peak emission, such as CO at $\mathrm{V_{LSR}} \sim 29\ \mathrm{km\ s^{-1}}$ towards multiple positions or [C II] at $\mathrm{V_{LSR}} \sim 20$–$23\ \mathrm{km\ s^{-1}}$ towards the Ridge; all such components originate from background features identified in channel maps.

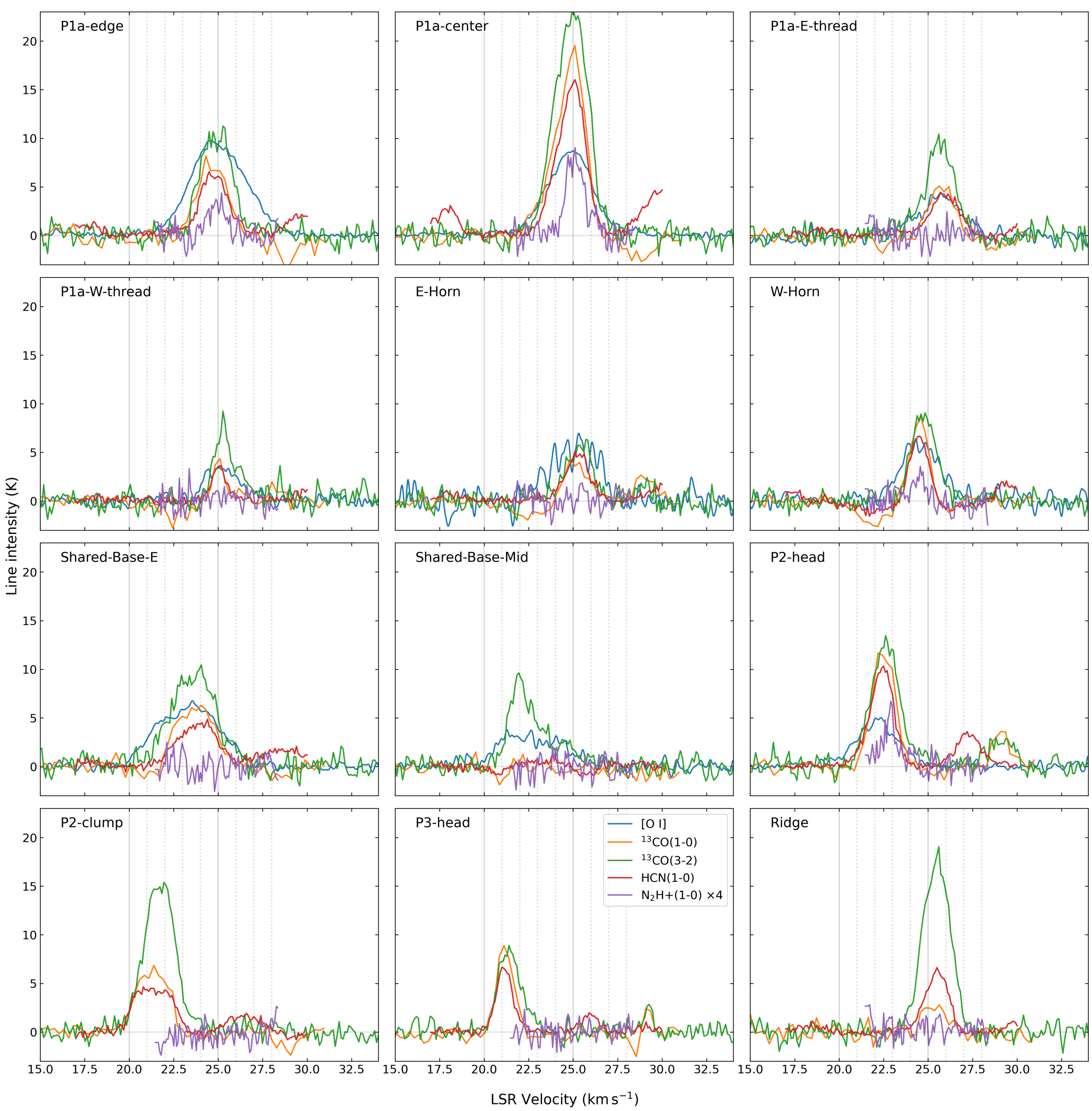

Figure B.2 Same as Figure B.1 showing different species. All data except ^{13}CO(J=3–2) are convolved to the [C II] resolution. The line intensity axis spans a smaller range here. Multiple satellite lines appear in the HCN spectra. The N_2H^+ line is the satellite line (J, F1, F) = (1–0, 0–1, 1–2). The CO emission around $\mathrm{V_{LSR}} \sim 29\ \mathrm{km\ s^{-1}}$ is from a background feature.

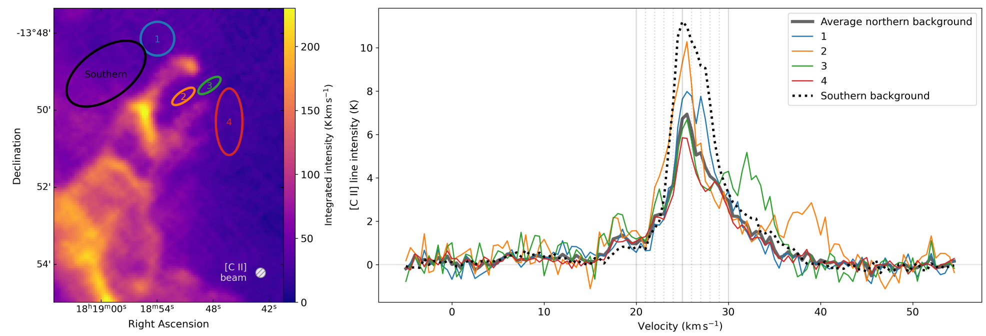

Figure B.3 *(Left)* The [C II] integrated intensity between $\mathrm{V_{LSR}} = 18\text{-}27\ \mathrm{km\ s^{-1}}$, the same interval shown earlier in Figure 2.2, is shown in color. The four northern background regions (numbered) and the single southern background region are outlined. *(Right)* The mean spectrum from within each individual background region on the left panel, labeled accordingly. The "Average" background spectrum drawn in the bold, solid line is the average across all pixels in the numbered northern regions and does not include the southern region. Vertical lines mark every $1\ \mathrm{km\ s^{-1}}$ between 20–30 $\mathrm{km\ s^{-1}}$.

born.

We investigate the background [C II] spectrum around the Pillars by integrating spectra within several handpicked, parsec-scale regions shown in Figure B.3, selected for their proximity to the Pillars and, for the four northern regions, lack of distinct morphological features in the channel maps. The southern region is selected for its proximity to P1b and inclusion of the diffuse feature which we suspect lies in the foreground/background of P1b and other "southern" features. The regions are kept at least one beam ($15''$) away from the optical/NIR edges of the Pillars, which ensures that the regions don't overlap with the Pillars and include Pillar emission while remaining close to the Pillars so that the background spectra are relevant to the Pillars. The [C II] spectra from within these regions include significant emission around $\mathrm{V_{LSR}} \sim 25\ \mathrm{km\ s^{-1}}$, demonstrating that the Pillars are not the only source of emission in those channels.

The peaks of the background line profiles are thin ($\sim$1–3 $\mathrm{km\ s^{-1}}$), which indicates that most of this emission originates from the atomic gas (Cuadrado et al., 2019). The ionized H II phase contributes $\sim$10% of the total [C II] emission on large ($\sim$500 pc) scales (Tarantino et al., 2021). [C II] line profiles from the diffuse, ambient H II region should have $\sim$10 $\mathrm{km\ s^{-1}}$ widths reflective of the turbulent velocity dispersion observed by Higgs et al. (1979) towards the M16 H II region in lines of H and He. The background [C II] line profiles have wings that could arise from a wide, low-intensity component originating from the ambient H II region. This will be explored in greater detail in a future study. The characteristic PDR velocity $\mathrm{V_{LSR}} \sim$ 25–26 $\mathrm{km\ s^{-1}}$ of the region surrounding the Pillars may originate from pre-cluster dynamics and poses a unique challenge for the analysis of P1, which lies almost exactly at this velocity.

On a more local scale around the Pillars, this diffuse emission is even brighter towards the southern end of P1, near P1b. Channel maps between $\mathrm{V_{LSR}} \sim$ 24–28 $\mathrm{km\ s^{-1}}$ indicate structure immediately east of P1b, as it is not clear if the structure is related to the Pillar system. This feature has a wider line profile than the northern background samples, as we see in the comparison in Figure B.3.

In order to mitigate adverse effects of this background on our analysis of the Pillars, we conduct a background sampling and subtraction in order to help isolate [C II] emission from the Pillars themselves. We use the average of all pixels in four northern regions, drawn with the bold, solid line on the right panel of Figure B.3, to correct "northern" targets such as P1a, P2, and P3. We use the average from within the southern region to correct spectra towards P1b and the Ridge; see the Background column of Table B.1. These corrections are made for all [C II] spectra we show going forward and particularly throughout the kinematic analysis in Section B.3 where the shape of the line is important to our analysis. We do not account for optical depth while subtracting background spectra; we find in Section 2.5.1.2 that [C II] has an optical depth $\lesssim 1$, so adverse effects of background subtraction on line shape should be minimal. We do not make a channel-by-channel spectral subtraction while calculating $\mathrm{C^+}$ column densities in Section 2.5.1.2.

Some distinct components are identified in the background spectra from Regions #2 and #3 around 30–40 km/s in Figure B.3. Referencing the channel maps in Figure 2.4, these can be associated with a morphologically distinct north-to-south strip of redshifted gas which does not appear directly associated with the Pillars. The influence of this redshifted component is not seen in the averaged background spectrum, and the feature itself has very little overlap with P1, so it should not adversely affect our background subtraction.

The background subtraction proves to be useful in determining whether characteristics of the [C II] line profile should be associated with the Pillars. The molecular and (unsubtracted) [C II] spectra through the pillar bodies, and particularly through the head of P1 in Figure B.1, differ noticeably in that the [C II] line profile has more emission at higher velocities than the other tracers. No shift is detected in the [C II] line center w.r.t. the molecular lines, so the asymmetry in the line profile must be limited to the low-intensity line wings. If we were to associate all [C II] emission towards the head of P1 with the pillar itself, then we would conclude that the PDR layer has a significantly different kinematic signature than the deeper molecular gas layers, thus resulting in an extended red tail in the [C II] spectrum. However, when we apply the [C II] background subtraction, we find that the redshifted [C II] tail disappears and the [C II] spectrum looks much more like the molecular lines, suggesting that the dynamics of the PDR and molecular layers are not dissimilar. The background identification and subtraction is therefore necessary in order to identify Pillar-related spectral characteristics and avoid ascribing background emission to the Pillars.

Jackknife tests using combinations of these and other background samples confirm that the choice of background samples doesn't upset results, i.e. change the profile and velocity of lines too much, but reveal limitations in our ability to make specific and precise claims about background-subtracted [C II] line intensities since the background varies throughout the system (see the velocity shift between Regions #1 and #2 in Figure B.3).

B.3 Kinematics and Geometry of P1a

P1a is composed of three morphologically and kinematically distinct components, making it the most complex structure in the pillar system. A 3D geometrical model, informed by an in-depth kinematic analysis of P1a, is necessary to contextualize other physical characteristics derived from our observations. We fit Gaussian line profiles to observed [C II] and molecular line spectra in order to quantify, or at least approximate, characteristics of the observed profiles. In advance of this kinematic modeling, we subtract channel-by-channel from [C II] spectra the background identified near the Pillars. We describe the identification and correction in Appendix B.2. Since we only model spectra towards P1a, we only use the northern background sample described in Appendix B.2.

B.3.1 Kinematic Modeling Towards P1a

We fit 1, 2, 3, and 4 component models to each HCO^+ and [C II] spectrum in a $\sim$ 1' box surrounding P1a ($\sim$500 [C II] spectra, $\sim$10,000 HCO^+ spectra). For each line, all spectra were modeled using the same model template and initial conditions. The strength of this unsupervised pixel grid fit is that real, physically meaningful patterns may emerge from this large number of modeled spectra. We visualize the fitted models in (RA, Dec, Velocity) space by plotting each pixel's fitted component line centers. There are 1–4 fitted components per pixel depending on the model template and the number of components with sufficiently large amplitudes with respect to the noise. We plot these components using a 2D histogram by projecting along Dec to view the RA-Velocity plane; due to the components' spatial orientations, we find the RA-Velocity projection easier to interpret than the Dec-Velocity projection and so we limit our discussion to the former. These histograms are similar in orientation and meaning to PV diagrams.

These projections, shown in Figure B.4, all illustrate a spread of components towards the east which move kinematically closer together towards the Merge Point in the west, where they appear to merge together in the [C II] series and the HCO^+ 1-component projection. In the HCO^+ model series, three line center groupings are observed towards the eastern side of the image: one at $\mathrm{V_{LSR}} \approx 25.5\ \mathrm{km\ s^{-1}}$, one at 24.5–25 $\mathrm{km\ s^{-1}}$, and one at 23.5 $\mathrm{km\ s^{-1}}$ in the east with a strong gradient towards higher velocity to the west. These velocities and their gradients are consistent with those of the two Threads and the Cap which we observed in the channel maps of most lines. These groupings are observed in the 1, 2, and 3 component figures, and these groupings do not fundamentally change or disappear even when a 4th component is made available. In the [C II] model series, we only observe two groupings at $\mathrm{V_{LSR}} \approx 23.5\ \mathrm{km\ s^{-1}}$ and 25.5 $\mathrm{km\ s^{-1}}$, and as with HCO^+ this pattern persists even when more than two components are allowed.

The HCO^+ results show a shift in behavior towards the western part of the head, near the Merge Point in Figure 2.1, between 1 and 2 allowed components. In the 1-component models, we observe the kinematic merging of the high- and low-velocity component groupings into a single group around $\mathrm{V_{LSR}} \approx 24.7\ \mathrm{km\ s^{-1}}$. When we make a second component available to the HCO^+ line models, we see the three eastern velocity groups converge towards the same velocity but then dramatically shift into a two-component grouping towards the Merge Point where the 1-component models converged. This pattern persists even as 3 and 4 components are available to the HCO^+ spectra. This is peculiar for two reasons: first, it is at odds with the picture of several

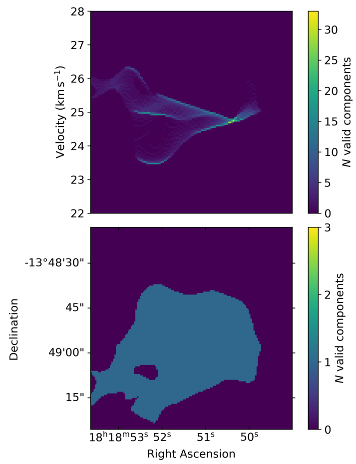

HCO$^+$ 1 component

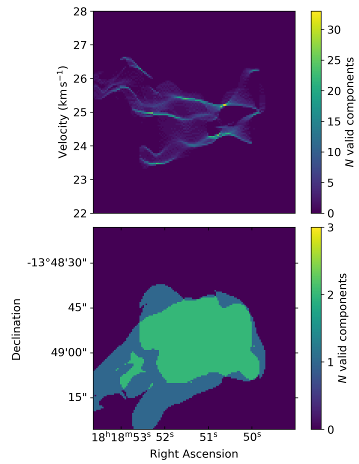

HCO$^+$ 2 component

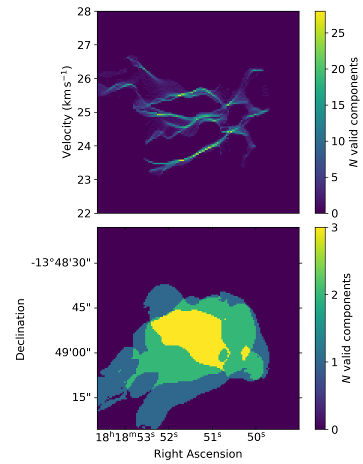

HCO$^+$ 3 component

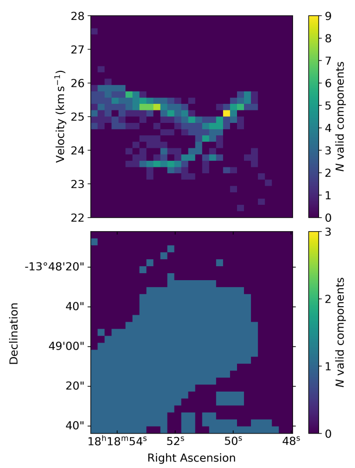

[C II] 1 component

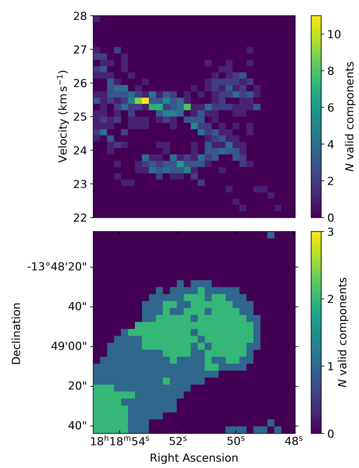

[C II] 2 component

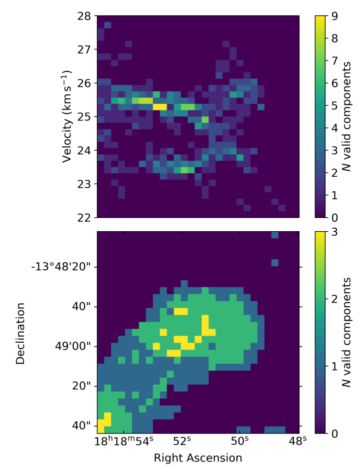

[C II] 3 component

Figure B.4 RA-Velocity projections of the 1, 2, and 3 component line center solutions. 4 component model results are not shown here but are not significantly different than the 3 component results.

components merging together which we see in the HCO^+ single component model and all the [C II] models; and second, it relies on an abrupt shift in component velocity coupled with the abrupt disappearance of an entire component. We suspect that, rather than a physical phenomenon, this is a sort of computational "phase shift" within the solution space of the model fit in which the result abruptly transitions from one solution to another between nearby pixels. A more detailed investigation of the affected spectra is required in order to tell if the components really do merge and the HCO^+ "phase shift" is really just a computational artifact, or if the situation too complex for us to make such a claim. For a few locations towards the head, we perturbed the models' initial conditions and examined the fitted models to check whether our results are robust and whether we come to the same conclusions as described above. Through this more supervised method, we find that all results from the unsupervised method are sound except those towards the northwestern corner of the head around the Merge Point, where the solution space phase shift occurs. We find that the 2-component solutions towards that location are not unique and that a single component works comparably well.

We conclude that HCO^+ line spectra towards the eastern and southern parts of the head can be decomposed into three distinct components in all the molecular lines, and the components are consistent from line to line. The [C II] spectrum towards these locations can be decomposed into two components which generally correspond to the highest and lowest velocity molecular gas components (the Eastern Thread and the Cap). HCO^+ line spectra towards the Merge Point can be decomposed into 1–3 components with similar reduced χ^2 and so a single component is the least complex solution. The three components merge into one towards the Merge Point, as we see in the single-allowed-component panel in Figure B.4, and become too indistinct to fit separately.

B.3.2 Geometry of P1a

We interpret these results to originate from a pillar head composed of three distinct molecular gas components, the two Threads and the Cap, embedded in a warm PDR gas envelope. We observe the two Threads as spatially separate entities south of the pillar head and we can distinguish the components in the eastern and southern regions of the head in velocity, even though they are spatially blended. Due to its strong velocity gradient, the Cap is the most kinematically separated from the rest of the head to the east. At that location, we observe the widest line profiles which we are able to decompose into three components. These spectra can also be fit with two components, where one represents the Cap and the other wider component represents a merged-Thread component, but they cannot be well fit with a single component.

These three morphologically distinct components spatially overlap towards the head and kinematically overlap towards the northwest part of the head, indicating that they are physically merged towards the northwest. The gradients of the components are similar in absolute value but not in sign and are organized radially around the Merge Point. Line profiles in every line towards the Merge Point are consistent with a single emitting component, while line profiles towards other locations of the head cannot be modeled by a single component. We detect N_2H^+ and $C^{18}O$ emission and high ^{13}CO column density towards the Merge Point, and all lines peak in brightness near that region. The N_2H^+ detection implies sufficiently cold, shielded gas in addition to high column density, which is more likely towards a physical intersection of clouds rather than a projected stack of clouds.

Component interactions and overlays like this one may be responsible for the broad [C II] line profiles observed towards other regions. Ossenkopf et al. (2013) describe "macro-turbulent" motions, which cause a greater portion of the [C II] line to be optically thick and create a broader line profile than expected for opacity-broadening. Our line profile analysis and high spatial resolution observations reveal the individual components towards P1a, but they are likely obscured by geometry or insufficient spatial resolution elsewhere.

The [C II] emission towards P1a shares broad kinematic characteristics like the gradients along the Threads with the molecular line emission as we see in Figure B.4, but some key differences noted in Section 2.3.2 lead us to conclude that the PDR gas forms an extended envelope around the molecular gas. We do not detect the threaded morphology just south of the pillar head in [C II] or [O I] (see Figure 2.3). This is not solely due to the coarser spatial resolution of the fine structure line observations because smoothing the CO to the same resolution preserves the structure. The [C II] emission along the pillar body towards the Threads is spatially broad, $\sim$0.3 pc, and is centered on the Eastern Thread; from a purely spatial standpoint, the [C II] emission appears to trace only the Eastern Thread. We do not detect the same transverse velocity gradient across the Eastern Thread in [C II] as we do in the molecular lines. The PV diagrams in Figure 2.9 show that [C II] shifts to lower velocities instead, such that the [C II] line peaks at similar velocities as the molecular lines towards both the Eastern and Western Threads. We interpret this as a kinematic detection of [C II] emission associated with the Western Thread. Modeled [C II] central velocities show that, while the Eastern Thread has a bulk molecular gas velocity $\sim 1\ \mathrm{km\ s^{-1}}$ higher than the Western Thread, the [C II] emission only shifts by $\sim 0.3\ \mathrm{km\ s^{-1}}$ between the same locations. The [C II] PV diagrams are spatially and kinematically broad and uniform, and the molecular line PV diagrams show more structure with more extreme velocities and narrower line widths.

Appendix C: Regarding the Study of M16

C.1 NGC 6611 Stars

Hillenbrand et al. (1993) and Stoop et al. (2023) both present catalogs of O and B stars in NGC 6611. The former is a well-established catalog which has been used in studies such as Karim et al. (2023) and the latter is a compilation of types from more recent literature (Evans et al., 2005; Hillenbrand et al., 1993; Martayan et al., 2008; Sana et al., 2009; Wolff et al., 2007) (cite, cite, cite). The most massive cluster member is listed by Hillenbrand et al. (1993) as O5 V((f*)) (No. 205) and by Stoop et al. (2023) as a binary O3.5 V((f)) + O7.5 V (No. 142); both of these refer to the same cluster member. This and 2–3 other early O stars near the cluster core dominate the FUV radiation and stellar wind production of the entire cluster. Notably, the more recent catalog includes a handful of stars re-identified as binaries.

We filter and analyze each catalog independently to understand the effect on the feedback capacity estimates of catalog choice. Using the `scoby` software, we associate each star with a stellar model from the PoWR grid (Hainich et al., 2019; Sander et al., 2015) so that it has an associated FUV luminosity L_{FUV}, which is tied to its ability to illuminate PDRs. Feedback capacities from multiple-star systems are summed over the individual stars. We select systems with $log_{10}(L_{\mathrm{FUV}}/L_{\odot}) > 4.49$, which is equivalent to stars O9 V and brighter, and which are within a projected distance of 2.5 pc (5′) of the cluster center $(\alpha, \delta) = (274.^{\circ}67, -13.^{\circ}78)$ (J2000) determined by Stoop et al. (2023). Selected stars are listed in Table C.1.

C.2 CO Analysis with Radex

A grid of observable CO line parameters is generated by varying $N(\mathrm{H}_2)$ and n along the two axes with $T_\mathrm{K} = 30$ K fixed based on derived dust temperatures and CO line intensities. Values of $N(\mathrm{H}_2)$ and n are spaced logarithmically from $\log_{10}(N(\mathrm{H}_2)/\mathrm{cm}^{-2}) = 20$–$24$ and $\log_{10}(n/\mathrm{cm}^{-3}) = 2$–$6$ in steps of 0.05 dex; values outside these ranges are unrealistic in this context at the resolution of our observations.

The peak intensity of an observed CO transition appears as a contour over the grid, and a collection of observations of different CO transitions is visualized as an overlay plot (see the colored lines in Figures C.1 and C.2). Line ratios are valuable as they are less sensitive to the absolute brightness and filling factor of a source, so we use the ratio ^{13}CO(J=3–2)/^{13}CO(J=1–0), which is sensitive to density where both transitions are not optically thick.

The ^{13}CO(J=3–2) observations are convolved to the 55″ PMO beam and regridded to the 30″ pixel grid to match the CO (J=1–0) observations. We create masks for N19 and the Bright Northern Ridge, the two regions for which we apply this method, using integrated ^{12}CO(J=3–2) intensities in the velocity intervals $\mathrm{V_{LSR}} = 10$–$21\ \mathrm{km\,s^{-1}}$ for N19 and 23–27 $\mathrm{km\,s^{-1}}$ for the Bright Northern Ridge and show the masked regions over the 160 μm image in Figure C.3. We use peak line intensities in these intervals as the measurements and take the ratio described above. We use the RMS noise for each line as statistical uncertainty and adopt a 10% systematic uncertainty for each measurement to account for differences in the absolute calibrations.

We calculate the χ^2 at each model gridpoint, representing an $(N(\mathrm{H}_2), n)$ pair, using all three

RA (J2000)	DE (J2000)	H Type	S Type	H Index	S Index	Within Filter?
M16						
274.6290	-13.7190	O8.5 V	O8.5 V	161	15	H, S
274.6343	-13.8134	O8.5 V	O9 V	166	10	H, S
274.6364	-13.7533	O5.5 V((f))	O4 V((f)) + O7.5 V	175	8	H, S
274.6502	-13.7935	O7 V((f))	O6.5 V((f)) + B0-1 V	197	1	H, S
274.6518	-13.8007	O5 V((f*))	O3.5 V((f)) + O7.5 V	205	142	H, S
274.6541	-13.7980	B1 III	B1 V	210	17	H
274.6562	-13.7276	O7 III((f))	O7 V((f))	222	35	H, S
274.6671	-13.7552	O7 II(f)	O7 II(f)	246	13	H, S
274.6910	-13.7753	B0 V	O7 V + B0.5 V + B0.5 V	314	6	S
274.7341	-13.8086	O8.5 V	O7 V + O8 V	401	2	H, S
N19						
274.5985	-13.6078	O9 V	O9 V	584	22	

Table C.1 Positions and types of stars/systems selected from the Hillenbrand et al. (1993) (H) and Stoop et al. (2023) (S) catalogs which are within 5′ (2.5 pc) of the cluster center and are above the FUV luminosity threshold according to their type in either catalog. Coordinates are ICRS at epoch J2000. Type and index columns are marked with "H" and "S" to indicate which catalog they reference. Indices are the "ID" value in Table 3A from Hillenbrand et al. (1993) and row numbers in Table C1 from Stoop et al. (2023). The last column states whether each member fulfills the filter criteria in each catalog: the letter "H" indicates that the system is above the FUV luminosity threshold according to the type in the Hillenbrand et al. (1993) catalog, and the letter "S" indicates the same for the Stoop et al. (2023) catalog type. All systems appear in both catalogs, but the type variation causes 1 system from each catalog to drop below the FUV luminosity threshold. The last row, separated with horizontal lines, lists the information for W584, the star powering N19. All of these stars, including W584, are considered NGC 6611 members.

measurements and their uncertainties towards each pixel (one line of sight) under the masks. The model whose $N(\mathrm{H}_2)$ and n gridpoint holds the minimum χ^2 value is considered the solution for that pixel. We use as an error ellipse the $\chi^2 = 1$ contour and plot the results for all pixels in Figures C.1 and C.2 as black points. We are fitting 2 parameters to 3 measurements, so we have one degree of freedom and the reduced χ^2 is the same as χ^2.

To obtain typical $N(\mathrm{H}_2)$ and n values for N19 and the Bright Northern Ridge, we take the median of the pixel solutions. We use the 16^{th} and 84^{th} percentile values as the lower and upper error bounds, respectively. This is visualized with the histograms along each axis in Figures C.1 and C.2 and their medians and error bounds marked in pink. The solution for each region is overlaid in pink on the cluster of point solutions in the central panel. The solutions and their uncertainties are listed in Table 3.1.

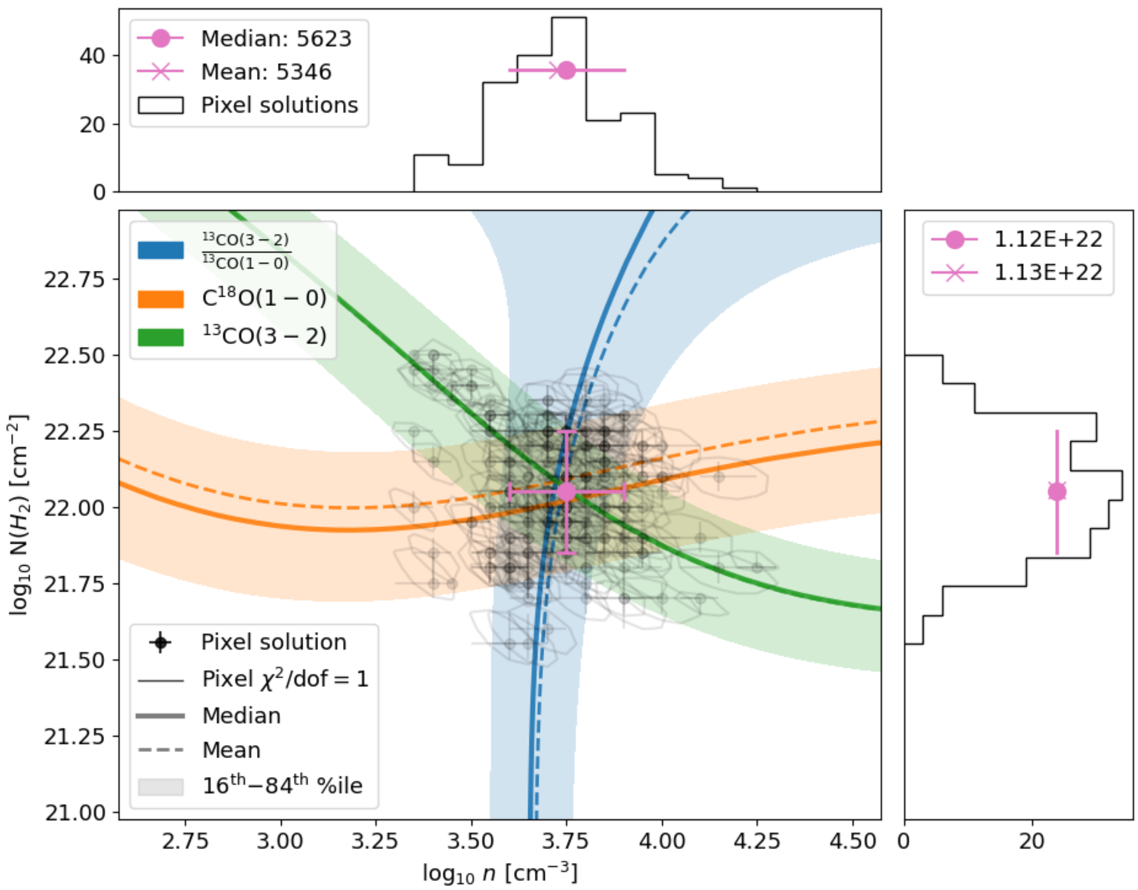

Figure C.1 The CO line model grid solutions for N19. Grey points in the central panels mark individual pixel solutions and their $\chi^2 = 1$ contours, which we use as error ellipses. Each pixel's error bars are calculated from the error ellipse. The curves show the median (solid) and mean (dashed) line measurements. The shaded regions around the curves show the 16$^{\text{th}}$ to 84$^{\text{th}}$ percentile ranges for the measurements. Histograms along each axis show the pixel solution distributions for each parameter. Their medians (circle) and means (X) are marked in pink along with the 16$^{\text{th}}$ to 84$^{\text{th}}$ percentile range, which is used as uncertainty. The median solutions and uncertainties are overlaid onto the central grid in pink.

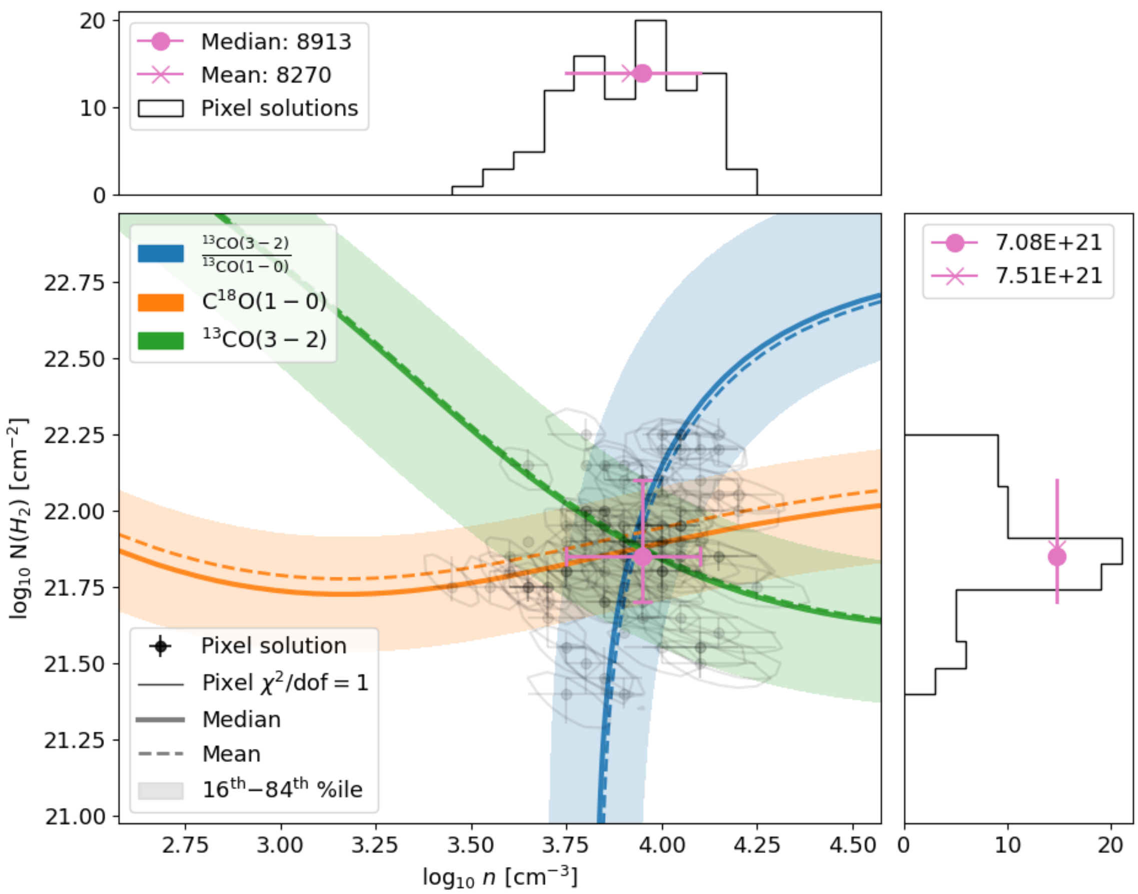

Figure C.2 Same as Figure C.1 for the Bright Northern Ridge.

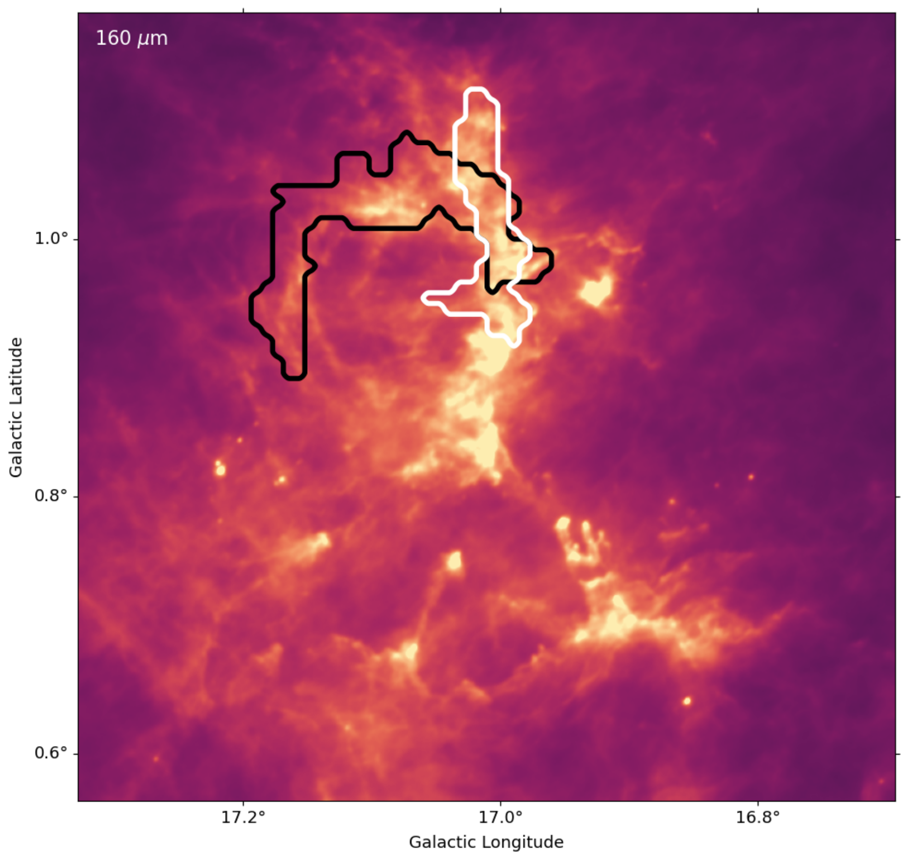

Figure C.3 The N19 (black) and Bright Northern Ridge (white) masks are contoured over the 160 μm image.

Bibliography

Abdullah, A., & Tielens, A. G. G. M. 2020, A&A, 639, A110, doi: 10.1051/0004-6361/202037796

An, L., Ji, F., Yin, Y., Liu, Y., & Zhou, C. 2022, Cells, 11, doi: 10.3390/cells11243987

Andersen, M., Knude, J., Reipurth, B., et al. 2004, A&A, 414, 969, doi: 10.1051/0004-6361:20031535

Anderson, L. D., Bania, T. M., Balser, D. S., et al. 2014, ApJS, 212, 1, doi: 10.1088/0067-0049/212/1/1

Anderson, L. D., Bania, T. M., Balser, D. S., & Rood, R. T. 2011, ApJS, 194, 32, doi: 10.1088/0067-0049/194/2/32

Astropy Collaboration, Robitaille, T. P., Tollerud, E. J., et al. 2013, A&A, 558, A33, doi: 10.1051/0004-6361/201322068

Astropy Collaboration, Price-Whelan, A. M., Sipőcz, B. M., et al. 2018, AJ, 156, 123, doi: 10.3847/1538-3881/aabc4f

Astropy Collaboration, Price-Whelan, A. M., Lim, P. L., et al. 2022, ApJ, 935, 167, doi: 10.3847/1538-4357/ac7c74

Axford, W. I. 1964, ApJ, 140, 112, doi: 10.1086/147899

Bailey, N. D., & Basu, S. 2014, ApJ, 780, 40, doi: 10.1088/0004-637X/780/1/40

Bakes, E. L. O., & Tielens, A. G. G. M. 1994, ApJ, 427, 822

Bally, J., & Reipurth, B. 2003, AJ, 126, 893, doi: 10.1086/376599

Bania, T. M., Anderson, L. D., Balser, D. S., & Rood, R. T. 2010, ApJL, 718, L106, doi: 10.1088/2041-8205/718/2/L106

Beaumont, C. N., & Williams, J. P. 2010, ApJ, 709, 791, doi: 10.1088/0004-637X/709/2/791

Belikov, A. N., Kharchenko, N. V., Piskunov, A. E., & Schilbach, E. 1999, A&AS, 134, 525, doi: 10.1051/aas:1999154

—. 2000, A&A, 358, 886

Benjamin, R. A., Churchwell, E., Babler, B. L., et al. 2003, PASP, 115, 953, doi: 10.1086/376696

Bennett, C. L., Fixsen, D. J., Hinshaw, G., et al. 1994, ApJ, 434, 587, doi: 10.1086/174761

Bergin, E. A., Plume, R., Williams, J. P., & Myers, P. C. 1999, The Astrophysical Journal, 512, 724, doi: 10.1086/306791

Berné, O., Marcelino, N., & Cernicharo, J. 2010, Nature, 466, 947, doi: 10.1038/nature09289

Bertoldi, F. 1989, ApJ, 346, 735, doi: 10.1086/168055

Bertoldi, F., & McKee, C. F. 1990, ApJ, 354, 529, doi: 10.1086/168713

Beuther, H., Schneider, N., Simon, R., et al. 2022, A&A, 659, A77, doi: 10.1051/0004-6361/202142689

Blitz, L., & Shu, F. H. 1980, ApJ, 238, 148, doi: 10.1086/157968

Bock, D. C. J., Bolatto, A. D., Hawkins, D. W., et al. 2006, in Society of Photo-Optical Instrumentation Engineers (SPIE) Conference Series, Vol. 6267, Society of Photo-Optical Instrumentation Engineers (SPIE) Conference Series, ed. L. M. Stepp, 626713, doi: 10.1117/12.674051

Bohlin, R. C., Savage, B. D., & Drake, J. F. 1978, ApJ, 224, 132, doi: 10.1086/156357

Bonne, L., Schneider, N., García, P., et al. 2022, ApJ, 935, 171, doi: 10.3847/1538-4357/ac8052

Bonne, L., Bontemps, S., Schneider, N., et al. 2023a, ApJ, 951, 39, doi: 10.3847/1538-4357/acd536

Bonne, L., Kabanovic, S., Schneider, N., et al. 2023b, A&A, 679, L5, doi: 10.1051/0004-6361/202347721

Bonne, L., Andersson, B. G., Minchin, R., et al. 2023c, AJ, 165, 243, doi: 10.3847/1538-3881/accf85

Bradley, L., Deil, C., Ginsburg, A., et al. 2022, astropy/regions: v0.7, v0.7, Zenodo, Zenodo, doi: 10.5281/zenodo.7259631

Brand, J., & Blitz, L. 1993, A&A, 275, 67

Braz, M. A., & Epchtein, N. 1983, A&AS, 54, 167

Briggs, D. S. 1995, in Bulletin of the American Astronomical Society, Vol. 27, American Astronomical Society Meeting Abstracts, 1444

Carlqvist, P., Gahm, G. F., & Kristen, H. 2002, Ap&SS, 280, 405, doi: 10.1023/A:1015602423235

Carretero-Castrillo, M., Ribó, M., & Paredes, J. M. 2023, A&A, 679, A109, doi: 10.1051/0004-6361/202346613

Chandrasekhar, S., & Fermi, E. 1953, ApJ, 118, 113, doi: 10.1086/145731

Churchwell, E. 2002, ARA&A, 40, 27, doi: 10.1146/annurev.astro.40.060401.093845

Churchwell, E., Whitney, B. A., Babler, B. L., et al. 2004, ApJS, 154, 322, doi: 10.1086/422504

Churchwell, E., Povich, M. S., Allen, D., et al. 2006, ApJ, 649, 759, doi: 10.1086/507015

Churchwell, E., Watson, D. F., Povich, M. S., et al. 2007, ApJ, 670, 428, doi: 10.1086/521646

Churchwell, E., Babler, B. L., Meade, M. R., et al. 2009, PASP, 121, 213, doi: 10.1086/597811

Codella, C., Felli, M., Natale, V., Palagi, F., & Palla, F. 1994, A&A, 291, 261

Codella, C., Palumbo, G. G. C., Pareschi, G., et al. 1995, MNRAS, 276, 57, doi: 10.1093/mnras/276.1.57

Comerón, F., & Torra, J. 2018, A&A, 618, A67, doi: 10.1051/0004-6361/201833929

Cooksy, A. L., Blake, G. A., & Saykally, R. J. 1986, ApJL, 305, L89, doi: 10.1086/184691

Cuadrado, S., Salas, P., Goicoechea, J. R., et al. 2019, A&A, 625, L3, doi: 10.1051/0004-6361/201935556

Dale, J. E., Ercolano, B., & Bonnell, I. A. 2012, MNRAS, 424, 377, doi: 10.1111/j.1365-2966.2012.21205.x

Davis, L. 1951, Physical Review, 81, 890, doi: 10.1103/PhysRev.81.890.2

De Marchi, G., Panagia, N., Guarcello, M. G., & Bonito, R. 2013, MNRAS, 435, 3058, doi: 10.1093/mnras/stt1499

de Winter, D., Koulis, C., The, P. S., et al. 1997, A&AS, 121, 223, doi: 10.1051/aas:1997284

Deharveng, L., Zavagno, A., Samal, M. R., et al. 2015, A&A, 582, A1, doi: 10.1051/0004-6361/201423835

Didelon, P., Motte, F., Tremblin, P., et al. 2015, A&A, 584, A4, doi: 10.1051/0004-6361/201526239

Diehl, R., Hartmann, D. H., & Prantzos, N. 2011, in Lecture Notes in Physics, Berlin Springer Verlag, ed. R. Diehl, D. H. Hartmann, & N. Prantzos, Vol. 812, 345–438, doi: 10.1007/978-3-642-12698-7_7

Draine, B. T. 2003, ARA&A, 41, 241, doi: 10.1146/annurev.astro.41.011802.094840

Dufton, P. L., Smartt, S. J., Lee, J. K., et al. 2006, A&A, 457, 265, doi: 10.1051/0004-6361:20065392

Eden, D. J., Liu, T., Kim, K.-T., et al. 2019, MNRAS, 485, 2895, doi: 10.1093/mnras/stz574

Edris, K. A., Fuller, G. A., & Cohen, R. J. 2007, A&A, 465, 865, doi: 10.1051/0004-6361:20066280

Elmegreen, B. G. 1979, ApJ, 232, 729, doi: 10.1086/157333

—. 2011, ApJ, 737, 10, doi: 10.1088/0004-637X/737/1/10

Elmegreen, B. G., & Lada, C. J. 1977, ApJ, 214, 725, doi: 10.1086/155302

Emig, K. L., White, G. J., Salas, P., et al. 2022, A&A, 664, A88, doi: 10.1051/0004-6361/202142596

Evans, C. J., Smartt, S. J., Lee, J. K., et al. 2005, A&A, 437, 467, doi: 10.1051/0004-6361:20042446

Fazio, G. G., Hora, J. L., Allen, L. E., et al. 2004, ApJS, 154, 10, doi: 10.1086/422843

Fixsen, D. J., Bennett, C. L., & Mather, J. C. 1999, ApJ, 526, 207, doi: 10.1086/307962

Flagey, N., Boulanger, F., Noriega-Crespo, A., et al. 2011, A&A, 531, A51, doi: 10.1051/0004-6361/201116437

Flagey, N., McLeod, A. F., Aguilar, L., & Prunet, S. 2020, A&A, 635, A111, doi: 10.1051/0004-6361/201833690

Fontani, F., Cesaroni, R., & Furuya, R. S. 2010, A&A, 517, A56, doi: 10.1051/0004-6361/200913679

Frieman, E. A. 1954, ApJ, 120, 18, doi: 10.1086/145877

Fukuda, N., & Hanawa, T. 2000, ApJ, 533, 911, doi: 10.1086/308701

Gahm, G. F., Carlqvist, P., Johansson, L. E. B., & Nikolić, S. 2006, A&A, 454, 201, doi: 10.1051/0004-6361:20054494

García-Rojas, J., Esteban, C., Peimbert, M., et al. 2006, MNRAS, 368, 253, doi: 10.1111/j.1365-2966.2006.10105.x

Geen, S., & de Koter, A. 2022, MNRAS, 509, 4498, doi: 10.1093/mnras/stab3245

Geen, S., Hennebelle, P., Tremblin, P., & Rosdahl, J. 2016, MNRAS, 463, 3129, doi: 10.1093/mnras/stw2235

Gies, D. R., & Bolton, C. T. 1986, ApJS, 61, 419, doi: 10.1086/191118

Ginsburg, A., Koch, E., Robitaille, T., et al. 2019, radio-astro-tools/spectral-cube: Release v0.4.5, v0.4.5, Zenodo, doi: 10.5281/zenodo.3558614

GLIMPSE Team. 2020, GLIMPSE I Archive, IPAC, doi: 10.26131/IRSA210

Goicoechea, J. R., Teyssier, D., Etxaluze, M., et al. 2015, ApJ, 812, 75, doi: 10.1088/0004-637X/812/1/75

Goldsmith, P. F., Langer, W. D., Pineda, J. L., & Velusamy, T. 2012, ApJS, 203, 13, doi: 10.1088/0067-0049/203/1/13

Gorti, U., & Hollenbach, D. 2002, ApJ, 573, 215, doi: 10.1086/340556

Griffin, M. J., Abergel, A., Abreu, A., et al. 2010, A&A, 518, L3, doi: 10.1051/0004-6361/201014519

Gritschneder, M., Burkert, A., Naab, T., & Walch, S. 2010, ApJ, 723, 971, doi: 10.1088/0004-637X/723/2/971

Guan, X., Stutzki, J., Graf, U. U., et al. 2012, A&A, 542, L4, doi: 10.1051/0004-6361/201218925

Guarcello, M. G., Caramazza, M., Micela, G., et al. 2012, ApJ, 753, 117, doi: 10.1088/0004-637X/753/2/117

Guarcello, M. G., Damiani, F., Micela, G., et al. 2010a, A&A, 521, A18, doi: 10.1051/0004-6361/201014237

Guarcello, M. G., Micela, G., Damiani, F., et al. 2009, A&A, 496, 453, doi: 10.1051/0004-6361/200810671

Guarcello, M. G., Micela, G., Peres, G., Prisinzano, L., & Sciortino, S. 2010b, A&A, 521, A61, doi: 10.1051/0004-6361/201014351

Guarcello, M. G., Prisinzano, L., Micela, G., et al. 2007, A&A, 462, 245, doi: 10.1051/0004-6361:20066124

Guevara, C., Stutzki, J., Ossenkopf-Okada, V., et al. 2020a, A&A, 636, A16, doi: 10.1051/0004-6361/201834380

—. 2020b, A&A, 636, A16, doi: 10.1051/0004-6361/201834380

Gum, C. S. 1955, MmRAS, 67, 155

Güsten, R., Nyman, L. Å., Schilke, P., et al. 2006, A&A, 454, L13, doi: 10.1051/0004-6361:20065420

Habing, H. J. 1968, BAN, 19, 421

Hainich, R., Ramachandran, V., Shenar, T., et al. 2019, A&A, 621, A85, doi: 10.1051/0004-6361/201833787

Harris, C. R., Millman, K. J., van der Walt, S. J., et al. 2020, Nature, 585, 357, doi: 10.1038/s41586-020-2649-2

Hartigan, P., Downes, T., & Isella, A. 2020, ApJL, 902, L1, doi: 10.3847/2041-8213/abac08

He, C.-C., & Ricotti, M. 2023, MNRAS, 522, 5374, doi: 10.1093/mnras/stad1289

He, C.-C., Ricotti, M., & Geen, S. 2019, MNRAS, 489, 1880, doi: 10.1093/mnras/stz2239

—. 2020, MNRAS, 492, 4858, doi: 10.1093/mnras/staa165

Healy, K. R., Hester, J. J., & Claussen, M. J. 2004, ApJ, 610, 835, doi: 10.1086/421759

Hennebelle, P., & Inutsuka, S.-i. 2019a, Frontiers in Astronomy and Space Sciences, 6, 5, doi: 10.3389/fspas.2019.00005

—. 2019b, Frontiers in Astronomy and Space Sciences, 6, 5, doi: 10.3389/fspas.2019.00005

Henney, W. J., Arthur, S. J., & García-Díaz, M. T. 2005, ApJ, 627, 813, doi: 10.1086/430593

Herrera-Camus, R., Bolatto, A. D., Wolfire, M. G., et al. 2015, ApJ, 800, 1, doi: 10.1088/0004-637X/800/1/1

Hester, J. J., Scowen, P. A., Sankrit, R., et al. 1996, AJ, 111, 2349, doi: 10.1086/117968

Hi-GAL Team. 2020a, Hi-GAL 70 micron Photometric Catalog, IPAC, doi: 10.26131/IRSA27

—. 2020b, Hi-GAL 160 micron Photometric Catalog, IPAC, doi: 10.26131/IRSA25

—. 2020c, Hi-GAL 250 micron Photometric Catalog, IPAC, doi: 10.26131/IRSA24

—. 2020d, Hi-GAL 350 micron Photometric Catalog, IPAC, doi: 10.26131/IRSA28

—. 2020e, Hi-GAL 500 micron Photometric Catalog, IPAC, doi: 10.26131/IRSA26

Higgs, L. A., Doherty, L. H., MacLeod, J. M., & Terzian, Y. 1979, AJ, 84, 77, doi: 10.1086/112391

Hill, T., Motte, F., Didelon, P., et al. 2011, A&A, 533, A94, doi: 10.1051/0004-6361/201117315

—. 2012, A&A, 542, A114, doi: 10.1051/0004-6361/201219009

Hillenbrand, L. A., Massey, P., Strom, S. E., & Merrill, K. M. 1993, AJ, 106, 1906, doi: 10.1086/116774

Hoare, M. G., Kurtz, S. E., Lizano, S., Keto, E., & Hofner, P. 2007, in Protostars and Planets V, ed. B. Reipurth, D. Jewitt, & K. Keil, 181, doi: 10.48550/arXiv.astro-ph/0603560

Hocuk, S., Szűcs, L., Caselli, P., et al. 2017, A&A, 604, A58, doi: 10.1051/0004-6361/201629944

Hollenbach, D. J., Takahashi, T., & Tielens, A. G. G. M. 1991, ApJ, 377, 192, doi: 10.1086/170347

Hollenbach, D. J., & Tielens, A. G. G. M. 1997, ARA&A, 35, 179, doi: 10.1146/annurev.astro.35.1.179

Hollenbach, D. J., & Tielens, A. G. G. M. 1999, Rev. Mod. Phys., 71, 173, doi: 10.1103/RevModPhys.71.173

Hopkins, P. F., Kereš, D., Oñorbe, J., et al. 2014, MNRAS, 445, 581, doi: 10.1093/mnras/stu1738

Howard, A. D. P., Whitworth, A. P., Marsh, K. A., et al. 2019, MNRAS, 489, 962, doi: 10.1093/mnras/stz2234

Hunter, J. D. 2007, Computing in Science & Engineering, 9, 90, doi: 10.1109/MCSE.2007.55

Indebetouw, R., Robitaille, T. P., Whitney, B. A., et al. 2007, ApJ, 666, 321, doi: 10.1086/520316

Jayasinghe, T., Dixon, D., Povich, M. S., et al. 2019, MNRAS, 488, 1141, doi: 10.1093/mnras/stz1738

Kaastra, J. S. 2017, A&A, 605, A51, doi: 10.1051/0004-6361/201629319

Kaastra, J. S., & Bleeker, J. A. M. 2016, A&A, 587, A151, doi: 10.1051/0004-6361/201527395

Kaastra, J. S., Mewe, R., & Nieuwenhuijzen, H. 1996, in UV and X-ray Spectroscopy of Astrophysical and Laboratory Plasmas, 411–414

Kabanovic, S., Schneider, N., Ossenkopf-Okada, V., et al. 2022, A&A, 659, A36, doi: 10.1051/0004-6361/202142575

Karim, R. L., Pound, M. W., Tielens, A. G. G. M., et al. 2023, AJ, 166, 240, doi: 10.3847/1538-3881/acff6c

Kaufman, M. J., Wolfire, M. G., & Hollenbach, D. J. 2006, ApJ, 644, 283, doi: 10.1086/503596

Kavak, Ü., Bally, J., Goicoechea, J. R., et al. 2022a, A&A, 663, A117, doi: 10.1051/0004-6361/202243332

Kavak, Ü., Goicoechea, J. R., Pabst, C. H. M., et al. 2022b, A&A, 660, A109, doi: 10.1051/0004-6361/202141367

Kavak, U., Wolfire, M., Pound, M., Schneider, N., & Tielens, A. 2023, in American Astronomical Society Meeting Abstracts, Vol. 55, American Astronomical Society Meeting Abstracts, 108.04

Kennicutt, R. C., Calzetti, D., Aniano, G., et al. 2011, PASP, 123, 1347, doi: 10.1086/663818

Kessel-Deynet, O., & Burkert, A. 2003, MNRAS, 338, 545, doi: 10.1046/j.1365-8711.2003.05737.x

Kim, J.-G., Kim, W.-T., & Ostriker, E. C. 2018, ApJ, 859, 68, doi: 10.3847/1538-4357/aabe27

Kim, K.-T., & Koo, B.-C. 2001, ApJ, 549, 979, doi: 10.1086/319447

Klaassen, P. D., Reiter, M. R., McLeod, A. F., et al. 2020, MNRAS, 491, 178, doi: 10.1093/mnras/stz3012

Klein, B., Hochgürtel, S., Krämer, I., et al. 2012, A&A, 542, L3, doi: 10.1051/0004-6361/201218864

Kuhn, M. A., Hillenbrand, L. A., Sills, A., Feigelson, E. D., & Getman, K. V. 2019, ApJ, 870, 32, doi: 10.3847/1538-4357/aaef8c

Kuhn, M. A., Benjamin, R. A., Zucker, C., et al. 2021, A&A, 651, L10, doi: 10.1051/0004-6361/202141198

Kumar, B., Sagar, R., Sanwal, B. B., & Bessell, M. S. 2004, MNRAS, 353, 991, doi: 10.1111/j.1365-2966.2004.08130.x

Lang, D., Hogg, D. W., Mierle, K., Blanton, M., & Roweis, S. 2010, AJ, 139, 1782, doi: 10.1088/0004-6256/139/5/1782

Lefloch, B., & Lazareff, B. 1994, A&A, 289, 559

Leitherer, C., Ekström, S., Meynet, G., et al. 2014, ApJS, 212, 14, doi: 10.1088/0067-0049/212/1/14

Leitherer, C., Ortiz Otálvaro, P. A., Bresolin, F., et al. 2010, ApJS, 189, 309, doi: 10.1088/0067-0049/189/2/309

Levenson, N. A., Graham, J. R., McLean, I. S., et al. 2000, ApJL, 533, L53, doi: 10.1086/312601

Li, G.-X., Urquhart, J. S., Leurini, S., et al. 2016, A&A, 591, A5, doi: 10.1051/0004-6361/201527468

Linsky, J. L., Gagné, M., Mytyk, A., McCaughrean, M., & Andersen, M. 2007, ApJ, 654, 347, doi: 10.1086/508763

Luisi, M., Anderson, L. D., Schneider, N., et al. 2021, Science Advances, 7, eabe9511, doi: 10.1126/sciadv.abe9511

Mackey, J., & Lim, A. J. 2010, MNRAS, 403, 714, doi: 10.1111/j.1365-2966.2009.16181.x

Malhotra, S., Helou, G., Stacey, G., et al. 1997, ApJL, 491, L27, doi: 10.1086/311044

Mangum, J. G., & Shirley, Y. L. 2015, PASP, 127, 266, doi: 10.1086/680323

Martayan, C., Floquet, M., Hubert, A. M., et al. 2008, A&A, 489, 459, doi: 10.1051/0004-6361:200809358

Martins, F., Hillier, D. J., Paumard, T., et al. 2008, A&A, 478, 219, doi: 10.1051/0004-6361:20078469

Martins, F., Schaerer, D., & Hillier, D. J. 2005, A&A, 436, 1049, doi: 10.1051/0004-6361:20042386

Matzner, C. D. 2002, ApJ, 566, 302, doi: 10.1086/338030

McKinney, W. 2010, in Proceedings of the 9th Python in Science Conference, Vol. 445, Austin, TX, 51–56

McLeod, A. F., Dale, J. E., Ginsburg, A., et al. 2015, MNRAS, 450, 1057, doi: 10.1093/mnras/stv680

McLeod, A. F., Gritschneder, M., Dale, J. E., et al. 2016, MNRAS, 462, 3537, doi: 10.1093/mnras/stw1864

Messier, C. 1781, Catalogue des Nébuleuses et des Amas d'Étoiles (Catalog of Nebulae and Star Clusters), Connoissance des Temps ou des Mouvements Célestes, for 1784, p. 227-267

Mizuta, A., Kane, J. O., Pound, M. W., et al. 2006, ApJ, 647, 1151, doi: 10.1086/505458

—. 2007, Ap&SS, 307, 183, doi: 10.1007/s10509-006-9252-3

Mohr-Smith, M., Drew, J. E., Barentsen, G., et al. 2015, MNRAS, 450, 3855, doi: 10.1093/mnras/stv843

Molinari, S., Swinyard, B., Bally, J., et al. 2010, A&A, 518, L100, doi: 10.1051/0004-6361/201014659

Moriguchi, Y., Onishi, T., Mizuno, A., & Fukui, Y. 2002, in 8th Asian-Pacific Regional Meeting, Volume II, ed. S. Ikeuchi, J. Hearnshaw, & T. Hanawa, 173–174

Motte, F., Bontemps, S., & Louvet, F. 2018, ARA&A, 56, 41, doi: 10.1146/annurev-astro-091916-055235

Motte, F., Zavagno, A., Bontemps, S., et al. 2010, A&A, 518, L77, doi: 10.1051/0004-6361/201014690

Mouschovias, T. C. 1991, ApJ, 373, 169, doi: 10.1086/170035

Nakagawa, T., Yui, Y. Y., Doi, Y., et al. 1998, ApJS, 115, 259, doi: 10.1086/313082

Nakamura, F., & Li, Z.-Y. 2008, ApJ, 687, 354, doi: 10.1086/591641

Newman, R. C., & Axford, W. I. 1967, ApJ, 149, 571, doi: 10.1086/149286

Nguyen Luong, Q., Motte, F., Hennemann, M., et al. 2011, A&A, 535, A76, doi: 10.1051/0004-6361/201117831

Nguyen-Lu'o'ng, Q., Motte, F., Carlhoff, P., et al. 2013, ApJ, 775, 88, doi: 10.1088/0004-637X/775/2/88

Nishimura, A., Fujita, S., Kohno, M., et al. 2021, PASJ, 73, S285, doi: 10.1093/pasj/psaa083

Okada, Y., Requena-Torres, M. A., Güsten, R., et al. 2015, A&A, 580, A54, doi: 10.1051/0004-6361/201525630

Oliveira, J. M. 2008, in Handbook of Star Forming Regions, Volume II, ed. B. Reipurth, Vol. 5, 599, doi: 10.48550/arXiv.0809.3735

Ossenkopf, V., Röllig, M., Neufeld, D. A., et al. 2013, A&A, 550, A57, doi: 10.1051/0004-6361/201219837

Pabst, C., Higgins, R., Goicoechea, J. R., et al. 2019, Nature, 565, 618, doi: 10.1038/s41586-018-0844-1

Pabst, C. H. M., Goicoechea, J. R., Teyssier, D., et al. 2017, A&A, 606, A29, doi: 10.1051/0004-6361/201730881

—. 2020, A&A, 639, A2, doi: 10.1051/0004-6361/202037560

Pabst, C. H. M., Hacar, A., Goicoechea, J. R., et al. 2021, A&A, 651, A111, doi: 10.1051/0004-6361/202140804

Pabst, C. H. M., Goicoechea, J. R., Hacar, A., et al. 2022, A&A, 658, A98, doi: 10.1051/0004-6361/202140805

Pattle, K., Ward-Thompson, D., Hasegawa, T., et al. 2018, ApJL, 860, L6, doi: 10.3847/2041-8213/aac771

Pellegrini, E. W., Baldwin, J. A., Ferland, G. J., Shaw, G., & Heathcote, S. 2009, ApJ, 693, 285, doi: 10.1088/0004-637X/693/1/285

Pellegrini, E. W., Baldwin, J. A., Brogan, C. L., et al. 2007, ApJ, 658, 1119, doi: 10.1086/511258

Peretto, N., & Fuller, G. A. 2010, ApJ, 723, 555, doi: 10.1088/0004-637X/723/1/555

Peretto, N., Lenfestey, C., Fuller, G. A., et al. 2016, A&A, 590, A72, doi: 10.1051/0004-6361/201527064

Pfalzner, S. 2009, A&A, 498, L37, doi: 10.1051/0004-6361/200912056

Pilbratt, G. L., Riedinger, J. R., Passvogel, T., et al. 2010, A&A, 518, L1, doi: 10.1051/0004-6361/201014759

Pineda, J. L., Velusamy, T., Langer, W. D., et al. 2010, A&A, 521, L19, doi: 10.1051/0004-6361/201015089

Poglitsch, A., Waelkens, C., Geis, N., et al. 2010, A&A, 518, L2, doi: 10.1051/0004-6361/201014535

Pound, M. W. 1998, ApJL, 493, L113, doi: 10.1086/311131

Pound, M. W., Kane, J. O., Ryutov, D. D., Remington, B. A., & Mizuta, A. 2007, Ap&SS, 307, 187, doi: 10.1007/s10509-006-9214-9

Pound, M. W., Reipurth, B., & Bally, J. 2003, AJ, 125, 2108, doi: 10.1086/368138

Pound, M. W., & Wolfire, M. G. 2008, in Astronomical Society of the Pacific Conference Series, Vol. 394, Astronomical Data Analysis Software and Systems XVII, ed. R. W. Argyle, P. S. Bunclark, & J. R. Lewis, 654

Pound, M. W., & Wolfire, M. G. 2023, AJ, 165, 25, doi: 10.3847/1538-3881/ac9b1f

Puls, J., Vink, J. S., & Najarro, F. 2008, A&A Rv, 16, 209, doi: 10.1007/s00159-008-0015-8

Ragan, S. E., Henning, T., Tackenberg, J., et al. 2014, A&A, 568, A73, doi: 10.1051/0004-6361/201423401

Ricotti, M. 2014, MNRAS, 437, 371, doi: 10.1093/mnras/stt1898

Rieke, M. J., Kelly, D. M., Misselt, K., et al. 2023, PASP, 135, 028001, doi: 10.1088/1538-3873/acac53

Risacher, C., Güsten, R., Stutzki, J., et al. 2018, Journal of Astronomical Instrumentation, 7, 1840014, doi: 10.1142/S2251171718400147

Rodgers, A. W., Campbell, C. T., & Whiteoak, J. B. 1960, MNRAS, 121, 103, doi: 10.1093/mnras/121.1.103

Röllig, M., Szczerba, R., Ossenkopf, V., & Glück, C. 2013, A&A, 549, A85, doi: 10.1051/0004-6361/201118190

Rygl, K. L. J., Wyrowski, F., Schuller, F., & Menten, K. M. 2010, A&A, 515, A42, doi: 10.1051/0004-6361/200913510

Samal, M. R., Deharveng, L., Zavagno, A., et al. 2018, A&A, 617, A67, doi: 10.1051/0004-6361/201833015

Sana, H., Gosset, E., & Evans, C. J. 2009, MNRAS, 400, 1479, doi: 10.1111/j.1365-2966.2009.15545.x

Sander, A., Shenar, T., Hainich, R., et al. 2015, A&A, 577, A13, doi: 10.1051/0004-6361/201425356

Sault, R. J., Teuben, P., & Wright, M. C. H. 2011, MIRIAD: Multi-channel Image Reconstruction, Image Analysis, and Display. http://ascl.net/1106.007

Sault, R. J., Teuben, P. J., & Wright, M. C. H. 1995, in Astronomical Society of the Pacific Conference Series, Vol. 77, Astronomical Data Analysis Software and Systems IV, ed. R. A. Shaw, H. E. Payne, & J. J. E. Hayes, 433. https://arxiv.org/abs/astro-ph/0612759

Schneider, N., Güsten, R., Tremblin, P., et al. 2012, A&A, 542, L18, doi: 10.1051/0004-6361/201218917

Schneider, N., Bontemps, S., Motte, F., et al. 2016, A&A, 591, A40, doi: 10.1051/0004-6361/201628328

Schneider, N., Simon, R., Guevara, C., et al. 2020, PASP, 132, 104301, doi: 10.1088/1538-3873/aba840

Schneider, N., Röllig, M., Polehampton, E. T., et al. 2021, A&A, 653, A108, doi: 10.1051/0004-6361/202140824

Schneider, N., Bonne, L., Bontemps, S., et al. 2023, Nature Astronomy, 7, 546, doi: 10.1038/s41550-023-01901-5

Sharpless, S. 1959, ApJS, 4, 257, doi: 10.1086/190049

Slaughter, C., Tielens, A., & Karim, R. 2023, in American Astronomical Society Meeting Abstracts, Vol. 55, American Astronomical Society Meeting Abstracts, 210.02

Sofia, U. J., Lauroesch, J. T., Meyer, D. M., & Cartledge, S. I. B. 2004, ApJ, 605, 272, doi: 10.1086/382592

Sofue, Y. 2020, MNRAS, 492, 5966, doi: 10.1093/mnras/staa226

Spitzer, Lyman, J. 1954, ApJ, 120, 1, doi: 10.1086/145876

Spitzer, L. 1978, Physical processes in the interstellar medium, doi: 10.1002/9783527617722

Steer, D. G., Dewdney, P. E., & Ito, M. R. 1984, A&A, 137, 159

Sternberg, A., Hoffmann, T. L., & Pauldrach, A. W. A. 2003, ApJ, 599, 1333, doi: 10.1086/379506

Sternberg, A., Le Petit, F., Roueff, E., & Le Bourlot, J. 2014, ApJ, 790, 10, doi: 10.1088/0004-637X/790/1/10

Stoop, M., Kaper, L., de Koter, A., et al. 2023, A&A, 670, A108, doi: 10.1051/0004-6361/202244511

Storm, S., Mundy, L. G., Lee, K. I., et al. 2016, ApJ, 830, 127, doi: 10.3847/0004-637X/830/2/127

Sugitani, K., Fukui, Y., & Ogura, K. 1991, ApJS, 77, 59, doi: 10.1086/191597

Sugitani, K., Tamura, M., Nakajima, Y., et al. 2002, ApJL, 565, L25, doi: 10.1086/339196

Sulentic, J. W., Tifft, W. G., & Dreyer, J. L. E. 1973, The revised new catalogue of nonstellar astronomical objects

Tarantino, E., Bolatto, A. D., Herrera-Camus, R., et al. 2021, ApJ, 915, 92, doi: 10.3847/1538-4357/abfcc6

Tauber, J. A., Lis, D. C., Keene, J., Schilke, P., & Buettgenbach, T. H. 1995, A&A, 297, 567

Tenorio-Tagle, G. 1979, A&A, 71, 59

Thompson, R. I., Smith, B. A., & Hester, J. J. 2002, ApJ, 570, 749, doi: 10.1086/339738

Tielens, A. G. G. M. 2008, ARA&A, 46, 289, doi: 10.1146/annurev.astro.46.060407.145211

—. 2010, The Physics and Chemistry of the Interstellar Medium

Tielens, A. G. G. M. 2021, Molecular Astrophysics (Cambridge University Press), doi: 10.1017/9781316718490

Tielens, A. G. G. M., & Hollenbach, D. 1985, ApJ, 291, 722, doi: 10.1086/163111

Tigé, J., Motte, F., Russeil, D., et al. 2017, A&A, 602, A77, doi: 10.1051/0004-6361/201628989

Tiwari, M., Karim, R., Pound, M. W., et al. 2021, ApJ, 914, 117, doi: 10.3847/1538-4357/abf6ce

Tiwari, M., Wolfire, M., Pound, M. W., et al. 2022, AJ, 164, 150, doi: 10.3847/1538-3881/ac8a44

Townsley, L. K., Broos, P. S., Garmire, G. P., et al. 2014, ApJS, 213, 1, doi: 10.1088/0067-0049/213/1/1

Tremblin, P., Audit, E., Minier, V., Schmidt, W., & Schneider, N. 2012a, A&A, 546, A33, doi: 10.1051/0004-6361/201219224

Tremblin, P., Audit, E., Minier, V., & Schneider, N. 2012b, A&A, 538, A31, doi: 10.1051/0004-6361/201118031

Umemoto, T., Minamidani, T., Kuno, N., et al. 2017, PASJ, 69, 78, doi: 10.1093/pasj/psx061

Vacca, W. D., Garmany, C. D., & Shull, J. M. 1996, ApJ, 460, 914, doi: 10.1086/177020

Valdettaro, R., Palla, F., Brand, J., & Cesaroni, R. 2005, A&A, 443, 535, doi: 10.1051/0004-6361:20053731

van der Tak, F. F. S., Black, J. H., Schöier, F. L., Jansen, D. J., & van Dishoeck, E. F. 2007, A&A, 468, 627, doi: 10.1051/0004-6361:20066820

Vázquez-Semadeni, E., Banerjee, R., Gómez, G. C., et al. 2011, MNRAS, 414, 2511, doi: 10.1111/j.1365-2966.2011.18569.x

Velusamy, T., Langer, W. D., Pineda, J. L., et al. 2010, A&A, 521, L18, doi: 10.1051/0004-6361/201015091

Virtanen, P., Gommers, R., Oliphant, T. E., et al. 2020, Nature Methods, 17, 261, doi: 10.1038/s41592-019-0686-2

Walker, C., Kulesa, C., Young, A., et al. 2022, in Society of Photo-Optical Instrumentation Engineers (SPIE) Conference Series, Vol. 12190, Millimeter, Submillimeter, and Far-Infrared Detectors and Instrumentation for Astronomy XI, ed. J. Zmuidzinas & J.-R. Gao, 121900E, doi: 10.1117/12.2629051

Walker, M. F. 1961, ApJ, 133, 438, doi: 10.1086/147047

Watkins, E. J., Peretto, N., Marsh, K., & Fuller, G. A. 2019, A&A, 628, A21, doi: 10.1051/0004-6361/201935277

Weaver, R., McCray, R., Castor, J., Shapiro, P., & Moore, R. 1977, ApJ, 218, 377, doi: 10.1086/155692

Westerhout, G. 1958, BAN, 14, 215

Westmoquette, M. S., Dale, J. E., Ercolano, B., & Smith, L. J. 2013, MNRAS, 435, 30, doi: 10.1093/mnras/stt1172

White, G. J., Nelson, R. P., Holland, W. S., et al. 1999, A&A, 342, 233

Whitworth, A. P., & Priestley, F. D. 2021, MNRAS, 504, 3156, doi: 10.1093/mnras/stab1125

Whitworth, A. P., Priestley, F. D., & Geen, S. T. 2022, MNRAS, 517, 4940, doi: 10.1093/mnras/stac2955

Williams, R. J. R., Ward-Thompson, D., & Whitworth, A. P. 2001, MNRAS, 327, 788, doi: 10.1046/j.1365-8711.2001.04757.x

Wilson, T. L., & Rood, R. 1994, ARA&A, 32, 191, doi: 10.1146/annurev.aa.32.090194.001203

Wolff, S. C., Strom, S. E., Dror, D., & Venn, K. 2007, AJ, 133, 1092, doi: 10.1086/511002

Wolfire, M. G., Vallini, L., & Chevance, M. 2022, ARA&A, 60, 247, doi: 10.1146/annurev-astro-052920-010254

Xu, J.-L., Zavagno, A., Yu, N., et al. 2019, A&A, 627, A27, doi: 10.1051/0004-6361/201935024

Yan, Y. T., Zhang, J. S., Henkel, C., et al. 2019, The Astrophysical Journal, 877, 154, doi: 10.3847/1538-4357/ab17d6

Zamora-Avilés, M., Vázquez-Semadeni, E., González, R. F., et al. 2019, MNRAS, 487, 2200, doi: 10.1093/mnras/stz1235

Zavagno, A., Russeil, D., Motte, F., et al. 2010a, A&A, 518, L81, doi: 10.1051/0004-6361/201014623

Zavagno, A., Anderson, L. D., Russeil, D., et al. 2010b, A&A, 518, L101, doi: 10.1051/0004-6361/201014587

Zeidler, P., Sabbi, E., Nota, A., & McLeod, A. F. 2021, AJ, 161, 140, doi: 10.3847/1538-3881/abd6ca

Zeidler, P., Sabbi, E., Nota, A., et al. 2015, AJ, 150, 78, doi: 10.1088/0004-6256/150/3/78

Zhan, X.-L., Jiang, Z.-B., Chen, Z.-W., Zhang, M.-M., & Song, C. 2016, Research in Astronomy and Astrophysics, 16, 56, doi: 10.1088/1674-4527/16/4/056

Zhou, J. W., Wyrowski, F., Neupane, S., et al. 2023, A&A, 676, A69, doi: 10.1051/0004-6361/202346500

Zinnecker, H., & Yorke, H. W. 2007, ARA&A, 45, 481, doi: 10.1146/annurev.astro.44.051905.092549